THE SPATIOTEMPORAL DYNAMICS OF MYCOBACTERIAL INFECTION

A Dissertation

Presented to

the Faculty of the Department of Biomedical Engineering

University of Houston

In Partial Fulfillment

of the Requirements for the Degree

Doctor of Philosophy

in Biomedical Engineering

by

Danielle L. Stolley

August 2019

THE SPATIOTEMPORAL DYNAMICS OF MYCOBACTERIAL INFECTION

Danielle L. Stolley

Approved:

Chair of the Committee
Dr. Elebeoba E. May, Associate Professor,
Department of Biomedical Engineering

Committee Members:

Dr. Muayyad Al-Ubaidi, Professor,
Department of Biomedical Engineering

Dr. Chandra Mohan, Hugh Roy and Lillie Cranz Cullen Endowed Professor,
Department of Biomedical Engineering

Dr. Yingchun Zhang, Associate Professor,
Department of Biomedical Engineering

Dr. Ying Lin, Assistant Professor,
Department of Industrial Engineering

Dr. Suresh K. Khator,
Associate Dean,
Cullen College of Engineering

Dr. Metin Akay, Founding Chair,
John S. Dunn Cullen Endowed Professor,
Department of Biomedical Engineering

ACKNOWLEDGEMENTS

I would like to acknowledge Dr. May, along with all past and present members of the May lab for their assistance and support throughout my graduate research. I would like to specifically thank Dr. Tharmalingam for his assistance in *Mycobacterium bovis* BCG studies. I would also like to acknowledge and thank my committee members: Dr. Zhang; Dr. Mohan for his donation of C56/Bl6 mice utilized for initial testing; Dr. Al-Ubaidi for Ubq-GFP mice utilized for preliminary testing; and Dr. Lin for instruction and assistance in machine learning concepts. Fluorescent mycobacterium strains provided by Dr. Cirillo, Texas A&M University College of Medicine. Research supported by University of Houston Department of Biomedical Engineering, NSF BIO/MCB Award #1445470.

THE SPATIOTEMPORAL DYNAMICS OF MYCOBACTERIAL INFECTION

An Abstract

Of a

Dissertation

Presented to

the Faculty of the Department of Biomedical Engineering

University of Houston

In Partial Fulfillment

of the Requirements for the Degree

Doctor of Philosophy

in Biomedical Engineering

by

Danielle L. Stolley

August 2019

ABSTRACT

Host response to *Mycobacterium tuberculosis* (Mtb) is distinctive in the use of a spatial immunological response to limit the progression of infection. This results in the formation granulomas, aggregations of immune cells that isolate invading microbes, a hallmark of the adaptive immune response to Mtb infection. Traditional *in vivo* studies have investigated the mature granuloma, but relatively fewer studies investigate how these structures form during the early stages of infection nor how spatial organization impacts control, resolution, or dissemination of the bacterium. Research has shown that initial aggregation of macrophages during innate immune response influences the progression of disease and formation of granulomas during adaptive immunity. However, current experimental methods for studying cellular interactions during early stages of infection are ill adapted for concurrent spatial and temporal quantification of host-pathogen dynamics, which is necessary for a quantitative understanding of the innate spatial immune response to Mtb and to inform the development of accurate computational models of tuberculosis disease. To address this, we developed a three-dimensional (3D) *ex vivo* model of mycobacterium infected macrophages cultured in reconstituted basement membrane and characterized the structural impact of 3D structure on infection dynamics in comparison to standard two-dimensional (2D) infection models. We quantified temporal immune response using standard biological sampling methodologies and long-term time-lapse confocal imaging to quantify the early spatiotemporal dynamics of macrophage response to mycobacterium infection. Our studies using *Mycobacterium smegmatis* indicate that the 3D environment induces a shift in dynamics. In 3D we see significantly higher cellular velocities in infected conditions as compared to control non-

infected conditions, whereas the converse occurs in 2D. This may impact computational models that utilize 2D assumptions. We developed a data analysis pipeline to quantify macrophage state with respect to infection and cellular microenvironment. Results show non-infected and non-active macrophages within infected environments present dynamics comparable to controls, while infected and activated macrophages exhibit comparable spatiotemporal dynamics in 2D and 3D. Using the more virulent *Mycobacterium bovis* BCG, we observe a greater distinction between control and infected conditions and preliminary evidence of a more distinct 3D immune response resulting in increased cell death and extracellular bacteria.

TABLE OF CONTENTS

LIST OF FIGURES

LIST OF TABLES

1 INTRODUCTION

The study of infection traditionally focuses on the biochemical responses produced during host-pathogen interactions. However, this focus does not highlight the importance of the cellular spatiotemporal dynamics that are vital to the progression of diseases such as tuberculosis, caused by the bacterium *Mycobacterium tuberculosis* (Mtb). During Mtb infection, the bacterial dissemination can be chemically and physiologically inhibited by a coordinated multicellular immune response process involving modulation of the biochemical components of the inflammatory microenvironment, extracellular matrix (ECM) remodeling, regulation of cellular interactions, and formation of cellular aggregates, which can lead to the eventual development of granulomas [1]–[3]. This highly spatial response of granuloma formation, traditionally associated with adaptive immune response, actually begins in the early innate immune response to infection by macrophages the primary phagocytic cell involved in immune response to Mtb, mobilizing in a three-dimensional environment and recruiting cells to the sight of infection and providing the inflammatory signals for their activation [4], [5]. Involvement of the ECM is critical in this context as it provides for physiological limitations on inflammatory signaling and the proteolytic migration and activity of macrophages that impact the course of infection [1], [6], [7].

1.1 Granulomas

In both mice and humans, the progression of early *Mycobacterium tuberculosis* infection is comparable. The early innate response after the initial uptake by local primary phagocytes leads to the accumulation of neutrophils, inflammatory monocytes, interstitial macrophages and dendritic cells in the lungs. These cells help to establish early nascent granulomas [4], [8]. Over time, granulomas become more defined following the initiation of the adaptive immune response and are characterized by organized collections of macrophages, lymphocytes, and fibroblasts that, along with biochemical effectors, help contain the bacterial infection. The mature adaptive granuloma has been classically described as a host-protective response as protective cellular barrier between the pathogen and the surrounding host tissue allowing the host immune system to localize its efforts to treat the infection[2], [9], [10]. However, granulomas that are unable to fully clear the infection produce a stalemate between the host pathogen that can eventually lead to bacterial dissemination [11]–[13]. While dissemination from granulomas has been primarily noted during late stage infection after the introduction of adaptive immunity, there is now evidence that the aggregation of macrophages during innate immune response can lead to the formation of nascent granulomas that benefit the pathogen and possibly promote bacterial dissemination during early infection [9], [14], [15]. The spatiotemporal dynamics governing the formation and immune function of nascent granulomas are pertinent to understanding host-pathogen dynamics during mycobacterial infection, disease, latency, and ultimately reactivation. However, in part due to imaging constraints, the investigation of the initial

dynamics of mycobacterium infection has mainly been limited to studies within zebrafish embryos.

1.2 *In vivo* models of Mtb infection

Animal *in vivo* models of Mtb infection have provided an in-depth view of structural features of the granuloma through histological analysis of cellular organization post activation of the adaptive immune response. Mouse models have granted insight into the roles that specific genes play in the progression of disease, [16]. Guinea pig and rabbit models have provided a method to study necrotic granulomas, and non-human primates infected with Mtb produce granulomas, cavitation and disease progression comparable to human, and allow for the study coinfection with HIV and treatment with anti-TNF compounds [17]–[20].

However, a significant limitation of *in vivo* investigations is that the study of the structural immune response to Mtb requires extraction and fixation of tissue samples, limiting temporal analysis of granuloma formation particularly during early granuloma formation and initial cell recruitment [16]–[19]. This temporal limitation makes it infeasible to monitor the formation of a specific granuloma over time and characterize the dynamic innate response that drives the complex developmental process of nascent granuloma. A few experimental models utilize live cell imaging to begin dissecting these dynamics, mainly utilizing either zebrafish embryo models [9], [14], [15] or short-term intravital imaging in mice [10] .

1.3 *In vitro* and *ex vivo* models of Mtb infection

In an effort to maintain the spatial components of *in vivo* models including nutrient and oxygen gradients, cell-matrix interactions, and gene expression that are vital in modeling mycobacterial infection, there has been recent focus on the development of 3D *in vitro* models[21]. These models have implemented multiple cell types and allowed for the investigation of individual variables of infection within a simplified environment and structure. The model developed by Puissegur et al. utilized human peripheral blood mononuclear cells (PBMCs) and mycobacterial antigen coated beads to induce the formation of cell aggregation comparable to native granulomas [22]. Braian et al. produced a model of human lung tissue which consisted of a collagen gel with embedded fibroblasts, epithelial cells and macrophages infected with Mtb [23]. Bielecka et al. developed a microfluidic model of Mtb infection to study antimicrobial resistance. This model applied microspheres with Mtb, human PBMCs and type I collagen in a bioelectrospray to analyze the impact of infection on cellular aggregation and antibiotic treatment [24]. Kapoor et al. produced a 3D model of Mtb dormancy, resuscitation and anti-tumor necrosis factor-alpha treatment with human PBMCs in a collagen I matrix [25]. Hoang et al. developed a 3D tissue model of human lung mucosa with human dendritic cells and implicated further application of their tissue model to study bacterial infection with Mtb [26]. Furthering the Hoang platform, Parasa et al. investigated early granuloma formation [27], [28]. These 3D *in vitro* models have been developed to isolate the individual components of infection and provide high-throughput platforms for analysis with standardized sampling. However, these vast

majority of these *in vitro* platforms encounter some of the same limitations of *in vivo* models requiring sample fixation and immunohistological staining to quantify the cellular spatial organization of the host response. The recent model development by Tezera et al. improved on the lack of longitudinal data through their investigated a collagen-alginate bioelectropsray model of human PMBC infection with Mtb and performed analysis utilizing fluorescent microscopy , histological staining, immunohistochemistry, and flow cytometric analysis over 21 days [29].

Still, these developed models do not enable isolation and characterization of the impact of individual cellular components on the host system and lack the ability to continuously monitor bacterial load dynamics. In addition, due to the lack of temporal quantification there is currently no existing 3D *in vitro* models that have the ability to monitor infection load-based dynamics at a single cell resolution which is key to understanding load based dynamics [30].

2 PRELIMINARY DETERMINATION OF INFECTION AND PREDICTION OF HOST CELL STATUS USING MACHINE LEARNING

2.1 Introduction

The study of cellular spatiotemporal dynamics is vital in the understanding of bacterial infection, particularly for *Mycobacterium tuberculosis* (Mtb), the causative agent of tuberculosis. During Mtb infection, Mtb can be contained in a granuloma via a multicellular dynamic process involving infiltration of immune cells, production of chemical effector molecules, and extracellular matrix (ECM) remodeling [1]–[3]. Granuloma formation and integrity depend on the ability of macrophages, the primary phagocytic cell involved in both innate and adaptive immune response to Mtb, to mobilize and respond in a three-dimensional (3D) environment. We present a preliminary investigation of the quantifiable spatiotemporal dynamics of macrophage response to bacterial infection through multi-area time-lapse confocal imaging. Through this application we identify features that correlate with bacterial load, and host cell dynamics in variable environments.

Current studies of *in vivo* Mtb infection provide an in-depth, static view of the mature granuloma through histological analysis of macrophage and lymphocyte spatial organization [31]. While representative of the complex state of static infection, these investigations require the extraction and fixation of living tissue samples, preventing temporal analysis of infection progression and granuloma formation. Additionally,

traditional *in vitro* models of infection simplify this highly spatial response to a two-dimensional (2D) plane [32]. A final challenge is that existing 3D *in vitro* models limit investigation of temporal dynamics due to their reliance on standard histological methods, or they employ techniques to induce granuloma formation [23]–[27], [29], [33].

While current 3D models can be highly representative, they tend to be complex and do not allow for the isolation and quantifiable determination of the impact of host-pathogen and cell-to-cell interactions on the overall system. Furthermore, they are unable to monitor infection load-based dynamics with single cell resolution, which can greatly influence general host response [30]. Our integrated *in vitro* and computational platform mitigates some of the drawbacks of existing models through: employing sample collection standards of traditional 2D *in vitro* studies, providing a 3D environment for spatial response, utilizing long-term time-lapse confocal imaging (Figure 1), image segmentation and tracking to capture the response of macrophages to Mtb infection, and a coupled analysis pipeline for analytical characterization of host-pathogen interactions.

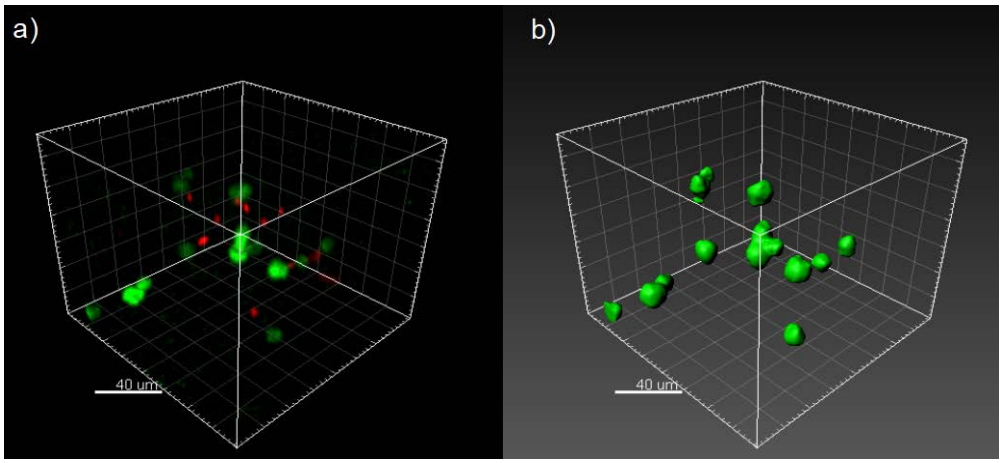

Figure 1: Example of confocal imaging datasets and image segmentation: mSmeg mCherry MOI 10 RAW 264.7 GFP Hour 0 Confocal Z-stack of 3D infections a) Imaris-Gaussian smoothing [1um] and contrast adjustment b) Imaris-Surface segmentation and tracking

To characterize the single cell, infection-dependent dynamics, we first employed unsupervised machine learning to segment the heterogeneous population of infected cells based on bacterial load determined by fluorescence levels. After this distinction is established, we then use supervised machine learning algorithms to determine which features can be used to distinguish infected cells from non-infected cells. Feature identification allows for the exploratory investigation of dynamics based on intracellular bacterial load and allows for future quantitative analysis and model development.

2.2 Materials and Methods

We adapted a 3D culturing protocol from Lee et al. [34] in reconstituted basement membrane (RBM) (Sigma Aldrich) and employed volumetric reduction to prevent hypoxia [35]. Standard 2D infection studies were conducted as previously reported [36], with and without gentamicin to allow for comparison to 3D RBM cultures, thus enabling

our focus on intracellular infection-driven response by reducing extracellular bacterial replication. The infection studies were conducted for 72 hours (with imaging for 55 hours) using green fluorescent protein (GFP) tagged *RAW 264.7* murine macrophage cell line (RelA) and mCherry tagged *M. smegmatis* (mSmeg) [37] at a multiplicity of infection (MOI) of 10 colony-forming units (CFU) per macrophage. Supernatant samples were collected every 24 hours and CFUs enumerated (data not presented). The 2D and 3D *in vitro* infection studies were conducted simultaneously with multi-area time-lapse confocal imaging of multiple experimental conditions.

2.2.1 Microscopy and Image Processing

3D confocal images (Olympus) were acquired every hour using a stage top incubation system (TokaiHit). The resulting 4D time appended acquisitions were rendered and analyzed using Imaris 8.1.2 (Bitplane) with surface creation and tracking of the macrophages. The same image processing parameters were used for all conditions. The 4D datasets were then transformed for time independence to provide a dataset of 3661 homogenous data points (control cells) and 2194 heterogeneous data points (infection cells). Features selected for analysis are summarized Table 1 below.

Table 1: Selected Features for Analysis (A.U. – Arbitrary units)		
Feature Explanation		
Feature	***Unit***	***Description***
RFP Maximum	A.U.	Maximum intensity in cell
RFP Sum	A.U.	Sum intensity in cell
RFP StdDev	A.U.	Standard Deviation of intensity in cell
RFP Median	A.U.	Median intensity in cell
RFP Mean	A.U.	Mean intensity in cell
Sphericity	A.U.	How spherical the cell is
Ellipicity Oblate	A.U.	How Flattened (z) the cell is
Elliplicity Prolate	A.U.	How Elongated (z) the cell is
Speed	µm/s	Nondirectional 3D vector speed of cell
Volume	μm^3	Volume of cell
Directedness	A.U	Inverse of random movement
Distance Traveled	µm	Total distance traveled

2.2.2 Noise Reduction and Normalization

The signal-to-noise ratio (SNR) during a long term time-lapse study varies if the acquisition parameters are not adjusted [38]. We reduced the impact of this variation in overall fluorescence levels (which indicates presence/absence of bacteria) post acquisition through background normalization by assuming that the bacterial red fluorescent protein (RFP) levels in the control conditions should remain constant (no bacteria present). By normalizing the control RFP summation minimum of the full image $RFP_{sum_{vol}}$, we account for the fold change in background fluorescence relative to the minimum. This can then be used to normalize all fluorescent features (RFP_X), except for standard deviation independent of time (t) to generate the adjusted feature (RFP'_x).

The adjusted RFP features were normalized to a range of (0,1) via feature scaling (RFP_x'') to reduce the impact of large magnitude difference [39] in the features given by equations 1 and 2 as

$$RFP_x'(t) = \frac{RFP_X(t) \cdot \min\left(RFP_{sum_{vol}}\right)}{RFP_{sum_{vol}}(t)} \text{ and} \quad (1)$$

$$RFP_x'' = \frac{RFP_X' - \min(RFP_X')}{\max(RFP_X') - \min(RFP_X')}. \quad (2)$$

All non-fluorescent features were unaltered for processing. The new datasets (adjusted RFP and original features) were then split into homogeneous (control condition) and heterogeneous (infection condition) datasets, independent of 2D or 3D status for this preliminary analysis to ensure that the applied methods would be consistent between dimensionalities.

2.2.3 Data Clustering – Infection Determination

The intracellular condition of a cell can change if its tracking is lost, if the cell phagocytizes bacteria, or if the cell kills the phagocytized bacteria. As each cell is already segmented and tracked with corresponding data through image processing in Imaris, the overall fluorescent data in each cell from phagocytized bacteria can easily provide features for use in unsupervised learning algorithms that can determine the infection state of the macrophage.

We utilized MatLab's k-means clustering algorithm (k=2) with k++ center initialization [40] and 10 replicates to reduce variability. Feature extraction through principal component analysis (PCA) was applied to compensate for feature correlation

and to lower data dimensionality [41]. The principal components were then ordered based on explanation of variability and iteratively added to assess cumulative explanation of variability and subsequent model fitness. Methods were applied both to the combined full dataset (control dataset and infection dataset) and the heterogeneous subset (infection dataset including cells with internalized bacteria and those without) with the homogenous (control) data points assigned to a cluster based on minimization of distance to cluster center point.

The control impurity (the percent homogenous data misclassified) was calculated by finding the intersection of the control data points (X_{ctrl}) and the cluster sets (C_k) from K-means (equation 3). The maximal intersection was taken as the non-infected cluster and any control points in the infected cluster contributed to control impurity (C_{imp}) as given by

$$C_{imp} = \left(\frac{1}{n_{ctrl}}\right) \min_{k=1:K} [X_{ctrl} \cap C_k]. \quad (3)$$

2.2.4 Linear Model Development

We applied supervised machine learning to explore the observable features of the cells and determine which can best characterize the infected nature of the cells, and how well the model can predict the infection status. This also provides a preliminary view into what features were impacted by the intracellular bacterial load of the cell.

MatLab's linear discriminant analysis (LDA) and classification trees were applied to the remaining features not used for cluster analysis (Table I). Parameter optimization of classification discriminant models was performed through the minimization of the misclassification rate using sequential forward selection (SFS).

Each model was 10-fold cross-validated, and the accuracy calculated. The receiver-operating curve (ROC) and resulting area under the curve (AUC) were used to determine the best-fit models. Kruskal-Wallis tests were run on best predictive feature to determine statistical significance.

2.3 Results

K-means clustering quickly separated the heterogeneous population of infected cells into two groups — those that actively contain bacteria and those that do not. Evaluation of the resulting clusters through the calculation of control impurity allows some control of accuracy and helps select for the optimum clustering method. For both datasets three principal components explain over 99% of the variability (Table 2) reducing the data dimensionality from five to three.

Table 2: K-Means Clustering with PCA		
Evaluation of PCA Accuracy and % Variability		
Feature	C_{imp}	***% Variability Explained***
Full Dataset		
1	0	84.45%
2	0	94.91%
3	0	99.20%
4	0	99.96%
5	0	100.00%
Heterogeneous Subset		
1	0	84.45%
2	0	94.91%
3	0	99.20%
4	0	99.96%
5	0	100.00%

We proceeded with the k-means algorithm applied to PCA feature scaled heterogeneous model with control data added post-clustering for further analysis to reduce the impact of imbalanced data [42]. This resulted in 4449 non-infected cells (3661 from homogenous subset) and 767 infected cells.

By applying LDA on the full dataset, sequential forward selection (SFS) determined the three features that minimized error (in order of selection) are Distance Traveled, Displacement, and Speed. Feature selection LDA increased the accuracy from 84.76% to 85.51% but reduced the AUC from 0.557 to 0.514. The heterogeneous subset shows a much different result. The four features that minimized error (in order of

selection) are Volume, Elliplicity Oblate, Elliplicity Prolate, and Speed. The SFS applied to the heterogeneous subset only shares one feature from the full dataset. The accuracy increases from 68.28% to 69.48% through SFS and the AUC increases from 0.641 to 0.653.

Classification trees applied to both the full dataset and heterogeneous only dataset were similarly feature selected. The results differed greatly from LDA in both magnitude of misclassification error and order of features selected. However, both data subsets used for classification trees maintain a similar predictor importance (Figure 2). Accuracy of 10-fold cross-validated classification trees decreases in the full dataset from 81.27% to 80.98% with SFS but increases from 68.38% to 70.06% in the heterogeneous subset. Conversely, the AUC in the full dataset decreased from 0.634 to 0.633, while increasing from 0.655 to 0.656 in the heterogeneous subset.

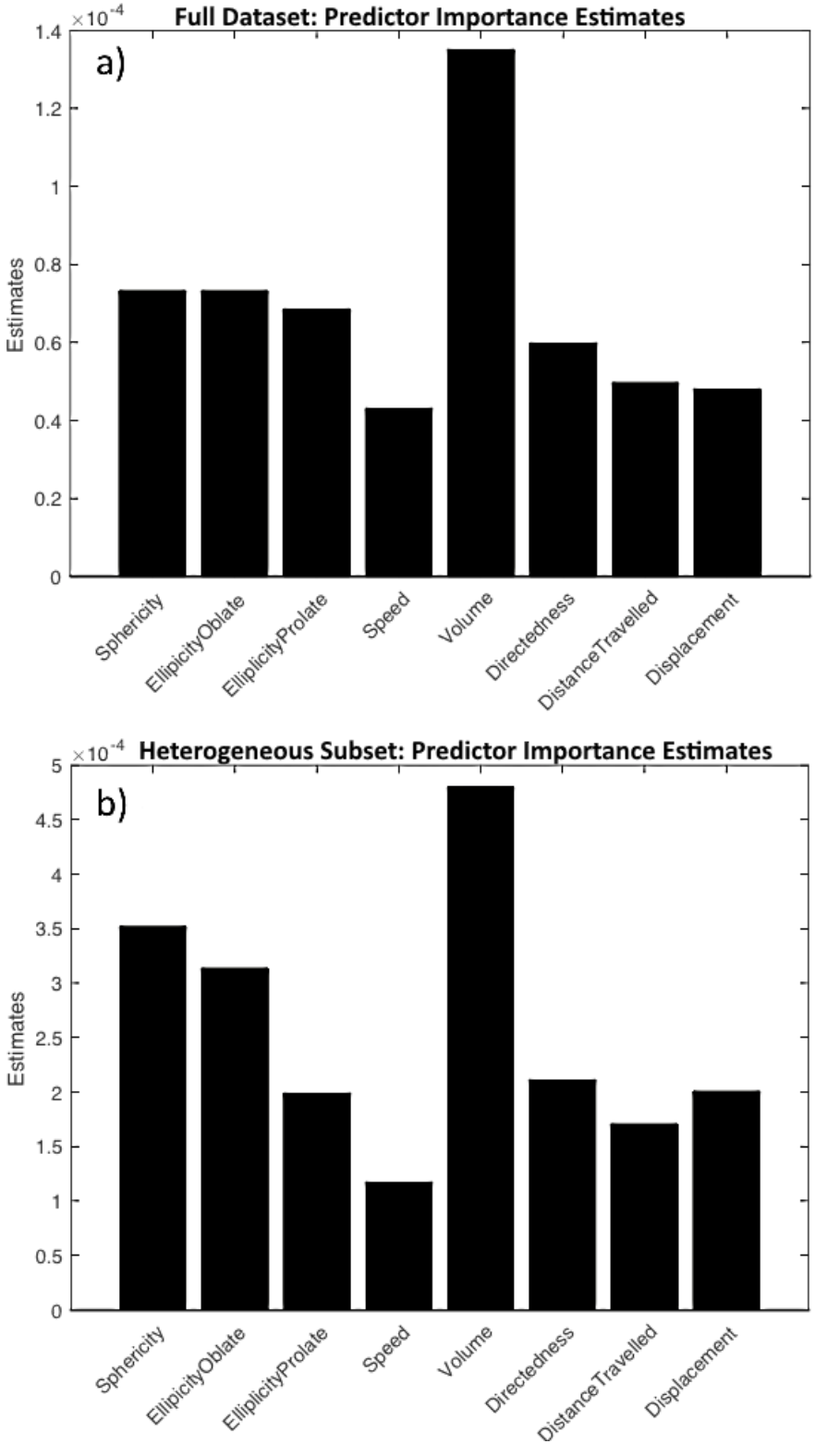

Figure 2: Predictor importance estimations (MatLab) – sum change in risk due to splits on every predictor divided by the number of branch nodes.

Kruskal-Wallis analysis (Figure 3) of volume data (highest predictor) shows a significant increase in average cell volume in the infection (heterogeneous) datasets likely due to the phagocytosis of bacteria [43].

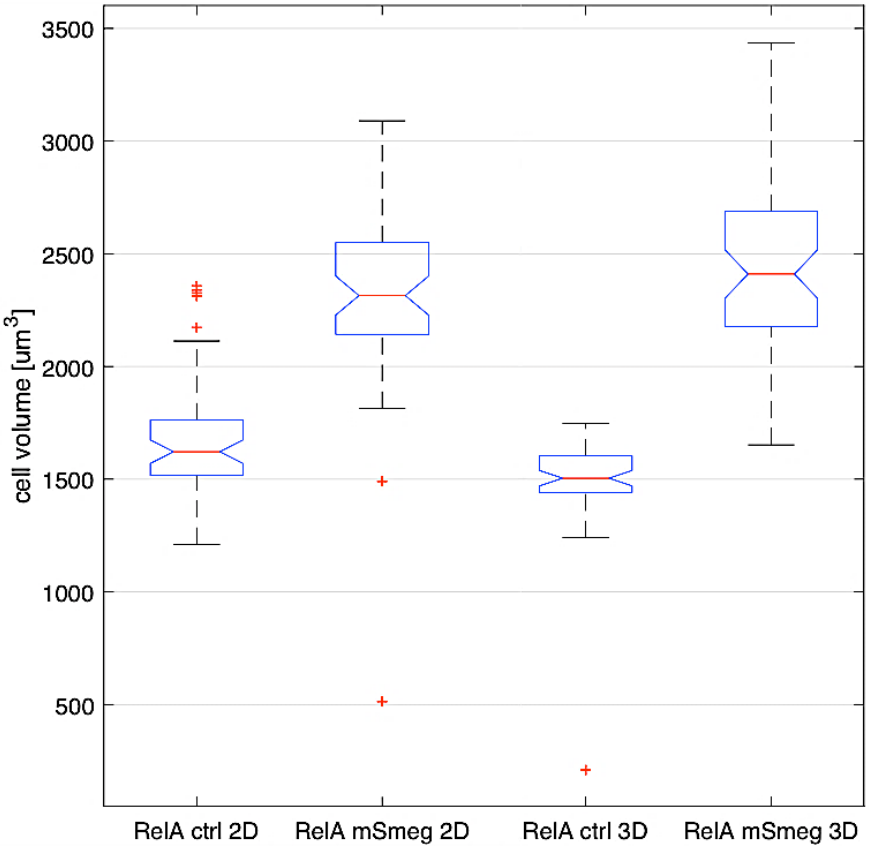

Figure 3: Kruskal-Wallis and rank-sum analysis on average cell volume per time point shows statistically significant difference between all data groups ($p < 0.001$) except RelA mSmeg 2D and RelA mSmeg 3D ($p > 0.05$).

2.4 Discussion

In this preliminary work we developed comparative 2D and 3D *in vitro* infection models, present an exploratory data analysis pipeline and machine learning algorithms to show the impact of intracellular mycobacterial load on macrophage spatiotemporal dynamics. We first applied k-means clustering to segment the heterogeneous subset based on assumed bacterial load and use this for further analysis. Both empirical

evidence [43] and statistical analysis on the imaging data support use of cell volume to predict infection. However, SFS of LDA performed on the full dataset identified volume as the lowest contributor to accuracy contradicting all other models that identifed volume as the most important feature, implying bias in the LDA.

When we removed a large subset of the data belonging to one class (homogenous control data) we decreased the class weight imbalance in the dataset reducing accuracy but increasing the AUC (which provides a more useful metric by considering the false positive rate) [44]. Overall, classification trees outperformed LDA in accuracy and AUC due to the ability to perform multiple linear separations for each feature and compensate for lack of data normality and homogeneity of covariance [45]. However, this increase in performance comes with increased model complexity and reduces the interpretability of the decision boundaries that can inform mechanistically driven models. Further analysis with additional features can determine algorithms that best balance model interpretability and performance.

Our work provides an initial platform for exploring the complex dynamics of macrophage-mycobacterium interactions and consequential outcomes. The use of machine learning methods to analyze 4D host-pathogen interaction data provides insight regarding the intracellular bacterial load's impact on behavior and dynamic response of macrophages during the initial phase of Mtb infection. This knowledge can be used in future work to develop more comprehensive computational platforms for quantitative characterization of single-cell and cellular neighborhood driven dynamics during mycobacterium infection.

3 OPTIMIZATION OF *EX VIVO* MODEL AND INVESTIGATION OF HOST RESPONSE TO *M. SMEGMATIS*

3.1 Introduction

To address some of the limitations in current models of granuloma formation, we have developed an experimental platform to comparatively investigate biochemical and spatiotemporal differences in individual cell and cell aggregate response to mycobacterial infection in 2D versus 3D cell culture. We utilize a reconstituted basement membrane (RBM) that recapitulates a 3D extracellular matrix microenvironment, an infection model consisting of fluorescently-labeled primary murine macrophages and mycobacterium to facilitate long-term multidimensional time-lapse confocal imaging for spatiotemporal monitoring and multi-time point sampling for biochemical assays, and an Imaris-MATLAB imaging processing platform to enable the use of 4D image segmentation, tracking, and analysis to capture and quantitatively characterize the structural immune response of macrophages to mycobacterial infection. Using this platform, we characterize the effect of bacterial load on macrophage spatiotemporal dynamics and investigate the correspondence between 2D/3D environment, macrophage structural response, production of effector molecules, and the dynamics of infection outcomes.

3.2 Materials and Methods

To develop a platform for the investigation of the spatiotemporal dynamics of infection, we take into consideration both the biological and technical constraints of live cell multi-area time-lapse confocal imaging. This involves macrophage and mycobacterium fluorescent variants, which are compared to their wildtype variants, and the subsequent generation of a 3D *ex vivo* infection platform permissible for mycobacterial infection and confocal imaging without inducing any variable effects to the cells or bacterium that are not accounted for in the standard 2D infection platform (Figure 4).

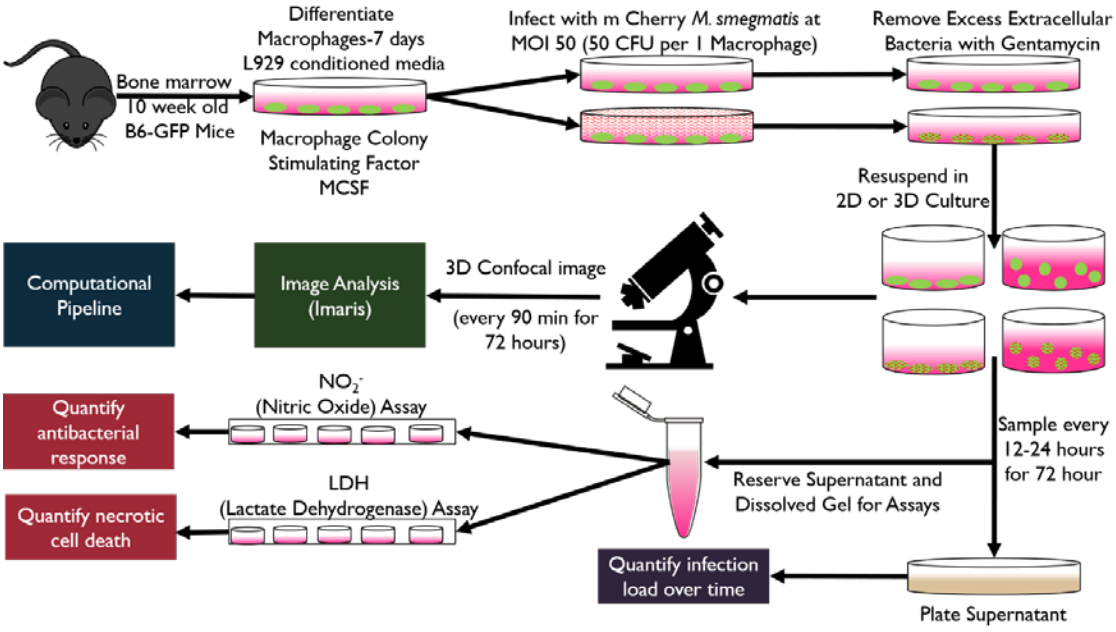

Figure 4: Outline of experimental methodology

3.2.1 Gas diffusion in 3D cell culture

Reliance on passive diffusion for the delivery of nutrients and oxygen to the system is a significant challenge in tissue engineering and in the development of 3D culture systems. Developing a system in which the cells receive adequate nutrient and remain well oxygenated, required constraints on ECM gel height and density to ensure oxygen diffusion and consumption throughout the system will be balanced. Using Colom et al.'s oxygen tension studies of human lung epithelial cell line A549 [35] we determined the theoretical maximum gel height that prevents hypoxia, which depends on maximal oxygen consumption rate (OCR) and cellular growth rate (Table 3) given by equation 4

$$h_{max} = \left(\frac{\phi_{limit}^2 K_m D_G^*}{\rho_0 V_{max}} e^{-\frac{t}{\tau}} \right)^{1\backslash 2} . \quad (4)$$

Table 3: Colom Formula for Maximal Gel Height to Prevent Hypoxia in RBM Culture

Variable	Description and Values Used
$\boldsymbol{h, h_{max}}$	(Maximum) gel thickness
$\boldsymbol{\phi_{limit}}$	Thiele modulus for normoxic environment (19 in for half gel depth, 16.45 for full gel depth (estimate)) assuming an oxygen tension limit of 50 mmHg [35] Normoxic oxygen tension is 20 to 50 mm Hg in most tissues (excluding high oxygenated environments such as arteries and aveoli).
$\boldsymbol{K_m}$	Oxygen concentration at which OCR is half of Vmax; V_{max} (0.45 mmHg = .58 E-3 mol m^{-3}) [35]
$\boldsymbol{D_G^*}$	Oxygen diffusivity in the gel in the presence of cells (1.7 E -5 cm^2/s, graphical estimation) [35]
$\boldsymbol{p_0}$	Initial cell seeding density (2.5 E 6 cells / mL)
$\boldsymbol{V_{max}}$	Maximum OCR per cell Maximum OCR for A549 in gel is ~ $3/10^{th}$ of 2D OCR (graphical estimation)[35] Maximum OCR for BMDM in 2D culture is ~ 1.7 E -16 moles/ (cell (second)) [46], which equates to an estimate of 5 E -17 moles/ (cell(second)) for BMDM in 3D RBM culture.
$\boldsymbol{\tau}$	Time constant describing cell proliferation rate (54 hours for A549 cells in gel) [35] However primary BMDM's do not proliferate well and attempts to extract cells from gel after 24 hours produce fewer cells than seeded, so the exponential $e^{-\frac{t}{\tau}}$ term will trend towards 1, changing the cell growth term from $p_0 e^{\frac{t}{\tau}}$ an assumption of exponential growth to $p_0$an assumption of no cell growth.
$\boldsymbol{t}$	Time in cell culture (hours)

The maximal OCR for bone marrow derived macrophages (BMDMs) from C57/BL6 mice (b6BMDM) in 2D culture is 1.7 E -16 moles/ (cell(second)) [46]. Using the derived equations from Colom et al. and the estimated change in OCR for BMDMs in RBM (5 E -17 moles/ (cell (second)), the estimated maximal height of RBM to maintain normoxia and prevent cell hypoxia is 1.46mm, approximately 140 µL of RBM per well of an 8 well chamber slide (Ibidi) or 48 well plate (VWR). The RBM used in the study by Colom et al. was 12 mg/mL concentration, 50% denser than the 8.5 mg/mL concentration for our 3D model. Using 140 µL as an upper limit, we tested various

volumes to find the minimal volume necessary to achieve a repeatable even gel layer, resulting in a 100uL RBM volume for 3D culture in 8 well chamber slides (1mm RBM height), sufficiently below the normoxic limit for resting OCR for non-infected b6BMDMs. The introduction of bacterial infection results in a heterogeneous cell population that includes resting, active (cells producing and responding to a proinflammatory environment), and infected macrophages, with active and infected cells conceivably having a higher OCR than their resting counterparts (estimated as two and three times the OCR of resting cells, respective) [47], [48]. Using these assumptions, we approximate the maximal height of RBM permissible under non-proliferating, homogenous cell-state assumptions. Cell cultures composed of active cells (max height permissible 1.023 mm) are still under normoxic conditions at 100 µL of RBM at a 1 mm gel, but a homogenous cell culture composed of infected cells (maximal height of .822 mm) is not.

3.2.2 Host Cells

All animal experiments were performed with the approval of the Institutional Animal Care and Use Committee at the University of Houston and in accordance with the recommendations in the Guide for the Care and Use of Laboratory Animals and the American Veterinary Medical Association (AVMA) Guidelines for the Euthanasia of Animals. The transgenic mouse line C57BL/6-Tg(CAG-EGFP)131Osb/LeySobJ (Jackson labs) were inbred for up to 4 generations. Bone marrow derived macrophages from the transgenic line (gfpBMDM) or from the C57BL/6 (Jackson labs) line (b6BMDM) were isolated from femoral and tibial bones of 10-week-old female mice unless otherwise

stated. The cells were subsequently aliquoted into freezing medium and stored in liquid nitrogen for up to four months according to the protocol outlined by Marim et al. [49]. One week prior to experiment start, macrophage aliquots were removed from liquid nitrogen, thawed and cultured as previously reported [50].

3.2.3 Homogeneity and persistence of mCherry expression in *M. smegmatis* culture

We selected the high expressing mCherry M. smegmatis (gifted by Dr. Cirillo Texas A&M University, TX) to minimize any potential spectral overlap with the gfpBMDM's EGFP during confocal imaging. To ensure a high correspondence between spatiotemporal image-based data and standard biological assays, we required a bacterial culture with homogenous and persistent expression of mCherry. We isolated and purified M. smegmatis strains with high, consistent expression of the mCherry plasmid through single colony isolation and expansion using the selective antibiotic hygromycin (80 µg/mL, VWR) (Figure 5).

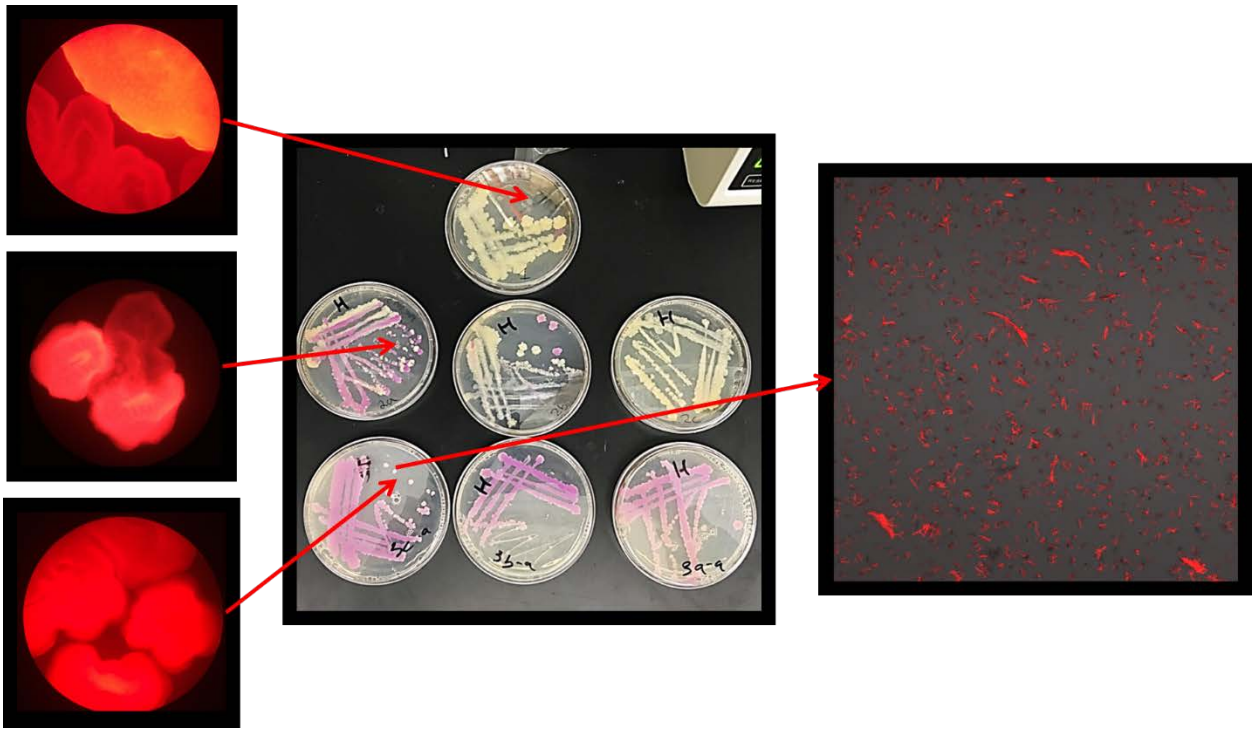

Figure 5: Purification of m. Cherry M. smegmatis with single colony expansion.

The accurate quantification of bacterial load via confocal imaging depends on the consistent ubiquitous expression of m. Cherry within each bacterium. To ensure even fluorescence bacterial stocks were streaked for singles on 7H11 plates with 80 µg/mL of hygromycin, the highest expressing CFU's were selected for (both colormetric and fluorescent) and subsequently streaked for singles until all colonies displayed a consistent level of m. Cherry expression. A single colony was then used to inoculate liquid culture which was then grown into the log phase (37 C at 250 RPM). The liquid stock was then plated to check for m. Cherry expression and used to make the working frozen aliquots of *m. Cherry M. smegmatis*.

Infection studies were performed in the absence of hygromycin, which affects both bacterial and mammalian cells, therefore we determined plasmid maintenance within *M. smegmatis* during extended culture in the absence of the selective antibiotic [51]. Persistence of the *mCherry* plasmid was determined using differential plating and microplate monitoring in a 96 well black well plate (Eppendorf). Briefly, *mCherry M. smegmatis* was grown in sealed (gas permeable Breathe-Easy, Diversified Biotech) black-walled 96 well plate (Eppendorf) in 7H9 media with and without hygromycin. Fluorescent measurements were taken every 90 minutes for 48 hours using FLUOstar OPTIMA microplate reader ((584nm/612 nm, excitation/emission; BMG Labtech). Concurrently, static culture *mCherry M. smegmatis* was grown in filter-top glass tubes in 7H9 media with and without hygromycin selective for 48 hours. Culture tubes were vortexed and OD600 readings were taken every 24 hours and bacterial suspension plated to determine colony forming units on 7H11 agar with and without hygromycin.

To determine the growth/death curve of *m. Cherry M. smegmatis* in 2D culture with and without gentamicin (Sigma Aldrich) (10 μg/ml), and 3D RBM, with a buffer solution that contains 50 μg/mL gentamicin, with standard bacterial 7H9 media with hygromycin (80 μg/mL) and 2D DMEM without antibiotics to serve as a control. Samples were collected and colony forming units (CFUs) were quantified at 0, 12, 24, 48, and 72 hours using 4˚C 1x PBS with 0.1% Tween 80 to disrupt the 3D extracellular matrix and remove any adhered bacteria form the tissue culture plates.

3.2.4 Comparing macrophage response to infection with wild-type versus m. Cherry M. smegmatis

Macrophage, gfpBMDM and b6BMDM, response to *mCherry M. smegmatis* infection was compared to determine any variation between wildtype and EGFP containing cells. Using our standard 2D infection protocols, BMDMs from 8-week-old male mice were infected at a MOI of 50 incubated in DMEM without gentamicin, and intracellular and extracellular samples collected and replicate plated (0, 24, 48 hours post-infection) for CFU enumeration using previously described methods [36].

A comparison of the host response between of b6BMDM under *m. Cherry M. smegmatis* compared to wild type *M. wmegmatis* infection was conducted using a 2D infection protocol to determine any variation between the cells derived from the mouse lines. The cells were infected at a MOI of 50 without the presence of gentamicin and the wells were sampled in replicate every 24 hours for 48 hours with BMDMs from 8-week-old male mice as previously described [36].

3.2.5 Development of 2D/3D ex vivo model of mycobacterial Infection

To minimize variability, a single batch of gfpBMDM cells were infected in tissue culture plates (VWR) for 1hr followed by 1hr gentamicin incubation to remove extracellular bacteria [36]. Cells were washed with 1x PBS twice and then cells were detached using Cellstripper® (Corning) and placed into 2D or 3D culture.

3.2.5.1 3D infection platform

High plasmid expressing *mCherry M. smegmatis* was cultured and prepared for bacterial infection as previously reported in DMEM-complete (Dulbecco's Modified Eagle Medium containing 10% fetal bovine serum,1% L-glutamine and 1% non-essential amino acid) [36].

Using an adaptation of Xu et al.'s protocol, for the 3D *ex vivo* model 250µL diluted RBM (.18 mg/mL) coating was added to 48-well plates (sample collection) and 8-well (Ibidi) chamber slides (confocal imaging) to prevent formation of an RBM-culture plate interface void of ECM proteins [52]. Plates were incubated (5% CO_2 at 37°C) for 30 minutes enabling matrix formation, aspirated and excess tapped onto low-lint tissue paper. Immediately following, control/non-infected or infected cells were resuspended in diluted 8.5mg/mL RBM (2.5E6 cells/mL at 0-8°C) and 100µL of cell suspension was plated onto the center of each coated well. To minimize uneven gel dispersion and reduce the effect of meniscus formation, the plate was quickly swiveled in a star pattern. Any large bubbles were disrupted using a 20 to 30-gauge sterile needle. The cell-containing matrix was incubated for 45 minutes, allowing gel to fully set, and 275µL of hydrating media (DMEM-complete) added to prevent gel dehydration.

The 2D *ex vivo* model was implemented using our standard protocol with the addition of 10µg/mL of gentamicin in the culture media, which, assuming passive diffusion of gentamicin into the hydrating media, we estimate as a concentration comparable to the buffer solution of RBM [53]. Prior studies indicate 10µg/mL of gentamicin inhibits extracellular but not intracellular growth of *M. smegmatis* [54] [53].

500µL of 2D cell suspension was added to each 24-well plate (sample collection) or 250 µL to each non-RBM coated well of the 8-well chamber slide (confocal imaging). Cells were incubated and allowed to adhere in 2D for 2 hours before any samples were collected for both the 2D and 3D cultures. We conducted two experimental trials comparing 3D/2D, with two biological duplicates per trial.

3.2.6 Analysis of biological response to infection

Supernatant samples were collected and bacterial CFU's enumerated at 0, 12, 24, 36, 48 and 72 hours post-infection. For the 3D model, supernatant was collected for assays and 375µL of ice-cold PBS (0-4˚C)was added and vigorously pipetted to disrupt and dissolve the RBM matrix. The liquefied RBM solution was collected into microcentrifuge tubes, centrifuged (1500 RPM, 4˚C) for 10 minutes, and 200µL of supernatant collected for assays, avoiding disruption of loose RBM/cell pellet. To disrupt cells, 200µL of 1% Triton-X 100 was added to RBM/cell pellet, incubated (20-25˚C, 5minutes), and vigorously pipetted and vortexed to lyse cells and release intracellular bacteria. The disrupted supernatant/lysate was serially diluted 10-fold and plated on 7H11 plates to enumerate the total colony forming units of bacteria in the 3D matrix.

For cells in 2D, using previously reported methods [36], supernatant was collected for enumeration of extracellular bacteria or stored at -80˚C until use for assays. Wells were gently washed twice (1xPBS), 500µL of 1% Triton-X100 added, incubated followed by vigorous pipetting to lyse cells and release intracellular bacteria. Supernatant/lysates were vortexed, serially diluted 10-fold and plated on 7H11 agar

plates. After 72 hours CFUs were used to quantify intracellular, extracellular or total bacterial loads.

Frozen supernatant from 3D and 2D models was used to quantify nitric oxide (Griess assay; Promega™, G2930) and cell death (LDH cytotoxicity assay; Pierce™, 88954).Assays were performed in replicate according to manufacturer protocol, with standards generated for gfpBMDM and potential interference of RBM quantified. Media supernatant was used for quantification of effector molecules in 3D as determined by comparison of dissolved RBM assay quantification in comparison to the hydrating media on top of the 3D culture.

3.2.7 Image-based quantification of the spatiotemporal response to infection

Infected and control/non-infected cells in the Ibidi 8-well chamber slides were incubated in a stage top incubation system (TokaiHit) and imaged for 72 hours using multi-area time-lapse confocal imaging (Olympus FV1200, UPLSAPO40X2 40x/0.95NA objective). Confocal images were acquired with Olympus Fluoview software version 4.2b every 90 minutes at a 1µm axial resolution for 100µm appended Z-stacks at each timepoint. The sampling resolution allows for image acquisition under the Nyquist limit of macrophages (10-20 µm approximate diameter) and M. smegmatis (2-8 µm approximate length) [55] [56]. The dwell time per pixel is minimized to 2 µs/Pixel (the fastest image acquisition available with unidirectional laser scanning) to reduce photobleaching and phototoxicity [57]–[59], which compounds over time.

To determine the number of sample points to image within each 8-well chamber, treating the population of BMDMs in 2D control/non-infected wells (0hr) as a homogenous normally distributed population, we applied the Yamane formula [60] to determine the proper sample size for a 95% confidence interval (equation 5). The 2D approximations were extrapolated into the 3D plane for the 3D wells as given by

$$n_o = \frac{z^2 p(1-p)N}{z^2 p(1-p)N\epsilon^2}. \quad (5)$$

Table 4: Yamane formula for determination of sample size in a homogenous normally distributed population

Variable	Description and Values Used
$\boldsymbol{n_o}$	Sample size (5E5 cells/mL * .250 uL)
$\boldsymbol{z}$	Confidence interval (1.96 for 95% confidence interval)
$\boldsymbol{p}$	Population proportion (.5)
$\boldsymbol{N}$	Population size (1.25E5 cells per 8 well chamber slide in 2D)
$\boldsymbol{\epsilon}$	Error limit (0.03)

3.2.8 Image Analysis

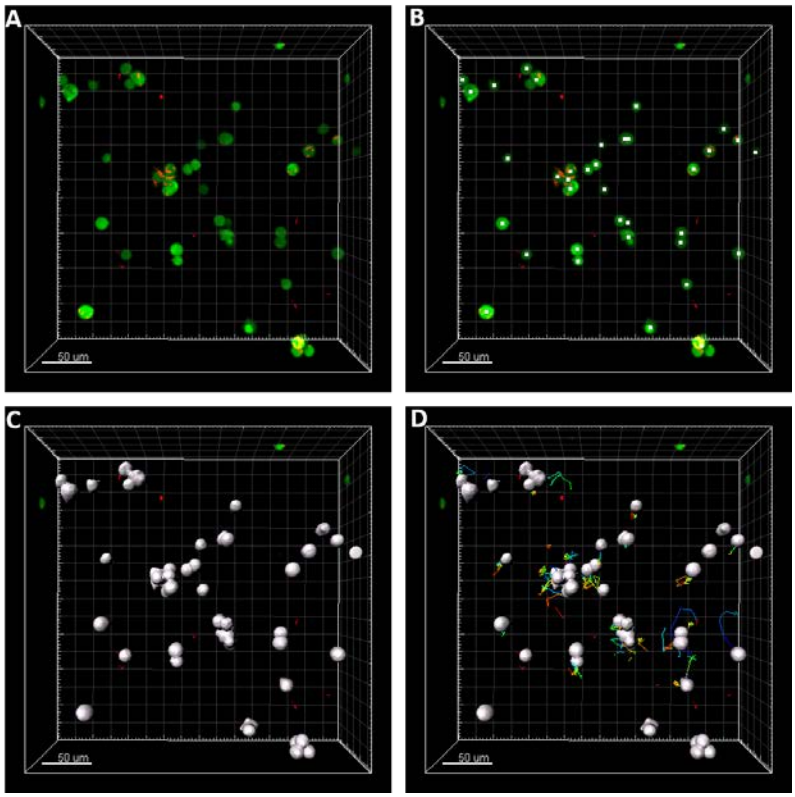

Figure 6: Image Processing in Imaris 8.1.2 of 3D infected cells at hour 0 of imaging: A) 3D rendering of confocal image B) Seed point diameters 8.25 µm B) watershed segmentation of cells in 3D D) autoregressive motion tracking applied to segmented cells to produce tracks over time.

The resulting 4D time appended 100µm image Z-stacks were rendered and analyzed using Imaris 8.1.2 (Bitplane) with surface creation and tracking of macrophages to monitor the change in cellular dynamics over time (Figure 6). The same image processing parameters (Table 5) were used for all conditions within an experimental trial, with trial-specific adjustments to fluorescent cutoffs due to variations in background fluorescence. Data for the entire imaging field was taken by reporting data of the entire Z-stack as a single surface to analyze the fluorescent and volumetric values of the entire 4D image. Imaging data was analyzed in time windows comparable to

sample acquisition timepoints and cellular dynamic features quantified, including velocity, acceleration, volume, and red fluorescent values.

Table 5: Image Processing Parameters for Imaris (*values adjusted for each trial due to variations in fluorescence between experiments)

	Parameter	Value
Algorithm	Enable Region of Interest	False
	Enable Region Growing	True
	Enable Tracking	True
Source Channel	Source Channel Index	1 (GFP)
	Enable Smooth	True
	Surface Grain size	1.00 µm
	Enable Eliminate Background	True
	Diameter of Largest Sphere	10.0 µm
Threshold	Enable Automatic Threshold	False
	Manual Threshold Value	*
	Active Threshold	True
	Enable Automatic Threshold B	True
	Manual Threshold Value B	*
	Active Threshold B	False
	Region Growing Estimated Diameter	8.25 µm
Classify Seed Points	Quality	Above 40.0
	Distance to Image Border XYZ	Above 3 µm
	Intensity Mean Ch=1	Above *
	Intensity StdDev Ch=1	Below *
Classify Surfaces	None applied	-
Tracking	Algorithm Name	Autoregressive Motion
	MaxDistance	20.0 µm
	MaxGapSize	0
	Fill Gap Enable	true
Classify Tracks	None applied	-

3.2.8.1 Feature analysis and data processing in MATLAB

We developed a MATLAB-based (MathWorks) computational pipeline for high-throughput analysis of the 4D spatiotemporal response dataset. Using MATLAB GUIDE to facilitate data organization based on conditions (2D/3D, control/infection) and biological replicates, the data was hierarchically processed to enable condition-based normalization of fluorescence-associated noise over the 4D datasets. Variations in signal

to noise ratio (SNR) over the time-lapse was reduced post acquisition by background normalization to the bacterial red fluorescent protein (RFP) levels in the control conditions, which should remain constant given the absence of bacteria in the control wells. The variation in RFP fluorescence in both control and infection wells were accounted for as previously described through normalization to the control image RFP signal minimum in chapter 2 [61]. Subsequently, the directedness of each for each macrophage was calculated as the ratio of the Euclidian (straight-line) distance over the total distance traveled from the initial timepoint to the current timepoint. Directedness represents the inverse of random movement, therefore a higher directedness value represents a cell with movement that is less random and a directedness value of 1 would represent movement in a straight line [62].

3.2.9 Statistical Analysis

R-Studio's dplyr, ggplot2 and ggpubr libraries were used for statistical analysis [63]–[66]. The Wilcoxon rank sum test was used to calculate statistical significance and Pearson's correlation used to assess relationships between variables. Reported rate of change values (differentials) were calculated using the non-averaged data to calculate the change in value from the previous reported timepoint. When initial concentrations differed, log2 fold change (Log2FC) of the data was calculated and used to statistically compare across experimental conditions as given by equation 6,

$$Log2FC = Log_2\left(\frac{X(t)}{X(0)}\right), \tag{6}$$

3.3 Results

3.3.1.1 Plasmid Persistence

The *mCherry* plasmid in *M. smegmatis* in the absence of the selective antibiotic was maintained in long-term static culture up to 48 hours through the bacterial log phase of growth. No significant differences in antibiotic resistance through differential plating (Figure 7B, Table 6), and no significant changes in bacterial fluorescence through microplate analysis was found between the 7H9 media containing hygromycin and 7H9 bacterial media without hygromycin conditions (Figure 7A). Results demonstrate the persistence of the purified *mCherry M. smegmatis strain* and indicate no significant loss of bacterial plasmid including antibiotic resistance and mCherry fluorescence during long-term culture in the absence of the selective antibiotic.

Table 6: Plasmid Persistence of mCherry *M.*smegmatis Differential Plating: Wilcoxon (n=4)

Hour	*Media:+Hygro/Plate:+Hygro CFU/mL*	*Media:-Hygro/Plate:+Hygro CFU/mL*	*p value*
0	2.28E+07	2.43E+07	0.665006
24	2.28E+07	2.43E+07	1
48	1.50E+08	1.53E+08	0.746886
Hour	*Media:+Hygro/Plate:-Hygro CFU/mL*	*Media:-Hygro/Plate:-Hygro CFU/mL*	*p value*
0	2.29E+07	2.57E+07	1
24	2.29E+07	2.57E+07	0.060602
48	1.83E+08	1.80E+08	1

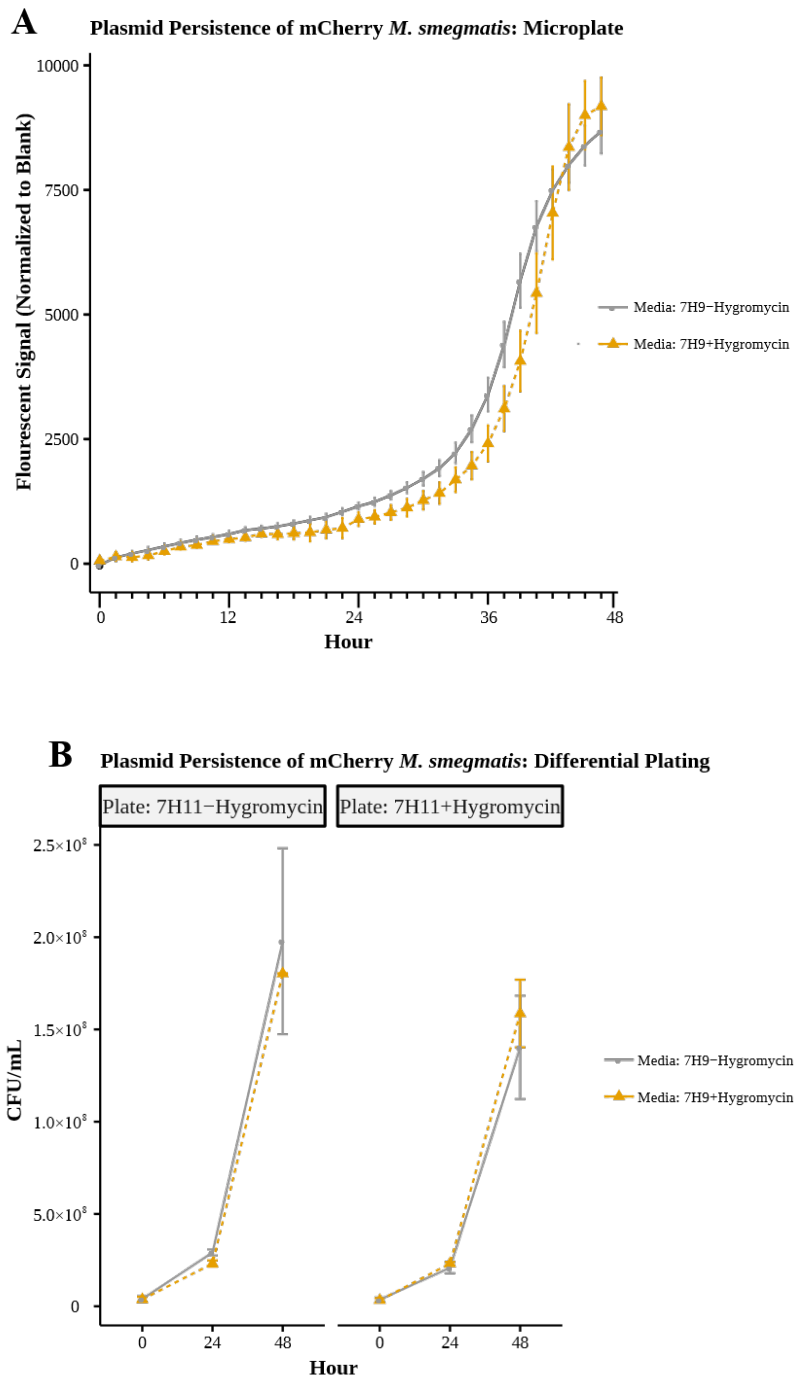

Figure 7: A) Microplate fluorescent readings of m. Cherry M. smegmatis cultured in 7H9 media in the presence or absence of selective antibiotic Hygromycin (n=6). B) Bacterial growth analysis represented as colony forming units at 0, 24 and 48 hours using differential plating (n=4)

3.3.2 Fluorescent host and mycobacteria strains exhibit comparable infection response and dynamics as wild type

Infection response of gfpBMDM and b6BMDM to wild type *M. smegmatis* (MOI 50) in the absence of gentamicin (Figure 8) were comparable with no significant differences in CFU (Table 7) Results indicate that the actin-tagged GFP does not interfere with macrophage-mycobacterium interaction during the low level infection.

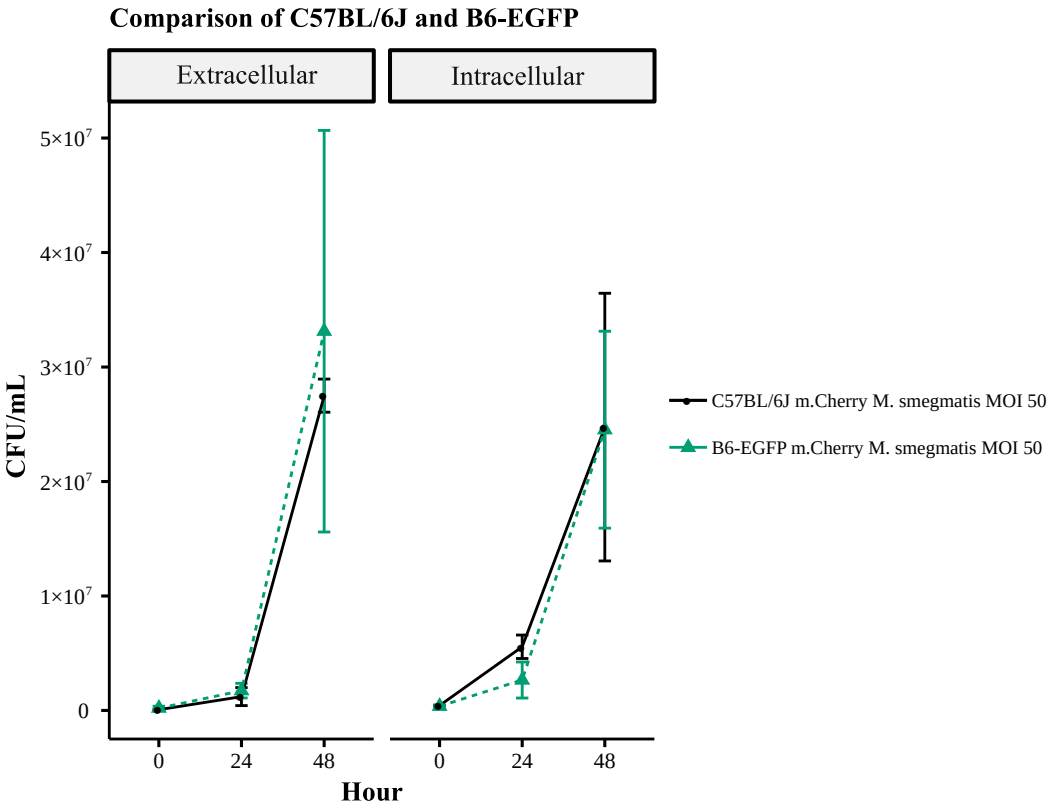

Figure 8: Comparison of gfpBMDM (from B6-EGFP mice) and b6BMDM (from C57BL/6J mice) under 2D infection with m.Cherry M.smegmatis at MOI 50. No significant difference under Wilcoxon analysis (n=4)

Table 7:	2D MOI 50 Comparison of C57BL/6J and B6-EGFP: Wilcoxon (n=4)		
Hour	*C57BL/6J: Intracellular CFU/mL*	*B6-EGFP: Intracellular CFU/mL*	*p value*
0	4.38E+05	3.69E+05	0.465124
24	5.56E+06	2.66E+06	0.312321
48	2.48E+07	2.45E+07	0.880933
Hour	*C57BL/6J: Extracellular CFU/mL*	*B6-EGFP: Extracellular CFU/mL*	*p value*
0	7.25E+04	2.04E+05	0.771503
24	1.21E+06	1.73E+06	0.665006
48	2.75E+07	3.31E+07	0.303525

Similarly, there were no significant difference between mCherry and wild type *M. smegmatis* infections of b6BMDM (mSmeg mCherry MOI 50 and 48, mSmeg MOI 18 and 17) in the absence of gentamicin. Using Log2FC CFU due to variations in bacterial concentrations of bacteria in the inoculate (Figure 9). No notable or significant differences were observed (Table 8).

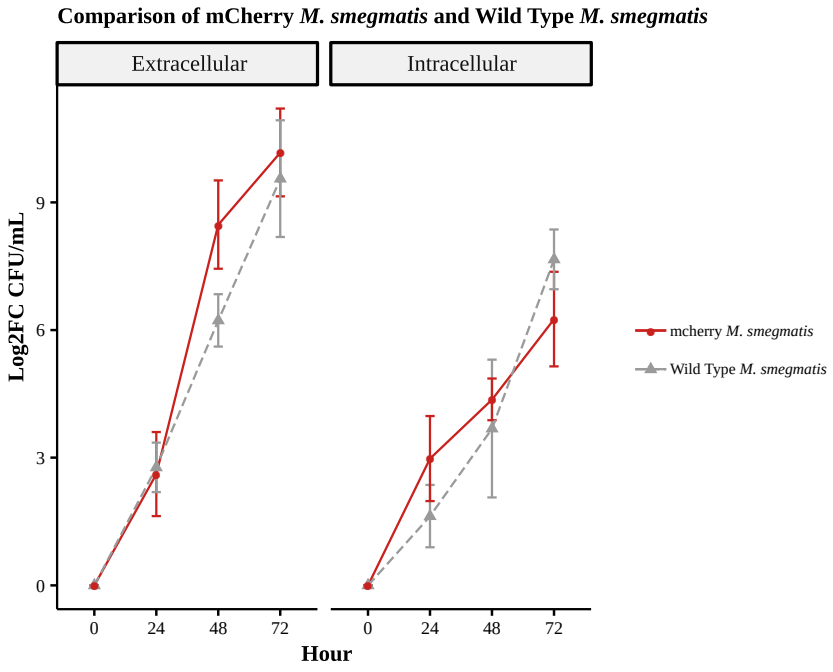

Figure 9: Comparison of wild type *M. smegmatis* and *m. Cherry M smegmatis* infection in B6BMDM. Note: Log2FC used due to different levels of starting infection, Wilcoxon N=6, except 72 hour n=3

Table 8*:* 2D MOI Comparison of mCherry M. smegmatis:and wild type M. smegmatis infection in b6BMDM Log2FC Wilcoxon (n=6,*n=3)

Hour	*mCherry: Intracellular log2FC*	*wild Type: Intracellular log2FC*	*p value*
0	0	0	-
24	2.980128	1.626583	0.29795
48	4.370521	3.684769	0.81018
72	6.258945	7.662005	0.38273*
Hour	*mCherry: Extracellular log2FC*	*wildType: Extracellular log2FC*	*p value*
0	0	0	-
24	2.614937	2.773342	1
48	8.478391	6.226576	0.09270
72	10.17503	9.55832	0.66252*

3.3.2.1 Growth Curve of *M. smegmatis* in gentamicin culture

The growth/death curve of *mCherry M. smegmatis* (Log2FC) in 2D culture in the presence of gentamicin (10 µg/mL) to account for the buffer solution of the RBM showed comparable bacterial fold change to 3D culture up to 48hrs. At 72hrs, the method of extraction for 3D culture yielded no viable CFUs, possibly due to the difficulty in extraction and higher dilution factor in combination with the already low bacterial concentration (Figure 10,Table 9,Table 10).

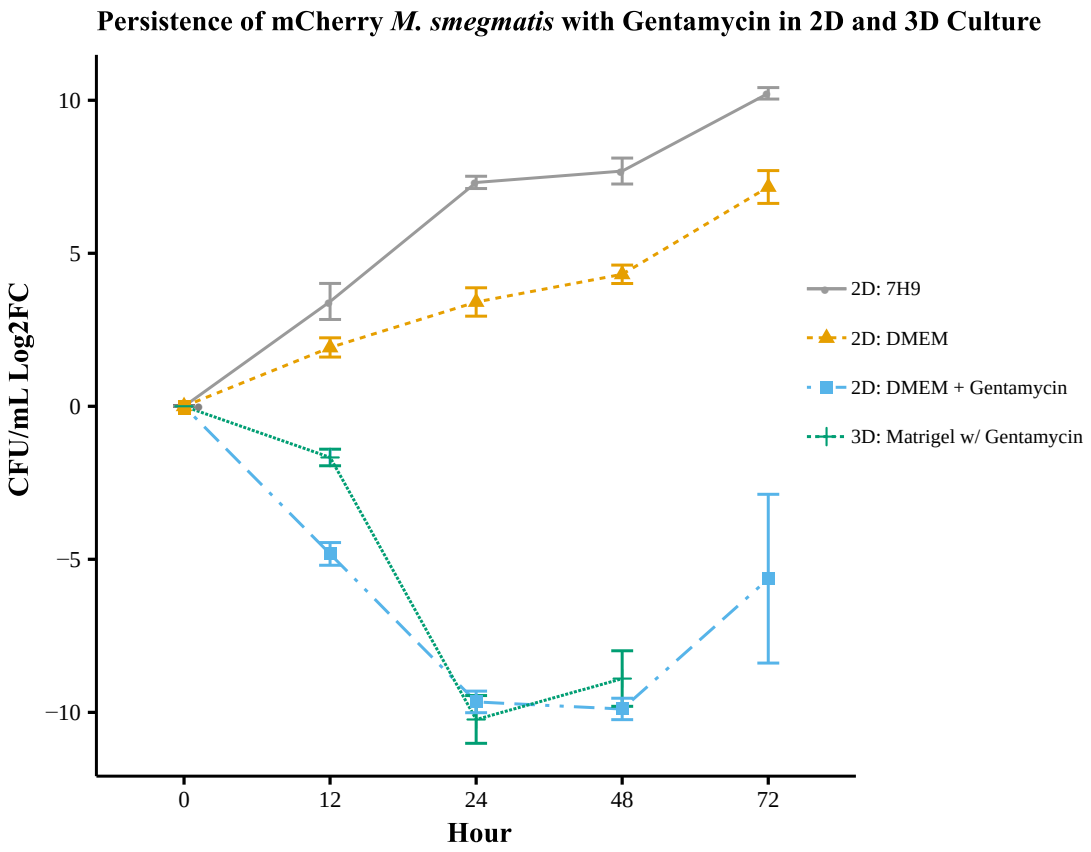

Figure 10: Comparison of dynamic growth of m. Cherry M. smegmatis in 2D culture with added Gentamycin at 10 µg/mL and within 3D culture of the bacterium in RBM (n=4).

Table 9: 2D 3D persistence of m.Cherry *M.Smegmatis* in 10 µg/mL Gentamycin: Log2FC Wilcoxon (n=4)

Hour	*2D-Gentamycin*	*3D-RBM*	*p value*
0	0	0	-
12	-5.419	-3.410	0.245278
24	-9.658	-10.232	0.665006
48	-9.889	-8.896	0.312321
72	-5.633	-3.410	n/a

Table 10: 2D static growth of m.Cherry *M.Smegmatis* in DMEM and 7H9 Media: Log2FC Wilcoxon (n=4)

Hour	*2D-DMEM*	*2D-7H9*	*p value*
0	0	0	-
12	1.741	2.788	0.245278
24	3.409	7.316	0.030383
48	4.312	7.687	0.030383
72	7.166	10.226	0.030383

3.3.2.2 Determination of method effector molecule quantification

Standard 2D cell culture and infection assays rely on the media supernatant to run immunological assays to determine effector molecule expression in response to stimulus. However, in the case of 3D studies, the hydrating supernatant is separated from intra-matrix cells by the RBM layer in which the cells are embedded. To determine the difference between the intra-matrix environment versus the supernatant and to determine a feasible method for quantifying the effector response we quantified two methods of sample extraction to determine significant differences and comparability to qualitative imaging data. We compared two methods, sampling the hydrating supernatant surrounding the RBM-cell suspension or the supernatant from disrupted RBM (disrupted using 1xPBS at 4°C) for sample extraction. The disrupted RBM is significantly diluted during this process leading to potential loss of signal even when the dilution is accounted for. The Griess assay for quantification of nitric oxide expression showed no significant difference between the two sample collection methods for 3D. However, this is likely attributed to the already very low signal from this assay (Figure 11A,Table 11). The LDH assay showed significant difference between intra-matrix versus extra-matrix supernatant for almost all time points (Figure 11,Table 12). In addition, the dynamics of the media hydrating supernatant sample matched most closely to qualitative biological observations of confocal imaging and the dynamical trends for 2D. Therefore, we proceeded to compare 2D supernatant assay samples with 3D media supernatant assay samples.

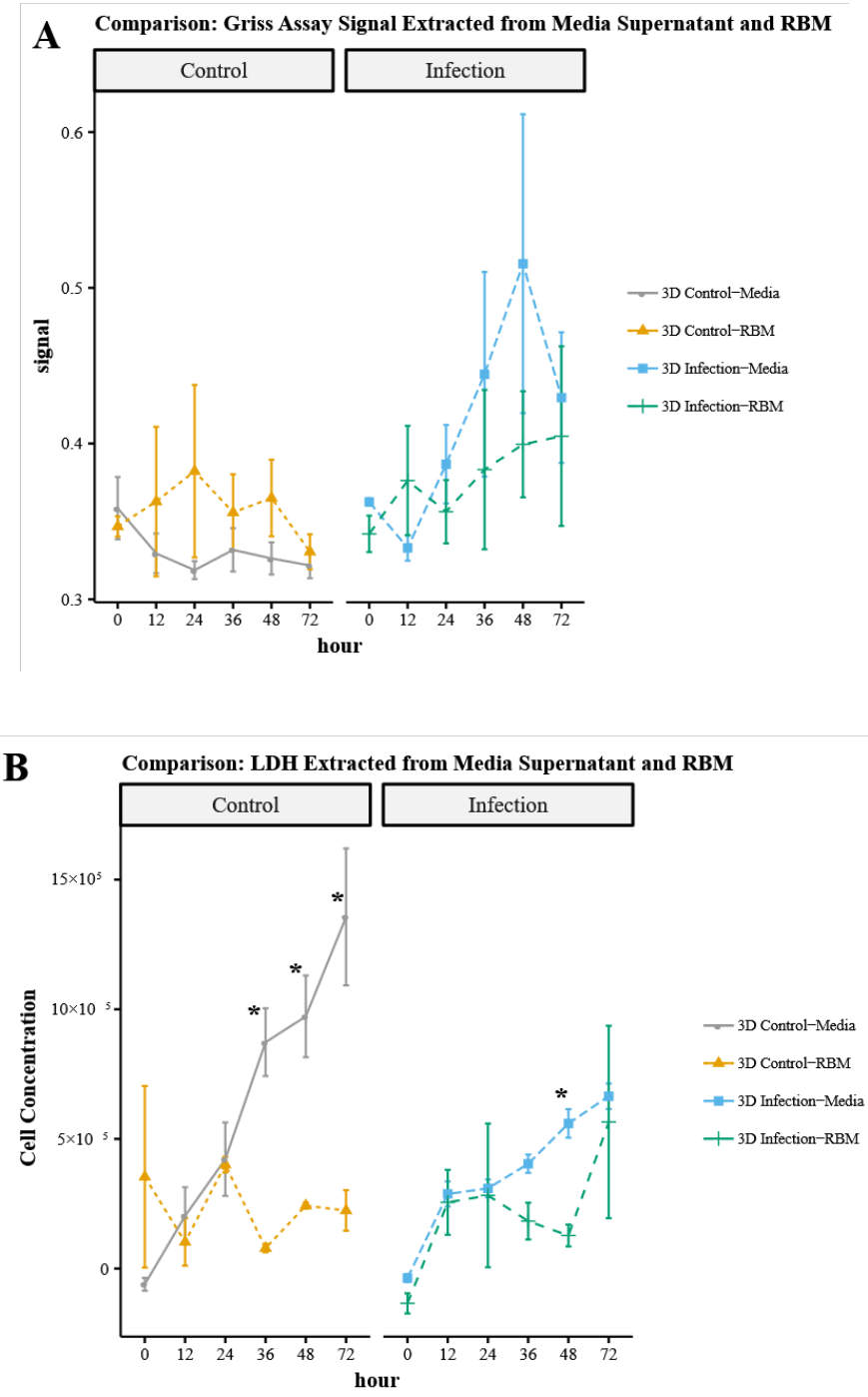

Figure 11: A) No significant difference between NO signal gathered from supernatant and RBM B) significant difference ($p<.05$) between LDH gathered from supernatant and RBM at multiple timepoints.

Table 11: Nitric Oxide Signal Extracted from Media Supernatant and RBM: Wilcoxon (n=4)

Hour	*Control: 3D-Supernatant*	*Control: 3D-RBM*	*p value*
0	0.3585	0.34675	1
12	0.3295	0.36275	0.885234
24	0.31875	0.38225	1
36	0.33175	0.35575	0.665006
48	0.32625	0.365	0.191267
72	0.32175	0.3305	0.885234
Hour	*Infected: 3D-Supernatant*	*Infected: 3D-RBM*	*p value*
0	0.3635	0.337	0.312321
12	0.3285	0.3465	0.312321
24	0.3835	0.354	0.470486
36	0.441	0.368	0.470486
48	0.521	0.383	0.665006
72	0.424	0.3715	0.665006

Table 12: LDH Assay: Cell Death Extracted from Media Supernatant and RBM: Wilcoxon (n=4)

Hour	*Control: 3D-Supernatant*	*Control: 3D-RBM*	*p value*
0	-60617.6	354040.9	1
12	203256	102841	0.312321
24	421959.1	400836.2	1
36	873339	78793.42	0.030383
48	972779.1	242902	0.030383
72	1356241	224053.9	0.030383
Hour	*Infected: 3D-Supernatant*	*Infected: 3D-RBM*	*p value*
0	-36570	-134060	0.030383
12	288072.5	255575.7	1
24	309195.4	282223.1	0.312321
36	404410.9	183108	0.112351
48	559745.3	127538.5	0.030383
72	664709.8	565269.8	0.312321

3.3.3 Comparison of infection dynamics in standard 2D infection assay vs 3D infection assay.

Comparison of 2D and 3D conditions shows that the dynamic of bacterial elimination during low level infection is similar (Figure 12A,Table 13) between the two conditions with a slight increase in the rate of change of bacteria in 3D culture between 12 and 24 hours ($p<.05$) (Figure 12B, Table 14).

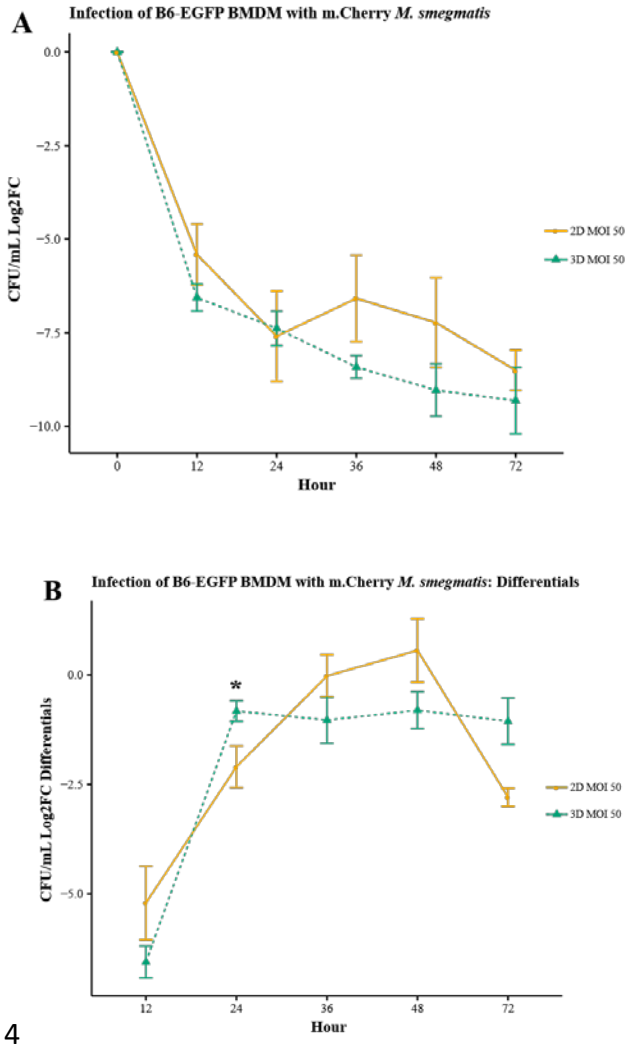

4

Figure 12: A) Comparison of bacterial load between 2D and 3D culture (n=4) B) Comparison of the rate of bacterial clearance between 2D and 3D culture (n=4)

Table 13: 2D 3D MOI 50 CFU/mL: Log2FC Wilcoxon (n=4)

Hour	*2D*	*3D*	*p value*
0	0	0	-
12	-5.4057	-6.5588	0.47049
24	-7.5916	-7.3823	1
36	-6.5644	-8.4127	0.37676
48	-7.2291	-9.0334	0.595883
72	-8.5010	-9.3100	0.487453

Table 14: 2D 3D MOI 50 differentials (tp1-tp0): Log2FC Wilcoxon (n=4)

Hour	*2D*	*3D*	*p value*
12	-5.4057	-6.5588	0.47049
24	-2.1858	-0.8235	0.03038
36	0.1209	-1.0304	0.11161
48	0.3625	-0.8060	0.19043
72	-3.1287	-1.0570	0.14891

3.3.4 Nitric Oxide expression does not significantly differ between 2D and 3D i during low level infection.

Quantification of nitric oxide shows a non-significant average higher concentration of nitric oxide in 3D infection cultures as compared to the 3D controls, 2D controls and 2D infection (Figure 13,Table 15, Table 16).

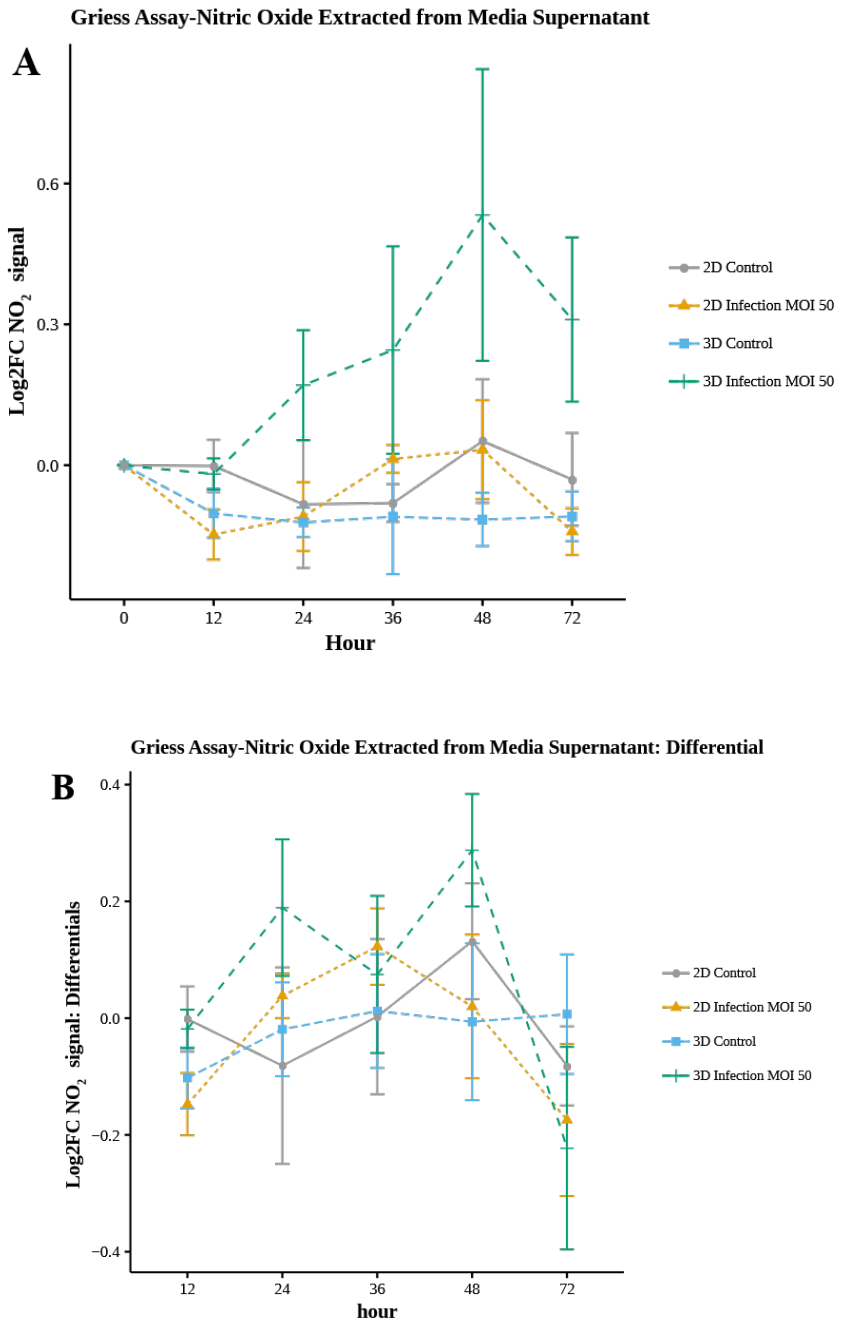

Figure 13: NO assay results: a) no significant difference between any conditions b) no significant difference between any conditions in rate of change – Wilcoxon N=4

Table 15: Nitric Oxide Extracted from Supernatant 2D vs. 3D: Log2FC Wilcoxon (n=4)

Hour	*2D: Control*	*3D: Control*	*p value*
0	0	0	-
12	-0.002	-0.102	0.112351
24	-0.083	-0.121	0.470486
36	-0.08	-0.109	1
48	0.0516	-0.115	0.470486
72	-0.03	-0.109	0.470486

Hour	*2D: Infection*	*3D: Infection*	*p value*
0	0	0	-
12	-0.147	-0.018	0.112351
24	-0.109	0.1707	0.112351
36	0.0134	0.2455	1
48	0.0333	0.533	0.312321
72	-0.141	0.3104	0.060602

Table 16: Nitric Oxide Extracted from Supernatant Control vs Infected Log2FC Wilcoxon (n=4)

Hour	*2D: Control*	*2D: infection*	*p value*
0	0	0	0.112351
12	-0.002	-0.147	0.665006
24	-0.083	-0.109	0.193931
36	-0.08	0.0134	1
48	0.0516	0.0333	0.470486
72	-0.03	-0.141	0.112351

Hour	*3D: Control*	*3D: Infection*	*p value*
0	0	0	-
12	-0.102	-0.018	0.112351
24	-0.121	0.1707	0.060602
36	-0.109	0.2455	0.470486
48	-0.115	0.533	0.112351
72	-0.109	0.3104	0.060602

3.3.5 Necrotic cell death is down regulated during 3D infection as compared to 2D

Results of the LDH assay show a consistent increase in cell death due to necrosis over time consistent with qualitative imaging observations (Figure 14). Control cells within 3D culture have a significantly higher fold change increase in LDH levels than 2D controls, 3D infection and 2D infection at 36, 48 and 72 hours ($p<.05$). At 24 hours, 3D controls have a significantly higher fold change increase in LDH as compared to 3D infection, and at 12 hours 3D controls have a significantly higher fold change increase in

LDH as compared to 2D controls (Table 17,Table 18). Investigation of the LDH rate of change (differentials) shows consistent LDH expression between 2D and 3D controls as well as 2D and 3D infection (Figure 14B,Table 19), while maintaining significant differences in rate of LDH expression between control and infection within the 2D and 3D conditions (Figure 14B,Table 20).

Table 17: LDH Extracted from Media Supernatant 2D vs. 3D: Log2FC Wilcoxon (n=4)

Hour	*2D: Control*	*3D: Control*	*p value*
0	0	0	-
12	0.852612	1.482648	0.193931
24	1.392919	2.184865	0.060602
36	2.14604	3.072038	0.030383
48	2.353846	3.193532	0.030383
72	2.770592	3.579989	0.030383
Hour	*2D: Infection*	*3D: Infection*	*p value*
0	0	0	-
12	1.477391	1.628312	1
24	1.530684	1.702693	1
36	1.846927	1.956242	1
48	2.143491	2.286088	1
72	2.790721	2.479411	0.193931

Table 18: LDH Extracted from Media Supernatant Control vs. Infected: Log2FC Wilcoxon (n=4)

Hour	*2D: Control*	*2D: Infection*	*p value*
0	0	0	-
12	0.852612	1.477391	0.312321
24	1.392919	1.530684	1
36	2.14604	1.846927	1
48	2.353846	2.143491	1
72	2.770592	2.790721	0.885234
Hour	*3D: Control*	*3D: Infection*	*p value*
0	0	0	-
12	1.482648	1.628312	0.885234
24	2.184865	1.702693	0.030383
36	3.072038	1.956242	0.030383
48	3.193532	2.286088	0.030383
72	3.579989	2.479411	0.030383

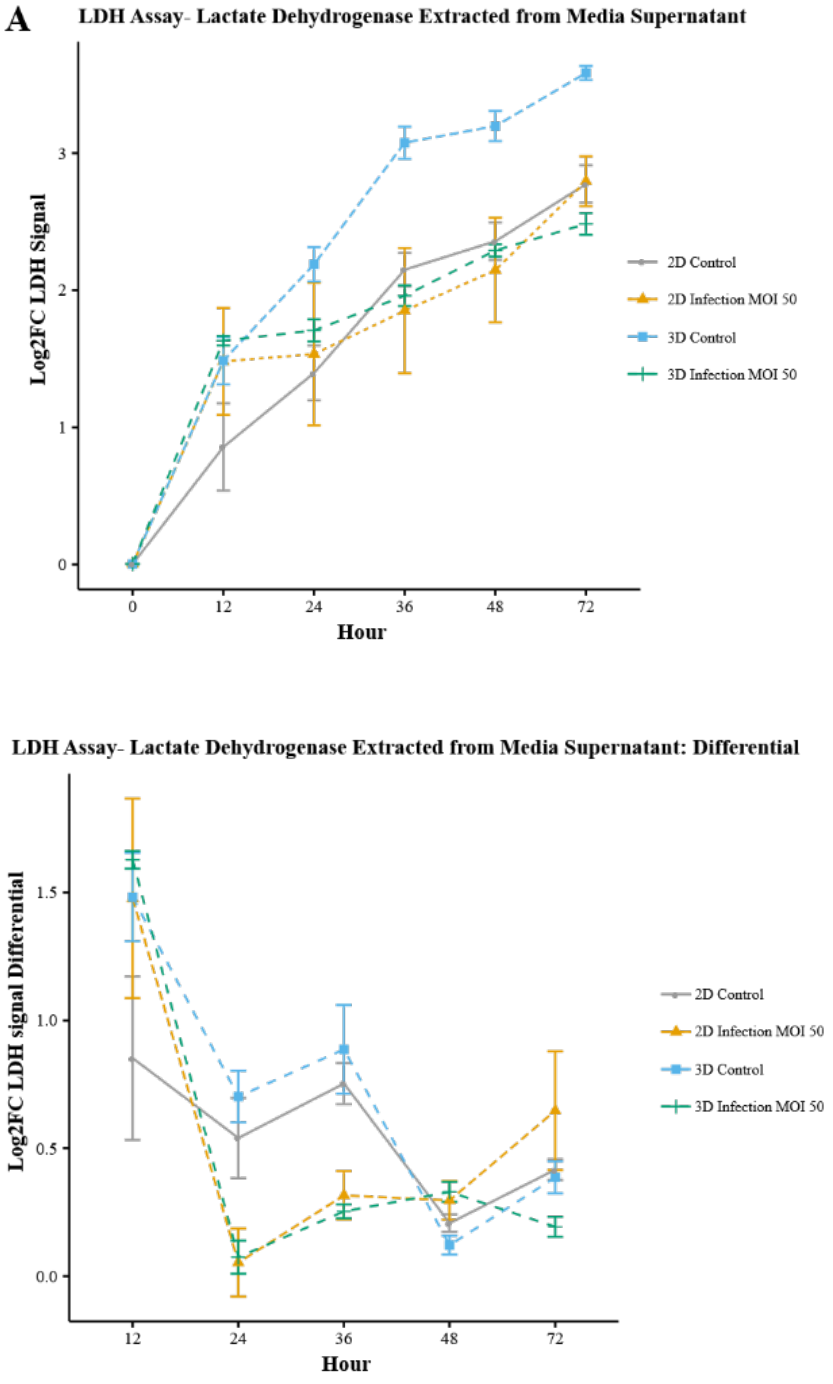

Figure 14: A) LDH assay results B) LDH Differential results, Wilcoxon N=4

Table 19: Differentials-LDH Extracted from Media Supernatant 2D vs. 3D: Log2FC Wilcoxon (n=4)

Hour	*2D: Control*	*3D: Control*	*p value*
12	0.852612	1.482648	0.193931
24	0.540307	0.702217	0.665006
36	0.753121	0.887173	0.665006
48	0.207806	0.121493	0.193931
72	0.416747	0.386457	0.885234
Hour	*2D: Infection*	*3D: Infection*	*p value*
12	1.477391	1.628312	1
24	0.053293	0.074381	1
36	0.316243	0.25355	1
48	0.296563	0.329846	0.885234
72	0.647231	0.193323	0.193931

Table 20: Differentials-LDH Extracted from Media Supernatant Control vs. Infected: Log2FC Wilcoxon (n=4)

Hour	*2D: Control*	*2D: Infection*	*p value*
12	0.852612	1.477391	0.312321
24	0.540307	0.053293	0.112351
36	0.753121	0.316243	0.060602
48	0.207806	0.296563	0.665006
72	0.416747	0.647231	0.885234
Hour	*3D: Control*	*3D: Infection*	*p value*
12	1.482648	1.628312	0.885234
24	0.702217	0.074381	0.030383
36	0.887173	0.25355	0.030383
48	0.121493	0.329846	0.030383
72	0.386457	0.193323	0.112351

3.3.6 Confocal imaging and quantification of cellular dynamics

Surface quantification and tracking analysis of 4D imaging data (Imaris) yielded 33,414 unique data points (cells at all timepoints) with 36 cell features, and 20 field

features, representing the entire image as a whole, over two independent trials with two imaging replicates in two biological replicate wells (total n=8 images per condition). The Imaris rendering of the 4D imaging data show constitutive high expression of actin-GFP in the BMDMs provided even, and consistent fluorescence in both the control and infected conditions. mCherry expression in M. smegmatis allowed visualization of M. smegmatis extracellularly and intracellularly (Figure 15A).

By acquiring 100um of Z-stack images for both 2D and 3D environments we were able to capture the distribution of cells in the 3D environment, as well as the rounded morphology of cells within the 2D infection condition as compared to 2D control conditions indicative of pro-inflammatory, M1 macrophage, phenotype (Figure 15A,B)

In addition, cells in the 2D environment did not form a perfect monolayer, macrophages can be seen in aggregations including dispersion in the Z-plane of cells on top of each other (Figure 15C). Cells in the 3D environment maintained Z-plane dispersion throughout the entire Z-dimension imaged, extended well beyond the maximal imaging depth. Cells beyond the imaging depth were observed under lower resolution bright-field microscopy (data not shown) but were unable to be captured with confocal imaging due to the working distance of the objective (Figure 15D).

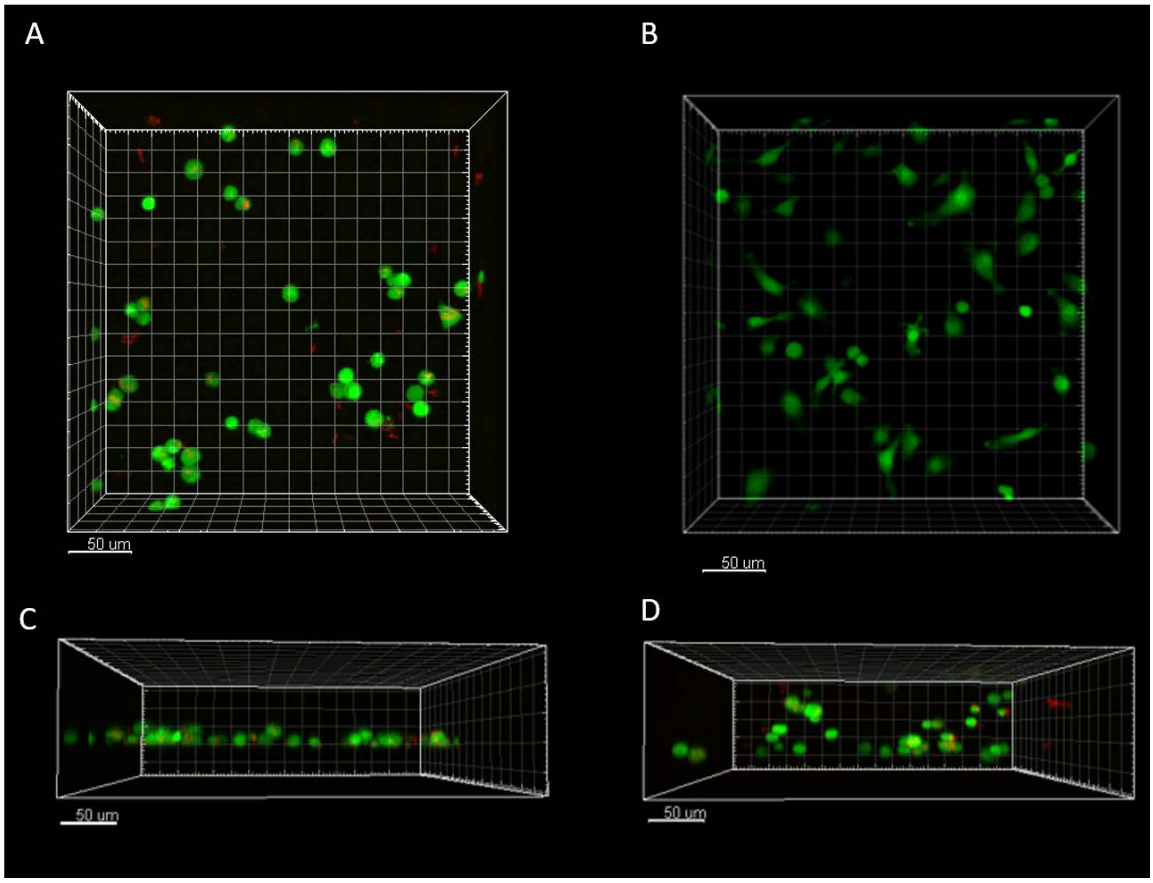

Figure 15: Imaris rendering of 2D and 3D infected and 2D noninfected-control cells at hour 0 of imaging A) 2D infected macrophages B) 2D control cells C) 2D infected macrophages side view D) 3D infected macrophages embedded in RBM

We used the RFP mean of each individual cell to observe the relative bacterial load over time, the mean cell speed (non-directional velocity), acceleration, volume and directedness. For time-based quantification the imaging data generated every 90 minutes was pooled based on condition into time windows comparable to those used for biological sampling. Table 21 shows the number of unique datapoints per time frame.

Table 21:	Number of Observations (cells) During Each Hour-Range			
Hour-Range	2D Control	3D Control	2D Infection MOI 50	2D Infection MOI 50
0-12	1586	740	1205	959
12-24	2171	855	1779	1309
24-36	2502	718	2044	1341
36-48	2337	453	2107	1452
48-72	3679	334	3542	2301
Total	12275	3100	10677	7362

Analysis of RFP mean levels in macrophages for the first experimental trial independently yields significant differences between control and infected cells as expected. Analyzed over all time for raw values there is a significant difference between controls (Figure 5A, Table S 20). Post RFP normalization, the significant difference is no longer observed for 2D/3D controls, but there remains significant differences between infected and control conditions, as well as 2D and 3D infected conditions (Figure 16a). By applying RFP normalization, the significance between controls is removed, and the significant difference between infected and control conditions is maintained (Figure 16b).

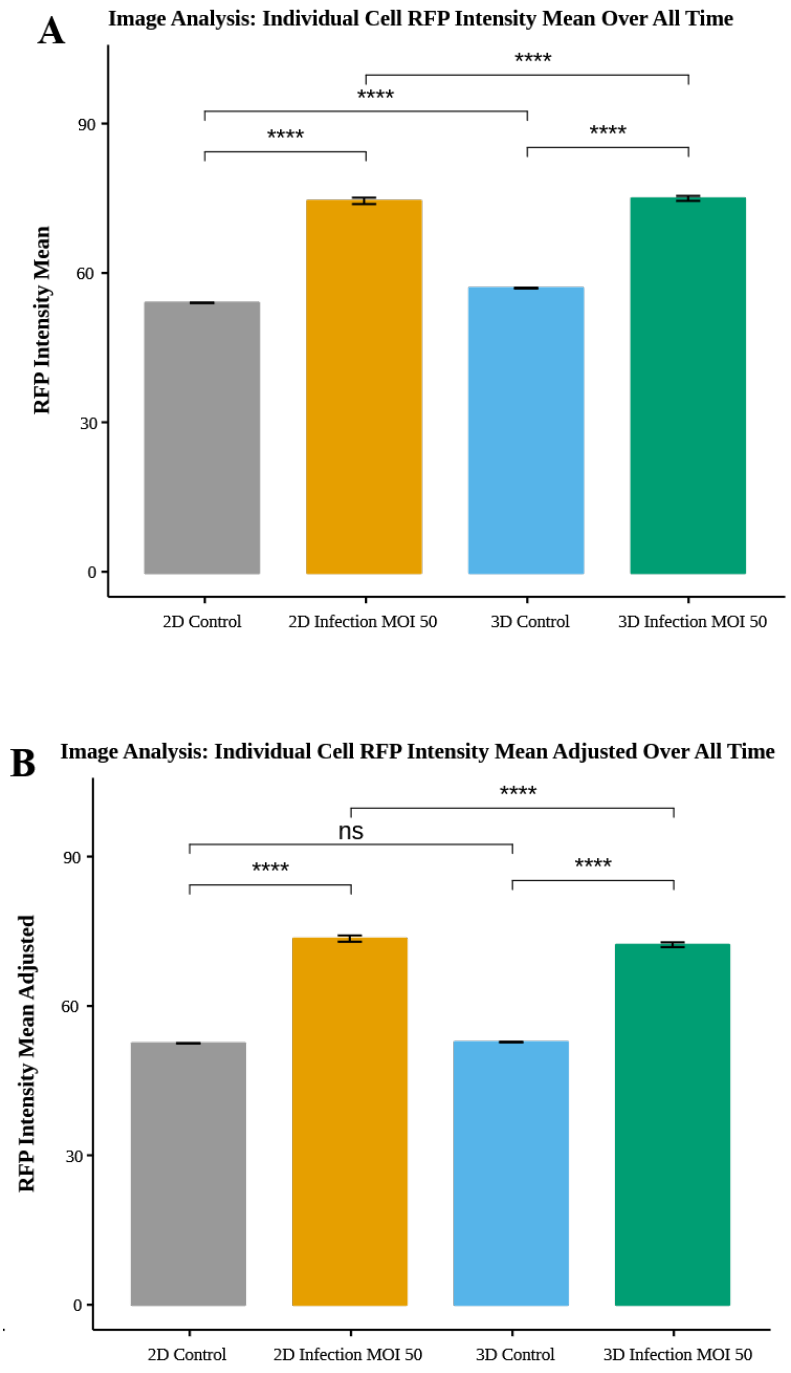

Figure 16: RFP mean of all cells at all timepoints (Trial 1 only) A) raw values B) values normalized to each timepoint. (ns- No significant difference, * - p<.05, **-p<.01,***-p<.001,****-p<.0001)

Analysis of the adjusted RFP mean over time shows a decrease in fluorescence comparable to the decrease in bacterial load over time (Figure 17), this is also observed in Pearson correlation analysis of the adjusted RFP mean and bacterial load.

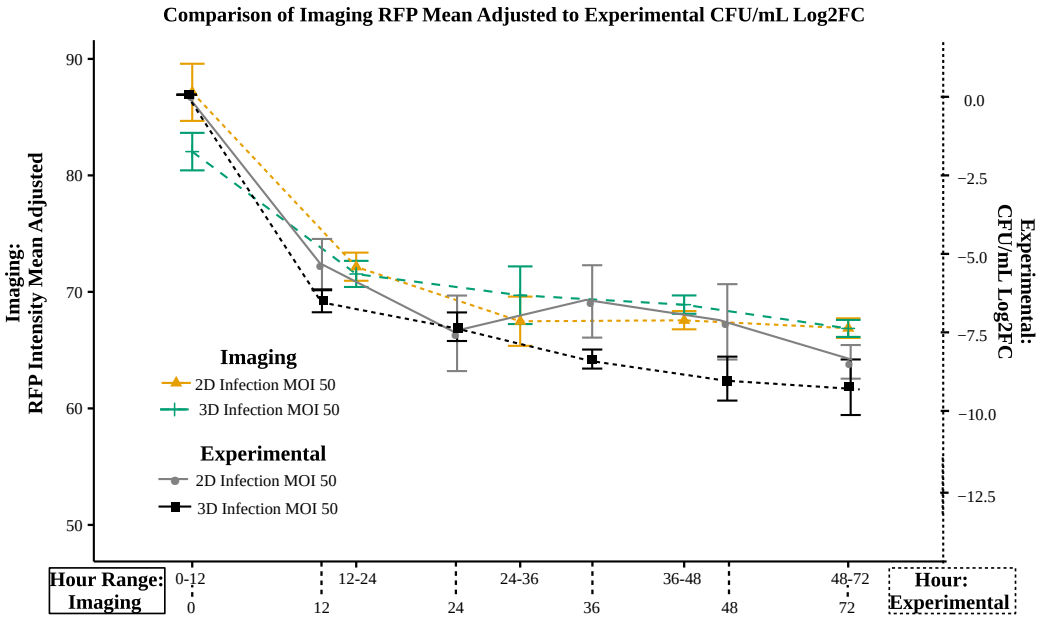

Figure 17: Overlay of Imaging RFP Mean Adjusted and Experimental Log2FC CFU/mL shows similarity in trends over time. Imaging data grouped into time windows to show comparison to experimental biological data.

3.3.7 Cell motility and migration is significantly impacted by both the presence of a 3D environment and mycobacterial infection

In 2D, the average speed of non-infected cells in the control condition (12.94E-4 µm/s) is significantly higher ($p<.0001$) than 2D infected cells (7.61E-4 µm/s). In 3D, the converse is shown with the overall average speed of 3D infected cells (3.8E-4 µm/s) being significantly higher ($p<.0001$) than 3D controls (2.75 E-4µm/s) (Figure 18A,Table 22).

Table 22: Average Individual Cell Speed Over All Time: Wilcoxon

Condition 1	*Speed µm/s*	*Condition 2*	*Speed µm/s*	*p value*
2D Control	1.29E-03	3D Control	2.75E-04	0
2D Infection	7.61E-04	3D Infection	3.80E-04	0
2D Control	1.29E-03	2D Infection	7.61E-04	0
3D Control	2.75E-04	3D Infection	3.80E-04	4.41E-41

The fold changes between the means of the individual cell speeds is highest between the 2D and 3D controls, with 2D controls having the highest overall cell speed. The absolute value of the Log2 fold change between 2D control and 2D infected cells is also higher than the Log2 fold change between 3D control and 3D infected cells (Table 23). Analysis of the trends in average cellular speed over the time-course of imaging show a decrease in average cellular speed at all times with significant differences between all conditions at all hour ranges except 3D control and 3D infected cells at the 36-48 and 48-72 hour ranges (Figure 18,Table 24,Table 25)

Table 23: Average Individual Cell Speed Over All Time: Log2 Fold Change of Means

Condition 1	Condition 2	Log2 Fold Change (Cond 1/ Cond 2)
2D Control	3D Control	2.235
2D Infection	3D Infection	1.0015
2D Control	2D Infection	0.766
3D Control	3D Infection	-0.467

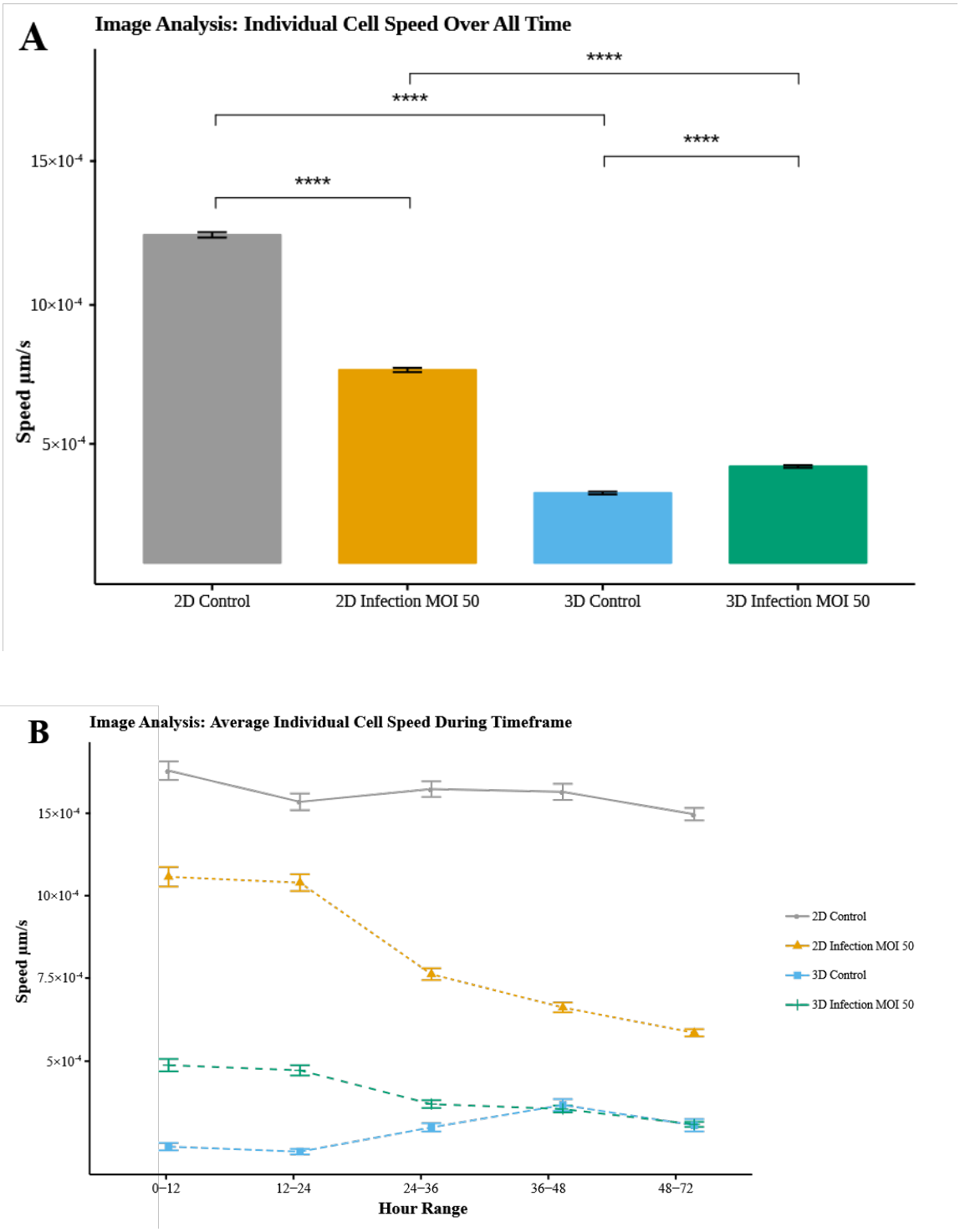

Figure 18: Image analysis of individual cell speed of gfpBMDM infected with mCherry M.smegmatis in 2D and 3D culture conditions over 72 hours. A) Averaged over all time B) Averaged based on hour range. (ns- No significant difference, * - p<.05, **-p<.01,***-p<.001,****-p<.0001)

Table 24: Average Individual Cell Speed 2D vs. 3D Over Time (timeframes): Wilcoxon

Hour Range	*Condition 1*	*Speed µm/s*	*Condition 2*	*Speed µm/s*	*p value*
0-12	2D Control	1.37E-03	3D Control	2.40E-04	2.99E-213
12-24	2D Control	1.28E-03	3D Control	2.25E-04	1.22E-208
24-36	2D Control	1.32E-03	3D Control	2.98E-04	1.35E-150
36-48	2D Control	1.31E-03	3D Control	3.66E-04	5.31E-82
48-72	2D Control	1.24E-03	3D Control	3.05E-04	1.88E-76
0-12	2D Infection	1.05E-03	3D Infection	4.86E-04	2.27E-47
12-24	2D Infection	1.04E-03	3D Infection	4.70E-04	7.94E-73
24-36	2D Infection	7.60E-04	3D Infection	3.69E-04	3.87E-86
36-48	2D Infection	6.60E-04	3D Infection	3.54E-04	9.12E-76
48-72	2D Infection	5.84E-04	3D Infection	3.08E-04	6.10E-127

Table 25: Average Individual Cell Speed Control vs. Infected Over Time (timeframes): Wilcoxon

Hour Range	*Condition 1*	*Speed µm/s*	*Condition 2*	*Speed µm/s*	*p value*
0-12	2D Control	1.37E-03	2D Infection	1.05E-03	2.93E-21
12-24	2D Control	1.28E-03	2D Infection	1.04E-03	2.48E-12
24-36	2D Control	1.32E-03	2D Infection	7.60E-04	5.56E-57
36-48	2D Control	1.31E-03	2D Infection	6.60E-04	1.10E-78
48-72	2D Control	1.24E-03	2D Infection	5.84E-04	3.07E-156
0-12	3D Control	2.40E-04	3D Infection	4.86E-04	1.51E-34
12-24	3D Control	2.25E-04	3D Infection	4.70E-04	1.87E-41
24-36	3D Control	2.98E-04	3D Infection	3.69E-04	0.000244
36-48	3D Control	3.66E-04	3D Infection	3.54E-04	0.403125
48-72	3D Control	3.05E-04	3D Infection	3.08E-04	0.829769

3.3.7.1 Cell acceleration

In 2D, the average acceleration of non-infected cells in the control condition (5.81E-8 $\mu m/s^2$) is significantly higher ($p<.0001$) than 2D infected cells (4.98E-8 $\mu m/s^2$). In 3D, the converse is shown with the overall average speed of 3D infected (3.28E-8 $\mu m/s^2$) cells being significantly higher ($p<.0001$) than 3D controls (2.49E-8 $\mu m/s^2$) (Table 26). The fold change of differences between control and infected within the 2D and 3D conditions is less than that observed with average cellular speed (Figure 19,Table 27).

Table 26: Average Individual Cell Acceleration Over All Time: Wilcoxon

Condition 1	*Acceleration $\mu m/s^2$*	*Condition 2*	*Acceleration $\mu m/s^2$*	*p value*
2D Control	5.81E-08	3D Control	2.49E-08	1.29E-225
2D Infection	4.98E-08	3D Infection	3.28E-08	1.72E-167
2D Control	5.81E-08	2D Infection	4.98E-08	4.94E-21
3D Control	2.49E-08	3D Infection	3.28E-08	1.67E-60

In general, there is an increase in average cellular acceleration in 3D conditions with a relatively more consistent average cellular acceleration in 2D conditions. Significant differences in cellular acceleration exist between all conditions at all hour ranges except 2D control and 2D infected cells at the 24-36 hour range(Figure 19,Table 28,Table 29).

Table 27: Average Individual Cell Acceleration Over All Time: Log2 Fold Change of Means

Condition 1	Condition 2	Log2 Fold Change (Cond 1/ Cond 2)
2D Control	3D Control	1.223
2D Infection	3D Infection	0.601
2D Control	2D Infection	0.224
3D Control	3D Infection	-0.389

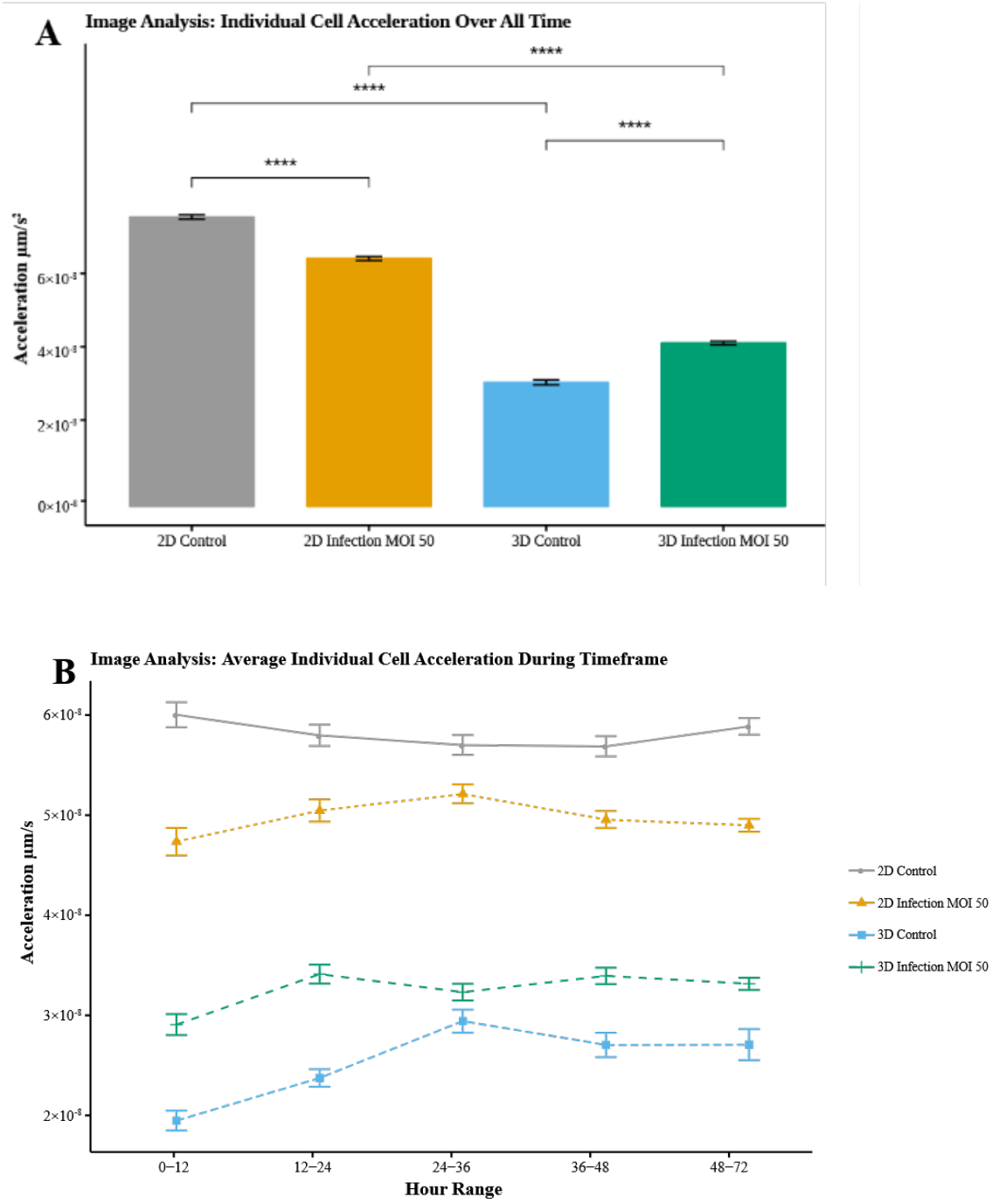

Figure 19: Image analysis of individual cell acceleration of gfpBMDM infected with mCherry M.smegmatis in 2D and 3D culture conditions over 72 hours. A) Averaged over all time B) Averaged based on hour range.

Table 28: Average Individual Cell Acceleration 2D vs. 3D Over Time (timeframes): Wilcoxon

Hour Range	*Condition 1*	*Acceleration µm/s²*	*Condition 2*	*Acceleration µm/s²*	*p value*
0-12	2D Control	6.00E-08	3D Control	1.95E-08	1.14E-65
12-24	2D Control	5.80E-08	3D Control	2.38E-08	1.97E-62
24-36	2D Control	5.70E-08	3D Control	2.94E-08	2.85E-36
36-48	2D Control	5.69E-08	3D Control	2.71E-08	2.20E-29
48-72	2D Control	5.89E-08	3D Control	2.71E-08	3.31E-26
0-12	2D Infection	4.74E-08	3D Infection	2.91E-08	2.74E-12
12-24	2D Infection	5.05E-08	3D Infection	3.41E-08	1.24E-15
24-36	2D Infection	5.21E-08	3D Infection	3.23E-08	5.77E-46
36-48	2D Infection	4.96E-08	3D Infection	3.39E-08	3.36E-37
48-72	2D Infection	4.90E-08	3D Infection	3.32E-08	4.67E-66

Table 29: Average Cell Acceleration Control vs. Infected Over Time (timeframes): Wilcoxon

Hour Range	*Condition 1*	*Acceleration µm/s*	*Condition 2*	*Acceleration µm/s*	*p value*
0-12	2D Control	6.00E-08	2D Infection	4.74E-08	2.46E-11
12-24	2D Control	5.80E-08	2D Infection	5.05E-08	4.86E-06
24-36	2D Control	5.70E-08	2D Infection	5.21E-08	0.095358
36-48	2D Control	5.69E-08	2D Infection	4.96E-08	0.002894
48-72	2D Control	5.89E-08	2D Infection	4.90E-08	6.93E-08
0-12	3D Control	2.38E-08	3D Infection	2.91E-08	1.75E-15
12-24	3D Control	2.94E-08	3D Infection	3.41E-08	2.45E-13
24-36	3D Control	2.71E-08	3D Infection	3.23E-08	0.000152
36-48	3D Control	2.71E-08	3D Infection	3.39E-08	4.29E-06
48-72	3D Control	2.38E-08	3D Infection	3.32E-08	3.24E-07

3.3.7.2 Cell directedness

In both 2D and 3D conditions the overall average directedness of non-infected cells (2D: 0.31165, 3D: 0.188757) in the control condition is significantly higher ($p<.0001$) than cells in the infected condition (2D: 0.241949, 3D: 0.163623) (Figure 20A,Table 30,Table 31).

Table 30: Average Individual Cell Directedness Over All Time: Log2 Fold Change of Means

Condition 1	Condition 2	Log2 Fold Change (Cond 1/ Cond 2)
2D Control	3D Control	0.723
2D Infection	3D Infection	0.564
2D Control	2D Infection	0.365
3D Control	3D Infection	0.206

In 3D the directedness of cells in the infected condition at each hour range is significantly higher than 3D control condition except during the 48-72 hour window (Figure 20b,Table 32). Over time, in all conditions, there is a decrease in average cell directedness as cells have accumulated more movement over time. There is significant differences between all conditions at all hour ranges except 2D control and 2D infected cells at the 0-12 hour range (Figure 20,Table 33).

Table 31: Average Individual Cell Directedness Over All Time: Wilcoxon

Condition 1	*Directedness*	*Condition 2*	*Directedness*	*p value*
2D Control	0.312	3D Control	0.189	9.36E-200
2D Infection	0.242	3D Infection	0.164	6.59E-207
2D Control	0.312	2D Infection	0.242	1.85E-152
3D Control	0.189	3D Infection	0.164	5.69E-35

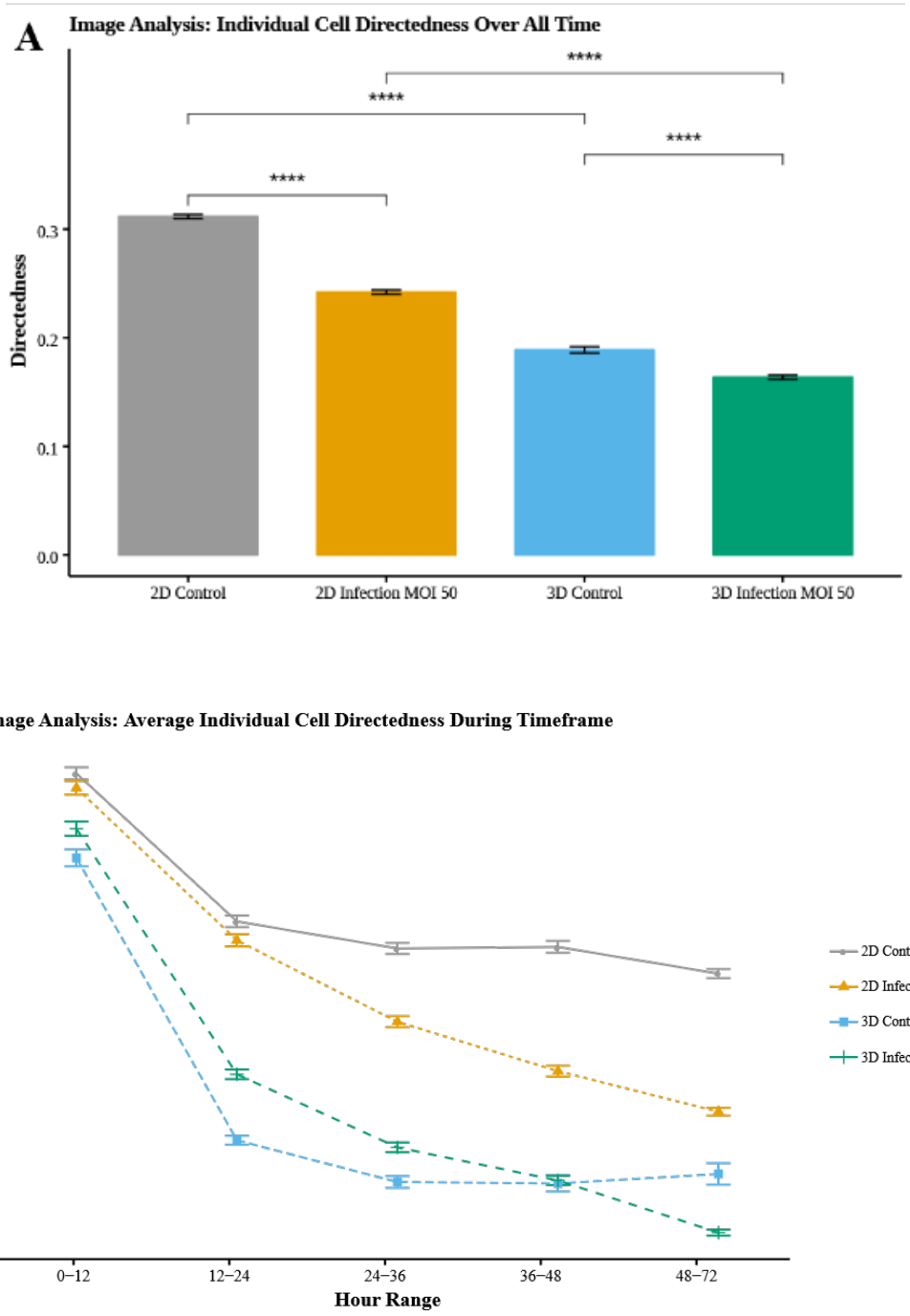

Figure 20: Image analysis of individual cell volume of gfpBMDM infected with mCherry M.smegmatis in 2D and 3D culture conditions over 72 hours. A) Averaged over all time B) Averaged based on hour range. (ns- No significant difference, * - p<.05, **-p<.01,***-p<.001,****-p<.0001)

Table 32: Average Individual Cell Directedness 2D vs. 3D Over Time (timeframes): Wilcoxon

Hour Range	Condition 1	Directedness	Condition 2	Directedness	p value
0-12	2D Control	0.428	3D Control	0.364	6.32E-18
12-24	2D Control	0.317	3D Control	0.153	6.06E-108
24-36	2D Control	0.297	3D Control	0.122	5.53E-112
36-48	2D Control	0.298	3D Control	0.121	1.44E-67
48-72	2D Control	0.278	3D Control	0.128	2.03E-44
0-12	2D Infection	0.417	3D Infection	0.386	7.14E-05
12-24	2D Infection	0.303	3D Infection	0.202	5.23E-44
24-36	2D Infection	0.242	3D Infection	0.148	9.45E-16
36-48	2D Infection	0.205	3D Infection	0.123	1.91E-108
48-72	2D Infection	0.174	3D Infection	0.084	2.54E-167

Table 33: Average Cell Directedness Control vs. Infected Over Time (timeframes): Wilcoxon

Hour Range	Condition 1	Directedness	Condition 2	Directedness	p value
0-12	2D Control	0.428	2D Infection	0.417	0.088243
12-24	2D Control	0.317	2D Infection	0.303	0.04272
24-36	2D Control	0.297	2D Infection	0.242	3.39E-18
36-48	2D Control	0.298	2D Infection	0.205	8.08E-45
48-72	2D Control	0.278	2D Infection	0.174	2.30E-104
0-12	3D Control	0.364	3D Infection	0.386	0.000579
12-24	3D Control	0.153	3D Infection	0.202	1.30E-32
24-36	3D Control	0.122	3D Infection	0.148	4.41E-13
36-48	3D Control	0.121	3D Infection	0.123	0.308664
48-72	3D Control	0.128	3D Infection	0.084	2.64E-07

3.3.7.3 Cell volume

In both 2D and 3D conditions the overall average cell volume of cells in the infected condition (2D: 3797.04 μm^3, 3D: 3031.24 μm^3) is significantly higher ($p<.0001$) than non-infected cells in the control condition (2D: 3731.124 μm^3, 3D: 2364.482 μm^3). The fold change of differences between control and infected within the 2D condition is less than that observed in 3D (Figure 21A, Table 34,Table 35).

Table 34: Average Individual Cell Volume Over All Time: Log2 Fold Change of Means

Condition 1	Condition 2	Log2 Fold Change (Cond 1/ Cond 2)
2D Control	3D Control	0.658
2D Infection	3D Infection	0.325
2D Control	2D Infection	-0.025
3D Control	3D Infection	-0.357

Over the time-span of imaging there is greater variation in average cell volume in the 2D and 3D infected conditions as compared to the 2D and 3D controls (Figure 21B). Significant differences are seen between all conditions at all hour ranges (Table 36, Table 37).

Table 35: Average Individual Cell Volume Over All Time: Wilcoxon

Condition 1	*Volume μm^3*	*Condition 2*	*Volume μm^3*	*p value*
2D Control	3.73E+03	3D Control	2.36E+03	0
2D Infection	3.80E+03	3D Infection	3.03E+03	3.99E-285
2D Control	3.73E+03	2D Infection	3.80E+03	4.04E-08
3D Control	2.36E+03	3D Infection	3.03E+03	6.11E-132

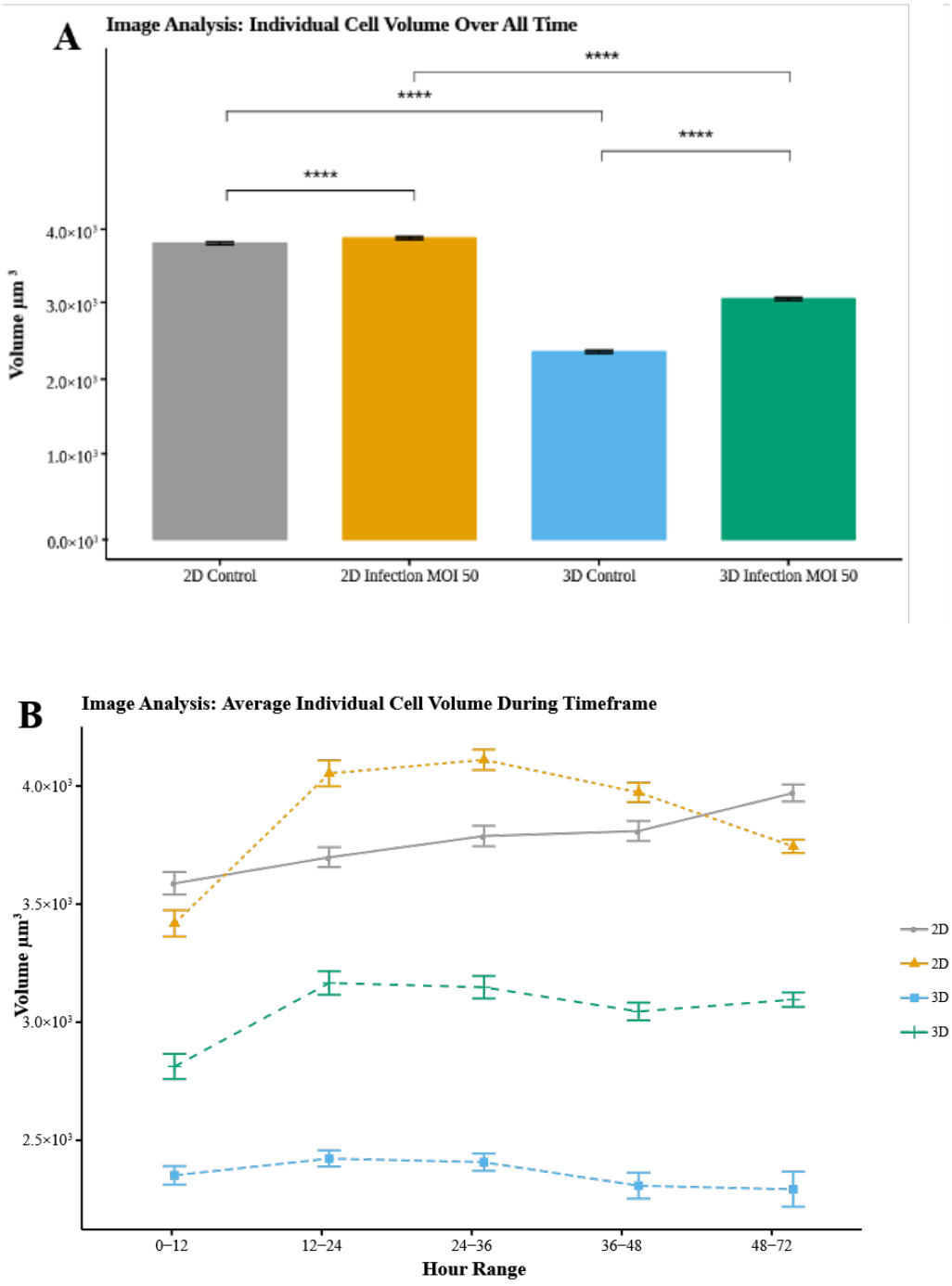

Figure 21: Image analysis of individual cell volume of gfpBMDM infected with mCherry M.smegmatis in 2D and 3D culture conditions over 72 hours. A) Averaged over all time B) Averaged based on hour range. (ns- No significant difference, * - p<.05, **-p<.01,***-p<.001,****-p<.0001)

Table 36: Average Individual Cell Volume 2D vs. 3D Over Time (timeframes): Wilcoxon

Hour Range	Condition 1	Volume μm^3	Condition 2	Volume μm^3	p value
0-12	2D Control	3.52E+03	3D Control	2.35E+03	2.61E-74
12-24	2D Control	3.63E+03	3D Control	2.41E+03	1.39E-87
24-36	2D Control	3.71E+03	3D Control	2.40E+03	1.04E-81
36-48	2D Control	3.74E+03	3D Control	2.30E+03	9.75E-79
48-72	2D Control	3.89E+03	3D Control	2.29E+03	1.32E-73
0-12	2D Infection	3.36E+03	3D Infection	2.79E+03	0.001391
12-24	2D Infection	3.97E+03	3D Infection	3.12E+03	3.96E-06
24-36	2D Infection	4.02E+03	3D Infection	3.10E+03	5.10E-15
36-48	2D Infection	3.89E+03	3D Infection	3.01E+03	8.16E-06
48-72	2D Infection	3.67E+03	3D Infection	3.05E+03	0.018879

Table 37: Average Individual Cell Volume Control vs. Infected Over Time (timeframes): Wilcoxon

Hour Range	Condition 1	Volume μm^3	Condition 2	Volume μm^3	p value
0-12	2D Control	3.52E+03	2D Infection	3.36E+03	8.36E-25
12-24	2D Control	3.63E+03	2D Infection	3.97E+03	1.09E-44
24-36	2D Control	3.71E+03	2D Infection	4.02E+03	2.58E-76
36-48	2D Control	3.74E+03	2D Infection	3.89E+03	1.38E-70
48-72	2D Control	3.89E+03	2D Infection	3.67E+03	1.95E-81
0-12	3D Control	2.35E+03	3D Infection	2.79E+03	7.47E-07
12-24	3D Control	2.41E+03	3D Infection	3.12E+03	1.89E-22
24-36	3D Control	2.40E+03	3D Infection	3.10E+03	3.40E-25
36-48	3D Control	2.30E+03	3D Infection	3.01E+03	2.70E-36
48-72	3D Control	2.29E+03	3D Infection	3.05E+03	2.99E-39

3.3.8 Correlation analysis shows stronger relationships depending on condition and environment.

Figure 22 shows the results of Pearson correlation performed on all conditions independently. Figure 23 highlights significant correlations p<.05.

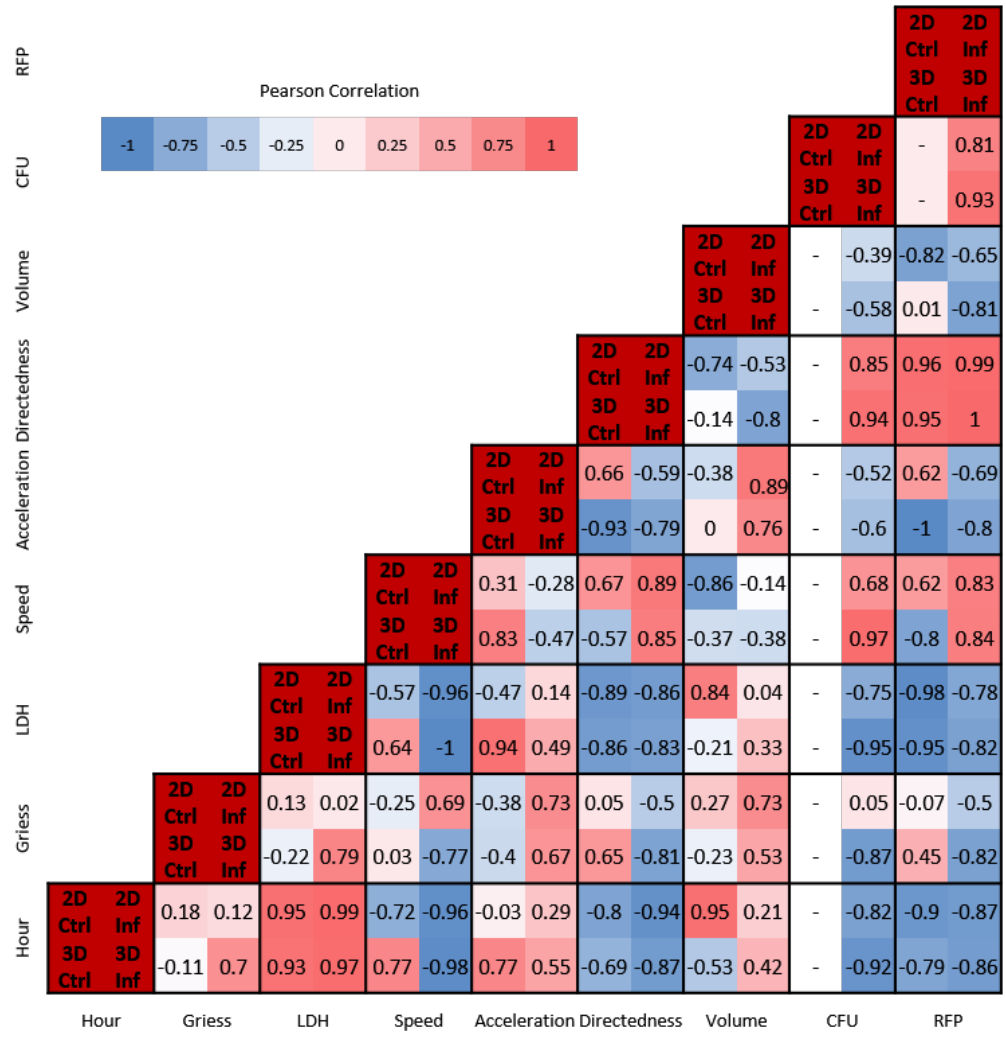

Figure 22: Pearson's correlation of all conditions. Each square includes correlation value for all conditions: Upper Left-2D Control, Upper Right-2D Infection, Lower Left- 3D Control, Lower Right-3D Infection. Rounded to two decimal places

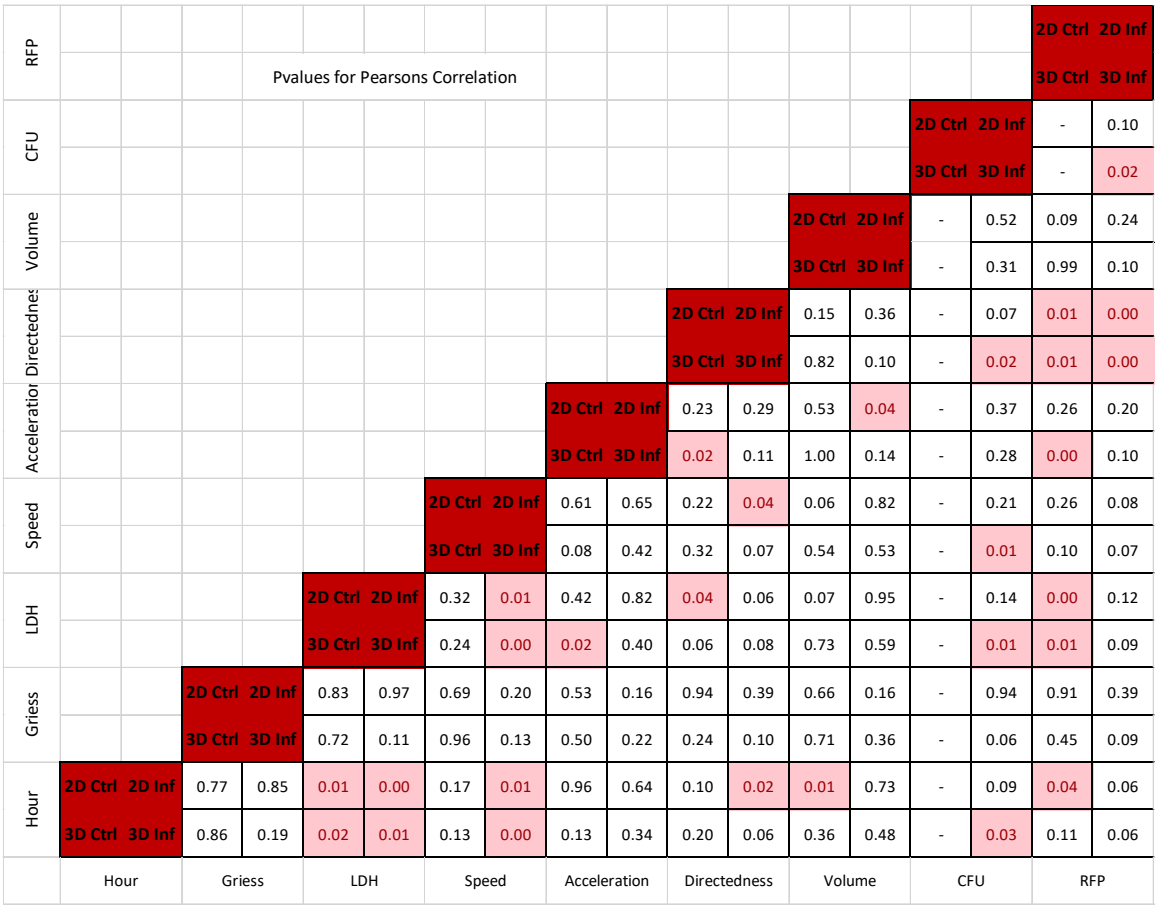

Figure 23: P values for Pearsons correlation rounded to 2 significant figures. Significant P values are highlighted in red.

3.3.8.1 Hours in Culture

3D Infection has a high positive correlation between nitric oxide and hours in culture (0.7); all other conditions have a low correlation with time (< +/-0.2). LDH and hours in culture maintains a high positive correlation regardless of condition (>0.9, p <.05). Cell speed and hours in culture presents a high positive correlation in 3D control condition (0.77) all other conditions have a high negative (<-0.7) correlation but only 3D and 2D infection are significant (p<.05). Acceleration and hours in culture presents a

minimal correlation in 2D (<+/-0.3), but both 3D control and infection present a high positive correlation (>0.5). Directedness and hours in culture maintains a high negative correlation regardless of condition (<-0.6), but only shows significance in 2D infection ($p<.05$). Cell volume and hours in culture shows a high positive correlation in 2D control (0.95, $p <.05$) and 3D control presents with a high negative correlation (-0.53). 2D and 3D Infected conditions both have low positive correlations (<0.5). CFU and hours in culture have a high negative correlation in both 2D and 3D infection (<-0.8), but only shows significance in 3D infection ($p<.05$). The adjusted RFP mean and hours in culture presents with a high negative correlation in all conditions even after the field-based normalization (<-0.7) but significance is only shown in 2D controls ($p<.05$).

3.3.8.2 Effector molecules, nitric oxide and LDH

Nitric oxide was not significantly correlated with any other measured variables. However, there are notable differences in correlation patterns, with nitric oxide exhibiting a high positive correlation with cell speed in 2D infection (0.69), but a high negative correlation with speed in 3D infection (-0.77). Differences between control and infection groups also emerged. We observed a high positive correlation between nitric oxide and cell volume in both 2D and 3D infected conditions (>0.5), but minimal correlation in both control conditions (<+/-0.3). Although not statistically significant, these variations in correlative relationships may suggest underlying mechanisms that may be differentially modulated by environment and infection condition.

LDH cytotoxicity assay exhibit high negative correlation to speed in all conditions (<-0.5) except 3D control, but significance is only present in both 2D and 3D infected

conditions. Correlation of LDH to acceleration only shows significance in 3D controls (0.94, p <.05). Directedness and LDH have a high negative correlation in all conditions (<-0.8), with significance only in 2D controls (p<.05). LDH is significantly correlated with bacterial load (CFU) in 3D infection only, but the correlation between adjusted RFP means to LDH levels is highly negative in all conditions (<-0.7), but only significant in controls (p<.01).

3.3.8.3 Cell dynamics, speed, acceleration and directedness.

Cell speed and acceleration do not present with any significant correlation. The only significance in cell speed is with directedness in 2D infection (.89, p<.05), and with CFU in 3D infection (.97 ,p<.05). Cell acceleration has a high negative correlation to directedness in 3D control (-.93,p<.05). Cell volume has a high positive correlation to cell acceleration in both infected conditions (>0.75), but is only significant for 2D infection (p<.05). Acceleration and adjusted RFP mean are significantly correlated in 3D controls (p<.01). We observe a high positive correlation between CFU counts and directedness under 3D infection only (.94,p<.05), but adjusted RFP mean has a high positive correlation with cell directedness in all conditions (>0.8, p <.05). The adjusted RFP mean exhibits a high positive correlation to CFU in both 2D and 3D Infection (>0.8), but is only significant for 3D infection (p<.01).

3.4 Discussion

In this study we developed a platform that integrates standard biological sampling methodologies with long-term time-lapse confocal imaging, enabling concurrent biochemical and imaging-based quantification of the spatiotemporal response to

infection in 3D. Through careful characterization of technical limitations and biological components of the system, we were able to address methodological limitations of current *in vitro* and *in vivo* models of nascent granuloma formation. Using fluorescent BMDM and *M. smegmatis* strains, we compare the 2D and 3D biochemical and structural immune response to a low-level mycobacterium infection and quantitatively analyze the impact of environment on effector response, cellular dynamics, and bacterial clearance. While many of the biochemical immune response measures including overall bacterial load, nitric oxide and LDH-based cytotoxicity were comparable regardless of the dimensionality of the environment, by utilizing 4D confocal imaging we observed significant differences in the spatiotemporal response to bacterial infection in 2D and 3D environments. Combining Imaris-based image processing and our MATLAB-based analysis pipeline enabled us to comparatively characterize differences in cellular velocity, acceleration, directedness, and volumetric response for macrophages in 2D versus 3D with single-cell resolution.

3.4.1 Availability of a 3D environment does not significantly impact the ability of macrophages to clear intracellular bacteria during low level infection

BMDMs in the 3D RBM environment did not demonstrate significantly altered clearance of bacteria as compared to the 2D infection when enumerating the CFUs over the course of the 72-hour infection. Both 2D and 3D conditions presented a low-level infection that reduced bacterial load consistently over time. The expression of nitric oxide, due to the low sensitivity of the assay, demonstrated significant variability between studies. These results show that the bactericidal activity in response to

mycobacterial infection within the 3D environment might have a slightly altered mechanism of action than in a standard 2D environment. Further investigation is needed to better elucidate the NO response in 3D versus 2D conditions. The expression of LDH did not show any significant difference between infected cells in the 3D environment compared to standard 2D, but there was a significant difference in control cells with 3D controls having the highest levels of cell death. However, analysis of the rate of cell death in the culture shows that both control and infected cells in 3D maintain a consistent rate with their 2D counterparts. The increase in cell death over time is consistent with previous results of low level infection[36].

3.4.2 Availability of a 3D environment significantly impacts macrophage migration and motility

Although we saw little to no levels of significant difference between conditions with respect to biochemical response to infection the quantification of cellular migration and motility demonstrated significant differences between control and infected cells and the impact of the 2D and 3D environment. In general, we observe a muted response in 3D, with reduced velocity, acceleration and directedness overall. This overall higher motility in 2D compared with 3D can be potentially attributed to differences in the mechanisms of cellular migration in a 3D matrix [67].

The overall decrease in motility in the 3D environment is expected due to the introduction of the physical structural proteins in the ECM. However, what is most interesting is that the relationship between these dynamics in response to infection differs in the two environments. In 3D the infected condition has a higher overall

average cell velocity and acceleration throughout the entire 72hour period. Directedness in the 3D infected condition is significantly higher for the majority of the time-course, only decreasing after the bacterial load in the system has significantly decreased in the 48 to 72-hour range. Conversely the infected condition in 2D shows lower average cell velocity, acceleration and directedness as compared to the 2D controls. This demonstrated that even though the overall biological representation of the systems shows no significant differences, the ability of the cells to migrate and mobilize is greatly impacted by the introduction of the 3D environment.

In addition, unlike previous studies of mycobacterial infection and granuloma formation *in vitro*, the developed platform allows for the evaluation of the host immune response in terms of cellular dynamics over extended culture through the use of multi-area time-lapse confocal imaging. Previous *in vivo* studies of *Mycobacterium marinum* infection in zebrafish conducted by Davis and Ramakrishnan [15] observed motility and directed motion of macrophages over time in correlation to bacterial load. They observed that the motility of infected macrophages was higher as their bacterial load increased and that the macrophages approaching, and phagocytosing dead cells had a more directed motion [15]. In particular their investigation found that the average cellular speed of uninfected macrophages (7.5E-2 um/s), was is in agreeance with the cellular speed utilized in the 2D chemotactic studies of macrophage migration[68]. Our observations in *M. smegmatis* infection found that macrophages within the infected conditions displayed different motility dependent on environment and based on the presence of infection. In the 2D environment we observed that cells in the infected

condition had a significantly lower average speed than non-infected condition in agreeance with Davis and Ramakrishnan but observed the converse in the 3D environment. Davis and Ramakrishnan identified that the RD1 virulence locus presence in *M. marinum* was the key factor in the regulation of the macrophage dynamics under mycobacterial infection. In comparison to our work, this virulence locus is not present in the less virulent *M. smegmatis*, and can explain the muted difference in cell motility under infection in the 2D environment, but our observation shows the converse occurring in 3D. In addition, the cellular migration induced by *M. smegmatis*, a less virulent mycobacterium, has been shown to induce a different migration mode primarily due to the lack of cell-surface-associated phthiocerol dimycoceroserate (PDIM) lipids which are present in virulent pathogenic mycobacterium variants including *M. tuberculosis, M. marinum* and many *M. bovis* strains [69]. Previous studies in zebrafish embryos with *M. smegmatis* and the more virulent PDIM marine variant *M. marinum* showed that the migration of macrophages in *M. smegmatis infection* was MyD88-dependent in contrast to a MyD88-independent migration in *M. marinum* infection which was discovered to be mediated specifically by the presence of PDIM [70]. In addition, this study also acknowledged a dependence of iNOS (a precursor of nitric oxide)-dependent microbicidal based on PDIM, showing a decrease in iNOS in response to the more virulent strains of mycobacterium [70].

We also acknowledge that these observations do not take into consideration the heterogenous makeup of the infected conditions, as cells within these environments can contain intracellular bacteria, whereas others may not. Previous studies have shown

that the activation of macrophages in a proinflammatory state exhibit markedly different migratory patterns compared to their non-activated or anti-inflammatory activated counterparts [71]. A preliminary effort into a high-throughput cell dynamic analysis for heterogenous cell populations has been previously reported [61], and an expansion of this initial platform may provide further insight into bacterial load dependent cellular dynamics.

3.4.3 Availability of a 3D environment significantly impacts changes in macrophage volume during intracellular infection.

Our study shows a significant difference in the impact of the environment on cell volume. While direct comparison between cell volume in 2D and 3D is difficult due to the differing morphologies even with consistent imaging analysis and watershed segmentation, the analysis within each condition shows an interesting trend in cellular volume. At most time points we see a significant increase in the cellular volume in the infected conditions which is consistent with the literature that show that macrophage volume can be correlated to phagocytosis of the bacterium [43]. However, we see a more dramatic fold change increase in the 3D condition as compared to 2D. This higher increase in volume in the 3D infection environment is consistent with correlation analysis that demonstrates a high correlation between LDH and cellular volume in 3D infection conditions (.33) compared to the lower correlation in 2D infection (0.04). However, we demonstrate a negative correlation between bacterial load and cell volume in both 2D (-0.39) and 3D infection (-0.58) showing an increase in cellular volume over time as the infection clears from macrophages in 2D and 3D. This time-

based increase in cell volume in the infected conditions in relation to the decreasing bacterial implies a more complex relationship between bacterial infection and the regulation of cellular volume during the process of active phagocytosis and after the infection has been cleared from an infected macrophage.

3.4.4 Correlation of cellular dynamics depending on condition and environment

We observed significant correlations between cell dynamics, attributes and biological response to infection. Of note is the correlation that exists between cell acceleration and volume. We note that, although not significant, the average individual cell acceleration in both the 2D and 3D environments has a positive correlation to the average cell volume (>.75). In the control conditions we see a slight non-significant negative correlation in 2D control (-0.38) and zero correlation in 3D controls, showing a shift in dynamics. We do see that the environment plays a significant role in the cellular dynamics of speed, acceleration and directedness. We see that there is a high positive correlation for 2D infection, 3D infection and 2D control cells between average cell speed and average cell directedness (>.65), with the infected conditions both having the highest correlation. The opposite is seen in 3D where the correlation is highly negative (-0.57). By looking back at the overall data for cellular speed we also not that 3D controls have the lowest average cellular speed per hour range as well as the lowest directedness (except the 48-72 hour range). Visual inspection of the 3D control cells shows very little distance traveled for the cells in this condition providing visual confirmation of the low speed. The calculation of directedness takes into consideration each timepoint of movement form the cells calculated center, so even minor

movements contribute overtime to the cells overall distance travelled and thus the directedness.

Significant correlations of bacterial load (CFU) are only seen for the 3D infected condition. We have significant correlation to LDH, cell speed, directedness and adjusted RFP mean. Contrary to previous investigations of low level *M. smegmatis* infection we found that in general there was a negative correlation between LDH and NO and bacterial load in 2D and 3D conditions[36]. The exception is the correlation between bacterial load and NO in 2D infection which presents with a very minor positive correlation (0.05). This divergence form previous observations can be due to the imposition of the 3D environment, or the presence of gentamicin in the infection culture leading to slightly different presentation of infection dynamics. This may suggest that the availability of the 3D environment has a significant impact on the cell behavior depending on bacterial load. Further investigation into bacterial load and cell dynamics may elucidate this relationship.

4 DEVELOPMENT OF QUANTITATIVE COMPUTATIONAL PIPELINE FOR INVESTIGATION OF HOST-PATHOGEN SPATIOTEMPORAL DYNAMICS

4.1 Introduction

Computational biology models that recapitulate the granuloma formation and the associated immune response to *Mycobacterium tuberculosis* (Mtb) infection have described the links between the structural immune response and the mechanistic drivers that can lead to bacterial adaptation and persistence. The mycobacterial granuloma, a defining characteristic of the adaptive immune response to Mtb infection, has been classically described as a host-protective response producing a cellular barrier between the infection and the surrounding host tissue, enabling the host immune system to spatially localize effector molecules produced to treat the infection[2], [9], [10]. The computational models developed to characterize this phenomenon have investigated the control mechanisms of effector molecules and T cells[72], the role of the proinflammatory cytokines like tumor necrosis factor-alpha (TNF-α)[73], [74], and the role of localized hypoxia in granuloma mediated immune response to Mtb infection [48]. While the majority of computational models focus on the granuloma mediated response, there are computational models that investigate the early infection dynamics [75].

A challenge in the development of computational models of Mtb infection and immune response is the reliance on disparate data sets collected from studies of various

TB and non-TB diseases, and data from diverse hosts including human patient data[76], [77], *in vivo* animal studies [78], 2D *in vitro*/chemotactic migration studies [68], [79]–[82], 2D infection studies, as well as bacterial characterization studies[83]–[85]. Often times uncertainty quantification methods are used with differentially sourced datasets to explore relationships between parameters and model outputs, and help establish plausible parameter values [86]. This process leads to an amalgamation of disparate datasets that can result in improperly inferred model parameters particularly for variables used to describe cellular dynamics, which are difficult to capture in 2D *in vitro* studies and in the absence of imaging-based methods and pipelines that can quantify the spatiotemporal dynamics of immune response during infection.

The dynamics and migration patterns of cells during mycobacterial infection are impacted by both the physical structure and cytokines, chemokines, and effector molecules produced by cells in the surrounding environment[7], [67], [87]. This complex microenvironment cannot be sufficiently replicated in a standard 2D study as the lack of the extracellular matrix cannot replicate the complex spatial organization of cells within this three dimensional (3D) environment, and how that spatial organization impacts control, resolution, or dissemination of the bacterium [1], [6]. *In vivo* studies, which naturally enable the study of host-pathogen interactions within the context of a 3D spatial environment, are less amenable to temporal sampling, as analysis of the spatial organization of cells requires sacrificing the animal, tissue fixation and histological staining [16]–[19]. However, recent investigations by Davis et. al and more recently the work of Davis and Ramakrishnan leverage the optical transparency of zebrafish embryo

infection models to investigate the initial innate response to mycobacterial infection *in vivo* [14], [15]. By coupling the zebrafish mycobacterium infection model with imaging, the study characterized initial macrophage aggregation and key factors impacting infection progression and granuloma formation, including the rate of macrophage aggregation, velocity of macrophages entering or exiting infected sites in a relatively small sample size (up to n = 12). Other studies have utilized short-term intravital imaging, up to only 3 hours. in mice to investigate the cellular dynamics within hepatic granulomas [10]. *In vivo* imaging studies of infection have provided significant insight into the dynamics of host-pathogen interactions and the role of cellular motility in mycobacterial infection. This inability to sufficiently image cell dynamics in a high temporal resolution in a live animal for extended periods due to imaging constraints severely limits the spatiotemporal insights that can be gained from *in vivo* animal models. Thus, there remains a notable lack of studies that capture host-mycobacterium infection dynamics for the duration of the early infection process, which can occur over the course of multiple days.

To address these limitations, we have developed a computational analysis pipeline coupled with a 3D *ex vivo* experimental model of the early macrophage infection with *Mycobacterium smegmatis*, an analog for Mtb. With this platform we utilize long-term time-lapse confocal imaging to investigate the host-pathogen response over the long-term course of infection (up to 72 hours in culture) and apply a high-throughput analysis of all cells within the imaging field to investigate the spatial and cell state-based dynamics that occur within mycobacterial infection. We quantify cell spatial

organization and cell state in comparison to 2D *ex vivo* experimental models of investigating cellular dynamics that have been utilized to inform computational models. We utilize this state-based quantification and provide tools to improve upon model parameters through the generation of biologically relevant empirical distributions.

Using our quantitative pipeline, we identified cellular features that correlate with bacterial load, host cell dynamics, and differences in spatial organization in 2D and 3D environments. In this approach we first employ machine learning to segment the heterogeneous population of infected cells based on bacterial load determined by fluorescence levels. We then use the presence of infection within cell aggregates determined by clustering algorithms to determine proinflammatory active cells responding to infection. Finally, we apply supervised machine learning algorithms to determine which features can be used to distinguish between the cellular states.

Our results of state based dynamics demonstrate that non-infected and non-active macrophages within infected environments present dynamics comparable to controls, while infected and activated macrophages exhibit comparable spatiotemporal dynamics in 2D and 3D. We compare our empirically generated results to our previously developed agent based model of the role of hypoxia in Mtb infection and granuloma formation and identify key findings based on the assumptions of cellular speed. Our quantification shows an overall disparity in dynamics between 2D and 3D environments, specifically in cellular speed where we see that infected and activated cells in the 2D condition present with a slower speed than 2D non-infected cells, which behave more comparably to control cells not in the presence of infection. This reduction in cellular

speed is in agreement with computational modeling assumptions garnered from 2D chemotactic assays [48]. However, we observe the converse in the 3D environment, where the cellular speed of infected and active cells is significantly faster than 3D non-infected cells, which behave more comparably to 3D control cells. This disparity in dynamics brings into question many of the cell velocity-based parameters utilized for computational models of Mtb infection.

The application of machine learning models to predict cellular state highlights an important characteristic of cellular dynamics, that the discrimination between cellular state is not dependent upon one single feature, but a combination of the observable cellular dynamics as demonstrated by a higher classification accuracy in the 3D environment, which had less distinguishable differences in individual cell dynamics. Through this application we identified several of the key cell dynamics previously investigated as well as a marker of proinflammatory macrophage activation, the cell shape feature sphericity[88]. This feature demonstrated a high capability of detecting proinflammatory infected and active cells in the 2D environment and demonstrated the cell shape disparities in comparison to 3D.

4.2 Materials and Methods

4.2.1 Infection Study

All animal experiments were performed with the approval of the Institutional Animal Care and Use Committee at the University of Houston and in accordance with the recommendations in the Guide for the Care and Use of Laboratory Animals and the

American Veterinary Medical Association (AVMA) Guidelines for the Euthanasia of Animals. GFP bone marrow derived macrophages (gfpBMDM) were isolated from the hind legs of 10-week-old female mice from the transgenic mouse line C57BL/6-Tg(CAG-EGFP)131Osb/LeySobJ and infected at a multiplicity of infection of 1 macrophage to 50 bacterium (MOI 50) with *m. Cherry M. smegmatis* (gifted by Dr. Cirillo Texas A&M University, TX) as previously reported [36].

After infection, cells were removed from culture dishes and distributed into the 2D or 3D culture for image analysis. In one 8 well chamber slide (Ibidi), a diluted RBM (.18 mg/mL) coating was added to 4 wells in for 3D culture [52], and incubated in a cell culture incubator for 30 minutes then the diluted RBM was aspirated. Immediately following, both infected and non-infected cells at 2.5E6 cells/mL were resuspended at 0-8˚C in diluted 8.5 mg/mL RBM and 100 µL of the resulting cell suspension was plated into the center of each coated chamber well (2 infected, 2 non-infected). For 2D culture, 250 uL of 5E5 cells/mL of non-infected cells in DMEM-complete (Dulbecco's Modified Eagle Medium containing 10% fetal bovine serum,1% L-glutamine and 1% non-essential amino acid) with 10 µg/mL gentamicin (Sigma Aldirch) were plated in replicate in two of the remaining uncoated wells. Infected cells (250 ul at 5E5 cells/mL) in DMEM-complete with 10 µg/mL gentamicin were then added to last two uncoated chamber wells. The addition of 10 µg/mL of gentamicin in the culture media for 2D infection culture allows for comparison to the buffer solution of RBM, which after dilution and hydrating media addition results in a gentamicin concentration of 10 µg/mL [53]. Previous studies have utilized this this concentration to inhibit the extracellular growth of mSmeg without

impacting the intracellular growth [54] [53]. The chamber slide was then incubated in a cell culture incubator for 45 minutes for gelation and then 275 µL of DMEM-complete was added to prevent gel dehydration during extended culture prior to imaging, and cells were allowed to adhere in 2D for two hours prior to sampling. he biological study was performed twice in biological replicate for a total n=4.

4.2.2 Imaging and Image Processing

4D confocal images of 512x512 resolution 100 um Z-stacks at axial resolution of 1um were acquired with scanning laser confocal imaging sequentially by line with 488 nm and 543 nm excitation lasers every 90 minutes for up to 72 hours (Olympus FV1200-IX83) utilizing the Olympus Fluoview software version 4.2b for image acquisition, a stage top incubation system (TokaiHit) to maintain cell viability, and 40X confocal objective with .95 numerical aperture (UPLSAPO40X2, Olympus). Zero drift compensation was utilized to prevent focal drift throughout the imaging time-lapse. In order to reduce the effects of phototoxicity due to exposure to confocal lasers, the dwell time per pixel for confocal imaging was minimized (2 µs/Pixel) [57]–[59]. Two points per well per experimental trial were imaged for a total of n=8 imaging samples per condition were acquired satisfying the population sampling criteria detailed by the Yamane formula [60].

Confocal images were appended over time in Olympus Fluoview software. The resulting 4D time appended confocal images were rendered and analyzed using Imaris 8.1.2 (Bitplane) with surface creation and tracking of macrophages to monitor change in cellular dynamics over time. The same image processing parameters were used for all

trials analyzed (Figure 24). Adjustments to fluorescent cutoffs were made between experimental trials due to variance in background fluorescence. Green fluorescent protein (GFP) was used to establish watershed segmentation and tracking of cells over the time course of imaging, and RFP values were used as a feature of each segmented cell object to denote the bacterial levels within each cell.

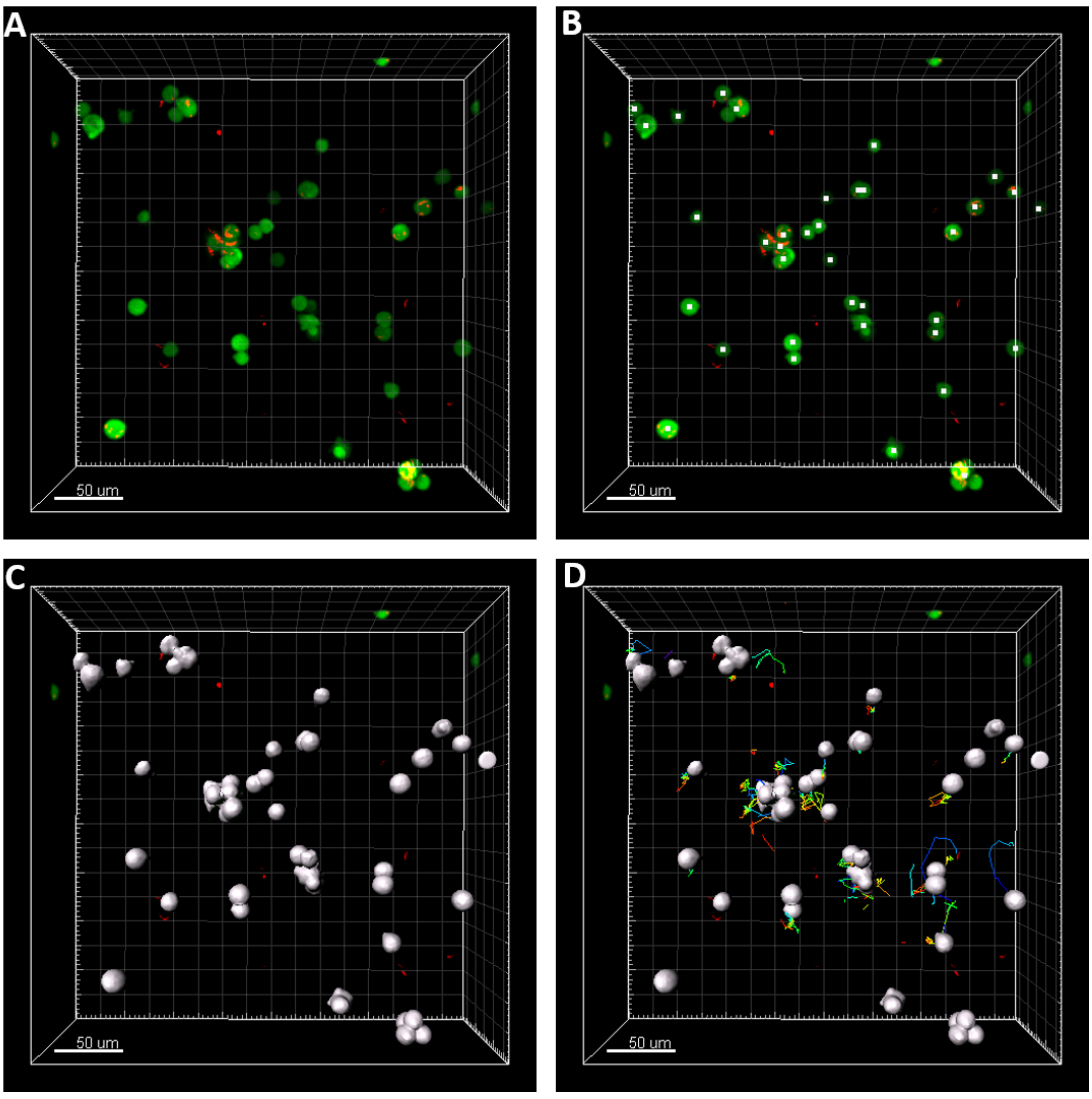

Figure 24: Image Processing in Imaris 8.1.2 of 3D infected cells at hour 0 of imaging: A) 3D rendering of confocal image B) Seed point diameters set to 8.25 µm C) Watershed segmentation of cells in 3D D) autoregressive motion tracking applied to segmented cells to produce tracks over time.

4.2.3 Computational Pipeline

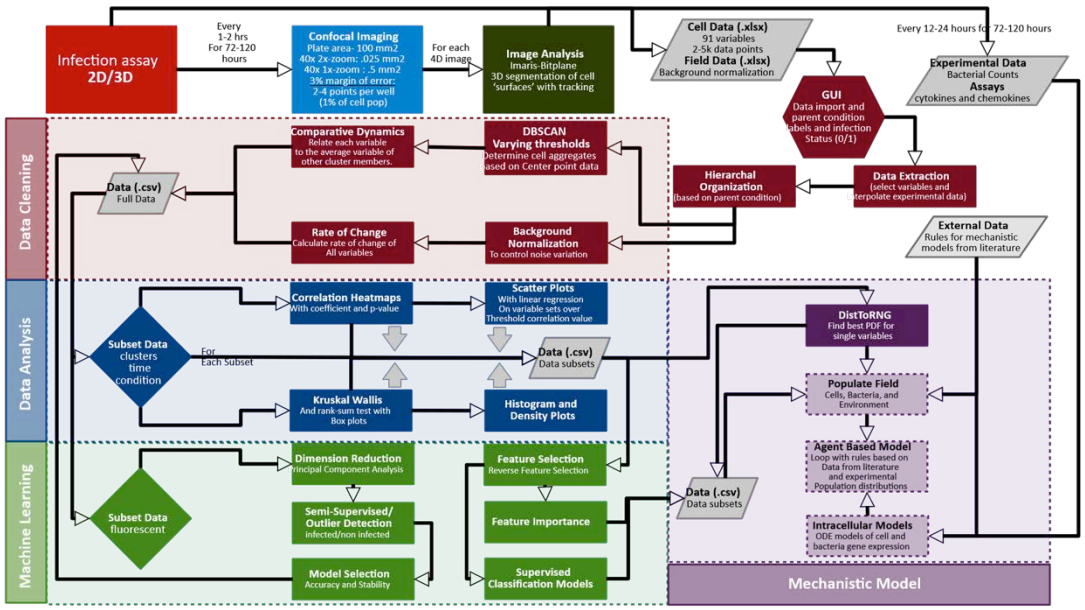

Figure 25: Overview of computational pipeline for automatic analysis of cellular dynamics using 4D confocal imaging data.

The computational pipeline (Figure 25)was developed to automatically quantify the cellular dynamics exported by Imaris through data organization (MATLAB), statistical analysis (R), and machine learning (python) code on both local and high-performance computing on the Core facility for Advanced Computing and Data Science (CACDS) performance research computing center at University of Houston, Houston, Texas (Maxwell Cluster). Bash scripting was used within the Maxwell cluster to allow for simultaneous computation of multiple datasets.

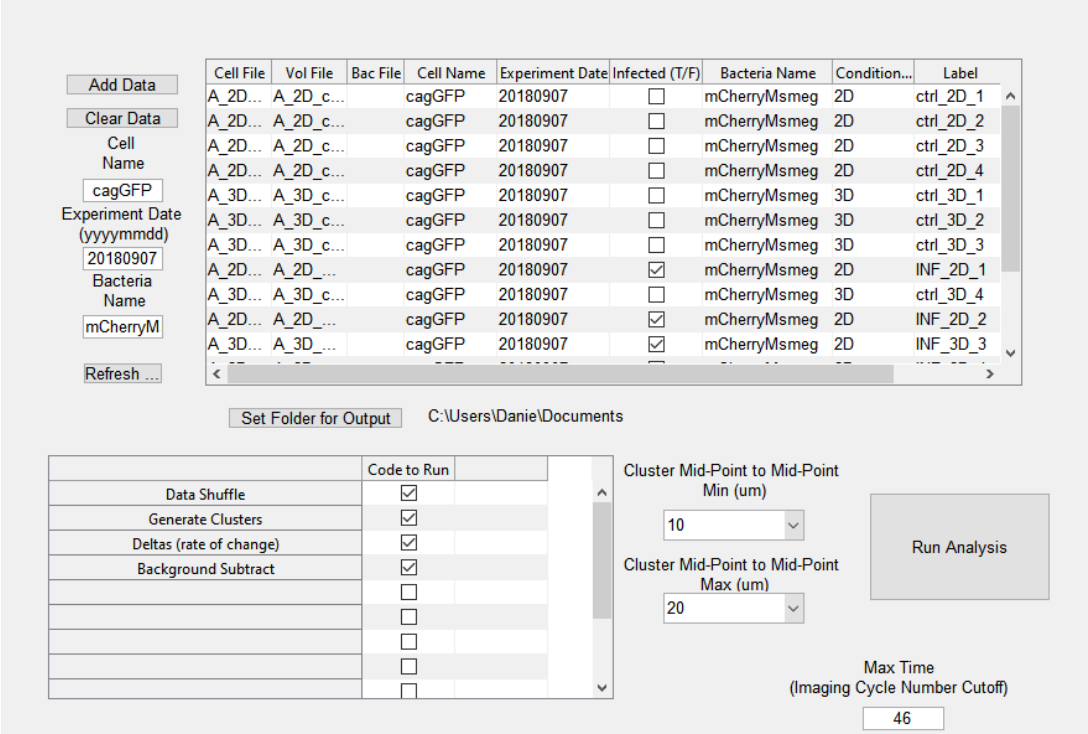

Figure 26: Matlab interface developed with GUIDE to import data from Imaris for data organization and further feature generation.

4.2.3.1 Data organization and feature generation in Matlab

Data from Imaris was imported into Matlab using an interface developed with Matlab's GUIDE (Figure 26). The data was pulled into data structures in a hierarchical manner based on condition and number of replicates and then sent to the Maxwell cluster. Data organization and further feature generation was conducted in MATLAB 2018b. The individual cell tracks over time generated using autoregressive motion tracking in Imaris were used to calculate the directedness of each cell equal to the ratio of the Euclidian (straight-line) distance over the total distance traveled from the initial timepoint to the current timepoint of analysis. A directedness score represents the inverse of random movement on scale of 0 to 1 [62].

The varying signal to noise ratio (SNR) that naturally occurs in time-lapse fluorescent imaging [38] was accounted for through background normalization as previously described through normalization to the control image RFP signal minimum[61]. The normalization scheme was then applied to green fluorescent protein levels resulting in adjusted fluorescent values outlined in Table 38 below.

Table 38: Fluorescent features generated for analysis

Fluorescent Feature	*Definition*
RFP intensity StDev	Standard Deviation of RFP fluorescence intensity in each segmented cell
RFP intensity Mean Adjusted	Mean of RFP fluorescence intensity in each segmented cell normalized to background fluorescence
RFP intensity Min Adjusted	Minimum of RFP fluorescence intensity in each segmented cell normalized to background fluorescence
RFP intensity Max Adjusted	Maximum of RFP fluorescence intensity in each segmented cell normalized to background fluorescence
RFP intensity Median Adjusted	Median of RFP fluorescence intensity in each segmented cell normalized to background fluorescence
RFP intensity Center Adjusted	RFP fluorescence intensity in the center each segmented cell normalized to background fluorescence
RFP intensity Sum Adjusted	Sum of RFP fluorescence intensity in each segmented cell normalized to background fluorescence
GFP intensity StDev	Standard Deviation of GFP fluorescence intensity in each segmented cell
GFP intensity Mean Adjusted	Mean of GFP fluorescence intensity in each segmented cell normalized to background fluorescence
GFP intensity Min Adjusted	Minimum of GFP fluorescence intensity in each segmented cell normalized to background fluorescence
GFP intensity Max Adjusted	Maximum of GFP fluorescence intensity in each segmented cell normalized to background fluorescence
GFP intensity Median Adjusted	Median of GFP fluorescence intensity in each segmented cell normalized to background fluorescence
GFP intensity Center Adjusted	GFP fluorescence intensity in the center each segmented cell normalized to background fluorescence
GFP intensity Sum Adjusted	Sum of GFP fluorescence intensity in each segmented cell normalized to background fluorescence

4.2.3.1.1 Quantification of cellular aggregates using DBSCAN

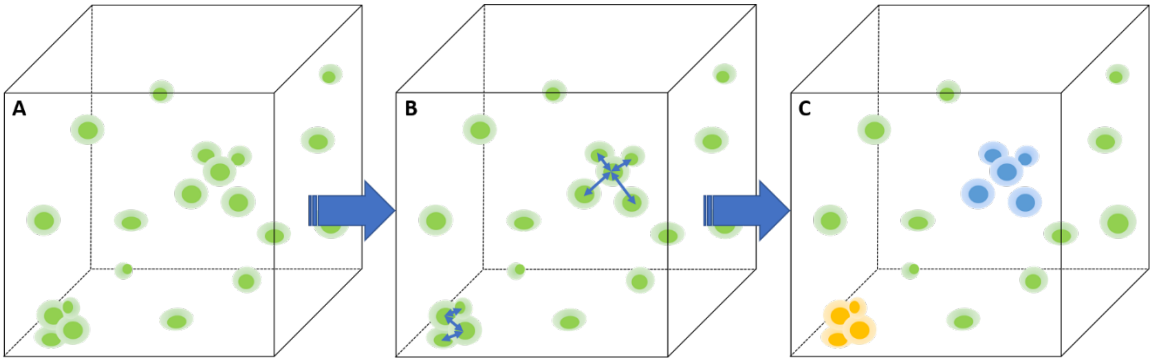

Figure 27: DBSCAN for determining cell clusters from center of homogeneous mass A) Diagram representing 3D Z-stack acquisition of cells in Imaris B) Detection of areas of density C) Representation of cell clusters as determined by DBSCAN algorithm

Early recruitment and aggregation of macrophages to the site of infection during innate response help in the elimination of infection and may contribute to the establishment of nascent granulomas that later form mature granulomas during the adaptive immune response to mycobacterium infection [4], [8]. Thus, one of the main concerns in analysis of the response to mycobacterial infection is the identification of macrophage aggregates. Therefore, a key step in our computational pipeline is the automatic detection and characterization of the spatiotemporal dynamics of macrophage response is identifying cellular aggregates. We determined aggregations of cells computationally using the density-based spatial clustering of applications with noise (DBSCAN) algorithm [89], applied for varying maximal distances between two cell centers of homogenous mass (Figure 27). DBSCAN at 12 µm center point to center point distance was used to generate 'tight clusters', denoted as clusters of cells that are in close physical proximity to each other such that they are likely in contact (Figure 27C,

yellow highlighted cells), and a maximal distance of 20 µm to generate 'loose clusters', denoted as clusters of cells that are within close proximity, but not necessarily in physical contact (Figure 27C, blue highlighted cells). Cell clusters of different sizes are generated independently for further evaluation, but a cluster size of 20 µm, the standard size of 2D grids used in computational models of granuloma formation, and the maximal macrophage diameter reported [55], was used for further analysis. For each identified cluster, we generate the following data: a cluster index, the identifying number of a cluster in each biological replicate at each timepoint; the location of the cluster center, the density center of each cluster of datapoints; and the cluster size, the number of cells associated with each unique cluster.

4.2.3.1.2 Comparative dynamics and rate of change

The rate of change (delta) of each feature was then calculated based on the timepoint to timepoint differentials of the features measured between the 90-minute image acquisitions (Table 39). Given the presence of cellular aggregates, a relationship between an individual cell's dynamics and the surrounding cells in the cellular aggregation were generated as the ratio between the individual cell's feature value and the average feature value of the remaining cells within the DBSCAN determined cellular aggregate for future analysis and quantification based on cluster membership in extension of this work.

Table 39: Features generated for analysis

Feature	*Definition*
speed	The instantaneous speed (nondirectional velocity) of the cell as reported by Imaris autoregressive tracking.
acceleration	The instantaneous acceleration of the cell as reported by Imaris autoregressive tracking.
volume	The volume of the cell as reported by Imaris.
directedness	The directedness of the cell as reported by Imaris displacement autoregressive tracking and then as the calculation of the Euclidian start to end-point distance over total distance travelled over time of tracking.
Ellipicity Oblate	A metric of the flatness of the cell as reported by Imaris .
Ellipicity Prolate	A metric of the elongation of the cell as reported by Imaris.
Sphericity	The ratio of the surface area of a sphere to the surface area of the cell as reported by Imaris[90].
total dist 2	Total distance traveled in 3D by cell to current timepoint of acquisition calculated by sum of the absolute value of timepoint displacement as reported by Imaris autoregressive tracking.
total dist x	Total distance traveled in the x plane by cell to current timepoint of acquisition calculated by sum of the absolute value of timepoint displacement in the x plane as reported by Imaris autoregressive tracking.
total dist y	Total distance traveled in the y plane by cell to current timepoint of acquisition calculated by sum of the absolute value of timepoint displacement in the x plane as reported by Imaris autoregressive tracking.
total dist z	Total distance traveled in the x plane by cell to current timepoint of acquisition calculated by sum of the absolute value of timepoint displacement in the z plane as reported by Imaris autoregressive tracking
total Edist 2	Total straight line (Euclidian) distance traveled in 3D by cell to current timepoint of acquisition calculated by displacement from first track acquisition to current timepoint.
total Edist x	Total straight line (Euclidian) distance traveled in the x plane by cell to current timepoint of acquisition calculated by displacement from first track acquisition to current timepoint.
total Edist y	Total straight line (Euclidian) distance traveled in the y plane by cell to current timepoint of acquisition calculated by displacement from first track acquisition to current timepoint.
total Edist z	Total straight line (Euclidian) distance traveled in the z plane by cell to current timepoint of acquisition calculated by displacement from first track acquisition to current timepoint.
tp disp 2	Timepoint displacement from previous timepoint to current timepoint of image acquisition as reported by Imaris autoregressive tracking algorithm.
tp disp x	Timepoint displacement in x plane from previous timepoint to current timepoint of image acquisition as reported by Imaris autoregressive tracking algorithm.

Table 39 continued:	Features generated for analysis
tp disp y	Timepoint displacement in y plane from previous timepoint to current timepoint of image acquisition as reported by Imaris autoregressive tracking algorithm.
tp disp z	Timepoint displacement in z plane from previous timepoint to current timepoint of image acquisition as reported by Imaris autoregressive tracking algorithm.
x acceleration	The instantaneous acceleration of the cell in the x plane as reported by Imaris autoregressive tracking.
x directedness	The directedness of the cell in the x plane as reported by Imaris displacement autoregressive tracking and subsequent calculations.
x velocity	The instantaneous velocity of the cell in the x plane as reported by Imaris autoregressive tracking.
y acceleration	The instantaneous acceleration of the cell in the y plane as reported by Imaris autoregressive tracking.
y directedness	The directedness of the cell in the y plane as reported by Imaris displacement autoregressive tracking and subsequent calculations.
y velocity	The instantaneous velocity of the cell in the y plane as reported by Imaris autoregressive tracking.
z acceleration	The instantaneous acceleration of the cell in the z plane as reported by Imaris autoregressive tracking.
z directedness	The directedness of the cell in the z plane as reported by Imaris displacement autoregressive tracking and subsequent calculations.

4.2.3.2 Statistical Analysis in R

Statistical analysis was performed in R or R-Studio [63] utilizing the dplyr, ggplot2 and ggpubr libraries to assist with dataframe generation and plotting [64]–[66]. The Wilcoxon rank sum test was used to test for statistical significance.

4.2.3.3 Infection and active cell determination in python machine learning algorithms

To enable high throughput analysis of the heterogenous cell population, we utilized machine learning (ML) algorithms for infection determination to identify which cells in the image acquisition contained bacteria in extension of our previously

developed ML method for segmenting heterogenous cell populations in an active infection environment [61].

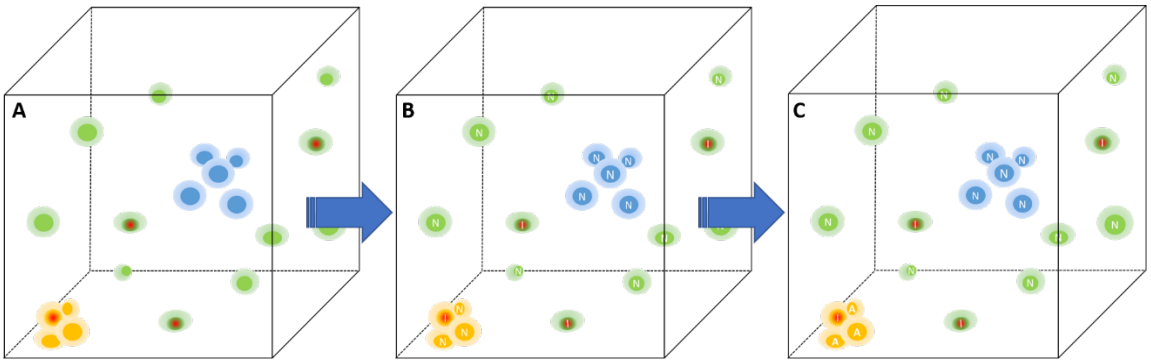

Figure 28: Workflow of infected cell and activated cell determination (I-infected cell, N-Noninfected cell, A-Active Noninfected cell). A) Cells with clusters and known RFP values B) Infected cells determined with ML C) Active cells determined by clusters around infected cells.

We employed unsupervised machine learning and outlier and novelty detection machine learning algorithms in Python to segment the heterogeneous population of infected cells based on bacterial load determined by the normalized fluorescence levels (Figure 28). We quantified the intracellular state of each cell at each timepoint independently as condition of a cell will alter over the course of infection as macrophages can phagocytose new bacteria or clear their internal bacterial load. We utilize the Imaris extracted cells that contains red fluorescent protein levels (RFP) that are indicative of the intracellular bacteria. We applied machine learning algorithms in an extension of previously reported work to determine the infection state of the macrophage [61].

RFP Data was scaled utilizing scikit learn's MinMaxScaler function to transform the data into the feature range (0,1) to prevent biasing of algorithms due to large variations in data range (Table 38) [39]. To identify highly discriminatory features for determining infected versus non infected cells, we used scikit learn's principal component analysis (PCA) algorithm with default settings to reduce feature correlation of the RFP features to project them to a lower dimensional space [41]. The principal components were then ordered based on explanation of data variability and iteratively augmented with additional components to assess how components contribute to the cumulative explanation of variability in the data. Using the components identified by PCA, we then applied ML methods to the principal components that comprised over 99% of the data variability. The same principal components were used for all methods of infection detection and subset into control or infection when specified. Infection determination algorithms were analyzed for qualitative stability between two different datasets performed under the same biological conditions by assessing the misclassification error and number of infected cells detected within each algorithm. The algorithm that produced the highest accuracy with low variability between variations in initializations of the algorithm, and application to both datasets was chosen to determine infected cells for further analysis.

A summation of the parameters utilized for ML quantification of infected cells is summarized in Table 40. Unsupervised methods clustered the unknown infection dataset into two groups using scikit learn's K-means clustering, and Gaussian Mixture Models. The principal components from the control datasets were applied to the

predicted clusters utilizing the prediction attribute of each method in order to calculate the number of misclassified control datapoints (MC_{error}), as previously reported [61]. Outlier and novelty detection ML methods involved trained novelty detection algorithms, one class support vector machine (OC-SVM) and local outlier factor (LOF) classification algorithms, on the principal components from experimental controls, which contain only non-infected cells, and outlier detection methods Isolation forests. OC-SVM and LOF were utilized to quantify potential infected cells as novelties based on training on the control dataset. Isolation Forests utilized all available datapoints from the selected principal components to determine datapoint outliers. For outlier and novelty detection algorithms, MC_{error} was reported as the control datapoints incorrectly identified as outliers or novelties through their inherent testing functions.

Table 40: Parameters used for infection determination ML methods

Algorithm	*Subset of PC's used to train or split*	*Parameters*
GMM	Infection data	k=2 and K++ initialization
K-Means	Infection data	2 components, 10 initializations and a covariance type of full, tied, diagonal or spherical
OC-SVM	control data	ν (an upper bound on the fraction of training errors and a lower bound of the fraction of support factors) = 0.00001, 0.0001, 0.001 or 0.01, kernel = linear, 3rd order polynomial, radial basis function (rbf) or sigmoid
LOF	control data	k-neighbors = 10, 20 or 30
iForest	Infection and control data	Automatic contamination[91]

4.2.3.3.1 Determining Activated Cells

Activated cells in the environment of infection are noninfected cells that are influenced by the proinflammatory cytokines released by infected cells in close proximity. The activation of these cells by TNF-α leads to a signaling cascade inducing

proinflammatory activation and an increased production of inducible nitric oxide synthase (iNOS), a primary precursor of bactericidal reactive nitrogen species [92]. In the innate immune response to infection, macrophages are primary producers and also responders to the TNF-a cytokine[92], [93], one of several inflammatory cytokines produced during infection. To generate our determination of activated state, we utilize approximations of cellular neighborhood induced activation utilized in the TB ABM which determines activated cells by the presence of infected cells within the cellular neighborhood [48]. In a 2D agent-based model of infection this cellular neighborhood is defined within the 2D grid by the Moore (1 central cell with 8 adjacent cells, Figure 29) neighborhood. However, this cellular neighborhood is a simplification of the biological 3D structure that induces the activated cellular response [94].

N	N	N
N	C	N
N	N	N

Figure 29: Representation of Moore neighborhood in agent-based models of cellular automata and infection, C-central cell, N-neighbor.

To develop a comparable neighborhood determination algorithm with an extension to 3D biological space, we utilized the data generated from the 20 µm DBSCAN clustering algorithm and determined which clusters contained infected cells. Non-infected cells that were contained within the same 20 µm DBSCAN cluster as an infected cell were then re-labeled as noninfected-active cells for further analysis (Figure 28 C). This activated cell state information was then combined with the remaining cell

states (including 20 µm DBSCAN cluster association) to generate 7 potential cell states that can be observed based on confocal imaging data (Table 41). Infected-activated cells are not reported as they require the consideration of time, and the image processing of cells in close proximity leads to failures in watershed segmentation and tracking which can cause difficulty in tracking cells from earlier imaging timepoints.

Table 41: Definition of cell states for variable distributions and multivariate classification models.

Cell State	Definition
Control	Cells within the control (no bacteria introduced) condition that are not contained within 20 µm clusters with other control cells as determined by DBSCAN.
Control-Cluster	Cells within the control (no bacteria introduced) condition that are contained within 20 µm clusters with other control cells as determined by DBSCAN.
Noninfected	Cells within the infected (bacteria introduced) condition that are not determined to be infected and not contained within 20 µm clusters with other control cells as determined by DBSCAN.
Noninfected-Cluster	Cells within the infected (bacteria introduced) condition that are not determined to be infected and are contained within 20 µm clusters with other noninfected cells as determined by DBSCAN.
Noninfected-Active	Cells within the infected (bacteria introduced) condition that are not determined to be infected and are contained within 20 µm clusters with at minimum one infected cell as determined by DBSCAN.
Infected	Cells within the infected (bacteria introduced) condition that are determined to be infected and are not contained within 20 µm clusters with other cells as determined by DBSCAN.
Infected-Cluster	Cells within the infected (bacteria introduced) condition that are determined to be infected and are contained within 20 µm clusters with other noninfected or infected cells as determined by DBSCAN.

4.2.3.4 Extension to mechanistic computational models

We then applied ML classification models to the cell dynamics segmented by cell state in order to quantify the multi-feature discrimination between cellular states. This allows us to perform the converse of state detection based on fluorescence and cluster localization, and instead predict cellular state based on the observable cellular dynamics regardless of this information. This prediction of cell state provides insight into the other cellular dynamics quantified under confocal imaging and demonstrates how multiple dynamics can be utilized to distinguish cell state. We utilize linearly separable ML models with lower model complexity, which can be investigated further by extracting resulting decision boundaries from ML classification models to inform mechanistically driven computational models.

4.2.3.4.1 Multivariate classification models for predicting cell state

After cellular states were established, supervised machine learning algorithms were employed to determine which features and feature rates of change (delta features, as previously described) (Table 39) best discriminate the various cell states. This inverse feature identification methodology allows for the exploratory investigation of dynamics based on cell state and provides a basis for future analysis and development of predictive computational models. Methods utilized for this determination were form the Python library scikit learn and included a supervised extension of gaussian mixture models (sGMM), linear discriminant analysis (LDA), and decision tree classifiers (cTree). The dataset was split using sciKitLearn's *StratifiedKFold* function to generate k=3 test and training datasets. Each method was subjected to

reverse feature selection in which the feature that contributed least to the accuracy was subsequently removed during each iteration to find the optimal feature set and the single feature that contributed to the highest model accuracy. In addition, each method was tested for the optimal solver (cTree and LDA) or covariance matrix (cGMM) at each iteration (Table 42). The importance of the feature was determined for cTrees using the built-in attribute *feature_importances_*. cTrees were bounded to prevent over-fitting to a minimum number of samples per split given by equation 7

$$\min\_samples\_split = \frac{\#\ \text{traning data points}}{\#\ \text{classes}^2}. \quad (7)$$

Table 42: ML parameters tested for multivariate classification

Algorithm	*Solvers or Covariances tested for highest accuracy*
cGMM	Covariance: spherical, diagonal (diag), tied, or full
LDA	Solver: single value decomposition (svd) or least squares solution (lsq)
cTree	Solver: Gini or Entropy

4.2.3.4.2 Univariate continuous distributions for computational model parameter generation

Standard computational models of cellular dynamics and infectious disease rely on uniform or gaussian approximations of biological parameters. This is not indicative of the complex biological variability that we see in empirical evaluation. In order to further develop the parameter generation for these computational models we generated empirical distributions that provide random parameters with increased biologically relevant variability. The function *DisttoRNG* was written in Python to aid in the generation of empirically derived continuous distributions for model populations

represented by a dataset. The function returns any number of datapoints for any given variable given a subset of data, and an optional evaluation parameter. Each distribution (Table 43) is attempted, those that generate errors discarded, and the negative log likelihood (NLL), the Akaike information criterion (AIC) and the Bayesian information criterion (BIC) calculated, with the option to select which metric is used for model evaluation. The NLL is calculated using the scipy.stats *nnlf* method for continuous distributions. The AIC [95] and BIC [96] were calculated by penalizing the NLL by the number of datapoints and parameters within the distribution and number of parameters in the distribution. The default metric for evaluation is set to AIC and was used to select the best continuous distribution which generated the random variables through the scipy.stats distribution method *rvs*.

Table 43: scipy.stats distributions tested for best fit

Distribution	Distribution definition
laplace	Laplace continuous distribution
norm	Normal continuous distribution
beta	Beta continuous distribution
fatiguelife	Fatigue-life (Birnbaum-Saunders) continuous distribution
expon	Exponential continuous distribution
gamma	Gamma continuous distribution
genextreme	Generalized Extreme Value continuous distribution
genpareto	Generalized Pareto continuous distribution
invgauss	Inverse Gaussian continuous distribution
logistic	Logistic (Sech-squared) continuous distribution
lognorm	Lognormal continuous distribution
nakagami	Nakagami continuous distribution
rayleigh	Rayleigh continuous distribution
rice	Rice continuous distribution
t	Student's t continuous distribution
weibull_min	Weibull minimum continuous distribution
weibull_max	Weibull maximum continuous distribution

4.3 Results

We applied the developed computational pipeline to investigate cellular dynamics of cell speed, acceleration, directedness and volume to determine the impact that cellular state plays in the presentation of these dynamics. Our results investigation the role that internal state (infection/active/noninfected), and spatial organization (20 µm DBSCAN cluster) plays in the regulation of cellular dynamics within each environment (2D and 3D) as well as how these resulting changes impact the difference between dynamics in each environment.

4.3.1 Cellular Recruitment

We see a significant difference in cellular recruitment dependent on environment. In 2D, we see a higher percentage of cells in general associated in a 20 µm DBSCAN cluster, but this percentage decreases over time in culture for both control and infected cells (Figure 30). In contrast, 3D infected and control cells see a dramatic increase in the percentage of cells in clusters over the course of experiment showing the significant impact that the 3D environment has on cellular recruitment and subsequent aggregation. We do note that the dramatic increase in 3D control cells associated in a cluster at later timepoints is potentially due to high levels of cell death leading to lower cell numbers at later timepoints and thus a higher percentage of cells associated in a cluster.

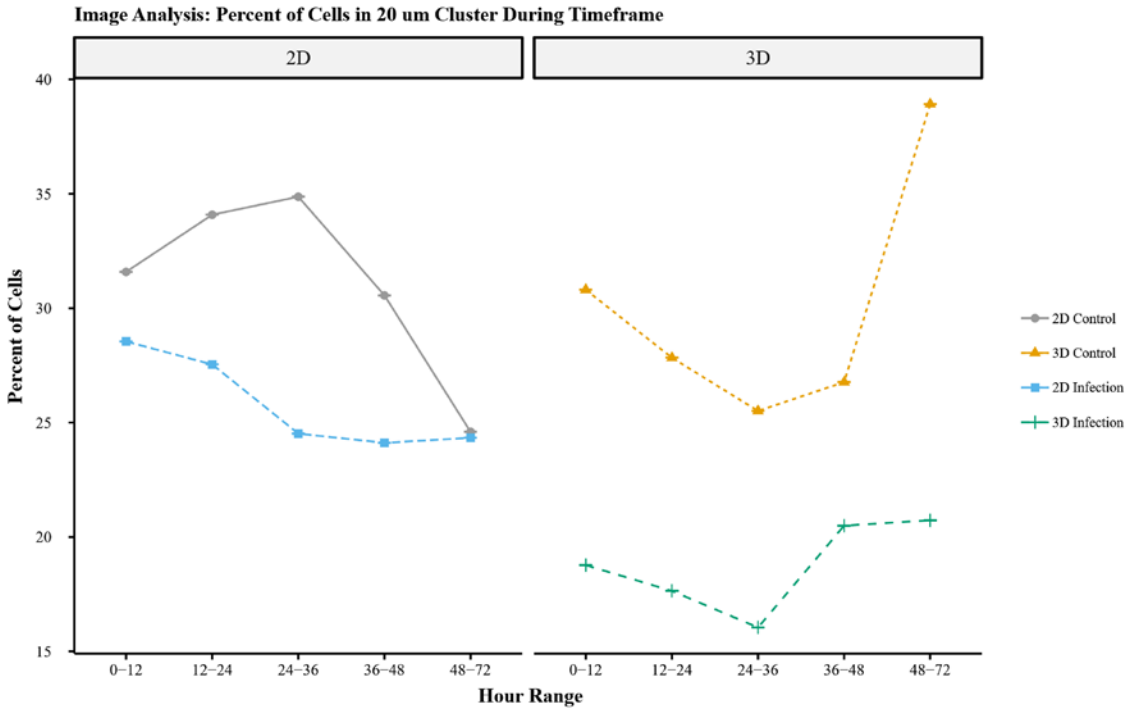

Figure 30: Percent of cells in the image field that are part of a DBSCAN cluster (20 µm).

4.3.2 Infection Determination

Application of principal component analysis to RFP variables for both independent experimental trials generated 2 principal components that described over 99% of the data variability. By overlaying the unknown infected cells (Figure 31-blue) with the known control cells (Figure 31-black) we can see that while there is significant delineation between the known uninfected cells there are still outlier points that can contribute to potential error regardless of algorithm. There is also a significant change in the datasets depending on experimental trial, although no significant differences were reported between independent trials for the biological data. Trial 1 (Figure 31 A) shows control cells with principal components that are very tightly associated with few observable outliers, whereas trial 2 (Figure 31 B) shows control cells that have higher

degrees of variability and more potential outliers. Through the application of multiple machine learning algorithms, we were able to determine the most appropriate algorithm to produce consistent, low error rate infection determination.

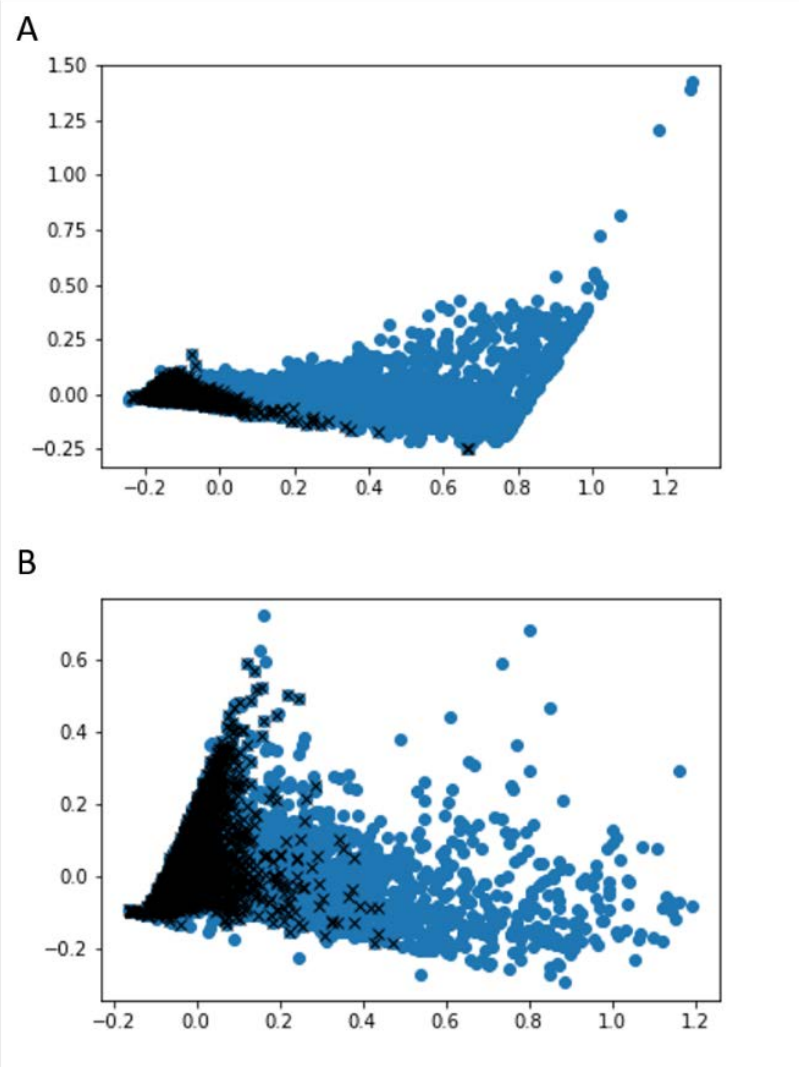

Figure 31: Representation of the 2 principal components that comprise over 99% of data variability from the RFP datasets. Black X's, overlaid control datapoints (known noninfected), Blue, unknown datapoints (infected and noninfected) A) Trial 1 B) Trial 2.

The unsupervised algorithms K-Means and GMM produced comparable results. Both methods produced misclassification error below 1% (Table 44) for trial 1 datasets except in the case of GMM with spherical covariance. However, Trial 2, with more qualitatively apparent outlier control datapoints produced a much higher misclassification error rate under GMM with diagonal, full, and spherical covariance (Table 44) showing the inability of GMM to handle both datasets with the same accuracy. Outlier detection with isolation forests produced low misclassification error in both datasets (<10%) but was not as low as the previous unsupervised methods Novelty detection algorithms ability train the classifiers on the known non-infected cells from the control datasets gave the ability to generate more complex delineations between non-infected and infected cells over the linear divisions seen in both K-means and GMM. Support vector machine produced the most varied results with misclassification error ranging from below 1% to 100% Local outlier factor methods with varying KNN initializations proved to be a stable and low error method for determining cell infected status as quantified by the minor variations in error between trials and between tested initializations. All methods attempted produced error below 1% and comparable error was seen for both trials (Table 44).

Table 44: Percentage of Infected Cells and Misclassification Error (mcError) for each algorithm performed independently on each trial

Algorithm	mcError-Trial 1	mcError-Trial 2	%Infected-Trial 1	%Infected-Trial 2
K-Means	0.001678108	0.004535147	27.93129	14.64915
GMM (Diagonal)	0.009000763	0.132312925	29.53697	41.01202
GMM (Full)	0.006254767	0.109297052	27.12223	40.52278
GMM (Spherical)	0.109297052	0.046834477	66.76624	34.95946
GMM (Tied)	0.000762777	0.001814059	19.94025	9.67291
Isolation Forest	0.04057971	0.056802721	63.36819	32.10791
LOF (KNN: 10)	0.005034325	0.003968254	34.64028	6.024602
LOF (KNN: 20)	0.005644546	0.005668934	33.17152	7.338552
LOF (KNN: 30)	0.008848207	0.007256236	41.97162	8.987979
SVM (Linear:1E-5)	0.006864989	0.009183673	45.28255	20.96729
SVM (Linear:1E-4)	0.079938978	0.009183673	62.67115	20.96729
SVM (Linear:1E-3)	0.050953471	0.138321995	50.01245	20.03075
SVM (Linear:1E-2)	0.410831426	0.320068027	82.66119	40.17333
SVM (Poly(3):1E-5)	0.019221968	0.42244898	0.746826	45.14957
SVM (Poly(3):1E-4)	0.019221968	0.42244898	0.746826	45.14957
SVM (Poly(3):1E-3)	0.154996186	0.400226757	5.078417	74.50377
SVM (Poly(3):1E-2)	0.337452326	0.429931973	11.55091	49.97204
SVM (RBF:1E-5)	1	0.000113379	92.0712	4.598826
SVM (RBF:1E-5)	1	0.000113379	92.0712	4.137545
SVM (RBF:1E-5)	0.000915332	0.001133787	16.28081	5.325692
SVM (RBF:1E-5)	0.01006865	0.010090703	39.74359	11.11266
SVM (Sigmoid:1E-5)	0.013272311	0.468480726	55.82524	76.40481
SVM (Sigmoid:1E-4)	0.013272311	0.005555556	55.82524	16.18675
SVM(Sigmoid:1E-3)	0.026697178	0.041836735	7.119741	29.43808
SVM (Sigmoid:1E-2)	0.001983219	0.282199546	22.37989	55.15795

Analysis of the results of infection determination show that GMM and LOF present with the lowest misclassification error for unsupervised and outlier detection categories respectively. Gaussian mixture models with a tied covariance produce the lowest misclassification error overall, but other covariances have high variability in misclassification error (Figure 32). Local outlier Factor presents with consistently low misclassification error regardless of independent trial or perturbation to the KNN initialization, in addition the ability to train the models with the single known class (control/non-infected) makes LOF a more appealing option (Figure 33). For all further analysis, infected cells are represented from the LOF novelty detection machine learning algorithm with KNN=20, as this produced the most comparable error between Trials and is the initialization recommended by the sklearn library.

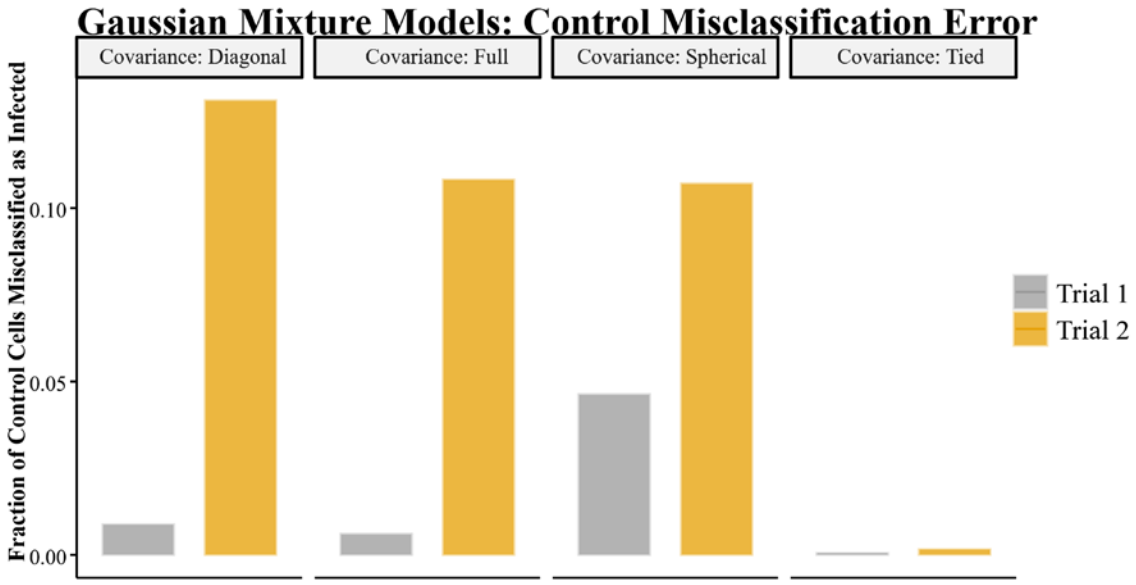

Figure 32: Unsupervised machine learning for infection determination GMM (k=2) Control misclassification error for varying covariance matricies.

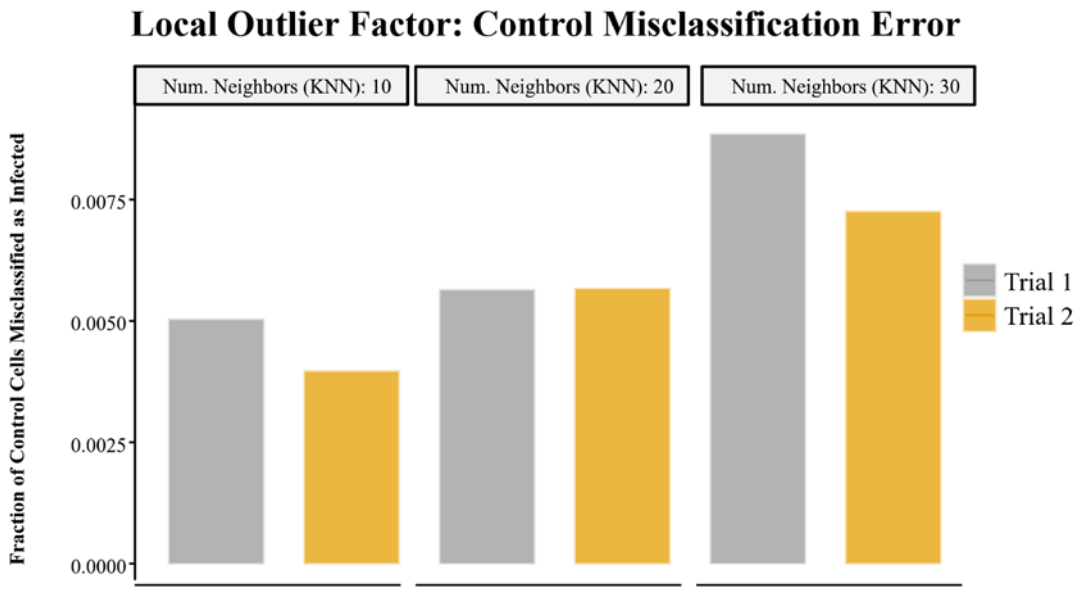

Figure 33: Single class classificaiton model (Novelty Detection) for infection determination with local outlier factor. Control misclassification error is reported for each independent trial at varying KNN initalizations.

4.3.2.1 Cell Dynamics Based on Cellular State

Determination of infection allowed for the identification of activated-non-infected cells based on the cell clusters determined by 20 µm DBSCAN analysis. This generated the cell statuses outlined in Table 41. This delineation between cell statuses allows for the investigation of cell dynamics based on the state of the cell at that point in time. Figure 34 outlines the percentage of cells in each state over the course of the study. As expected, we see a consistent decrease in the percentage of infected cells over time in both the 2D and 3D environment, as this is a low-level clearing infection.

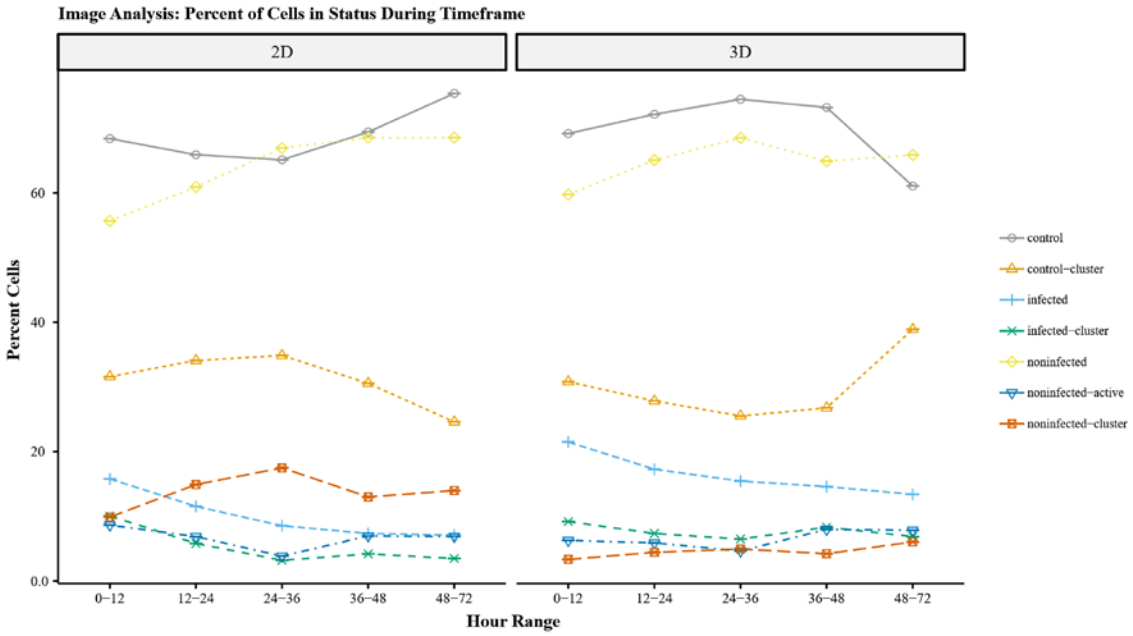

Figure 34: Percent of cells in specific cell status (determined by number of cells present in status over total number of cells in the condition).

4.3.2.1.1 Impact of Dimensionality and Cell Status on Cell Motility and Migration

Comparing cells with comparable cell status in the 2D and 3D environment we can determine not only the impact that the cell status has on the cellular dynamics, but also the magnitude the state of cell activation or infection has as compared to the effect of the environment. Looking at cellular speed, acceleration and directedness we start to see a trend in the relationship between the cells in 2D and 3D that highlights the importance of the availability of the 3D environment, but also the overwhelming effect that cell status has on the resulting cellular dynamics. In general, results show non-infected and non-active macrophages within infected environments present dynamics comparable to controls, while infected and activated macrophages exhibit comparable spatiotemporal dynamics in 2D and 3D.

Cellular speed in general is observed to be significantly lower in 3D as compared to the 2D condition (Figure 35). If we compare the log 2-fold change in means between cell states calculated by equation 8

$$Log2FC = Log_2\left(\frac{2D_{mean}}{3D_{mean}}\right). \quad (8)$$

We see that infected, infected cluster and noninfected-active cells have a much lower fold change (Log2FC<0.7) than noninfected or control cells (Log2FC>1) (Table 45), although the relationships to their respective controls or noninfected cells maintains a converse relationship.

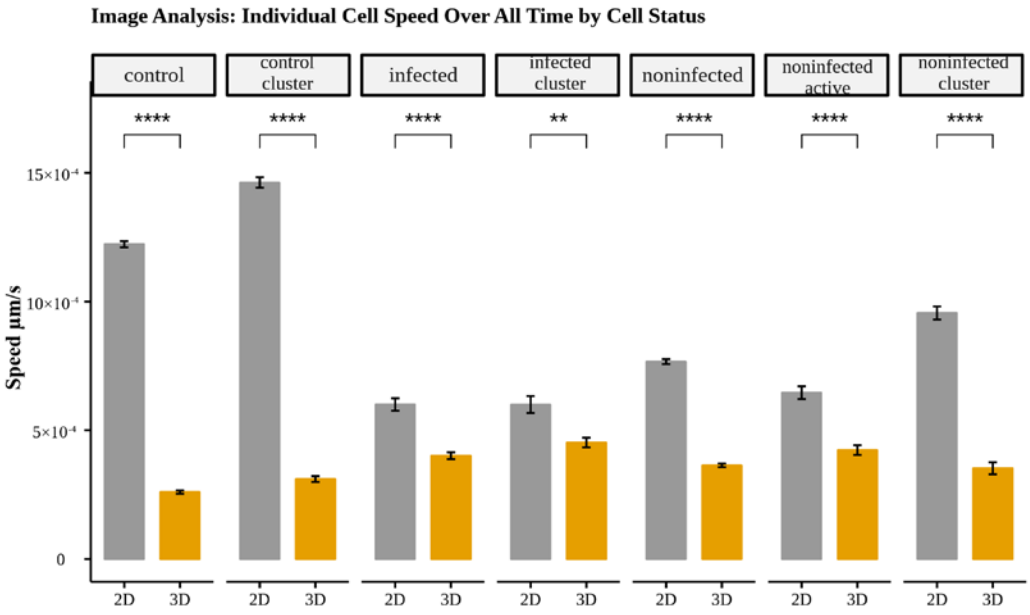

Figure 35: Individual cell speed of gfpBMDM infected with mCherry M.smegmatis in 2D and 3D culture conditions over 72 hours by cell status (ns- No significant difference, * - p<.05, **-p<.01,***-p<.001,****-p<.0001)

Table 45:	Average Individual Cell Speed Over All Time: Wilcoxon				
2D Cell State	*Speed um/s*	*3D Cell State*	*Speed um/s*	*Log2FC*	*p value*
Control	1.22E-03	Control	2.60E-04	1.02	0
Control-Cluster	1.46E-03	Control-Cluster	3.11E-04	1.28	5.11E-222
Noninfected	7.67E-04	Noninfected	3.64E-04	1.08	8.93E-304
Infected	6.00E-04	Infected	4.01E-04	0.58	7.44E-12
Noninfected-Active	6.46E-04	Noninfected-Active	4.23E-04	0.61	6.10E-13
Noninfected-Cluster	9.56E-04	Noninfected-Cluster	3.52E-04	1.44	4.20E-48
Infected-Cluster	6.00E-04	Infected-Cluster	4.52E-04	0.41	1.64E-03

Likewise, we see a comparable effect on cellular acceleration (Figure 36). Infected cells (infected and infected-cluster) and those associated with infection (noninfected-active) have a much lower log2FC (logf2C<.4) than those not associated with infection (log2FC>.65) (Table 46), and the converse relationship observed in cellular speed still holds.

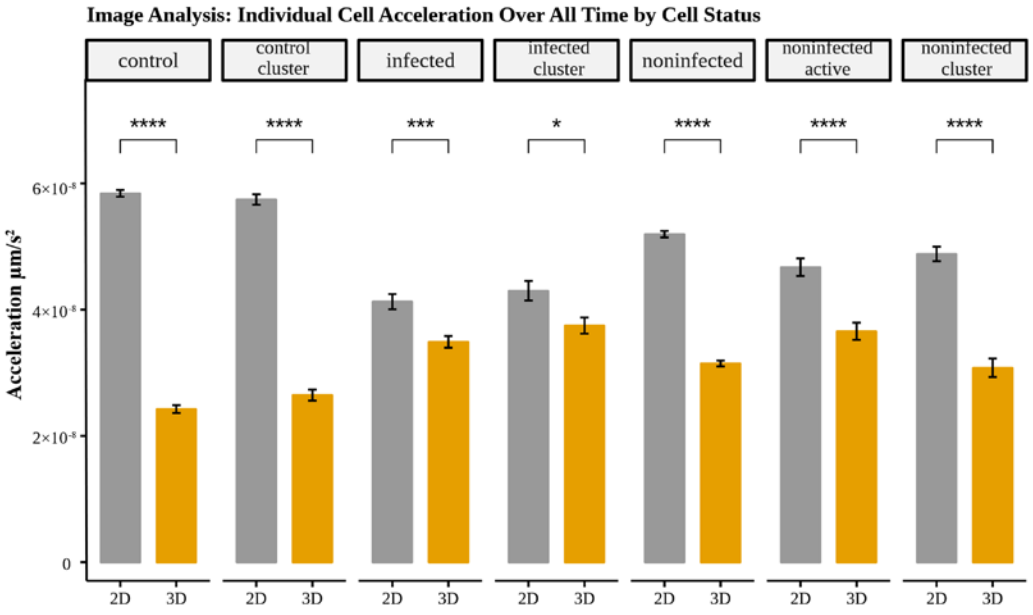

Figure 36: Individual cell acceleration of gfpBMDM infected with mCherry M.smegmatis in 2D and 3D culture conditions over 72 hours by cell status (ns- No significant difference, * - p<.05, **-p<.01,***-p<.001,****-p<.0001)

Table 46:	Average Individual Cell Acceleration Over All Time: Wilcoxon				
2D Cell State	Acceleration *um/s²*	*3D Cell State*	Acceleration *um/s²*	*Log2FC*	*p value*
Control	5.84E-08	Control	2.42E-08	1.27	2.25E-186
Control-Cluster	5.74E-08	Control-Cluster	2.65E-08	1.12	3.66E-46
Noninfected	5.19E-08	Noninfected	3.15E-08	0.72	1.44E-163
Infected	4.13E-08	Infected	3.49E-08	0.24	2.25E-04
Noninfected-Active	4.67E-08	Noninfected-Active	3.66E-08	0.35	8.78E-07
Noninfected-Cluster	4.88E-08	Noninfected-Cluster	3.08E-08	0.66	9.63E-10
Infected-Cluster	4.30E-08	Infected-Cluster	3.75E-08	0.20	1.52E-02

We see this effect continue into the calculations of cell directedness. We see no significant difference between directedness in infected-cluster cells in 2D and 3D (Figure 37). Once again, we see that infected cells (infected and infected-cluster) and those associated with infection (noninfected-active) have a much lower log2FC (logf2C<.5) than those not associated with infection (log2FC>.5)(Table 47)

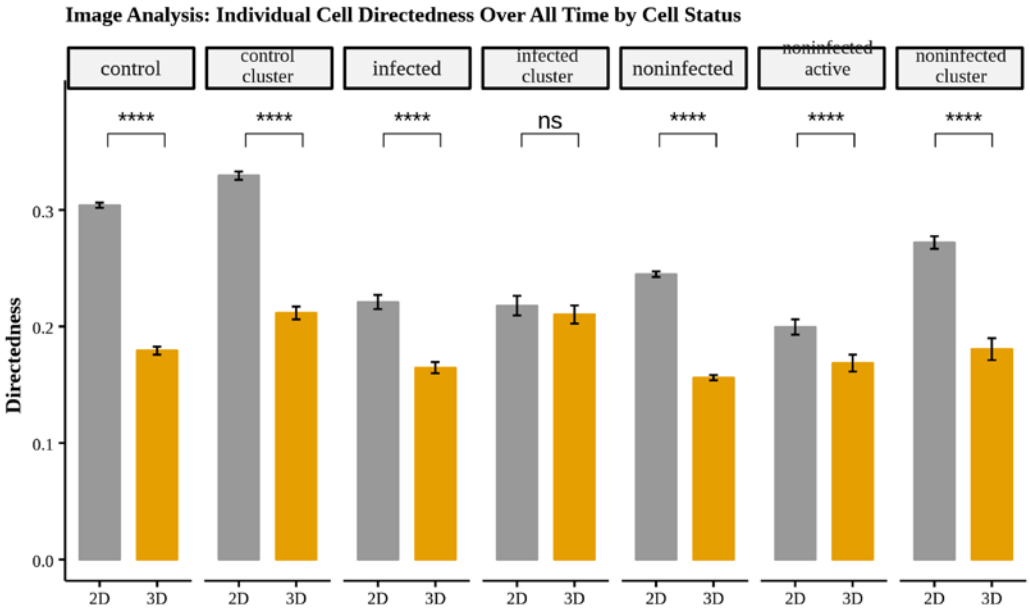

Figure 37: Individual cell directedness of gfpBMDM infected with mCherry M.smegmatis in 2D and 3D culture conditions over 72 hours by cell status (ns- No significant difference, * - p<.05, **-p<.01,***-p<.001,****-p<.0001)

Table 47: Average Individual Cell Directedness Over All Time: Wilcoxon

2D Cell State	Directedness	*3D Cell State*	Directedness	*Log2FC*	*p value*
Control	0.304	Control	0.179	0.76	2.04E-147
Control-Cluster	0.330	Control-Cluster	0.212	0.64	8.23E-55
Noninfected	0.245	Noninfected	0.156	0.65	2.70E-173
Infected	0.221	Infected	0.165	0.42	1.36E-18
Noninfected-Active	0.200	Noninfected-Active	0.169	0.24	7.30E-05
Noninfected-Cluster	0.272	Noninfected-Cluster	0.181	0.59	2.80E-18
Infected-Cluster	0.218	Infected-Cluster	0.210	0.05	9.38E-01

4.3.2.1.2 Impact of Dimensionality and Cell Status on Cell Volume

Cell volume as a feature of cellular dynamics is vital as it has been shown in previous empirical studies that macrophage volume is correlated to phagocytosis of the bacterium [43]. Our preliminary investigation of using machine learning to determine cell infection and feature importance also highlighted cell volume as one of the best features to discriminate the cell population[61]. This study emphasizes the impact that cell infection has on cell volume. We see that infected cells have a higher volume within their respective 2D or 3D condition, and that infected-cluster cells have no significant difference in cell volume between 2D and 3D condition (Figure 38). The trend continues and infected cells (infected and infected-cluster) and those associated with infection (noninfected-active) have a lower log2FC (logf2C<.2) than those not associated with infection (log2FC>.3)(Table 48).

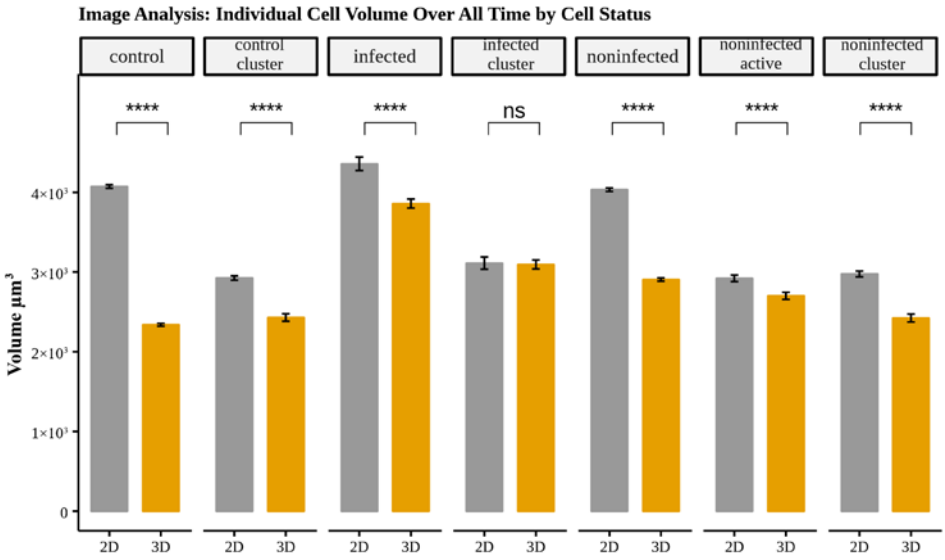

Figure 38: Individual cell volume of gfpBMDM infected with mCherry M.smegmatis in 2D and 3D culture conditions over 72 hours by cell status (ns- No significant difference, * - p<.05, **-p<.01,***-p<.001,****-p<.0001)

Table 48:	Average Individual Cell Volume Over All Time: Wilcoxon				
2D Cell State	*Volume um³*	*3D Cell State*	*Volume um³*	*Log2FC*	*p value*
Control	4.07E+03	Control	2.34E+03	0.80	0
Control-Cluster	2.93E+03	Control-Cluster	2.43E+03	0.27	3.24E-23
Noninfected	4.03E+03	Noninfected	2.91E+03	0.47	0
Infected	4.36E+03	Infected	3.86E+03	0.18	2.99E-05
Noninfected-Active	2.92E+03	Noninfected-Active	2.70E+03	0.11	1.77E-06
Noninfected-Cluster	2.98E+03	Noninfected-Cluster	2.42E+03	0.30	2.54E-17
Infected-Cluster	3.11E+03	Infected-Cluster	3.09E+03	0.01	8.03E-01

4.3.2.1.3 Impact of cell-state on cell dynamics over time

Investigation of infected status of the cells as well as the spatial organization we can delineate impact of proximity to infection (active-noninfected) as opposed to a noninfected cell that is in proximity to another noninfected cell (noninfected-cluster). Through our analysis we see that cells determined to be in a proinflammatory state,

infected cells, infected-cluster cells and active-noninfected cells, show more comparable dynamics to each other, whereas non-proinflammatory cells, noninfected cells and noninfected-cluster cells, demonstrate dynamics more comparable to their respective controls. This highlights the impact that cellular infection plays on the behavior of neighboring cells. We also note that in general, we that proinflammatory macrophages, cells in the presence of infection (noninfected-active) or infected themselves, (infected and infected-cluster) demonstrate distinct trends over time that are easily identified in the 2D condition. While we do see distinct groupings of dynamics based on proinflammatory or non-proinflammatory state in 3D, the differences are less apparent.

For the average cellular speed over all time in 2D we see little ($p < .05$) to no significant difference between noninfected and noninfected-active cells, infected and infected-cluster cells, and infected cluster and noninfected-active cells (Figure 39 A, Table 49). We observe that noninfected-cluster cells have a significantly higher speed than their counterparts in proximity to infection. We also observe that over time, the average cellular speed of noninfected cells and noninfected-cluster cells decrease over time, whereas infected, infected-cluster and noninfected-active cells maintain a more consistent speed over the course of observation (Figure 39 B).

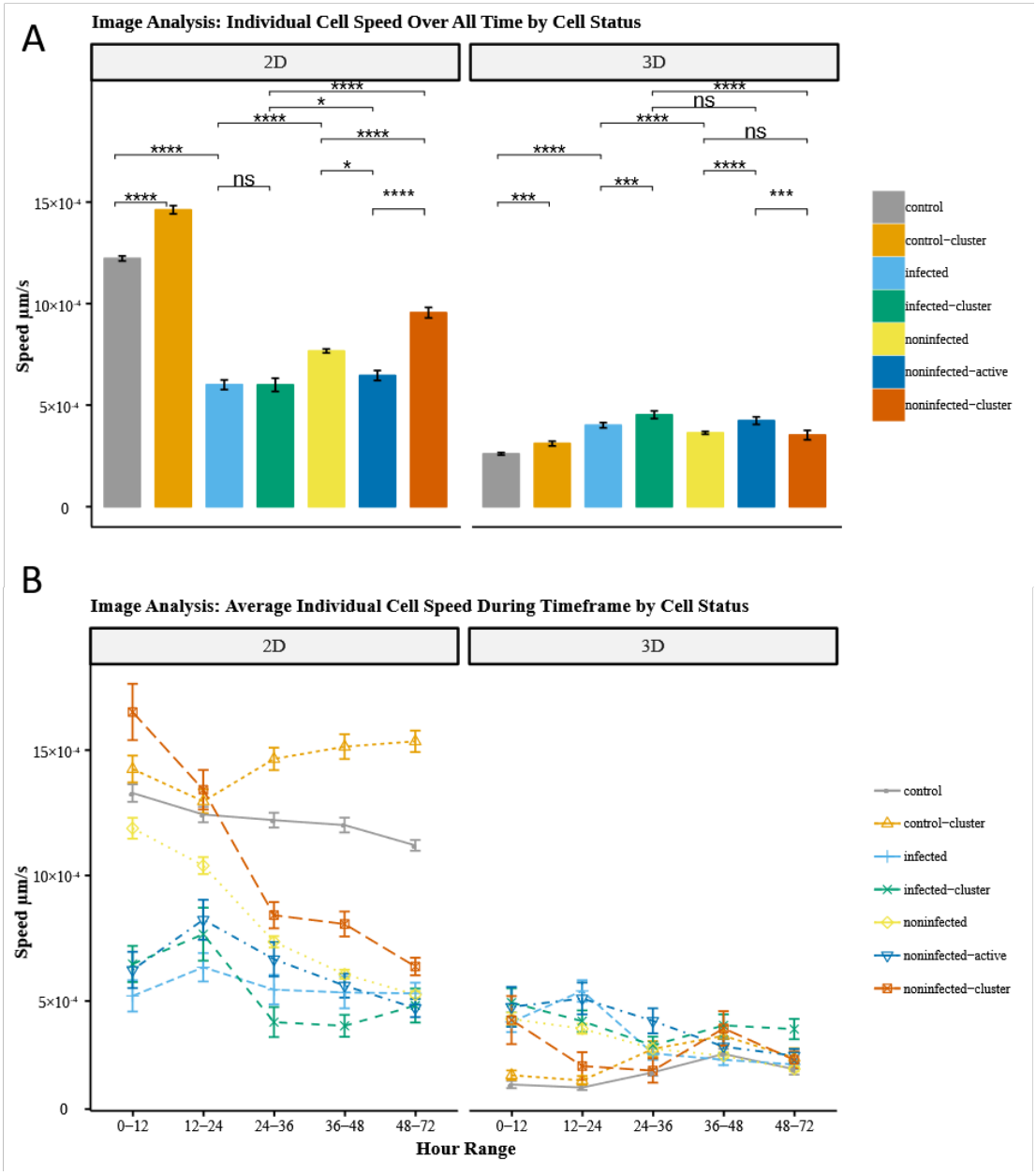

Figure 39: Individual cell speed of gfpBMDM infected with mCherry M.smegmatis in 2D and 3D culture conditions over 72 hours by cell status A) Averaged over all time B) Averaged based on hour range. (ns- No significant difference, * - p<.05, **-p<.01,***-p<.001,****-p<.0001)

Table 49: 2D Average Individual Cell Speed Over All Time: Wilcoxon

2D Cell State	*Speed um/s*	*2D Cell State*	*Speed um/s*	*p value*
Control	1.22E-03	Control-Cluster	1.46E-03	1.85E-23
Control	1.22E-03	Noninfected	7.67E-04	5.84E-160
Control	1.22E-03	Infected	6.00E-04	1.42E-83
Infected	6.00E-04	Infected-Cluster	6.00E-04	0.2471
Infected	6.00E-04	Noninfected	7.67E-04	1.64E-15
Infected-Cluster	6.00E-04	Noninfected-Active	6.46E-04	0.012802
Infected-Cluster	6.00E-04	Noninfected-Cluster	9.56E-04	2.64E-18
Noninfected	7.67E-04	Noninfected-Cluster	9.56E-04	2.58E-14
Noninfected	7.67E-04	Noninfected-Active	6.46E-04	0.010106
Noninfected-Cluster	9.56E-04	Noninfected-Active	6.46E-04	4.02E-13

In 3D we see no significant difference in cell speed between noninfected cells and noninfected-cluster cells, or infected-cluster and noninfected-active cells. However we do see a significant difference between noninfected-active cells and noninfected-cluster cells showing the impact of proximity of infection on dynamics (Figure 39 A, Table 50). Unlike in 2D, we do not see an easily distinguishable difference in cellular speed over time (Figure 39 B).

Table 50: 3D Average Individual Cell Speed Over All Time: Wilcoxon

3D Cell State	*Speed um/s*	*3D Cell State*	*Speed um/s*	*p value*
Control	2.60E-04	Control-Cluster	3.11E-04	3.72E-04
Control	2.60E-04	Noninfected	3.64E-04	2.20E-23
Control	2.60E-04	Infected	4.01E-04	2.14E-28
Infected	4.01E-04	Infected-Cluster	4.52E-04	8.84E-09
Infected	4.01E-04	Noninfected	3.64E-04	1.00E-04
Infected-Cluster	4.52E-04	Noninfected-Active	4.23E-04	1.49E-01
Infected-Cluster	4.52E-04	Noninfected-Cluster	3.52E-04	2.64E-18
Noninfected	3.64E-04	Noninfected-Cluster	3.52E-04	3.69E-01
Noninfected	3.64E-04	Noninfected-Active	4.23E-04	9.35E-10
Noninfected-Cluster	3.52E-04	Noninfected-Active	4.23E-04	6.00E-04

In 2D we see little ($p < .05$) to no significant difference in cellular acceleration between: noninfected and noninfected-active, control and control-cluster, infected and infected-cluster, infected-cluster and noninfected-active, noninfected and noninfected-active, and infected-cluster and noninfected-cluster cells.(Figure 40 A, Table 51). We do not see any significant difference between noninfected-cluster and noninfected-active cells. We see similar trends in infected and infected cluster cells over time with increasing cell acceleration as the infection progresses. In contrast, control, control-cluster and noninfected cells present steady acceleration over time (Figure 40 B).

Table 51: 2D Average Individual Cell Acceleration Over All Time: Wilcoxon

2D Cell State	Acceleration *um/s²*	*2D Cell State*	Acceleration *um/s²*	*p value*
Control	5.84E-08	Control-Cluster	5.74E-08	0.524892
Control	5.84E-08	Noninfected	5.19E-08	0.003098
Control	5.84E-08	Infected	4.13E-08	3.87E-15
Infected	4.13E-08	Infected-Cluster	4.30E-08	0.104355
Infected	4.13E-08	Noninfected	5.19E-08	9.59E-05
Infected-Cluster	4.30E-08	Noninfected-Active	4.67E-08	0.058622
Infected-Cluster	4.30E-08	Noninfected-Cluster	4.88E-08	0.204627
Noninfected	5.19E-08	Noninfected-Cluster	4.88E-08	0.197946
Noninfected	5.19E-08	Noninfected-Active	4.67E-08	0.892141
Noninfected-Cluster	4.88E-08	Noninfected-Active	4.67E-08	0.882455

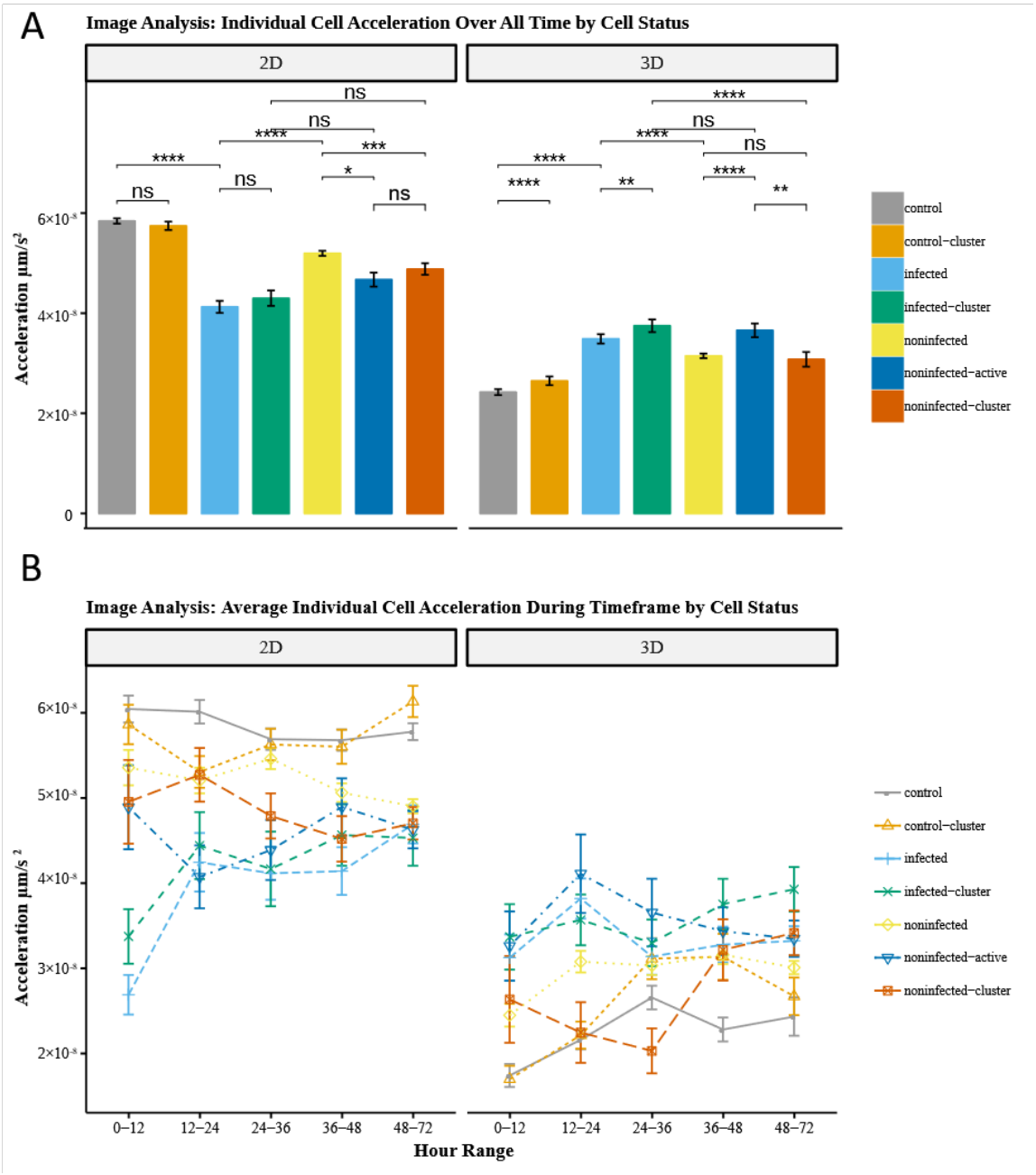

Figure 40: Individual cell acceleration of gfpBMDM infected with mCherry M.smegmatis in 2D and 3D culture conditions over 72 hours by cell status A) Averaged over all time B) Averaged based on hour range. (ns- No significant difference, * - p<.05, **-p<.01,***-p<.001,****-p<.0001)

In 3D we see an overall higher degree of significant difference in cellular acceleration based on cell state, but we still see no significant difference between control and control-cluster cells, noninfected cells and noninfected-cluster cells, or infected-cluster and noninfected-active cells (Figure 40 A, Table 52). However, in contrast to 2D, we do see a significant difference in cellular acceleration between noninfected-active and noninfected-cluster cells which demonstrates that the proximity to infection plays a role in cellular acceleration. We begin to see more distinct patterns in cellular acceleration over time as compared to cell speed in 3D. The trends show that infected and noninfected-active cells have similar dynamics increasing acceleration at the 12-24 hour range, followed by a decrease at 24-36 hour range, followed by another subsequent increase in cellular acceleration. Comparable to 2D control, control cluster and noninfected cells show similar dynamics with a moderate increase in cell acceleration in the earlier timepoints followed by stabilization in the later timeframes (Figure 40 B).

Table 52: 3D Average Individual Cell Acceleration Over All Time: Wilcoxon

3D Cell State	Acceleration *um/s²*	*3D Cell State*	Acceleration *um/s²*	*p value*
Control	2.42E-08	Control-Cluster	2.65E-08	0.252612
Control	2.42E-08	Noninfected	3.15E-08	2.59E-07
Control	2.42E-08	Infected	3.49E-08	2.89E-09
Infected	3.49E-08	Infected-Cluster	3.75E-08	0.987993
Infected	3.49E-08	Noninfected	3.15E-08	8.02E-05
Infected-Cluster	3.75E-08	Noninfected-Active	3.66E-08	0.88529
Infected-Cluster	3.75E-08	Noninfected-Cluster	3.08E-08	0.037454
Noninfected	3.15E-08	Noninfected-Cluster	3.08E-08	0.626437
Noninfected	3.15E-08	Noninfected-Active	3.66E-08	0.000493
Noninfected-Cluster	3.08E-08	Noninfected-Active	3.66E-08	0.002063

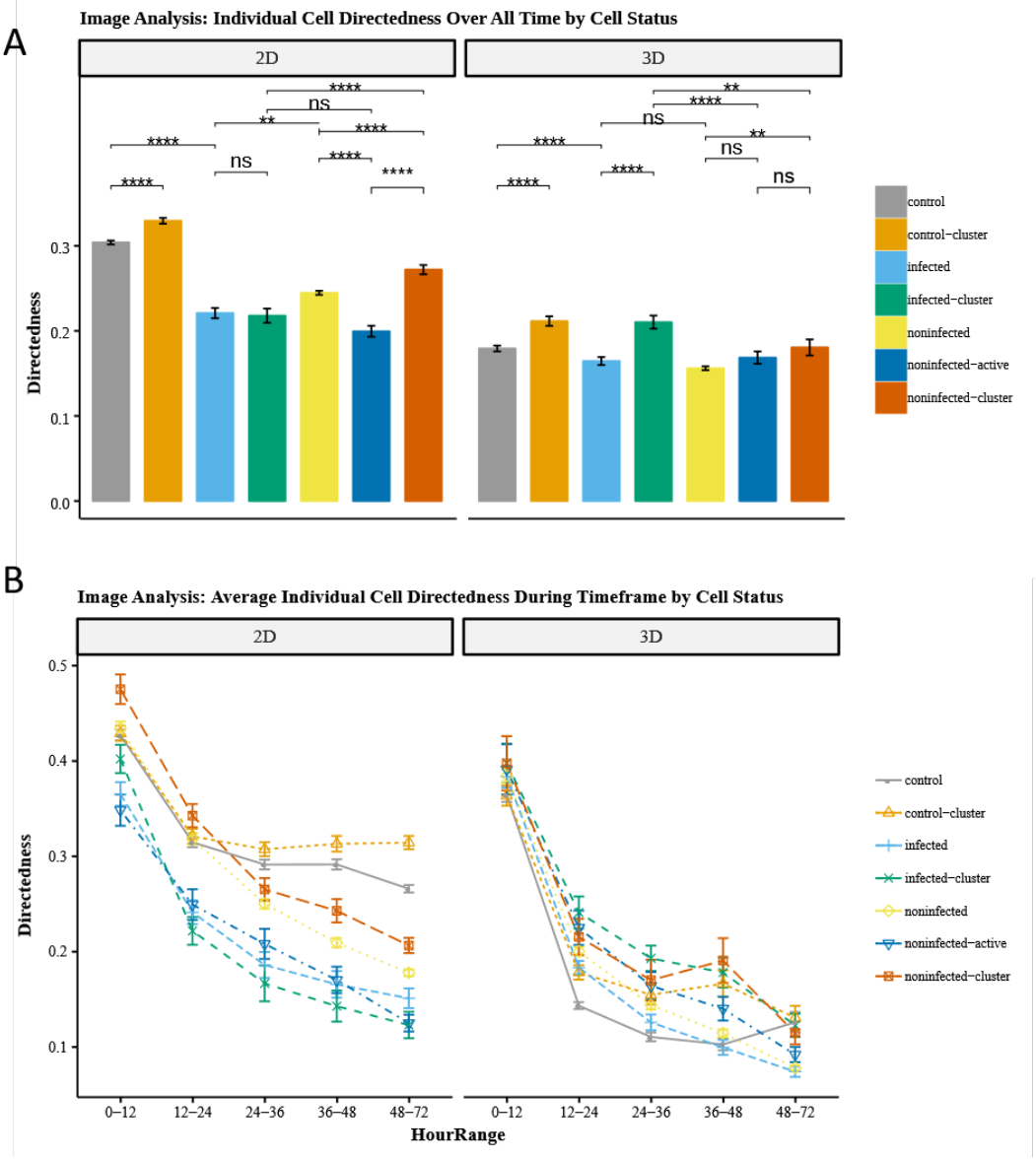

Figure 41: Individual cell directedness of gfpBMDM infected with mCherry M.smegmatis in 2D and 3D culture conditions over 72 hours by cell status A) Averaged over all time B) Averaged based on hour range. (ns- No significant difference, * - p<.05, **-p<.01,***-p<.001,****-p<.0001)

Directedness in 2D shows three distinct groupings over time (Figure 41 B), control and control-cluster, noninfected-cluster and noninfected, and infected, infected cluster and noninfected-active. Overall, we see no significant difference between average directedness in infected and infected-cluster cells, and infected-cluster and noninfected-active cells (Figure 41 A,Table 53), but a significant difference between non-

proinflammatory noninfected-cluster and the proinflammatory noninfected-active cells. In general, we do see that cells in clusters have a higher directedness than their non-clustered counterparts, however this is likely due to the failing of watershed segmentation of overlapping and touching cells.

Table 53: 2D Average Individual Cell Directedness Over All Time: Wilcoxon

2D Cell State	*Directedness*	*2D Cell State*	*Directedness*	*p value*
Control	0.304	Control-Cluster	0.33	2.54E-11
Control	0.304	Noninfected	0.245	7.72E-74
Control	0.304	Infected	0.221	8.96E-33
Infected	0.221	Infected-Cluster	0.218	0.165891
Infected	0.221	Noninfected	0.245	0.001691
Infected-Cluster	0.218	Noninfected-Active	0.200	0.394694
Infected-Cluster	0.218	Noninfected-Cluster	0.272	6.95E-10
Noninfected	0.245	Noninfected-Cluster	0.272	2.83E-07
Noninfected	0.245	Noninfected-Active	0.200	4.11E-10
Noninfected-Cluster	0.272	Noninfected-Active	0.200	5.71E-18

The significant difference in cell directedness in 3D is much more subdued than 2D. We see very little difference in the cell directedness overtime (Figure 41 B), and we see no significant difference in average cell directedness between infected and noninfected cells, noninfected and noninfected-active cells, and noninfected-cluster and noninfected-active cells(Figure 41 A, Table 54).

Table 54: 3D Average Individual Cell Directedness Over All Time: Wilcoxon

3D Cell State	*Directedness*	*3D Cell State*	*Directedness*	*p value*
Control	0.179	Control-Cluster	0.212	3.75E-12
Control	0.179	Noninfected	0.156	2.53E-21
Control	0.179	Infected	0.165	7.86E-08
Infected	0.165	Infected-Cluster	0.210	3.22E-09
Infected	0.165	Noninfected	0.156	0.175714
Infected-Cluster	0.210	Noninfected-Active	0.169	3.77E-06
Infected-Cluster	0.210	Noninfected-Cluster	0.181	0.004181
Noninfected	0.156	Noninfected-Cluster	0.181	0.003096
Noninfected	0.156	Noninfected-Active	0.169	0.115197
Noninfected-Active	0.169	Noninfected-Cluster	0.181	0.18549

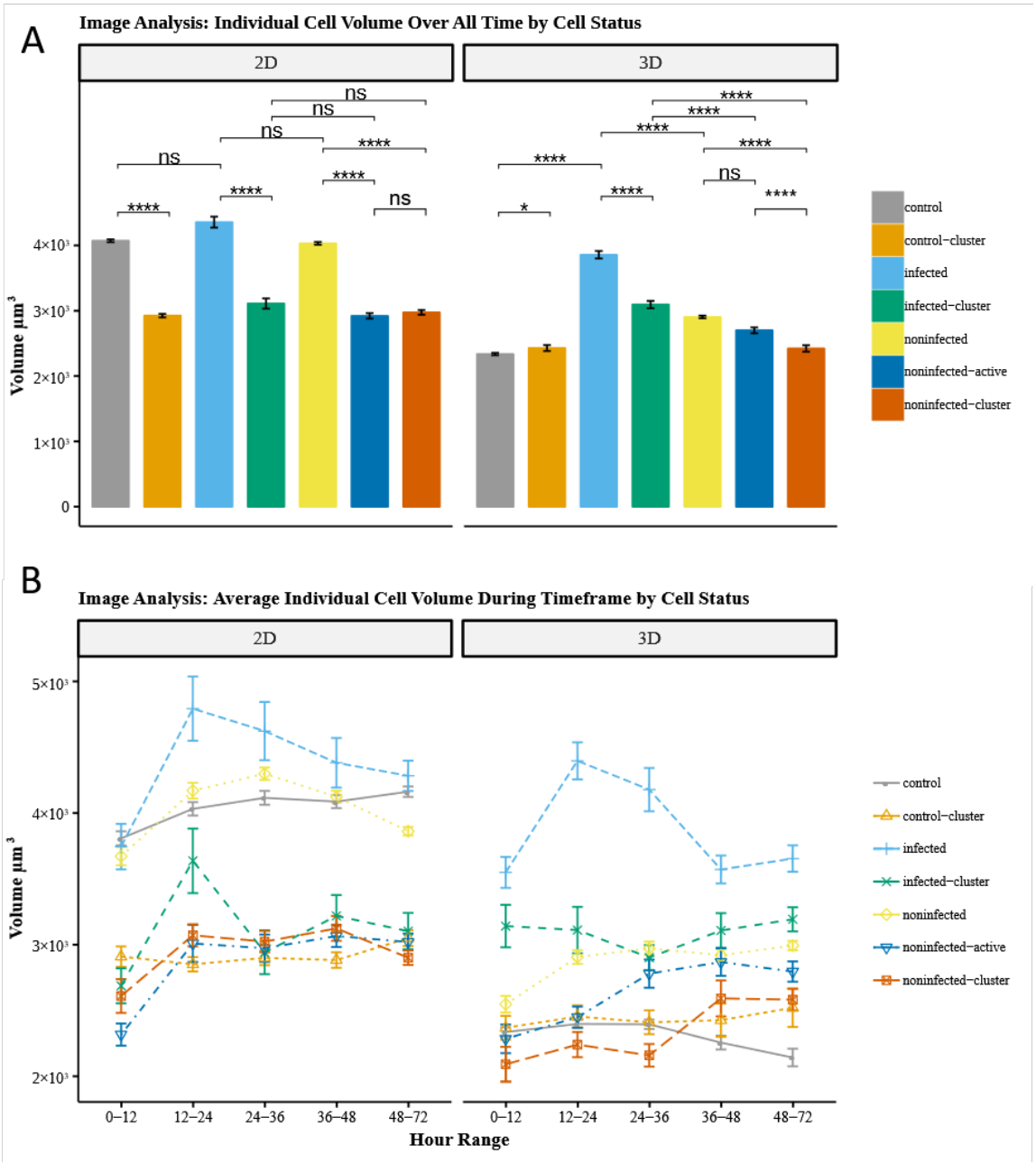

Figure 42: Individual cell volume of gfpBMDM infected with mCherry M.smegmatis in 2D and 3D culture conditions over 72 hours by cell status A) Averaged over all time B) Averaged based on hour range. (ns- No significant difference, * - p<.05, **-p<.01,***-p<.001,****-p<.0001)

Cell volume in 2D is highest in infected cells but is not significantly different from control cells or noninfected cells (Figure 42 A, Table 55). We also do not observe any significant difference between infected-cluster, noninfected-active cells and noninfected cluster cells.

Table 55: 2D Average Individual Cell Volume Over All Time: Wilcoxon

2D Cell State	*Volume um^3*	*2D Cell State*	*Volume um^3*	*p value*
Control	4.07E+03	Control-Cluster	2.93E+03	1.78E-283
Control	4.07E+03	Noninfected	4.03E+03	0.221718
Control	4.07E+03	Infected	4.36E+03	0.400461
Infected	4.36E+03	Infected-Cluster	3.11E+03	1.55E-27
Infected	4.36E+03	Noninfected	4.03E+03	0.714533
Infected-Cluster	3.11E+03	Noninfected-Active	2.92E+03	1.27E-08
Infected-Cluster	3.11E+03	Noninfected-Cluster	2.98E+03	0.112621
Noninfected	4.03E+03	Noninfected-Cluster	2.98E+03	6.28E-114
Noninfected	4.03E+03	Noninfected-Active	2.92E+03	4.86E-77
Noninfected-Cluster	2.98E+03	Noninfected-Active	2.92E+03	0.979739

In 3D we see a much more apparent distinction between cell volume in infected cells and all other cell statuses. We see an initial increase in cell volume during the first 24 hours, followed by a gradual decrease as the infection clears (Figure 42 B). We see little ($p > .05$) to no significant difference between control and control-cluster, and noninfected and noninfected-active cells (Figure 42 A, Table 56) , but we do see a significant increase in cell volume of noninfected-active cells as compared to noninfected-cluster cells which poses an interesting quantification in the cell volume regulation of proinflammatory macrophages that are not under active infection.

Table 56: 3D Average Individual Cell Volume Over All Time: Wilcoxon

3D Cell State	*Volume um^3*	*3D Cell State*	*Volume um^3*	*p value*
Control	2.34E+03	Control-Cluster	2.43E+03	0.024023
Control	2.34E+03	Noninfected	2.91E+03	1.01E-60
Control	2.34E+03	Infected	3.86E+03	2.48E-202
Infected	3.86E+03	Infected-Cluster	3.09E+03	2.78E-67
Infected	3.86E+03	Noninfected	2.91E+03	3.03E-97
Infected-Cluster	3.09E+03	Noninfected-Active	2.70E+03	5.32E-09
Infected-Cluster	3.09E+03	Noninfected-Cluster	2.42E+03	8.79E-20
Noninfected	2.91E+03	Noninfected-Cluster	2.42E+03	9.45E-13
Noninfected	2.91E+03	Noninfected-Active	2.70E+03	0.221598
Noninfected-Cluster	2.42E+03	Noninfected-Active	2.70E+03	1.24E-07

4.3.3 Multivariate Classification Models

Prediction of cell status using multivariate classification models provides further insight into the other cellular dynamics quantified under confocal imaging and demonstrates how multiple dynamics can be utilized to distinguish cell state. While we saw much less significant difference in 3D between the previously observed cell dynamics, the application of multivariate classification models results in higher accuracy for the 3D dataset as compared to 2D demonstrating that a combination of observable cell dynamic features in 3D provides higher discrimination between cell states.

4.3.3.1 Linear discriminant analysis for cell status classification

LDA with reverse feature selection applied to the 2D and 3D datasets independently show increasing accuracy over time, with the accuracy for 3D being higher at all hour ranges (Figure 43 A). When analyzed for the highest accuracy for a single feature we see that 3D maintains the highest accuracy over all hour ranges (Table 57, Figure 43 B).

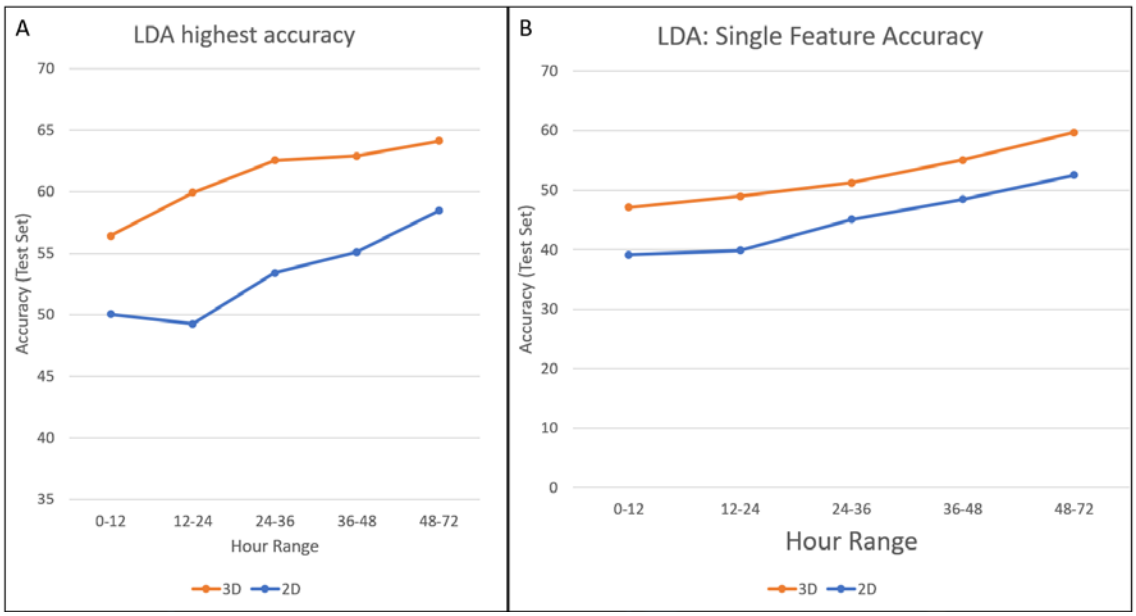

Figure 43: Multivariate classification of cell status over time using LDA A) Highest accuracy reported with reverse feature selection B) Accuracy for best single feature predictor

Table 57: LDA-Cell Status Classification Models, Single Feature Accuracy

Condition	*Hour Range*	*test accuracy %*	*Feature*	*solver*
2D	0-12	39.12809	Sphericity	svd
2D	12-24	39.88593	Ellipicity Prolate	svd
2D	24-36	45.07926	speed	svd
2D	36-48	48.47973	speed	lsqr
2D	48-72	52.53533	speed	svd
3D	0-12	47.12644	Delta total dist y	svd
3D	12-24	48.95833	Delta total dist y	lsqr
3D	24-36	51.24088	Delta total dist y	svd
3D	36-48	55.09077	tp disp z	svd
3D	48-72	59.69213	tp disp z	svd

Further investigation of the single feature accuracy for 2D and 3D shows features previously identified including speed, as well as new features including “delta total dist y”, which is the change in total distance traveled in the y plane between timepoints of imaging (equivalent to absolute value of distance traveled in one timepoint in y), and

the “tp disp z” which is the directional distance travelled in the z direction between timepoints of imaging. Another feature of significance that is observed is “sphericity” which is a value calculated directly by Imaris that is representative of how spherical the imaged object is [90].

4.3.3.2 Gaussian mixture models for classification

Gaussian mixture models provide a similar linear delineation between variables as LDA but provide posterior probability of class assignment for existing and new variables. As a part of this, the multivariate Gaussian assumptions for a multivariate GMM allow for the generation of new datapoints within the gaussian distribution making them a very attractive option for model informing. cGMM with reverse feature selection applied to the 2D and 3D datasets independently show increasing accuracy over time, with the accuracy for 3D being higher at all hour ranges (Figure 44 A). When analyzed for the highest accuracy for a single feature we see that 2D maintains higher accuracy over all hour ranges except 0-12 hours (Figure 44 B, Table 58). Single feature accuracy also highlights cell dynamics not previously analyzed primarily focused around cell timepoint displacement and distance traveled over time for both 2D and 3D conditions, however these displacement and distance features are components of cell directedness. Analysis of directional displacement over time includes vectorized components of cellular migration and will differ depending on localized context of cell spatial organization.

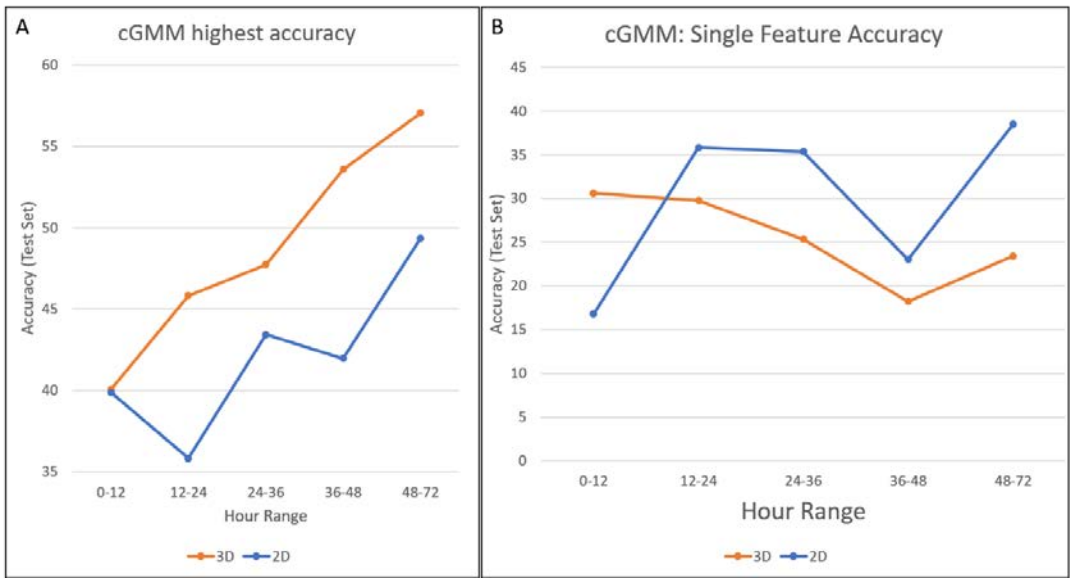

Figure 44: Multivariate classification of cell status over time using cGMM A) Highest accuracy reported with reverse feature selection B) Accuracy for best single feature predictor

Table 58: cGMM Cell Status Classification Models, Single Feature Accuracy

Condition	*Hour Range*	*test accuracy %*	*Feature*	*Covariance*
2D	0-12	16.79	total dist 2	spherical
2D	12-24	35.82	total dist z	tied
2D	24-36	35.37	tp disp y	tied
2D	36-48	23.04	cell volume	tied
2D	48-72	38.51	total dist z	tied
3D	0-12	30.59	delta cell volume	tied
3D	12-24	29.79	tp disp y	tied
3D	24-36	25.33	cell volume	tied
3D	36-48	18.23	total dist y	tied
3D	48-72	23.43	cell volume	spherical

4.3.3.3 Decision tree models for classification

Decision trees provide the benefit of multiple linear delineations for a single feature unlike LDA and cGMM, but do not provide generation of new datapoints within an assumed gaussian distribution. However, they do inherently report the predictor importance for each feature making them a very attractive option for determining which features are vital for computational model informing. cTree with reverse feature

selection applied to the 2D and 3D datasets independently show the best accuracy over all of the tested models and show increasing accuracy over time, with the accuracy for 3D being higher at all hour ranges (Figure 45 A). When analyzed for the highest accuracy for a single feature we see that 3D maintains higher accuracy over all hour ranges (Table 59, Figure 45 B), consistent with other methods of cell state classification. Single feature accuracy also highlights cell dynamics previously identified by other multivariate classification methods including sphericity, cell volume, tp disp y and tp disp z (directional displacement in the y and z planes between timepoints, which are components of cell directedness).

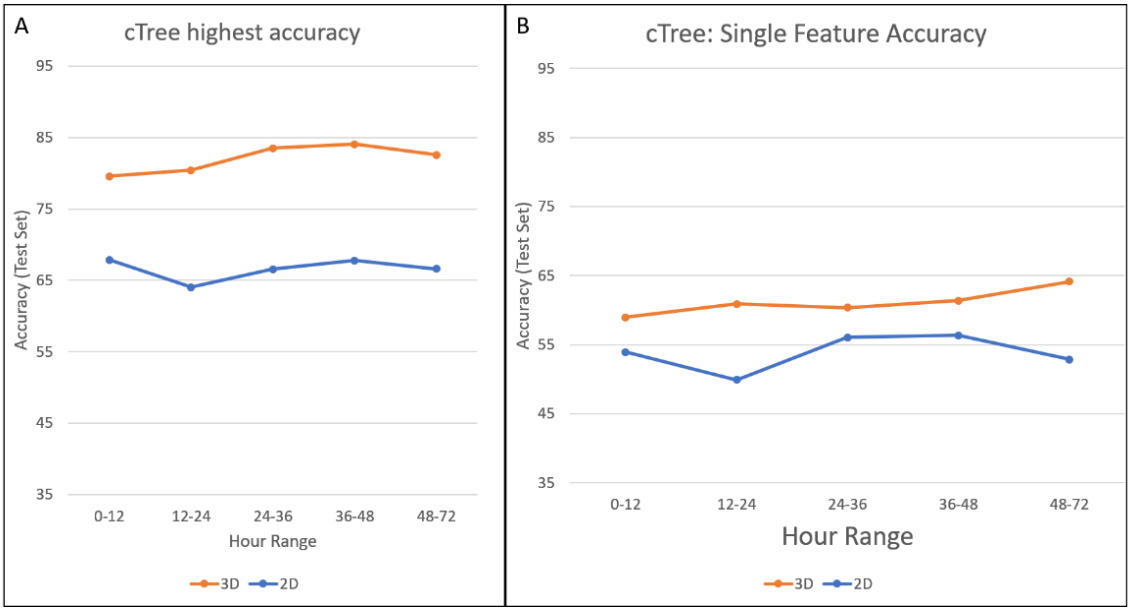

Figure 45: Multivariate classification of cell status over time using cTree A) Highest accuracy reported with reverse feature selection B) Accuracy for best single feature predictor

Table 59: cTree-Cell Status Classification Models, Single Feature Accuracy

Condition	*Hour Range*	*test accuracy %*	*feature*	*solver*
2D	0-12	53.93	Sphericity	gini
2D	12-24	49.92	cell volume	gini
2D	24-36	56.05	speed	gini
2D	36-48	56.34	speed	gini
2D	48-72	52.87	cell volume	gini
3D	0-12	58.97	tp disp y	gini
3D	12-24	60.90	tp disp y	gini
3D	24-36	60.36	tp disp z	gini
3D	36-48	61.40	cell volume	gini
3D	48-72	64.14	tp disp z	gini

Analysis of predictor importance for cTrees on the non-reverse feature selected datasets shows that many of the same key features are identified (Figure 46, Figure 47). Many of these features identified involve the displacement of cells overtime, which are relative to each individual experiment. However, one feature that has appeared during multivariate classification analysis that warrants further investigation is sphericity, as macrophage phenotype has been linked to cell shape, with rounder phenotype cells (presumably correlated to a higher sphericity) being linked to classical, proinflammatory, macrophage activation [88].

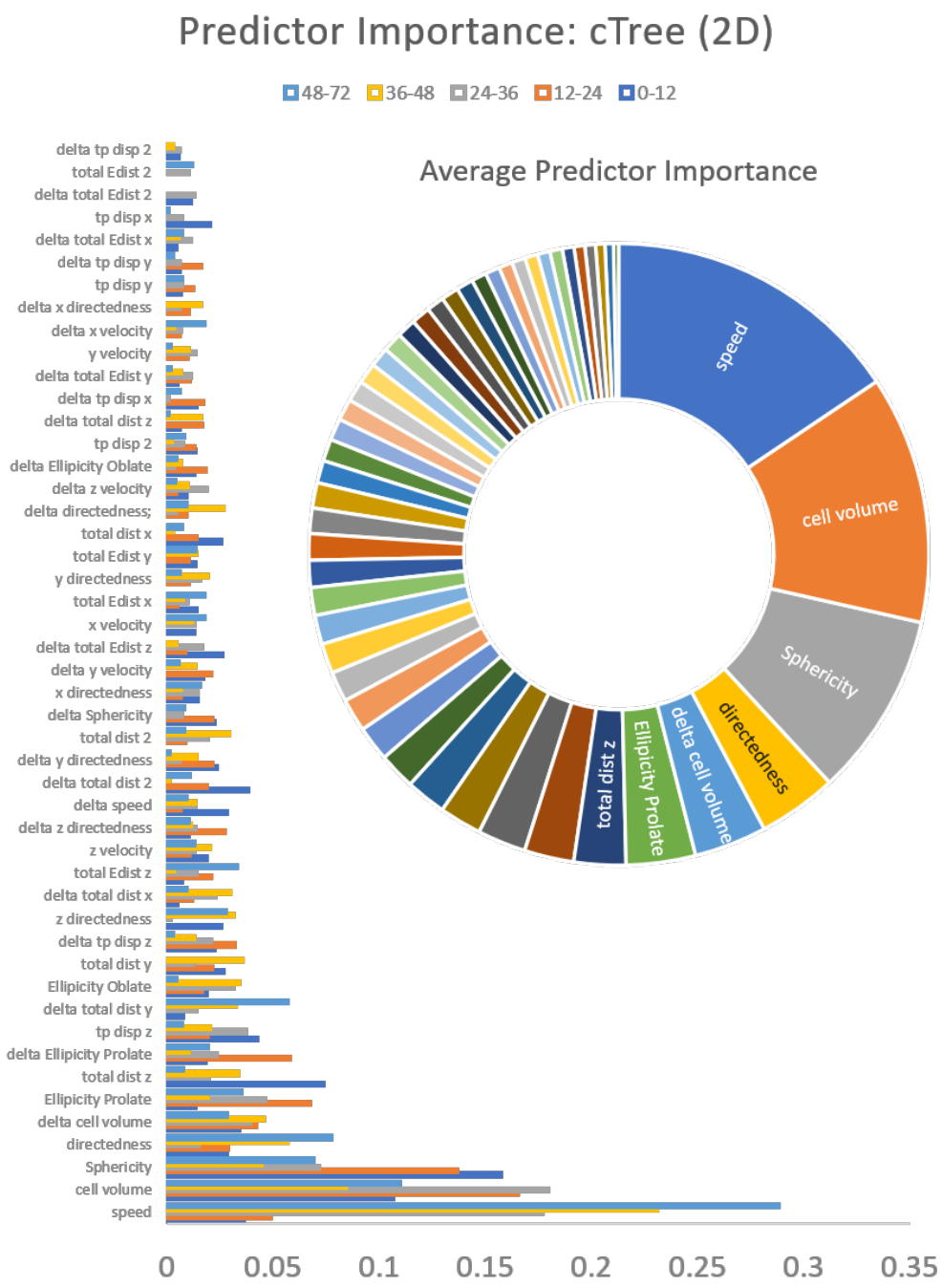

Figure 46: Predictor importance for 2D cell status cTree determination by hour range (bar graph) and overall (sunburst).

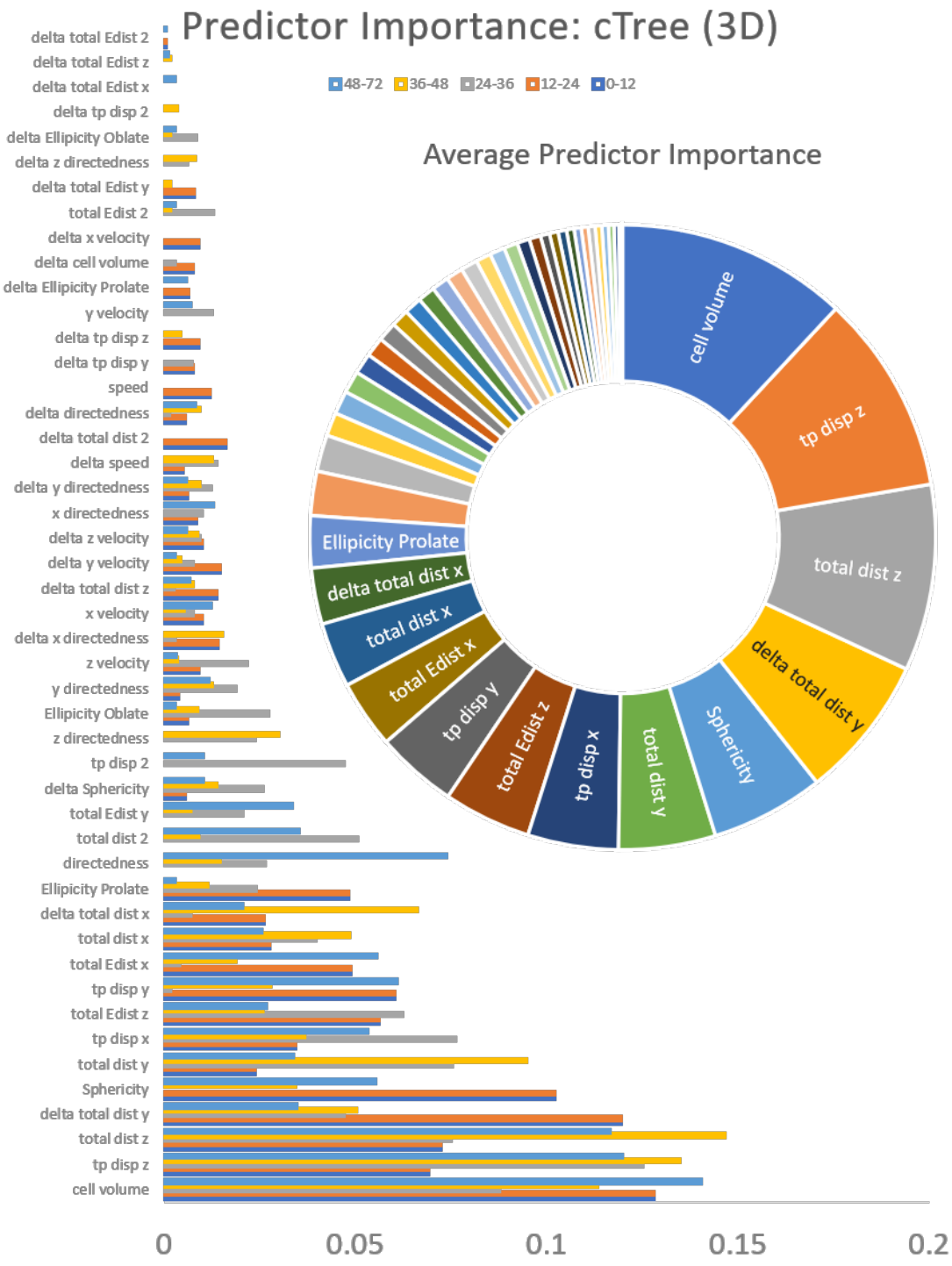

Figure 47: Predictor importance for 3D cell status cTree determination by hour range (bar graph) and overall (sunburst).

4.3.3.4 Cell Sphericity Identified by multivariate classification models

Cell sphericity in the 2D condition shows significant delineation between cell status comparable to the distinction of previously quantified cellular dynamics based on proinflammatory state. This analysis shows that infected, infected-cluster and non-infected active cells have the highest cell sphericity compared to the noninfected or control counterparts (Figure 25 A, Table 23).

Table 60: 2D Average Individual Cell Sphericty Over All Time: Wilcoxon

2D Cell State	*sphericty*	*2D Cell State*	*sphericty*	*p value*
Control	0.710	Control-Cluster	0.743	4.69E-49
Control	0.710	Noninfected	0.760	1.72E-107
Control	0.710	Infected	0.841	1.17E-159
Infected	0.841	Infected-Cluster	0.858	2.02E-01
Infected	0.841	Noninfected	0.760	1.67E-69
Infected-Cluster	0.858	Noninfected-Active	0.846	2.73E-03
Infected-Cluster	0.858	Noninfected-Cluster	0.784	1.47E-43
Noninfected	0.760	Noninfected-Cluster	0.784	1.69E-11
Noninfected	0.760	Noninfected-Active	0.846	2.07E-61
Noninfected-Active	0.846	Noninfected-Cluster	0.784	3.70E-35

We also see that these cell statuses in 2D also follow very similar trends over the course of time (Figure 48 B). The same trends are not seen in 3D, where the majority of cells follow the same trend in sphericity over time except for control cells which have an overall higher sphericity (Figure 48 A, Table 60). We do see a marked increase in sphericity over time in 3D infected cells and infected-cluster cells that is not present in the non-infected states (Table 61).

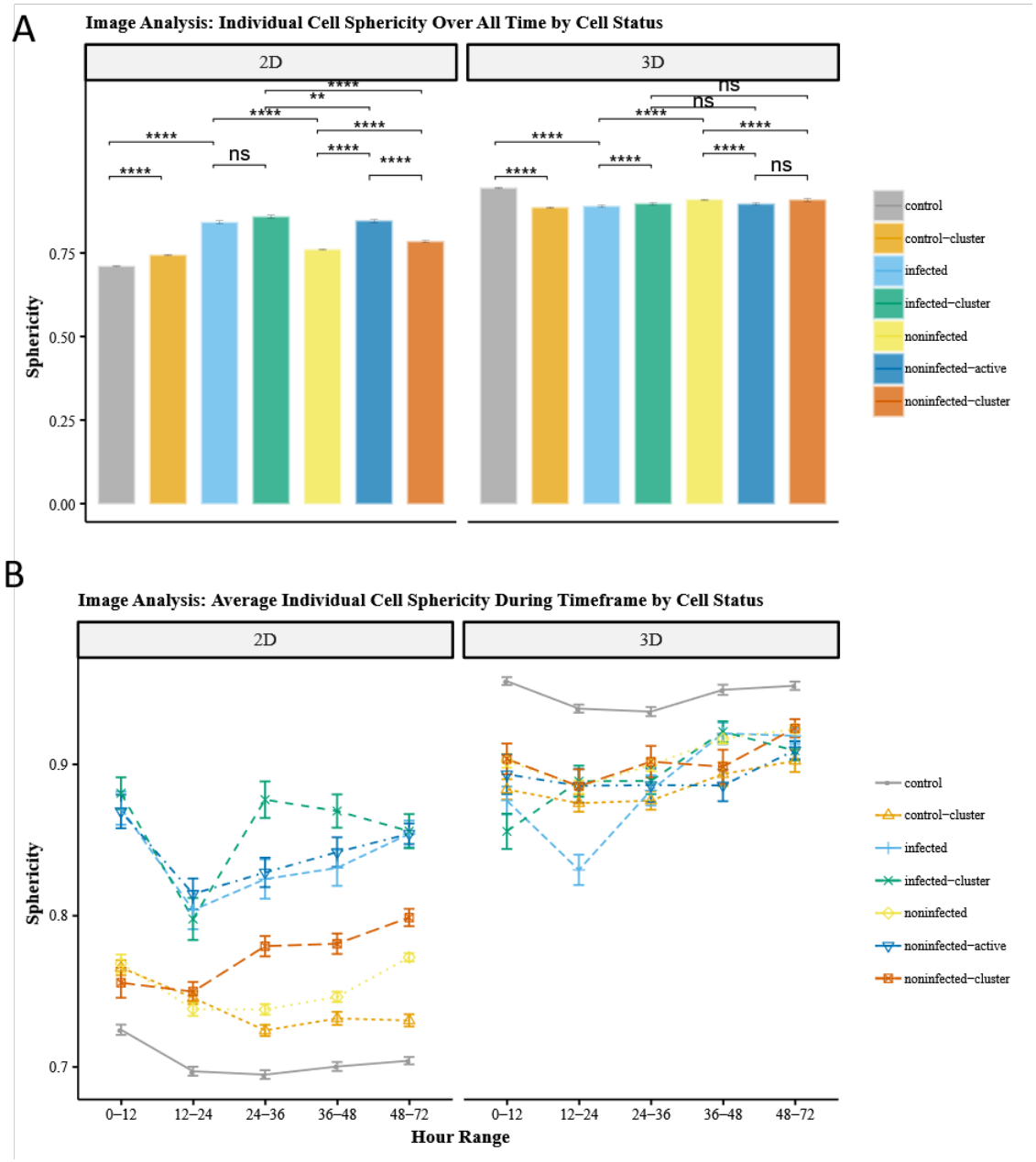

Figure 48: Individual cell spehericty of gfpBMDM infected with mCherry M.smegmatis in 2D and 3D culture conditions over 72 hours by cell status A) Averaged over all time B) Averaged based on hour range. (ns- No significant difference, * - p<.05, **-p<.01,***-p<.001,****-p<.0001)

Table 61: 3D Average Individual Cell Sphericty Over All Time: Wilcoxon

3D Cell State	*sphericty*	*3D Cell State*	*sphericty*	*p value*
Control	0.944	Control-Cluster	0.886	3.24E-97
Control	0.944	Noninfected	0.909	6.82E-38
Control	0.944	Infected	0.889	2.66E-12
Infected	0.889	Infected-Cluster	0.897	7.98E-08
Infected	0.889	Noninfected	0.909	6.53E-07
Infected-Cluster	0.897	Noninfected-Active	0.896	7.74E-01
Infected-Cluster	0.897	Noninfected-Cluster	0.909	1.65E-01
Noninfected	0.909	Noninfected-Cluster	0.909	1.71E-14
Noninfected	0.909	Noninfected-Active	0.896	4.11E-23
Noninfected-Active	0.896	Noninfected-Cluster	0.909	0.2923

4.3.3.5 Empirical distributions to populate computational models

Variable generation for model development executed through *disttoRNG*, generated the best fitting distribution for the features of interest for all cells over all imaged time and returned one random value from the distribution for analysis. AIC was selected as the method of evaluation as it does bias away from more complex models as strictly as BIC. Cellular speed generated a predominantly inverse gaussian distribution except in the case of 2D-Control and 2D-Control-Cluster cell states (Table 62) and generated random values within the parameters of previously reported data [68].

Table 62: Empirical distribution of cell speed over all time and random variable generation based on cell state

Cell State	*distribution*	*AIC*	*Random Value (um/s)*
2D-Control	gamma	-98616.24	3.55E-4
2D-Control-Cluster	gamma	-40452.31	8.95E-5
2D-Noninfected	invgauss	-87402.82	1.91E-4
2D-Infected	invgauss	-12447.31	1.61E-4
2D-Noninfected-Active	invgauss	-9529.42	7.47E-4
2D-Noninfected-Cluster	invgauss	-17238.56	1.88E-3
2D-Infected-Cluster	invgauss	-6732.07	4.12E-4
3D-Control	invgauss	-32319.91	1.25E-4
3D-Control-Cluster	invgauss	-13013.61	1.94E-4
3D-Noninfected	invgauss	-67091.77	6.075E-5
3D-Infected	invgauss	-15866.12	6.20E-4
3D-Noninfected-Active	invgauss	-7241.19	1.79E-4
3D-Noninfected-Cluster	invgauss	-4914.84	3.15E-5
3D-Infected-Cluster	invgauss	-7701.86	1.46E-4

Cellular acceleration is described best by a nakagami distributoin in 3D. In 2D we do see a difference of distributions with gamma, nakagami (related to gamma distribution), and beta (Table 63).

Table 63: Empirical distribution of cell acceleration over all time and random variable generation based on cell state

Cell State	*distribution*	*AIC*	*Random Value (um/s2)*
2D-Control	beta	-401848.69	2.54E-9
2D-Control-Cluster	beta	-182425.58	3.57E-8
2D-Noninfected	gamma	-254594.01	3.93E-9
2D-Infected	nakagami	-34422.30	5.07E-10
2D-Noninfected-Active	nakagami	-28207.80	1.19E-8
2D-Noninfected-Cluster	gamma	-62732.58	2.18E-8
2D-Infected-Cluster	nakagami	-18667.05	1.85E-9
3D-Control	nakagami	-76624.94	1.87E-8
3D-Control-Cluster	nakagami	-32114.84	5.10E-8
3D-Noninfected	nakagami	-163600.91	5.95E-9
3D-Infected	nakagami	-37270.44	1.97E-8
3D-Noninfected-Active	nakagami	-17633.55	2.06E-8
3D-Noninfected-Cluster	nakagami	-13131.67	1.88E-12
3D-Infected-Cluster	nakagami	-20493.40	5.38E-8

Cellular volume is described best by a t distribution in both 2D, 3D except for 2D-nonifected and 2D-noninfected-cluster cells which are best described by a inverse gaussian and lognormal distribution respectively (Table 64).

Table 64: Empirical distribution of cell volume over all time and random variable generation based on cell state

Cell State	*distribution*	*AIC*	*Random Value (um^3)*
2D-Control	t	153755.02	3753.49
2D-Control-Cluster	t	63467.22	1686.07
2D-Noninfected	Invgauss	123262.21	12175.43
2D-Infected	t	17414.21	9739.37
2D-Noninfected-Active	t	12427.97	2937.80
2D-Noninfected-Cluster	lognorm	24688.09	2373.01
2D-Infected-Cluster	t	8882.05	4191.95
3D-Control	t	35241.10	3228.78
3D-Control-Cluster	t	15502.15	1467.15
3D-Noninfected	t	80968.80	3295.40
3D-Infected	t	20226.62	2966.09
3D-Noninfected-Active	t	8713.65	3336.30
3D-Noninfected-Cluster	t	5628.67	1740.12
3D-Infected-Cluster	t	9715.85	4664.25

Cellular directedness is described best by an inverse gaussian distribution in 3D, except for 3D-infected-cluster cells. In 2D, a variety of distributions best describe cell directedness based on cell state with only 2D-infected and 2D-nonifnected-active having distributions described by inverse gaussian (Table 65).

Table 65: Empirical distribution of cell directedness over all time and random variable generation based on cell state

Cell State	*distribution*	*AIC*	*Random Value*
2D-Control	nakagami	-4924.27	0.11
2D-Control-Cluster	Beta	-1964.54	0.41
2D-Noninfected	gamma	-6493.74	0.03
2D-Infected	invgauss	-1077.00	0.28
2D-Noninfected-Active	invgauss	-993.76	0.12
2D-Noninfected-Cluster	weibull_min	-1074.61	0.26
2D-Infected-Cluster	gamma	-561.27	0.22
3D-Control	invgauss	-3728.44	0.23
3D-Control-Cluster	invgauss	-1213.77	0.09
3D-Noninfected	invgauss	-9540.85	0.063
3D-Infected	invgauss	-2169.38	0.092
3D-Noninfected-Active	invgauss	-951.48	0.46
3D-Noninfected-Cluster	invgauss	-588.40	0.029
3D-Infected-Cluster	expon	-739.69	0.12

Cellular sphericity is described best by a variety of distributions (Table 66), but what is of note is that the three cell states previously identified in statistical analysis as having similar trends over time (2D-control, 2D-control-cluster and 2D-noninfeted cells) all share the beta distribution along with 2D-noninfected-cluster cells. Active and infected cells in 2D and 3D are both described by weibull_max/min.

Table 66: Empirical distribution of cell sphericity and random variable generation based on cell state

Cell State	*distribution*	*AIC*	*Random Value*
2D-Control	beta	-12649.17	0.75
2D-Control-Cluster	beta	-5751.42	0.80
2D-Noninfected	beta	-9185.60	0.55
2D-Infected	weibull_min	-1181.14	0.99
2D-Noninfected-Active	weibull_max	-1448.67	0.86
2D-Noninfected-Cluster	beta	-2320.77	0.76
2D-Infected-Cluster	weibull_max	-1066.15	0.88
3D-Control	weibull_min	-7261.85	0.93
3D-Control-Cluster	weibul_max	-2248.98	0.82
3D-Noninfected	t	-10777.65	0.99
3D-Infected	weibull_min	-2084.86	0.78
3D-Noninfected-Active	weibull_min	-2084.86	0.78
3D-Noninfected-Cluster	weibull_max	-1068.94	0.97
3D-Infected-Cluster	genextreme	-1540.36	0.91

Pulling from the TB ABM one of the key areas that we can most readily utilize these empirical distributions is in the improvement of the calculations of cellular speed, which has different values based on cell state. A comparison of the average empirical cell speeds for 2D and 3D and the comparable TB-ABM cell speeds derived from 2D chemotactic chamber studies by Webb et al. [68] are summarized in Table 67.

Table 67: Average Cell Speed Over All Time Empirical vs Computational

2D Cell State	*Speed um/s*	*3D Cell State*	*Speed um/s*	*TB-ABM[68]*	*Speed um/s[68]*
Control	1.22E-03	Control	2.60E-04	Resting	1.667E-2
Control-Cluster	1.46E-03	Control-Cluster	3.11E-04		
Noninfected	7.67E-04	Noninfected	3.64E-04		
Noninfected-Cluster	9.56E-04	Noninfected-Cluster	3.52E-04		
Infected	6.00E-04	Infected	4.01E-04	Infected	1.667E-5
Infected-Cluster	6.00E-04	Infected-Cluster	4.52E-04		
Noninfected-Active	6.46E-04	Noninfected-Active	4.23E-04	Active	2.08E-4 to 1.667E-2

We note that the resting macrophages, which are non-active non-infected macrophages could potentially span all the noninfected and control cell states. The reported values for the 2D chemotactic study report a significantly higher cell speed than observed in our studies [68]. Most importantly however, the shift in dynamics between resting, and infected and active cells differed depending on the environment. In our investigation we found, in agreement with the Webb study, that 2D infected cells travelled at a significantly slower speed than their resting counterparts, whereas the converse was seen in 3D. This shift in dynamics, if applied to computational models of mycobacterial infection should produce results that differ from the current understanding of this initial infection process.

4.4 Discussion

4.4.1 Cell dynamics-the impact of the ECM and cell state

In this study we present a large-scale computational platform for semi-automatic analysis of imaging-based 2D and 3D mycobacterial infection data. Using 4D confocal imaging of murine bone marrow derived macrophages infected with and responding to *Mycobacterium smegmatis.* We demonstrate the ability to characterize cellular dynamics based on cell state, determined by spatial organization of cells and machine learning determined infection status. The use of novelty detection LOF algorithm to detect infected cells showed consistency between different datasets and had very low misclassification error (<1%) for the known non-infected control datapoints. This determination of cell infection then allowed for the subsequent identification of

activated cells by finding noninfected cells associated in 20 µm DBSCAN clusters with at least one infected cell.

Through the analysis of the cell dynamics of the cell state we quantified the impact that the availability of a 3D environment has on the cell dynamics relative to the cell state. We see that in many cases, including cell speed, cell acceleration, cell directedness and cell volume, that the cell status of infection had a significant impact on the resulting dynamics within each environment. While the 3D environment reduced the cellular motility compared to 2D, we saw that infected and active cells in both conditions resulted in comparable dynamics regardless of environment. However, we demonstrated a converse relationship between dynamics in 3D infected cells and controls when compared to 2D. In the 3D environment the proinflammatory cells displayed significantly faster cellular speed and acceleration than their noninfected or control cells, whereas the converse was observed in 2D.

Through our analysis of the impact of structure on cellular response (cellular aggregation and clustering) we found that noninfected-activated cells behaved more similarly to infected cells than other noninfected-clustered cells in the same environment. This observation demonstrates that cell response dynamics are being influenced by proximity to infection and not solely dependent on spatial organization. In addition, we found that the noninfected nonactive cells within the infected condition demonstrated comparable dynamics to their respective noninfected counterparts in the control conditions. This difference is markedly more apparent in 2D than 3D where we see less differences in the distribution of dynamics. In particular, the trends of cellular

speed, acceleration, and directedness over time are most notable in the 2D environment.

Comparing to recent studies of mycobacterial induced cellular migration, we consider the *in vivo* zebrafish infection with *M. marinum* by Davis and Ramakrishnan who quantified the migration and cellular speed of noninfected and infected macrophages in the heterogenous environment[15]. This study found that the chemotactic signals inducing migration of uninfected cells towards nascent granulomas induced increased velocities depending on the virulence of the bacterium utilized. The key virulence factor isolated as the primary contributor to cell migration speed was the RD1 mycobacterial virulence locus, which is not present in *M. smegmatis*. Their investigation isolated the effect of this factor on cellular speed and found that the cellular speed of uninfected macrophages to be on average 4.5 um/min (7.5E-2 um/s), which is in agreement with the cellular speed utilized in the computational TB-ABM and based on the 2D chemotactic study[68]. Additionally, in their investigation of infected macrophages in nascent granulomas, they demonstrated that the motility of infected macrophages increased as the bacterial load decreased. One of the limitations of our study in its current form is the identification of infected cells is performed through novelty detection machine learning algorithms and the level of bacterial load in a cell is not directly reported. However, we can observe the trends of cellular speed of infected cells over time in coordination with the known bacterial load decrease in the system over the course of infection. With this we can demonstrate that in our model of *M. smegmatis* infection, that the overall cell speed of determined infected cells decreases

as the bacteria is cleared form the system. However, what is more interesting is the cellular speed quantified for noninfected cells in the presence of infection. In concurrence with the observations by Davis and Ramakrishnan and the chemotactic studies utilized to inform the TB-ABM by Webb et al [15], [68], the cellular speed of noninfected macrophages in the infected condition decrease as the bacterial load clears from the system, showing that in the converse, these noninfected cells display a higher motility in the initial stages of infection when the bacterial load is significantly higher. In our 3D model, this relationship is more difficult to extrapolated due to the very low variance in the cellular speeds between individual cell states over time. We see a relatively constant speed regardless of bacterial load in the system. However, we do note that on average we do see higher cell speeds in infected and active cells than their noninfected counterparts, which does not concur with the previously established studies. This discrepancy between the 2D and 3D environment and the role it plays in cell migration poses the question of the exact role of the ECM in migratory patterns.

In analysis of cellular dynamics in murine models, the investigations of murine hepatic granulomas induced by *Mycobacterium bovis* BCG (BCG) infection, Egen et al quantified mainly T-cell dynamics[10]. Their primary findings showed lower displacement of T-cells within granulomas, but primarily a slightly lower velocity. However, this study did also report the presence of limited macrophage and mycobacterial dynamics during the development of granulomas. They were unable to detect significant macrophage migration in the immature granulomas in the early stages of infection. Specifically, they noted that the macrophages in the later stages of the

granuloma formation presented with very little mobility compared to the other observed neutrophils and monocytes, macrophage precursors, in the system. However, because they were unable to utilize cellular tracking for these macrophages, direct comparisons from our presented work to the motility of macrophage's in the murine hepatic granuloma is not quantifiable. On an observational level our migration patterns observed in the 3D does concur more with the BCG model of the murine hepatic granuloma with very little macrophage motility. This observed lower motility in our 3D infection study and the 3D murine hepatic granuloma as compared to the *M. marinum* zebrafish nascent granuloma could be due to a few potential factors. Firstly, the study of Davis and Ramakrishnan identified the RD1 virulence locus as a key factor to macrophage's migration. This virulence locus is not present in *M. smegmatis*, or BCG [97] potentially causing the difference in observed macrophage dynamics. Secondly. The use of zebrafish embryos for quantification of human disease provide a powerful tool for investigation due to optical transparency, however there are a variety of factors that could potentially induce discrepancies to mammalian models. Firstly, the mode of infection for zebrafish models, as in the Davis and Ramakrishnan study, is traditionally direct injection, which is not the typical inhaled aerosol route of infection for mycobacterial infection[14], [15], [98]. Secondly, the temperature required for zebrafish husbandry is 28C, which is significantly lower than the 37C of mammalian studies and human relevant bacterial infections. Thirdly, the toll-like receptor 4 (TLR4) signaling pathway in zebrafish has been shown to be an overall negative regulator of TLR signaling in zebrafish, and the TLR4 receptor does not recognize bacterial endotoxin LPS, the

primary signaling pathway necessary for the proinflammatory response to gram-negative bacteria[99]. While mycobacterial species are not gram-negative and are not known to produce endotoxins[100], they do induce signaling through the TLR4 signaling pathway, but the TLR4 response is shown to be less vital to host immune response to infection than TLR2[101], [102]. This relationship of cellular signaling pathway discrepancies between zebrafish and mammalian might induce a significant disparity in cellular motility due to the cell signaling processes in the TLR pathways, in addition the zebrafish embryos only present with an innate immune response, and the murine models have a full adaptive immune response including multiple T-cell types. Further investigation in to the comparative response of zebrafish macrophages to murine or human macrophages in response to mycobacterial challenge may elucidate the exact signaling cascade differences and the resulting changes to the overall proinflammatory response and how this may be impacting macrophage motility in the early stages of mycobacterial infection.

4.4.2 Generation of parameters for computational models.

The exploration of multiclass classification models provides an interesting avenue for future investigation into multi-feature cell dynamic analysis, as the linear discriminations in LDA can be utilized to generate classifications of unknown cell datapoints and the gaussian distributions in cGMM allows the ability to generate new multi-variate parameters from the high-dimensional gaussian distributions. We observe in our investigation of individual cell dynamics features that the discrimination between 2D cellular states is more apparent for individual cell dynamic features as compared to

3D. However, the multi-feature analysis regardless of model applied demonstrated a higher accuracy in discriminating 3D cellular state as opposed to 2D, indicating that multi-feature quantification provides better description of individual cellular state in the 3D environment. This provides a potential avenue for future multi-feature investigation in the quantification of cell dynamics which may further our understanding of how these features relate and coordinate within each environment and cell state.

Additionally, these classification methods provided insight into potential cell dynamic features that could be further investigated. Specifically, classification trees identified cell sphericity as a predictor of high importance for both 2D and 3D cell state. Quantification of this feature illustrates high sphericity values of infected, infected-cluster and noninfected-active cells in 2D which ties to the modulation of macrophage phenotype under proinflammatory conditions [88]. A rounded macrophage phenotype (which can be correlated to a higher sphericity values) is indicative of M1, classically activated proinflammatory macrophages[88]. Our results for 2D cell state-based analysis demonstrate that this higher sphericity does hold for our proinflammatory cells in comparison to the lower sphericity for noninfected and control cells. However, this distinction does not appear significantly in 3D where control cells have the highest sphericity overall. Further investigation into this area is warranted as the availability of the 3D environment can elucidate the effect that macrophage activation has on cell phenotype and shape.

For the most applicable method for generating parameters for computational models we presented an automatic analysis of the distribution of empirical data with

subsequent random number generation. In general, such as in the case of the TB-ABM the majority of distributions of cellular dynamics are assumed to be most simplified description-a uniform distribution in a given biologically relevant range. These parameters are typically pulled from various biological systems and studies leading to a significant mismatch in datasets used in the computational modeling process. A more biologically relevant approach should include biological complexity relative comparable to the system being modeled. In our case, we have focused on the biological impact that the ECM and availability of a 3D structure to investigate the very initial stages of murine macrophages infection with *Mycobacterium smegmatis* in comparison to 2D studies. We also observe and analyze response data at a single cell level allowing for a higher resolution in our spatiotemporal analysis. We survey a variety of possible distributions so that we can best represent empirical cellular dynamic data generated.

With this empirical data generated distributions can be used to inform computational models that are more biologically representative than the current parameters used in modeling infection response. The reported values of cellular speed for the TB-ABM utilized parameters generated in a 2D chemotactic study, which report a significantly higher cell speed than observed in our studies [68]. A possible explanation for this is how this study was conducted. The study utilized the mouse immortalized macrophage cell line BAC1.2F5, which have been reported to behave comparably to primary mouse macrophages [103]. The cells were then cytokine stared of colony stimulating factor 1 (CSF-1) leading to an upregulation of the receptors for this cytokine. The cells were then placed into a chemotactic chamber with an increasing CSF-1

gradient and TNF-a to observer the resulting migration. Here in lies the first area in which the Webb study significantly differs from the biological context of cellular migration under infection. There is no active infection taking place in the migration analysis, the cells have been preconditioned to increase cytokine receptors, and the migration takes place in a forcibly directed (through increasing chemotactic gradient) 2D environment. Secondly, the metric of analysis for cell speed is not based on individual cell migration, but the cells as a collection measured in 5-minute intervals over a 1-hour period. The progression of our infection study takes place over a much longer timeframe with less frequent acquisition. The rate of acquisition of the confocal images for our study is 90 minutes between Z-stacks for a single image point for up to 72 hours.

Most importantly however, is the shift in dynamics that we have observed between resting, and infected and active cells depending on the environment. The assumption of slower infected cell speed in an infection environment, according to our observations, may differ in a 3D matrix. Our study demonstrates, in agreement with previous assumptions used for the TB-ABM, that infected cells in the 2D environment demonstrate lower cell speed than noninfected cells. However, in the 3D environment the infected cells displayed significantly faster cellular speed than their noninfected or control cells.

4.4.3 Future work

Quantification of cell state based on proximity to infected cells borrows from the same assumptions made in computational agent-based models of mycobacterial infection [48]. In these models the cell state can change due to the presence cytokines

and chemokines, cells in proximity, or due to the presence of bacteria in proximity. We have simplified and extended this assumption with the utilization of DBSCAN clustering algorithms and the determination of an activated cell only being labeled activated if it is within the same cluster as at least one infected cell. The inability to determine localized levels of cytokines in the system leads to a level of uncertainty in the determination of activated macrophages. Macrophages in an infected system present with varying phenotypes depending on how they are activated, we postulate that the primary makeup of the cells within our infected condition belong primarily to the classically activated M1 subset of macrophage phenotypes primarily due to the production of TNF-a that stems from infected macrophages [92], [93]. However, we do acknowledge the complexities and heterogenicity of macrophage activation and the significant implication of our state based assumptions [104], [105]. Studies have shown that there is a presence of both classically (M1) and alternatively (M2) activated macrophages within the host-response to bacterial infection[106], and have even demonstrated significance in granuloma and tuberculosis disease progression[107], [108]. However, without single cell level quantification of the transcriptomes of cells within our environment this discrimination in macrophage activation remains elusive.

Our classification models of cellular state informed us of the importance of many cellular features quantified with confocal imaging to the discrimination of cellular state within the 2D and 3D conditions. Many of these features involved the vectorized components of cellular migration in the x, y, or z plane. Analysis of the directional timepoint displacement or distance travelled over time will differ depending on

localized context of cell spatial organization and location within the imaging space relative to other cells. Features quantified in our analysis do not determine behavior or location of cells outside the immediate cellular neighborhood as determined by DBSCAN 20 μm clustering algorithms, therefore vectorized components of cellular migration including timepoint displacement and distance travelled in the x, y, or z plane will require further integration of overall imaging spatial states and quantification of the dimensional organization of cells outside of the immediate cellular neighborhood.

We also acknowledge the potential inaccuracies in cell segmentation that can occur during image processing and that it may have a significant impact on the results presented. One of the areas of focus for future work in the generation of data for computational models is in the area of image processing, as the quantifications of the observed data rely on the accuracy of the image processing. The data presented in this study relies on watershed segmentation[109] which has a tendency to over-segment and fail when objects are in contact and overlapping. This is even more of a concern when dealing with cellular tracking over time when cells are moving in and out of cellular aggregations. There has been recent advancement in the areas of watershed segmentation to address the concerns of overlapping biological images through contour analysis or prior knowledge of the dataset to apply clustering algorithms of watershed segmentations [110]–[113] There has also been recent advancement in the use of convolutional neural networks with and without watershed segmentation for segmenting complexly aggregated cells in a biological context [114]–[116]. However, the majority of these advances focus on 2D or 3D datasets, not 4D involving the tracking of

cells in a 3D environment over time. Improvements upon the segmentation and tracking algorithms will lead to more accurately representative datasets for informing computational models and the overall investigation of cell state-based dynamics in a 2D and 3D environment.

5 SPATIOTEMPORAL ANALYSIS OF MYCOBACTERIUM BOVIS BCG INFECTION

5.1 Introduction

Mycobacterium tuberculosis (Mtb), the causative agent of tuberculosis, is an intracellular bacteria that induces a unique host immune response resulting in the containment of the bacterium in a host immunological structure called a granuloma[2]. The innate immune response to Mtb infection involves a complex multicellular process resulting in the spatial organization of macrophages, the primary phagocytes, in response to infection [1]–[3]. This initial recruitment and spatial organization of macrophages in the innate immune response to mycobacterial infection has been implicated as the key contributor to the formation of granulomas after the introduction in the adaptive immune response, but current biological and computational analysis methods do not adequately permit the investigation of this early response in a high-throughput manner in direct comparison to current 2D methodologies, in effect isolating the variable of the presence of the 3D environment on the dynamics of host-pathogen interactions. This work adapts previously developed biological and computational methods of 2D/3D ex vivo mycobacterial infection of primary bone marrow derived macrophages to *Mycobacterium bovis* BCG (BCG) allowing for the quantification of the impact of the availability of 3D environment on the biological and cell dynamic response with a bacterium more comparable to Mtb. Previous studies in *Mycobacterium smegmatis*, a non-pathogenic relative of Mtb but shares a similar

structure, provides advantage for early investigation of methodologies and study due to its fast-doubling time and growth on agar plates [54]. BCG presents with a more virulent infection in mouse models with a pathogenesis more comparable to human Mtb infection[117], [118].

5.2 Materials and Methods

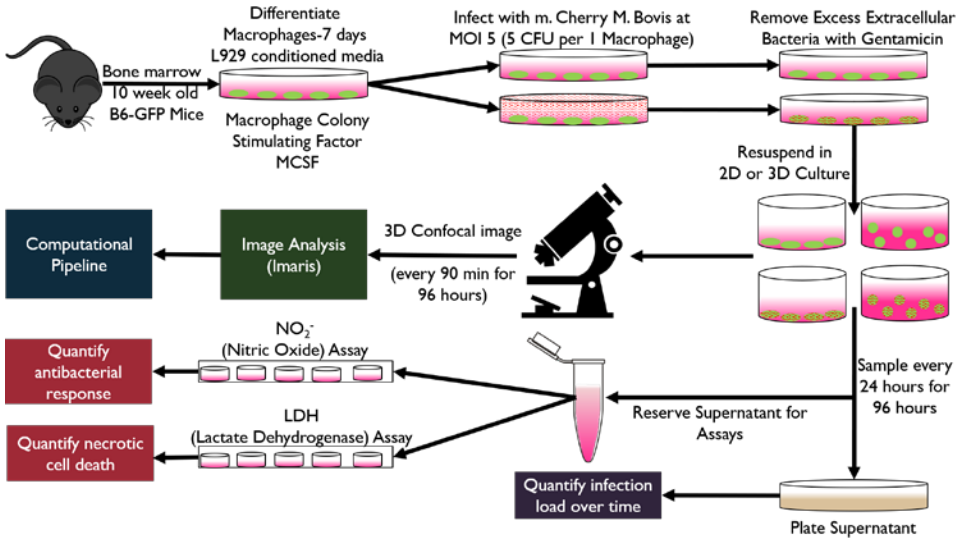

Figure 49: Outline of experimental methodology for 2D and 3D *ex vivo* platform for the investigation of the spatiotemporal dynamics of *m. Cherry M. Bovis* BCG infection

The methodology for the biological and image-based quantification of murine bone marrow derived macrophage response to *m. Cherry M. Bovis* BCG in 2D and 3D culture is outlined in Figure 49. This approach is a direct application of the methodologies outlined in Chapters 3 and 4.

5.2.1 Homogeneity and persistence of mCherry expression in *M. bovis* BCG culture

The high expressing *m. Cherry M. Bovis* BCG (mcBCG) (gifted by Dr. Cirillo Texas A&M University, TX) was chosen for infection as the *m. Cherry* excitation and emission

spectra did not overlap with the EGFP from the gfpBMDM. The bacterial stock was purified through single colony isolation and expansion using the selective antibiotic hygromycin (VWR) at 80 μg/mL within the bacterial media and agar.

Extended culture in the absence of the selective antibiotic hygromycin through differential plating was tested for persistence of the antibiotic resistance and thus the persistence of the *m. Cherry* florescence [51]. In short, static culture mcBCG was grown in filter top glass tubes in 7H9 media with and without the hygromycin selective antibiotic (80 μg/mL) for 96 hours. Culture tubes were vortexed and OD600 readings were taken every 24 hours and bacterial suspension plated to determine colony forming units on 7H11 agar with and without the hygromycin selective antibiotic (80 μg/mL).

To determine the growth/death curve of mcBCG 2D culture with and without gentamicin (Sigma Aldrich) (10 μg/ml), and 3D RBM, with a buffer solution that contains 50 μg/mL gentamicin, with standard bacterial 7H9 media with hygromycin (80 μg/mL) and 2D DMEM without antibiotics to serve as a control. Samples were collected and colony forming units (CFUs) were quantified at every 24 hours for 96 hours using 4˚C 1x PBS with 0.1% Tween 80 to disrupt the 3D extracellular matrix and remove any adhered bacteria form the tissue culture plates.

5.2.2 Comparison of infection dynamics *m. Cherry M. bovis* BCG and wild type *M. bovis* BCG in gfp BMDM with gentamicin

A comparison of the host response between *m Cherry M. bovis* BCG (mcBCG) and wild type *M. bovis* BCG (BCG) under 2D infection protocol to determine any variation

between the cells derived from the mouse lines. The cells were infected at a MOI of 5 in the presence of 10 µg/mL gentamicin and the wells were sampled in replicate every 24 hours for 96 hours with BMDMs from 10-week-old female mice as described below in the 2D infection assay. BCG and mcBCG were prepared for bacterial infection as previously reported in DMEM-complete (Dulbecco's Modified Eagle Medium containing 10% fetal bovine serum,1% L-glutamine and 1% non-essential amino acid)[50].

5.2.3 2D/3D ex vivo model of *M. bovis* BCG Infection

gfpBMDM cells were infected in tissue culture plates (VWR) as previously reported [50] at a multiplicity of infection of 1 macrophage to 5 bacterial colony forming units (MOI 5) After 4 hours of infection, plates were washed twice with 1x PBS and incubated for 12 hours with 50 µg/mL gentamicin to remove extracellular bacteria. Cells were removed from culture dishes with Cellstripper® (Corning) according to manufacture protocol and placed into 2D or 3D culture.

5.2.3.1 3D infection

250 µL of the diluted RBM (.18 mg/mL) coating was added to all wells that would be used for 3D culture to prevent the formation of an RBM-culture plate interface that lacks extracellular matrix proteins [52]. Plates were then incubated (5% CO_2 at 37°C) for 30 minutes for matrix formation, then the wells aspirated and tapped out onto a low-lint laboratory tissue paper. Immediately following, cells for 3D culture were resuspended at 0-8°C in diluted 8.5 mg/mL RBM (2.5E6 cells/mL) and 100 µL of cell suspension was plated into the center of each well in a 48 well plate for experimental sampling or 8 well chamber slide for confocal imaging as previously outlined in chapter

3. If any large bubbles were present a 20 to 30-gauge sterile needle was used to disrupt them. The matrix was then incubated for 45 minutes to allow gel to set fully and then 275 µL of hydrating media (DMEM-complete) was added on top of the set gel to prevent gel dehydration.

5.2.3.2 2D infection platform

The 2D infection model was conducted as previously reported with the addition of 10 µg/mL of gentamicin in the culture media to allow for comparison to the buffer solution of RBM[50]. Assuming passive diffusion of gentamicin into hydrating media from the RBM, we obtain a concentration of 10 µg/mL [53]. Previous studies have shown that this concentration inhibits the extracellular growth cycle of M. smegmatis without affecting the intracellular growth of the mycobacterium [54] [53], and M. bovis BCG has a lower sensitivity to the antibiotic as demonstrated by the longer culture time required to remove extracellular bacteria and the presence of extracellular bacteria after 14 hours of incubation in 50 µg/mL[50]. 250 µL of 2D cell suspension was added to each well of the 8-well chamber slide for imaging and 500 µL was added to each well of a 24 well plate (VWR) for sample quantification over the 96 hours as previously outlined in chapter 3. Cells were incubated and allowed to adhere for 2 hours before any supernatant samples were collected.

5.2.4 Analysis of biological response to infection

Infection was monitored for 96 hours with multi-area time-lapse confocal imaging (Fluoview, FV1200, Olympus) in the same manner outlined in Chapter 3, with the exception of increased imaging time. Supernatant samples were collected and CFU's

enumerated every 24 hours for 96 hours. For cells within the 3D matrix, hydrating media supernatant was collected for assays then 375 µL of ice-cold 1% Triton-X 100 (0-4 ˚C) was added and incubated for 5 minutes at room temperature. The disrupted cell and gel solution and vigorously pipetted to fully disrupt the RBM matrix and lyse macrophages. The resulting supernatant/lysate was serially diluted 10-fold and plated on 7H11 plates to enumerate the total colony forming units of bacteria in the 3D matrix.

For cells in 2D, the supernatant was collected for assays and for extracellular bacteria. The wells were gently washed twice with 1xPBS to remove excess extracellular bacteria. After washing 500 µL ice-cold 1% Triton-X 100 (0-4 ˚C) was added and incubated for 5 minutes at room temperature and then vigorously pipetted to lyse cells to release intracellular bacteria. The resulting lysates were vortexed and serially diluted 10-fold and plated on 7H11 agar plates as previously reported [36]. After 2 weeks the colony forming units were enumerated to quantify intracellular, extracellular or total bacterial load.

Collected supernatants were stored at -80˚C to be used for reactive species quantification. Frozen supernatant was used to perform assays in replicate according to manufacturer protocol. Griess reagent (Promega™, G2930) was used to quantify nitric oxide and LDH cytotoxicity assay (Pierce™, 88954) was used to quantify cell death. An LDH standard curve for was generated through quantification of lysed serial dilution of 5e6, 5e5, 5e4, 5e3, 5e2 gfpBMDM per mL according to manufacturer protocol.

5.2.5 Imaging and Image Processing

4D confocal images (Olympus Fluoview) were acquired every 90 minutes using a stage top incubation system (TokaiHit) and 40x confocal objective with .95 numerical aperture (UPLSAPO40X2, Olympus). 100 images were acquired for at an axial resolution of 1 µm to produce appended z-stacks at each timepoint which were acquired and analyzed as previously outlined using 8.1.2 (Bitplane) with surface creation and tracking as previously described in chapter 3 and 4.

5,600 unique cell datapoints were generated for all conditions at all timepoints combined for further analysis. Green fluorescent protein (GFP) was used to establish watershed segmentation and tracking of cells over the time course of imaging, and RFP values were used as a feature of each segmented cell object to denote the bacterial levels within each cell. Utilizing the python library scikit-learn, principal component analysis was applied to the RFP features to determine the principal components that described over 99% of data variability. The resulting principal components were then utilized in machine learning based detection of infected cells based on novelty detection of the RFP principal components. Local outlier factor was utilized to quantify potential infected cells as novelties based on training on the known control datapoints of the RFP principal components. Local density of the selected principal components of the control datasets was quantified with k-neighbor queries 20 neighbors. Novelties were determined to be infected cells as outlined in chapter 4.

Aggregations of cells were determined and identified using a density-based spatial clustering of applications with noise (DBSCAN) algorithm in Matlab [89], at 20 µm

between centers of homogenous of mass as quantified by Imaris image analysis. Activated cells, noninfected cells that are influenced by the proinflammatory cytokines released by infected cells, were then classified as noninfected cells that belong to the same 20 µm DBSCAN cellular cluster as at least one infected cell as outlined in chapter 4. Cellular states are reported as a combination of their internal state and spatial state as given by Table 68.

Table 68: Definition of cell states for variable distributions and multivariate classification models.

Cell State	Definition
Control	Cells within the control (no bacteria introduced) condition that are not contained within 20 µm clusters with other control cells as determined by DBSCAN.
Control-Cluster	Cells within the control (no bacteria introduced) condition that are contained within 20 µm clusters with other control cells as determined by DBSCAN.
Noninfected	Cells within the infected (bacteria introduced) condition that are not determined to be infected and not contained within 20 µm clusters with other control cells as determined by DBSCAN.
Noninfected-Cluster	Cells within the infected (bacteria introduced) condition that are not determined to be infected and are contained within 20 µm clusters with other noninfected cells as determined by DBSCAN.
Noninfected-Active	Cells within the infected (bacteria introduced) condition that are not determined to be infected and are contained within 20 µm clusters with at minimum one infected cell as determined by DBSCAN.
Infected	Cells within the infected (bacteria introduced) condition that are determined to be infected and are not contained within 20 µm clusters with other cells as determined by DBSCAN.
Infected-Cluster	Cells within the infected (bacteria introduced) condition that are determined to be infected and are contained within 20 µm clusters with other noninfected or infected cells as determined by DBSCAN.

5.2.6 Statistical Analysis

Statistical analysis for effector molecules was performed in R-Studio [63] utilizing the dplyr, ggplot2 and ggpubr libraries [64]–[66]. Statistical analysis for bacterial load over time is ongoing pending colony forming unit results. The Wilcoxon rank sum test

was used to test for statistical significance. When initial concentrations differed, log2 fold change (Log2FC) was calculated for statistical testing to allow for comparison across experimental conditions as given by equation 9,

$$Log2FC = Log_2\left(\frac{X(t)}{X(0)}\right). \quad (9)$$

5.3 Results

5.3.1 Plasmid Persistence

The *m. Cherry* plasmid in *M. bovis BCG* in the absence of the selective antibiotic was maintained in long-term static culture for 96 hours. No significant differences in colony forming units (CFUs) through differential plating (Figure 50, Table 69). This confirms the persistence of the *m. Cherry* plasmid in long term culture and implies no significant loss of bacterial fluorescence within infection studies that lack the selective hygromycin antibiotic.

Table 69: Plasmid Persistence of mCherry *M. bovis* BCG Differential Plating: Wilcoxon (n=3)

Hour	*Media:+Hygro/Plate:+Hygro CFU/mL*	*Media:-Hygro/Plate:+Hygro CFU/mL*	*p value*
0	1.10E+04	4.27E+04	0.268286
24	1.57E+05	2.33E+05	0.375825
48	1.77E+06	1.43E+06	0.382733
72	1.50E+06	1.57E+06	1
96	1.10E+06	1.27E+06	1
Hour	*Media:+Hygro/Plate:-Hygro CFU/mL*	*Media:-Hygro/Plate:-Hygro CFU/mL*	*p value*
0	1.30E+04	4.77E+04	1
24	1.95E+05	1.50E+05	0.662521
48	2.27E+06	1.80E+06	0.657905
72	1.70E+06	1.95E+06	0.662521
96	1.25E+06	1.55E+06	1

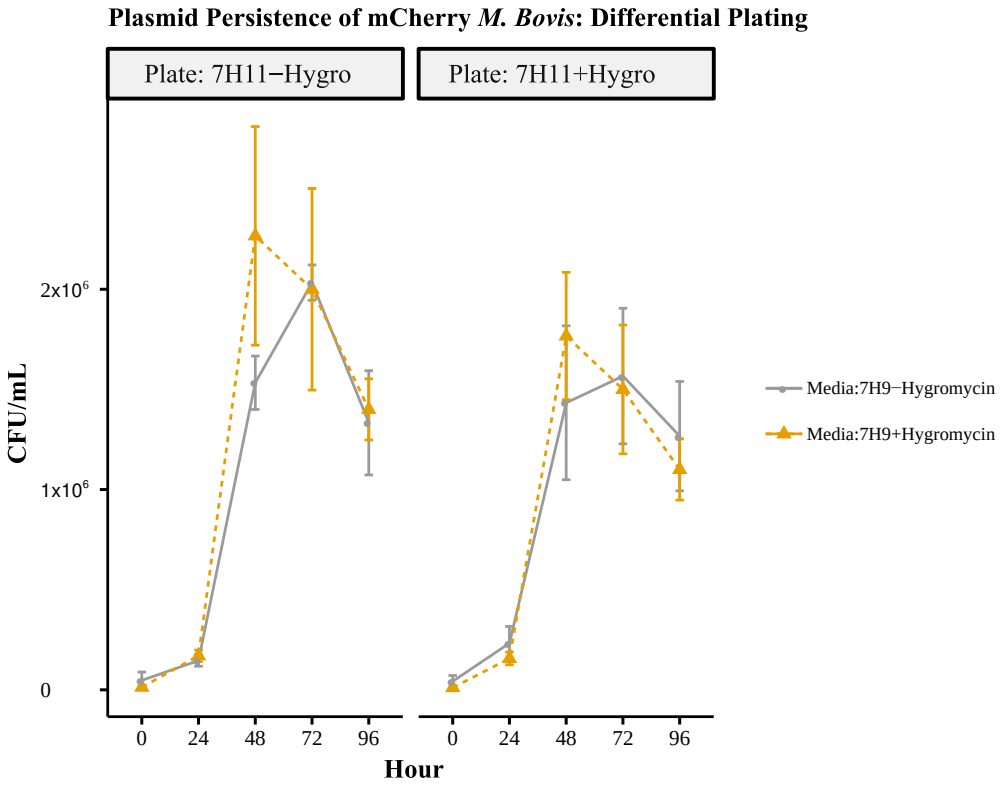

Figure 50: Bacterial growth analysis represented as colony forming units at 0, 24, 48, 72 and 96 hours using differential plating (n=3)

5.3.2 Comparison of infection dynamics *m. Cherry M. bovis BCG* and wild type *M. bovis BCG*

No notable differences were observed in cellular appearance during infection. There was no significantly apparent extracellular growth denoted in mcBCG or BCG infection in the presence of gentamicin quantified through cell culture scope imaging (Figure 51).

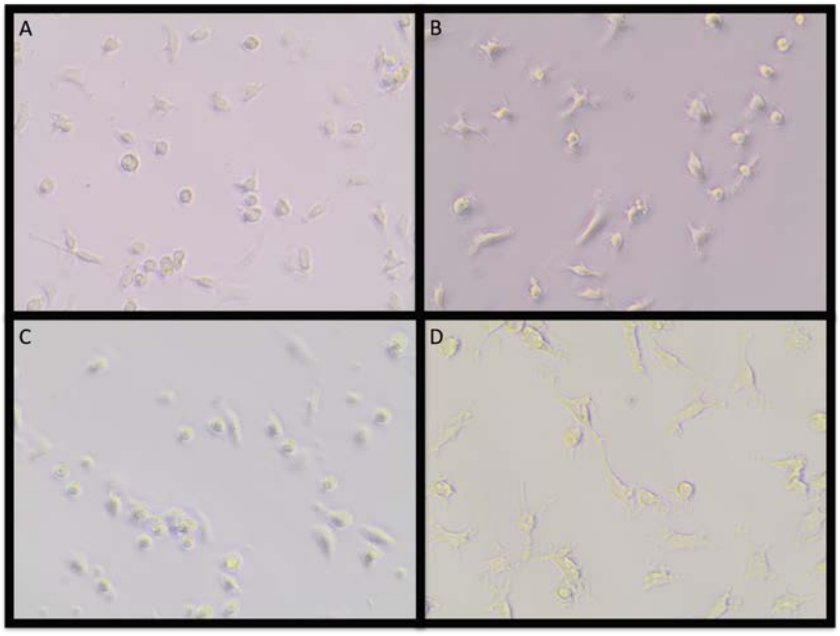

Figure 51: mcBCG comparison to BCG in gfpBMDM with 10 µg/ml gentimicin a) BCG infection at hour 0, B) BCG infection at hour 72, C) mcBCG infection at hour 0 D) mcBCG infection at hour 72

We see no significant difference in infection dynamics between mcBCG and wild type *M. bovis* BCG in gfpBMDM at a MOI 5 (BCG MOI 8.5, mcBCG MOI 17.5) in the presence of 10 µg/mL gentamicin. No significant differences ($p>.05$) are observed between log2FC in CFU concentrations for any of the timepoints. Log2FC was utilized due to different starting MOIs(Table 70, Figure 52).

Table 70: mcBCG vs wild type BCG MOI in gfpBMDM (* third datapoint unavailable for analysis so mean of n=2 was used to generate n=3): Log2FC Wilcoxon (n=3)

Hour	*Condition 1*	*Condition 2*	*p value*
0	mcBCG Intracellular	BCG Intracellular*	-
24	mcBCG Intracellular	BCG Intracellular	0.19043
48	mcBCG Intracellular*	BCG Intracellular	0.080856
72	mcBCG Intracellular	BCG Intracellular	0.382733
96	mcBCG Intracellular	BCG Intracellular	0.080856
0	mcBCG Extracellular	mcBCG Extracellular	-
24	mcBCG Extracellular	mcBCG Extracellular	0.080856
48	mcBCG Extracellular	mcBCG Extracellular	0.662521
72	mcBCG Extracellular	mcBCG Extracellular	1
96	mcBCG Extracellular	mcBCG Extracellular	0.080856

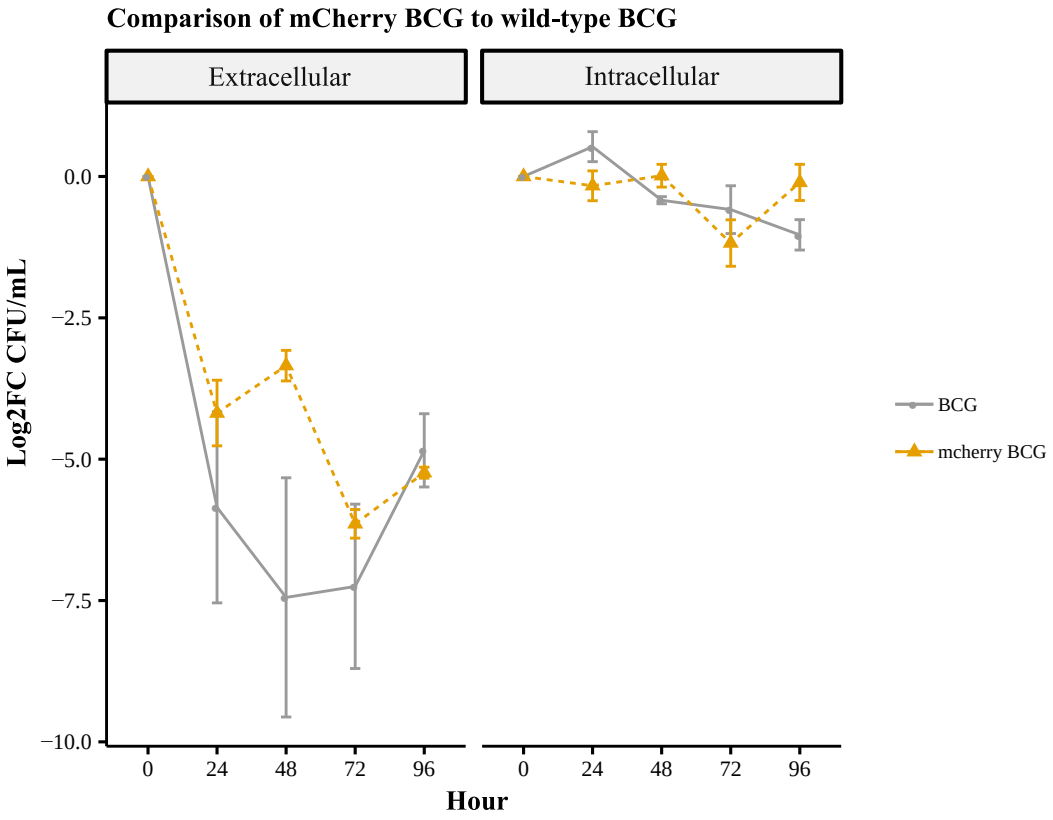

Figure 52: Comparison of infection dynamics of mcBCG (MOI 17.5) and BCG (MOI 8.5) in gfpBMDM in the presence of 10 µg/mL gentamicin. Note log2FC used to different starting MOI. N=3.

5.3.3 Growth Curve of *m. Cherry M. bovis BCG* in gentamicin culture

The growth/death curve of mcBCG in 2D culture in the presence of gentamicin (10 µg/mL) did not produce any quantifiable colonies on agar plates. This is primarily due to the significantly lower (approximately one order of magnitude) CFU/mL in the lower log phase (OD600: .4-.6) of the mcBCG as compared to wild type (Figure 53). Adaptation to this lower bacterial count was accounted for in the 2D mcBCG vs BCG wildtype 2D comparison infection study and 2D/3D *ex vivo* infection study.

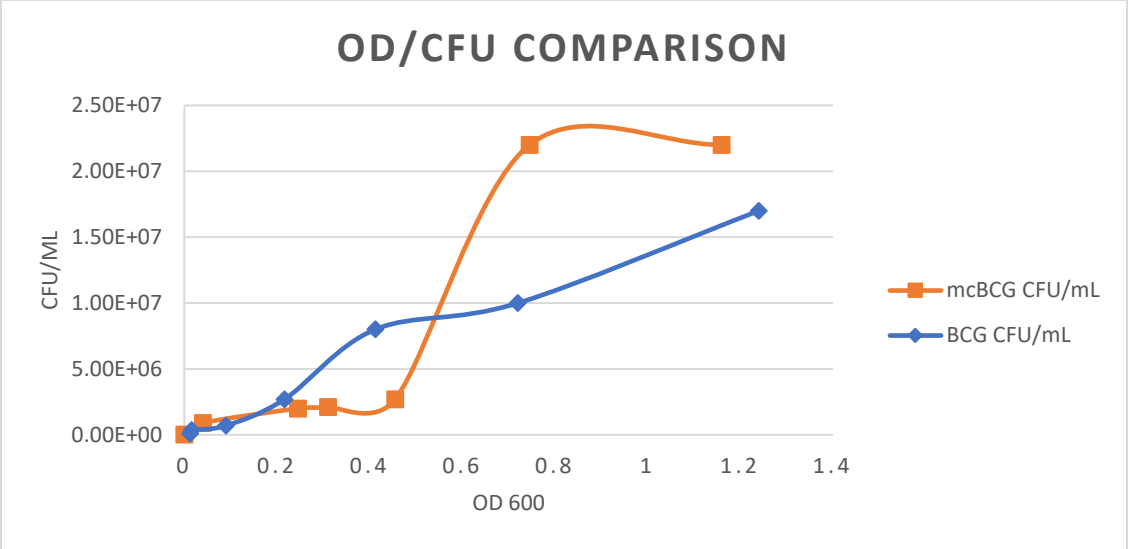

Figure 53: OD/CFU comparison of mcBCG and wild type M. bovis BCG (BCG)

5.3.4 Significant increase in the fold change of nitric oxide expression in 3D infected conditions at 24 hours in culture

Quantification of nitric oxide through Griess assay of the 3D and 2D supernatant show high nitric oxide in 3D infection cultures as compared to the 3D controls, 2D controls and 2D infection, with this difference being significant between 3D infection and 2D infection at 24 hours (Figure 54 A, Table 71). We also see a significantly higher rate of nitric oxide production in 3D infection than 2D infection at 24 hours (Figure 54 B, Table 72). Most notably, in comparison to the 2D/3D investigation of *Mycobacterium smegmatis* (mSmeg) infection, where we noted no noticeable trends in nitric oxide expression, we now see trends in both nitric oxide expression and the rate of nitric oxide expression. We notice that the while 3D infection has a noticeably higher nitric oxide production than its controls, the nitric oxide in 2D infection and controls follows very comparable trends over time. In the rate of production, we now see that the 3D control and infection have comparable rates of expression overtime as well as 2D

control and infection. This demonstrates the impact that the environment has on the expression of nitric oxide more clearly than the mSmeg studies.

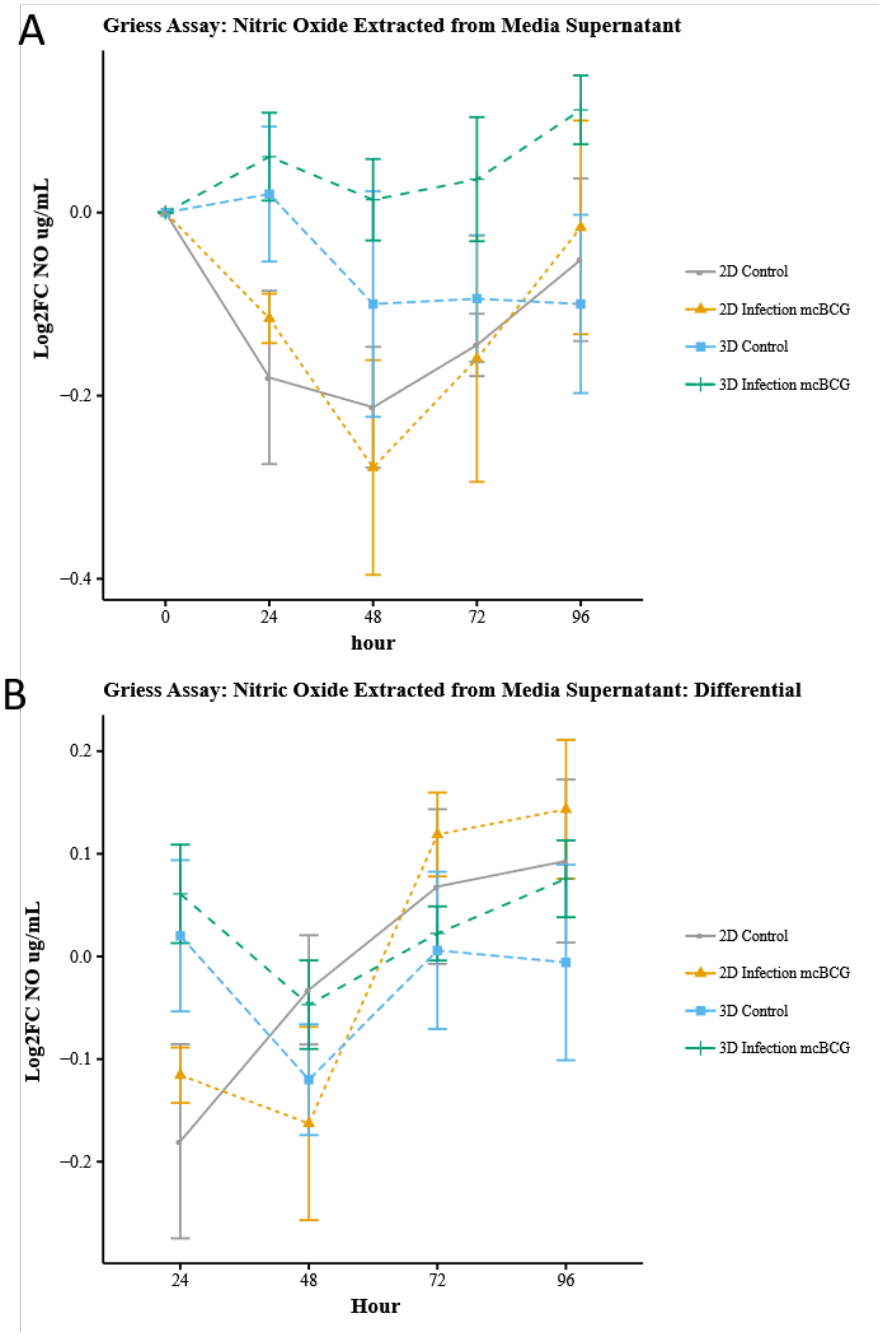

Figure 54: NO assay results (log2FC of griess assay signal) : a) no significant difference between any conditions b) no significant difference between any conditions in rate of change – Wilcoxon N=4

Table 71: Griess Assay-Nitric Oxide Extracted from Media Supernatant 2D vs. 3D: Log2FC Wilcoxon (n=4)

Hour	*2D: Control*	*3D: Control*	*p value*
0	0.00	0.00	-
24	-0.18	0.02	0.312321
48	-0.21	-0.10	0.885234
72	-0.14	-0.09	0.665006
96	-0.05	-0.10	1
Hour	*2D: Infection*	*3D: Infection*	*p value*
0	0.00	0.00	-
24	-0.12	0.06	0.030383
48	-0.28	0.01	0.193931
72	-0.16	0.04	0.193931
96	-0.02	0.11	0.470486

Table 72: Griess Assay-Rate of Nitric Oxide (differentials) Extracted from Media Supernatant 2D vs. 3D: Log2FC Wilcoxon (n=4)

Hour	*2D: Control*	*3D: Control*	*p value*
24	-0.18	0.02	0.312321422
48	-0.03	-0.12	0.312321422
72	0.07	0.01	1
96	0.09	-0.01	0.470486422
Hour	*2D: Infection*	*3D: Infection*	*p value*
24	-0.12	0.06	0.030382822
48	-0.16	-0.05	0.312321422
72	0.12	0.02	0.112351198
96	0.14	0.08	0.470486422

5.3.5 Necrotic cell death is downregulated during 3D infection as compared to 2D

Results of the LDH assay show a consistent increase in cell death due to necrosis over time consistent with qualitative imaging observations (Figure 55 A). 2D and 3D control cells do not have a significantly different fold change increase in LDH levels over the course of the 96-hour culture. At 48 and 72 hours, 3D infected cells have a significantly higher LDH expression than 2D infected cells ($p<.05$) (Figure 55 A, Table 73).

We do not see any significant difference between 3D control and 3D infection LDH expression at any timepoint analyzed, but we do see significant increase in LDH expression in 2D infection as compared to 2D control at 24 hours (Figure 55 A, Table 74).

Table 73: LDH Extracted from Media Supernatant 2D vs. 3D: Log2FC Wilcoxon (n=4)

Hour	*2D: Control*	*3D: Control*	*p value*
0	0.00	0.00	-
24	1.60	1.34	1
48	1.82	1.74	1
72	1.94	2.07	0.665006
96	1.99	2.21	0.470486
Hour	*2D: Infection*	*3D: Infection*	*p value*
0	0.00	0.00	-
24	2.09	1.65	0.112351
48	1.75	2.08	0.030383
72	1.73	2.28	0.030383
96	2.10	2.44	0.112351

Table 74: LDH Extracted from Media Supernatant Control vs. Infected: Log2FC Wilcoxon (n=4)

Hour	*2D: Control*	*2D: Infection*	*p value*
0	0.00	0.00	-
24	1.60	2.09	0.030383
48	1.82	1.75	0.885234
72	1.94	1.73	0.665006
96	1.99	2.10	0.665006
Hour	*3D: Control*	*3D: Infection*	*p value*
0	0.00	0.00	-
24	1.34	1.65	0.885234
48	1.74	2.08	0.665006
72	2.07	2.28	0.112351
96	2.21	2.44	0.193931

Investigation of the LDH rate of change (differentials) calculated as the change in LDH expression between the timepoint of collection, and the previous timepoint of

sample collection, shows consistent LDH expression between 2D and 3D controls as well as 2D and 3D infection except at 48 hours, where the rate of LDH expression is significantly higher in 3D (Figure 55 B, Table 75Table 74). There is no significant difference in rate of LDH expression between 3D control and infection, but we do see a significant difference in the rate of LDH expression between 2D control and infection at 24 and 48 hours 3D (Figure 55 B, Table 76, Table 74).

Table 75: Differentials-LDH Extracted from Media Supernatant 2D vs. 3D: Log2FC Wilcoxon (n=4)

Hour	*2D: Control*	*3D: Control*	*p value*
24	1.60	1.34	1
48	0.23	0.41	0.665006
72	0.12	0.33	0.885234
96	0.05	0.14	0.470486
Hour	*2D: Infection*	*3D: Infection*	*p value*
24	2.09	1.65	0.112351
48	-0.35	0.43	0.030383
72	-0.02	0.20	0.030383
96	0.37	0.16	0.060602

Table 76: Differentials-LDH Extracted from Media Supernatant Control vs. Infected: Log2FC Wilcoxon (n=4)

Hour	*2D: Control*	*2D: Infection*	*p value*
24	1.60	2.09	0.030383
48	0.23	-0.35	0.885234
72	0.12	-0.02	0.665006
96	0.05	0.37	0.665006
Hour	*3D: Control*	*3D: Infection*	*p value*
24	1.34	1.65	0.885234
48	0.41	0.43	0.665006
72	0.33	0.20	0.112351
96	0.14	0.16	0.193931

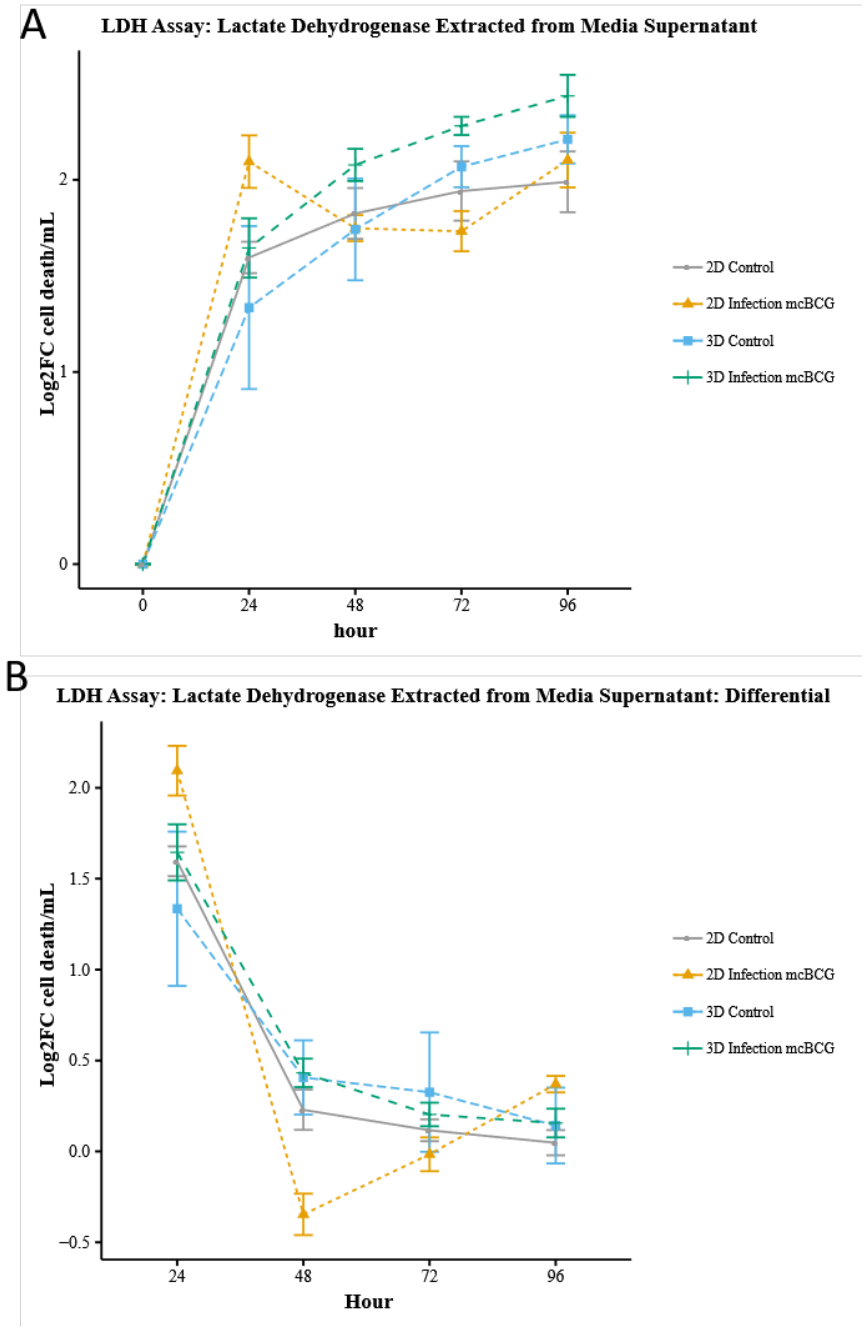

Figure 55: Log2FC of LDH signal (cell death) A) LDH assay results, significant difference between 2D and 3D infection at 24 and 48 hours. B) LDH Differential results, significant difference between 2D control and 2D infection at 24 hours, Wilcoxon (n=4)

5.3.6 Comparison of mCherry *M. bovis* BCG bacterial load in 2D vs 3D

We note that through fluorescent confocal imaging observations that there exists a higher-level extracellular bacterium in the 3D infection condition as compared to 2D (Figure 56). These bacterial aggregates in the extracellular matrix are in the presence of faint GFP signals indicating potential early cell death in the system that may have occurred prior to image quantification releasing the bacterium from the lysed cells into the extracellular matrix. Current extraction methods are unable to isolate 3D extracellular bacterium from intracellular for agar plate quantification of bacterial growth, so the quantification of the totallcellular bacterial load is represented for 3D, and the intracellular and extracellular load is aggregated to represent 2D totalcellular bacterial load.

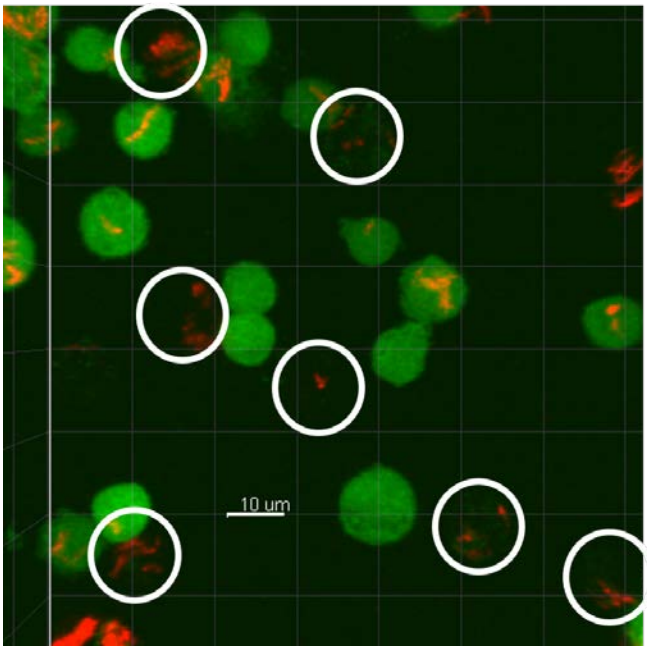

Figure 56: mcBCG infection in the 3D environment at hour 0 of imaging. Closer inspection details dead cells (apparent from faint GFP signals). Dead cells with bacterium are circled for clarity.

In 2D, in the absence of significant levels of extracellular bacteria, we see very little phagocytosis of extracellular bacteria. However, there is evidence of cell death, presumably apoptosis due to significant membrane blebbing [119] (Figure 57 B,C) of infected cells and subsequent phagocytosis of cell debris and BCG (Figure 57 E,F).

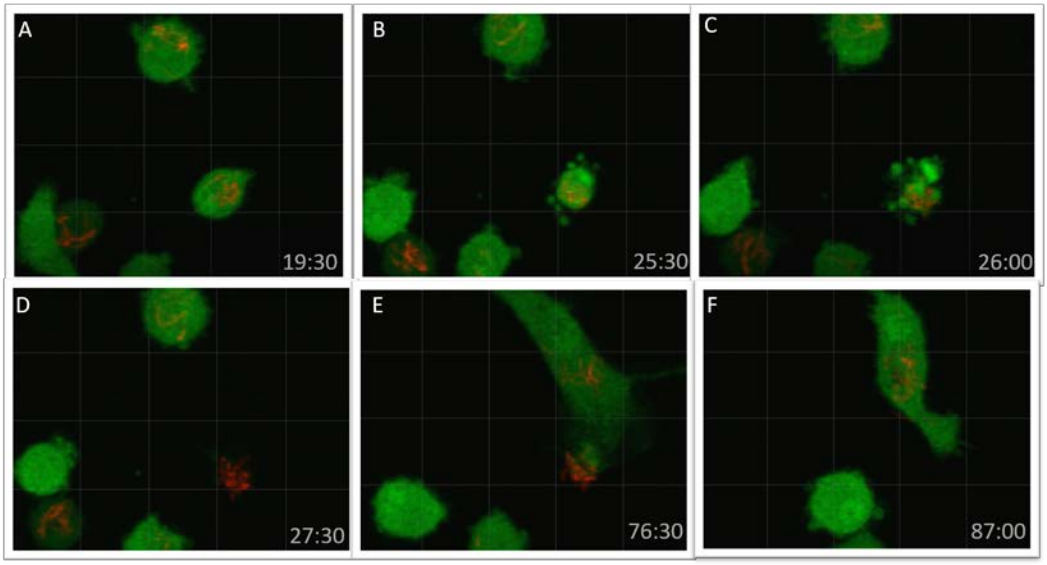

Figure 57: Apoptosis of infected cell followed by phagocytosis. A) 19.5 hours under infection B) 25.5 hours under infection, C) 26 hours under infection, D) 27.5 hours under infection, E) 76.5 hours under infection, F) 87 hours under infection.

We see an increase concentration of bacteria in the 3D environment as opposed to 2D at the end of the 96 hours of infection, with the difference in the Log2FC of bacterial concentration from timepoint zero (which contains the same MOI-ratios of bacteria to macrophage-in both 2D and 3D) at 48 and 96 hours (Figure 58 A, Table 77). Most notable however, is the rate in change of bacteria, as we see a consistent decrease in bacteria in the 2D environment after 48 hours in culture, however in 3D there is an increase in bacteria followed by a levelling off of bacteria at 96 hours, this is denoted by

the significant differences in the rate of change of bacterial concentrations at 48 and 72 hours (Figure 58 B, Table 78).

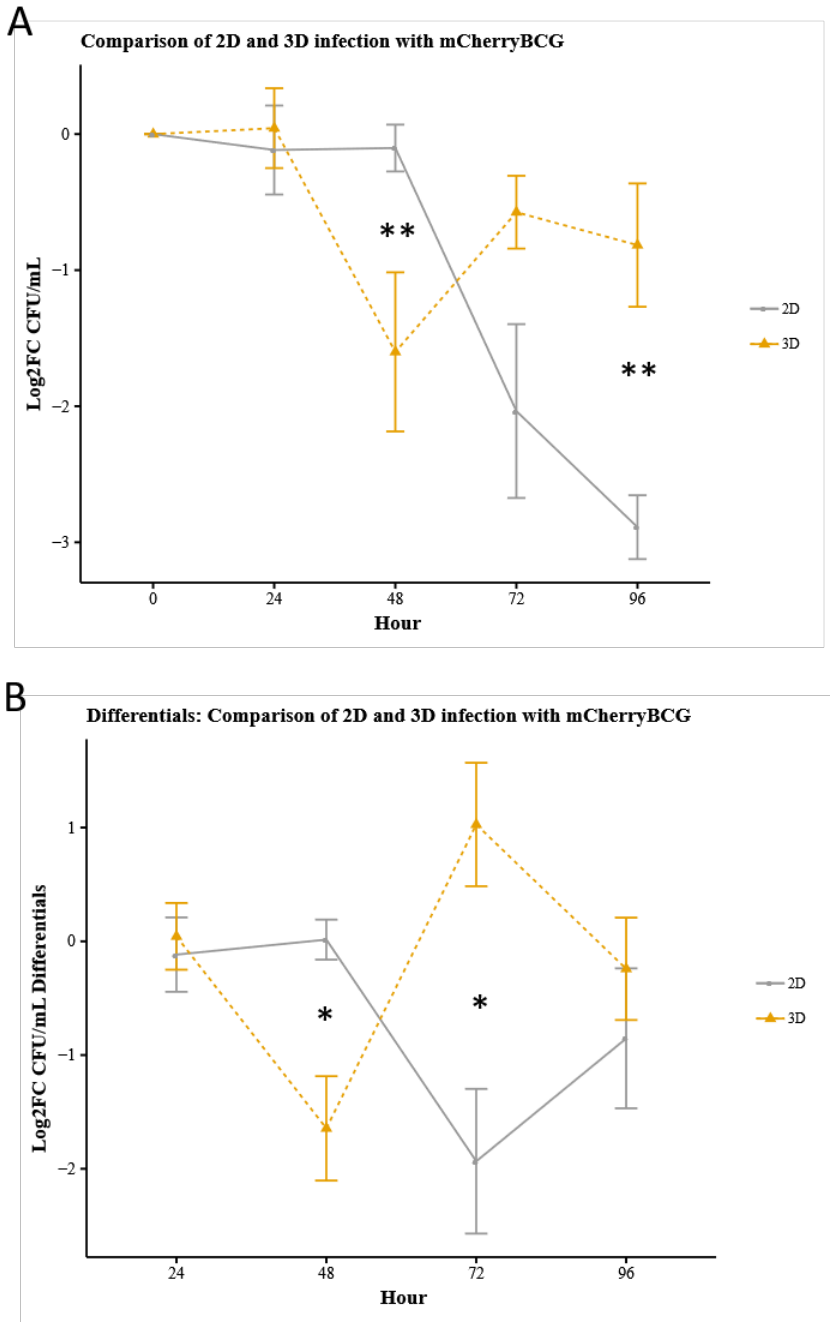

Figure 58: Total bacterial load over time for 2D and 3D infection study with mcBCG, A) total Log2FC CFU/mL B) differentials (rate of change of bacterial load Log2FC) ** p<.01, *p<.05

Table 77: mcBCG gfpBMDM infection in 2D and 3D Log2FC CFU/mL Total- Wilcoxon (n=4)

Hour	*2D Total log2FC CFU/mL*	*3D Total log2FC CFU/mL*	*p value*
0	0	0	-
24	-0.11709	0.043473	0.872559
48	-0.10251	-1.60071	0.004772
72	-2.03581	-0.57398	0.378478
96	-2.88897	-0.81588	0.004772

Table 78: Differential: mcBCG gfpBMDM infection in 2D and 3D Log2FC CFU/mL Total- Wilcoxon (n=4)

Hour	*2D Total log2FC CFU/mL*	*3D Total log2FC CFU/mL*	*p value*
24	-0.11709	0.043473	0.885234
48	0.014585	-1.64419	0.030383
72	-1.9333	1.026729	0.030383
96	-0.85316	-0.24189	0.885234

5.3.7 Image analysis of cell dynamics under BCG infection

Surface quantification and tracking analysis of confocal images utilizing Imaris yielded 36 cell features, and 20 field features over 90 hours of imaging. The constitutive expression of actin-GFP in the BMDMs allows visualization of macrophages in both the control and infected conditions, and mCherry expression in BCG allowed visualization of the bacterium extracellularly and intracellularly. Cells in the 3D infection demonstrated higher observable levels of aggregation as compared to 2D infection with BCG (Figure 59, Figure 60).

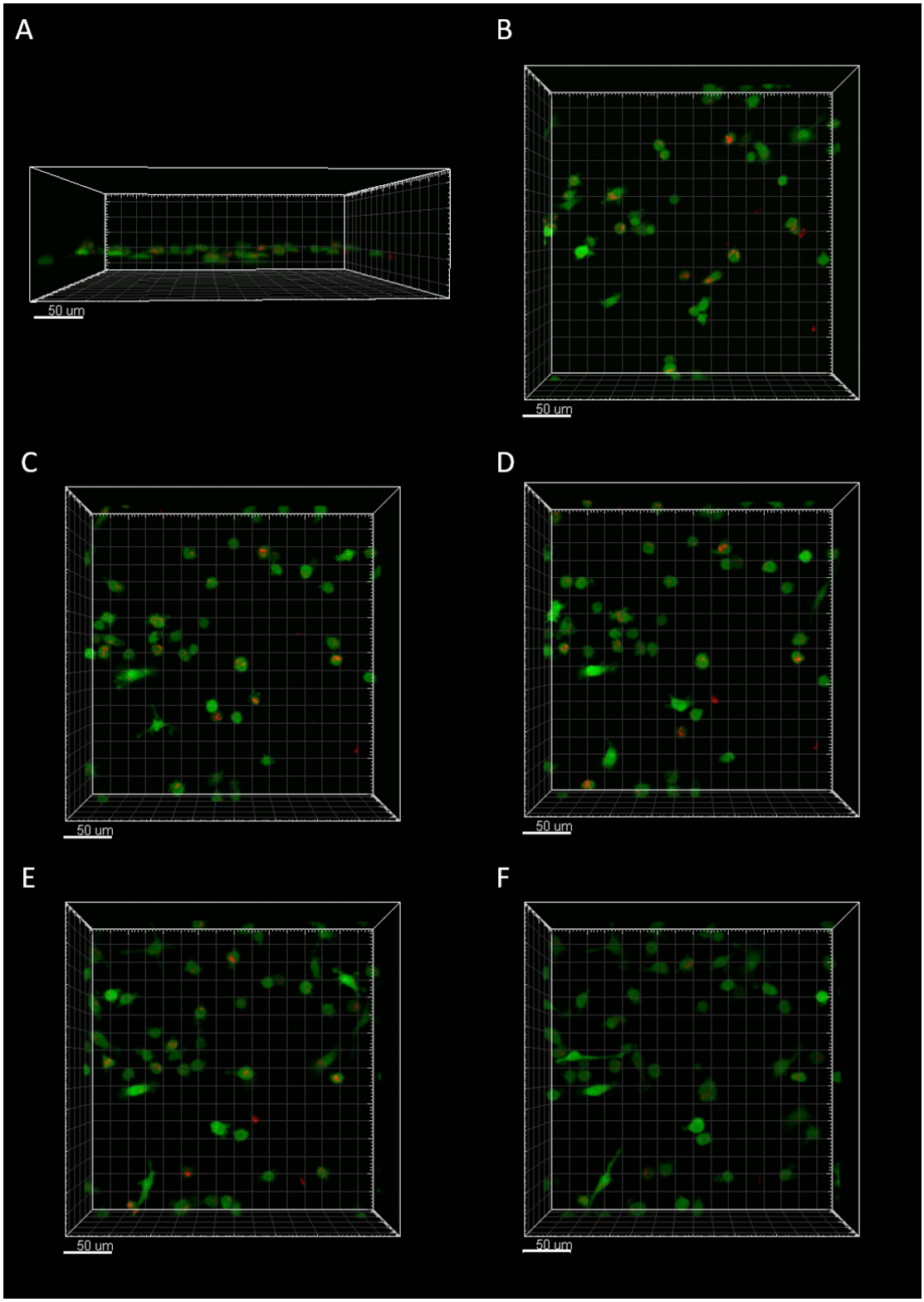

Figure 59: mcBCG Infection in 2D. Confocal image rendered in Imaris A) side view 0 hr B) 0 hr top view, C) 24 hr top view, D) 48 hr top view, E) 72 hr top view, F) 90 hr top view. Scale bar 50 µm.

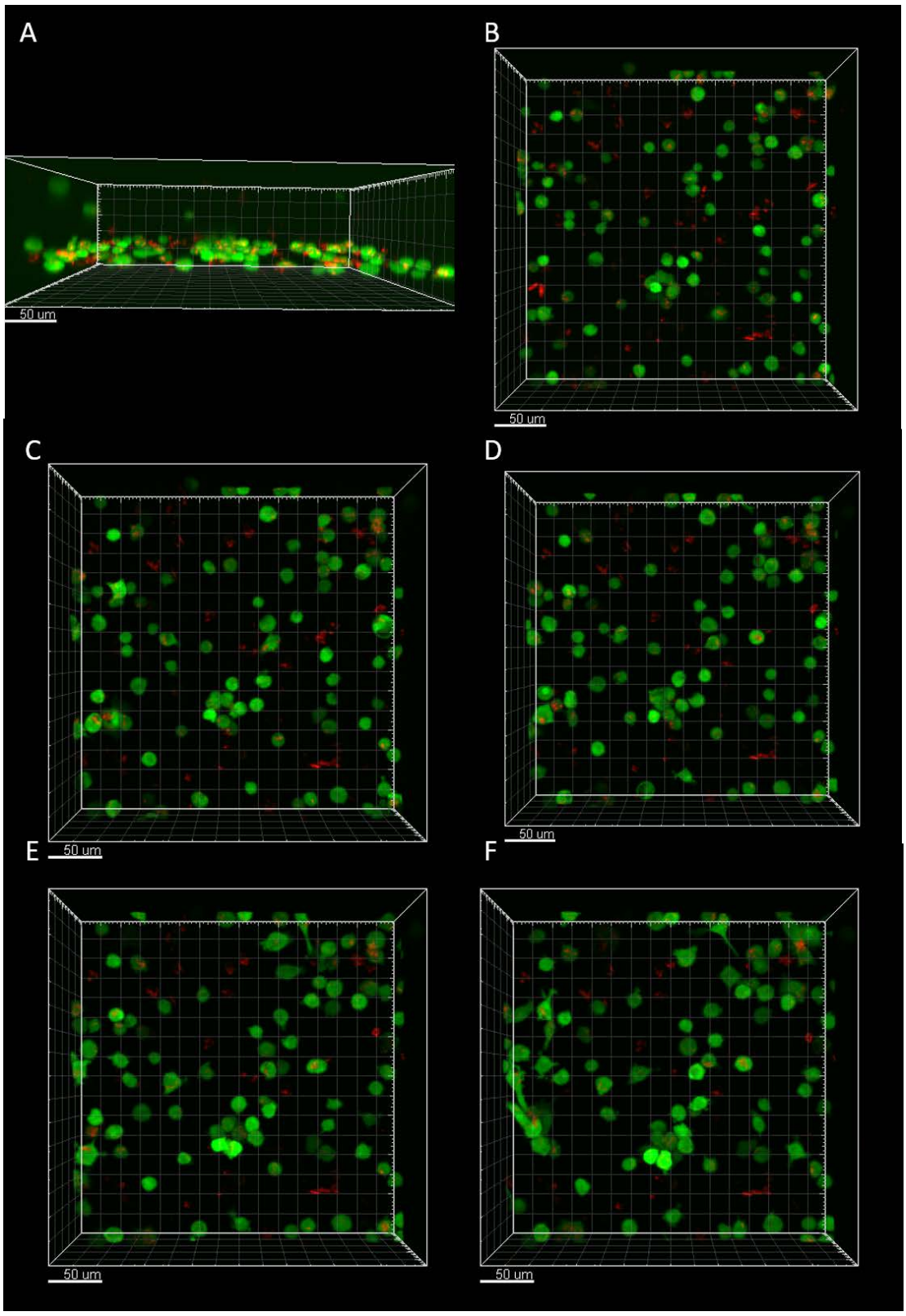

Figure 60: mcBCG Infection in 3D. Confocal image rendered in Imaris A) side view 0 hr B) 0 hr top view, C) 24 hr top view, D) 48 hr top view, E) 72 hr top view, F) 90 hr top view. Scale bar 50 µm.

We also observe an increase of cells to the areas of initial cellular aggregation around the mcBCG infection in the 3D condition over the course of time. Observation of confocal time-lapse imaging does not show an observable increase of cellular aggregation in the 2D mcBCG infected condition over the course of time (Figure 61).

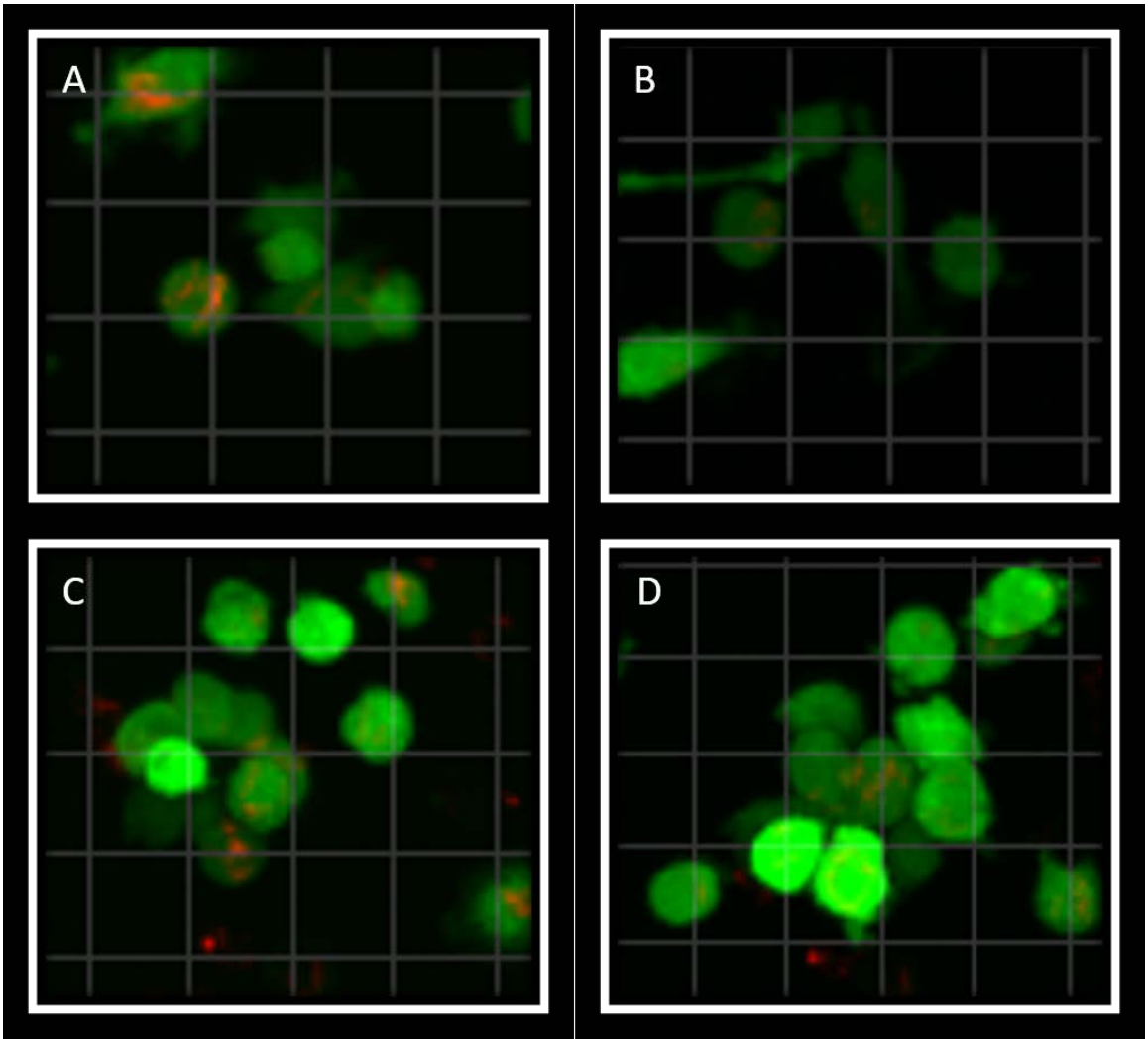

Figure 61: Imaris rendering of mcBCG infection demonstrating cellular aggregation around infected cells over time in A) 2D mcBCG infection 0 hr B) 2D mcBCG infection 90 hr C) 3D mcBCG infection 0hr D) 3D mcBCG infection 90 hr

5.3.7.1 Cell speed

In 2D, the average speed of non-infected cells in the control condition (6.26E-4 µm/s) is significantly higher (p<.0001) than 2D infected cells (3.85E-4 µm/s). In 3D, no significant difference is seen between cellular speed in control and infected (Figure 62 A, Table 79).

Table 79: Average Individual Cell Speed Over All Time: Wilcoxon

Condition 1	*Speed µm/s*	*Condition 2*	*Speed µm/s*	*p value*
2D Control	6.26E-04	3D Control	3.85E-04	4.58E-18
2D Infection	4.22E-04	3D Infection	3.67E-04	1.53E-26
2D Control	6.26E-04	2D Infection	4.22E-04	1.14E-13
3D Control	3.85E-04	3D Infection	3.67E-04	0.10384

The fold changes between the means of the individual cell speeds is highest between the 2D and 3D controls, with 2D controls having the highest overall cell speed, but the smallest fold change is seen between the 2D and 3D infection conditions (Table 80). Analysis of the trends in average cellular speed over the time-course of imaging show that control cells in 2D and 3D have a generalized decrease in cellular speed overtime, whereas cellular speed in 2D and 3D infection increases over time. At all hour ranges, control cells have a significantly different cellular speed than their infected counterparts. There is no significant difference in 2D and 3D control cell speed, or 2D and 3D infection cells after the 24-48 hour range (Table 81, Table 82, Figure 62 B) .

Table 80:	Average Individual Cell Speed Over All Time: Log2 Fold Change of Means	
Condition 1	Condition 2	Log2 Fold Change (Cond 1/ Cond 2)
2D Control	3D Control	0.70036
2D Infection	3D Infection	0.06072
2D Control	2D Infection	0.56825
3D Control	3D Infection	0.18709

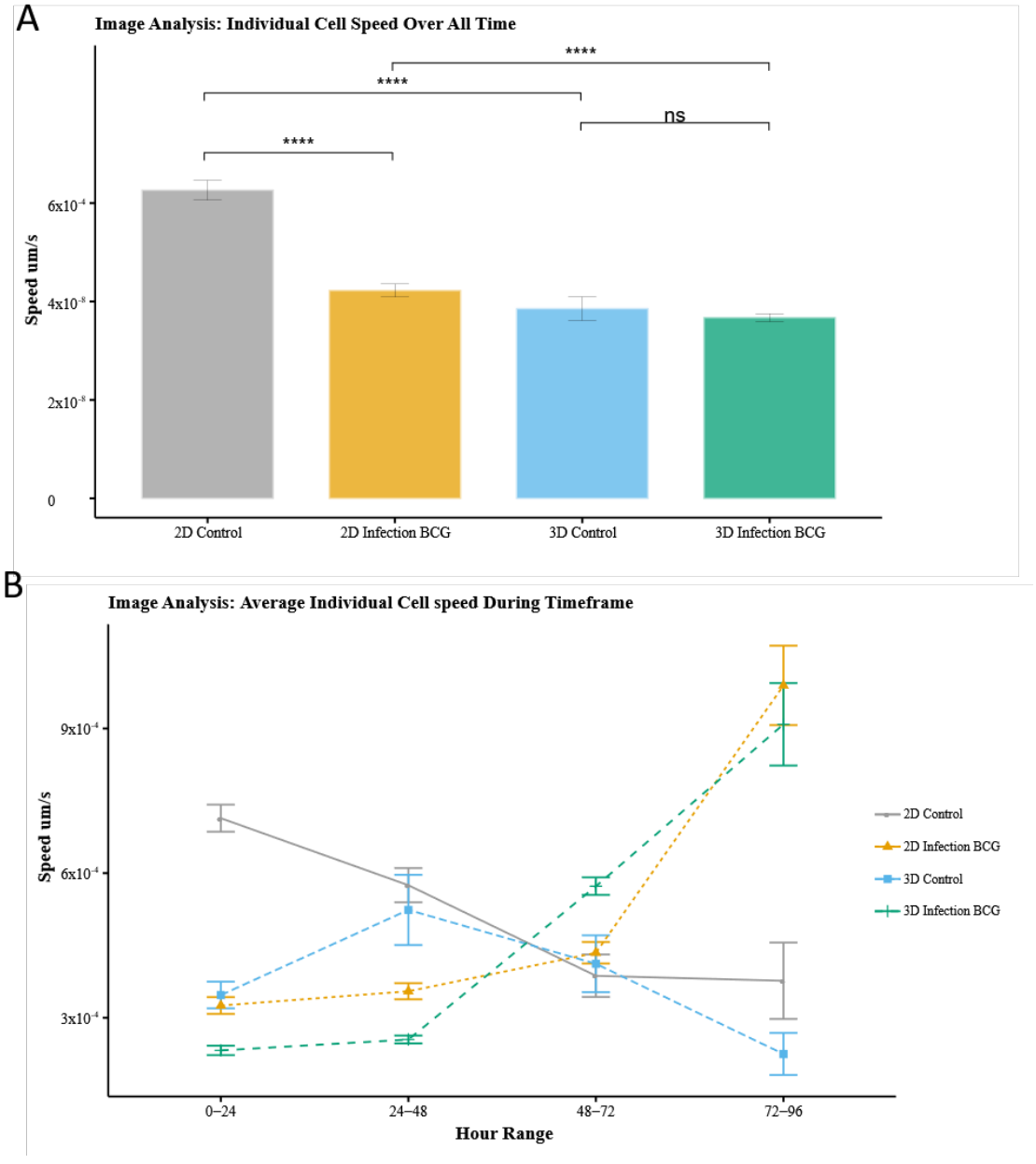

Figure 62: Image analysis of individual cell speed of gfpBMDM infected with mCherry M.bovis in 2D and 3D culture conditions over 72 hours. A) Averaged over all time B) Averaged based on hour range. (ns- No significant difference, * - p<.05, **-p<.01,***-p<.001,****-p<.0001)

Table 81: Average Individual Cell Speed 2D vs. 3D Over Time (timeframes): Wilcoxon

Hour Range	*Condition 1*	*Speed µm/s*	*Condition 2*	*Speed µm/s*	*p value*
0-24	2D Control	7.14E-04	3D Control	3.47E-04	3.26E-21
24-48	2D Control	5.75E-04	3D Control	5.24E-04	4.06E-02
48-72	2D Control	3.87E-04	3D Control	4.12E-04	9.65E-01
72-96	2D Control	3.77E-04	3D Control	2.25E-04	6.10E-02
0-24	2D Infection	3.26E-04	3D Infection	2.32E-04	9.86E-20
24-48	2D Infection	3.55E-04	3D Infection	2.55E-04	9.09E-14
48-72	2D Infection	4.35E-04	3D Infection	5.73E-04	5.87E-01
72-96	2D Infection	9.89E-04	3D Infection	9.09E-04	5.43E-01

Table 82: Average Individual Cell Speed Control vs. Infected Over Time (timeframes): Wilcoxon

Hour Range	*Condition 1*	*Speed µm/s*	*Condition 2*	*Speed µm/s*	*p value*
0-24	2D Control	7.14E-04	2D Infection	3.26E-04	1.01E-25
24-48	2D Control	5.75E-04	2D Infection	3.55E-04	2.44E-05
48-72	2D Control	3.87E-04	2D Infection	4.35E-04	2.27E-03
72-96	2D Control	3.77E-04	2D Infection	9.89E-04	3.87E-05
0-24	3D Control	3.47E-04	3D Infection	2.32E-04	1.44E-11
24-48	3D Control	5.24E-04	3D Infection	2.55E-04	1.13E-02
48-72	3D Control	4.12E-04	3D Infection	5.73E-04	3.87E-02
72-96	3D Control	2.25E-04	3D Infection	9.09E-04	9.70E-07

5.3.7.2 Cell acceleration

In 2D, the average acceleration of non-infected cells in control cells (4.67E-8 µm/s^2) is not significantly different from 2D infected cells (4.06E-8 µm/s^2). In 3D, there is minor significance in overall acceleration 3D infected (3.05E-8 µm/s^2) cells is significantly higher ($p<.05$) than 3D controls (3.3E-8 µm/s^2) (Table 83). The fold change of differences between control and infected within the 2D and 3D conditions is less than that observed

with average cellular speed, but the foldchange between 2D and 3D controls remains the largest (Table 84,Figure 63 A).

Table 83: Average Individual Cell Acceleration Over All Time: Wilcoxon

Condition 1	*Acceleration µm/s²*	*Condition 2*	*Acceleration µm/s²*	*p value*
2D Control	4.67E-08	3D Control	3.30E-08	3.77E-09
2D Infection	4.06E-08	3D Infection	3.50E-08	1.15E-24
2D Control	4.67E-08	2D Infection	4.06E-08	0.185211
3D Control	3.30E-08	3D Infection	3.50E-08	0.012005

In general, there is an increase in cellular acceleration over time in 2D infection but a decrease in 2D controls. 3D control cells show a relatively consistent acceleration over time, whereas 3D infected cells increase in average acceleration until the 72-96 hour range at which point cellular acceleration decreases. Comparable to the observed average cell speed, cell acceleration in 2D and 3D infection cells are not significantly different after the 24-48 hour range (Figure 63 B, Table 85, Table 86).

Table 84: Average Individual Cell Acceleration Over All Time: Log2 Fold Change of Means

Condition 1	Condition 2	Log2 Fold Change (Cond 1/ Cond 2)
2D Control	3D Control	0.15073
2D Infection	3D Infection	0.06479
2D Control	2D Infection	0.06142
3D Control	3D Infection	-0.024518

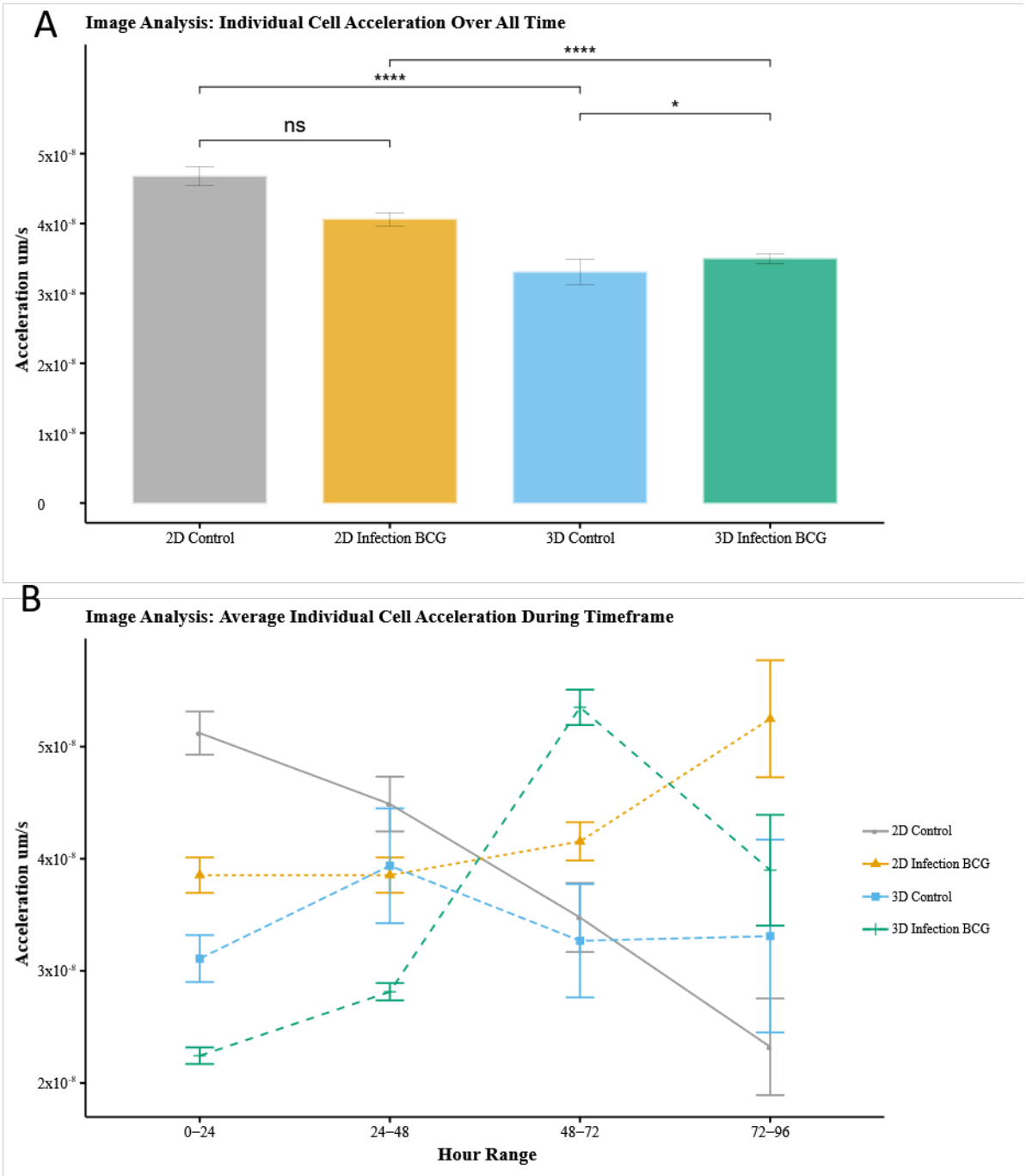

Figure 63: Image analysis of individual cell acceleration of gfpBMDM infected with mCherry M. bovis BCG in 2D and 3D culture conditions over 72 hours. A) Averaged over all time B) Averaged based on hour range.

Table 85: Average Individual Cell Acceleration 2D vs. 3D Over Time (timeframes): Wilcoxon

Hour Range	*Condition 1*	*Acceleration µm/s²*	*Condition 2*	*Acceleration µm/s²*	*p value*
0-24	2D Control	5.12E-08	3D Control	3.11E-08	1.83E-09
24-48	2D Control	4.49E-08	3D Control	3.94E-08	0.075398
48-72	2D Control	3.48E-08	3D Control	3.27E-08	0.255789
72-96	2D Control	2.32E-08	3D Control	3.31E-08	0.630538
0-24	2D Infection	3.85E-08	3D Infection	2.24E-08	1.54E-32
24-48	2D Infection	3.85E-08	3D Infection	2.81E-08	7.00E-12
48-72	2D Infection	4.16E-08	3D Infection	5.35E-08	0.940148
72-96	2D Infection	5.25E-08	3D Infection	3.90E-08	0.110817

Table 86: Average Cell Acceleration Control vs. Infected Over Time (timeframes): Wilcoxon

Hour Range	*Condition 1*	*Acceleration µm/s²*	*Condition 2*	*Acceleration µm/s²*	*p value*
0-24	2D Control	5.12E-08	2D Infection	3.85E-08	0.001602
24-48	2D Control	4.49E-08	2D Infection	3.85E-08	0.644932
48-72	2D Control	3.48E-08	2D Infection	4.16E-08	0.005008
72-96	2D Control	2.32E-08	2D Infection	5.25E-08	0.048555
0-24	3D Control	3.11E-08	3D Infection	2.24E-08	0.016983
24-48	3D Control	3.94E-08	3D Infection	2.81E-08	0.290533
48-72	3D Control	3.27E-08	3D Infection	5.35E-08	0.00136
72-96	3D Control	3.31E-08	3D Infection	3.90E-08	0.900902

5.3.7.3 Cell directedness

In both 2D and 3D conditions the overall average directedness of non-infected cells in the control condition is significantly higher ($p<.0001$) than cells in the infected condition (Table 87, Table 88, Figure 64 A).

Table 87: Average Individual Cell Directedness Over All Time: Log2 Fold Change of Means

Condition 1	Condition 2	Log2 Fold Change (Cond 1/ Cond 2)
2D Control	3D Control	0.28987
2D Infection	3D Infection	0.24508
2D Control	2D Infection	0.70101
3D Control	3D Infection	0.24508

The directedness of 2D cells for up to the 48-72 hour range is significantly higher than all other conditions (Figure 64 B, Table 89). Over time, in the control conditions, there is a decrease in average cell directedness as cells have accumulated more movement over time. For both 2D and 3D infected conditions there is an increase in directedness during the 72-96 hour range. There is significant differences between 2D and 3D control directedness at all timepoints, but 2D and 3D infected cell directedness is significantly different only in the 0-24 and 72-96 hour range (Figure 64 B,Table 90).

Table 88: Average Individual Cell Directedness Over All Time: Wilcoxon

Condition 1	*Directedness*	*Condition 2*	*Directedness*	*p value*
2D Control	0.26241	3D Control	0.214645	1.28E-06
2D Infection	0.161419	3D Infection	0.136201	2.64E-06
2D Control	0.26241	2D Infection	0.161419	1.55E-42
3D Control	0.214645	3D Infection	0.136201	4.52E-17

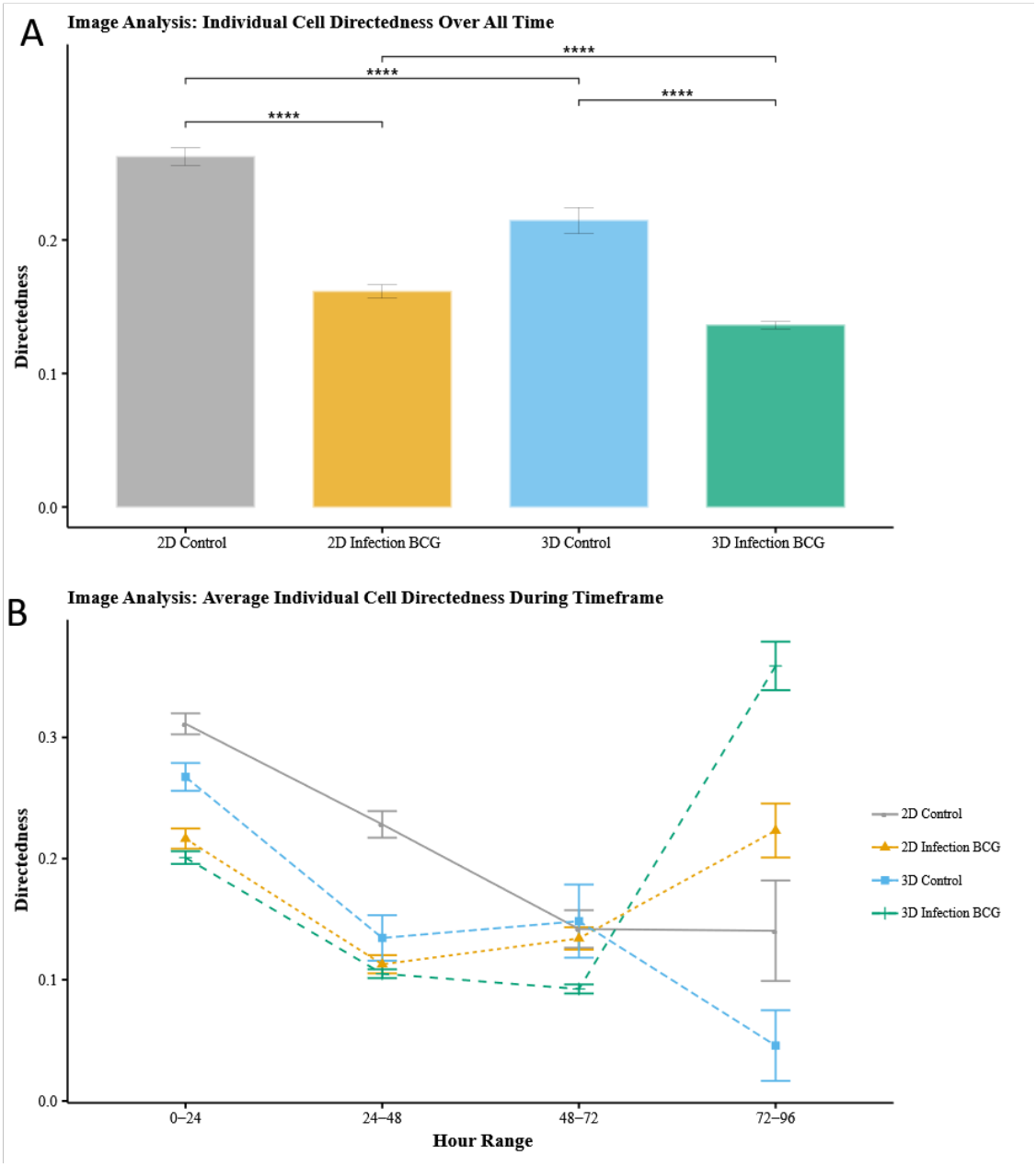

Figure 64: Image analysis of individual cell volume of gfpBMDM infected with mcBCG in 2D and 3D culture conditions over 72 hours. A) Averaged over all time B) Averaged based on hour range. (ns- No significant difference, * - p<.05, **-p<.01,***-p<.001,****-p<.0001)

Table 89: Average Individual Cell Directedness 2D vs. 3D Over Time (timeframes): Wilcoxon

Hour Range	Condition 1	Directedness	Condition 2	Directedness	p value
0-24	2D Control	0.311274	3D Control	0.267461	0.004908
24-48	2D Control	0.228272	3D Control	0.134572	1.43E-07
48-72	2D Control	0.141963	3D Control	0.148428	0.049645
72-96	2D Control	0.140518	3D Control	0.045754	0.000135
0-24	2D Infection	0.216482	3D Infection	0.200846	0.00094
24-48	2D Infection	0.112856	3D Infection	0.105043	0.622024
48-72	2D Infection	0.134192	3D Infection	0.092453	0.107092
72-96	2D Infection	0.223202	3D Infection	0.359013	7.94E-07

Table 90: Average Cell Directedness Control vs. Infected Over Time (timeframes): Wilcoxon

Hour Range	Condition 1	Directedness	Condition 2	Directedness	p value
0-24	2D Control	0.311274	2D Infection	0.216482	6.71E-14
24-48	2D Control	0.228272	2D Infection	0.112856	2.06E-25
48-72	2D Control	0.141963	2D Infection	0.134192	0.227679
72-96	2D Control	0.140518	2D Infection	0.223202	0.005064
0-24	3D Control	0.267461	3D Infection	0.200846	4.76E-11
24-48	3D Control	0.134572	3D Infection	0.105043	0.260161
48-72	3D Control	0.148428	3D Infection	0.092453	0.212489
72-96	3D Control	0.045754	3D Infection	0.359013	4.41E-09

5.3.7.4 Cell volume

In both 2D and 3D conditions the overall average cell volume of cells in the infected condition is significantly higher ($p<.0001$) than cells in the control. The fold change of differences between control and infected within the 2D condition is less than that observed in 3D (Table 91, Table 92, Figure 65 A).

Table 91: Average Individual Cell Volume Over All Time: Log2 Fold Change of Means

Condition 1	Condition 2	Log2 Fold Change (Cond 1/ Cond 2)
2D Control	3D Control	0.852778
2D Infection	3D Infection	-0.06159
2D Control	2D Infection	-0.68567
3D Control	3D Infection	-1.60004

Over the time-span of imaging there is a marked difference in cellular volume between control and infected cells within their respective conditions. Unlike in previous investigations of mSmeg we note more comparable levels of cellular volume in 2D infection as compared to 3D infection with the increase in 3D infection cell volume overall time compared to 2D infection is significant at $p<.05$ (Table 91, Table 92, Figure 65 A). We observe that the 3D infected cell volume on average increases over the course of infection, being significantly higher than 2D infection after the 24-48 hour range. This matches image observations of increased bacterial load relative to 2D (Table 93, Table 92, Figure 65 B).Over the time course of infection and image analysis we The infected cells maintain a significantly higher cell volume over time than their control counterparts. (Table 94, Table 92, Figure 65 B).

Table 92: Average Individual Cell Volume Over All Time: Wilcoxon

Condition 1	*Volume µm³*	*Condition 2*	*Volume µm³*	*p value*
2D Control	1.12E+03	3D Control	6.21E+02	2.39E-89
2D Infection	1.80E+03	3D Infection	1.88E+03	0.026679
2D Control	1.12E+03	2D Infection	1.80E+03	7.24E-129
3D Control	6.21E+02	3D Infection	1.88E+03	4.08E-206

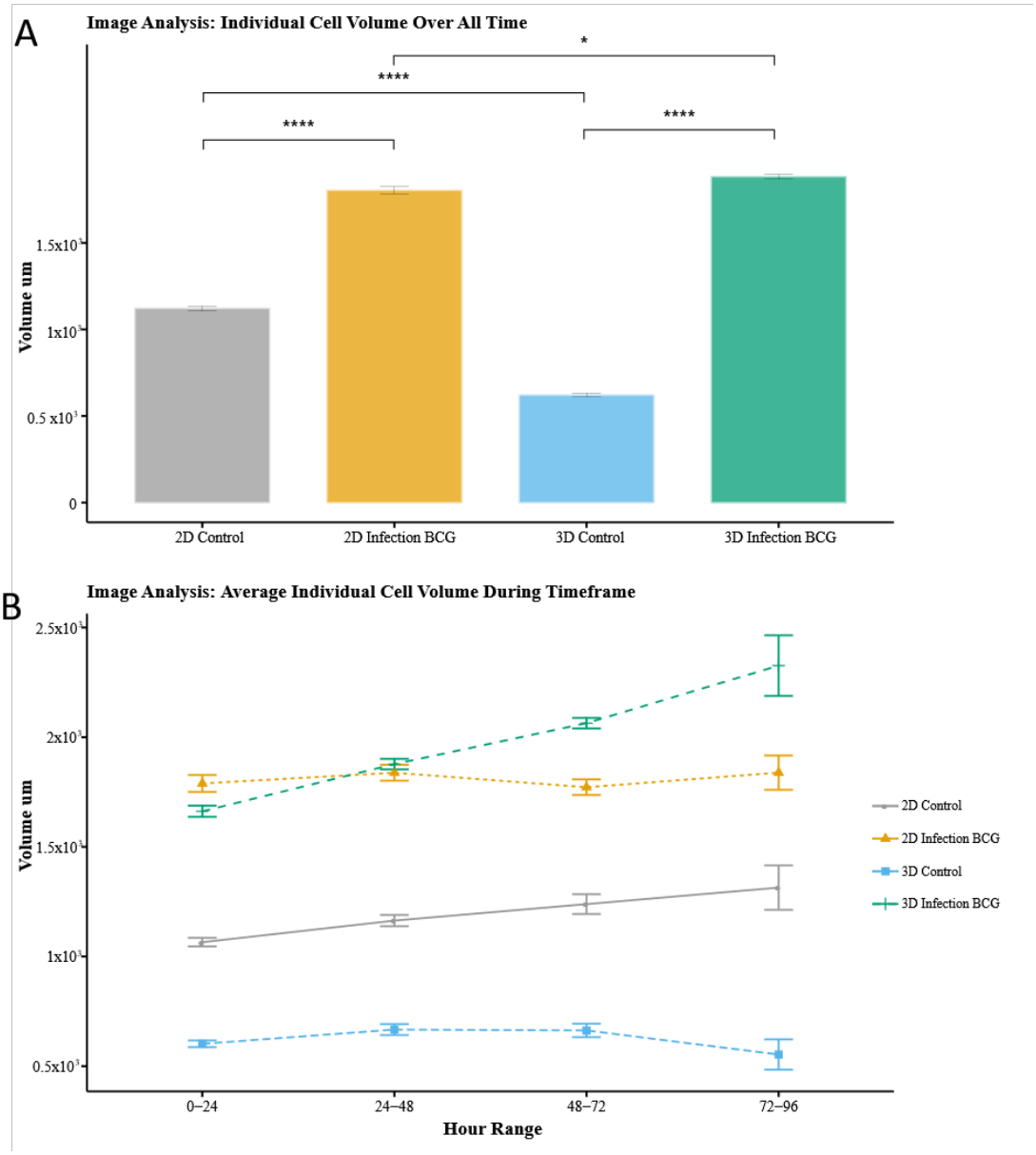

Figure 65: Image analysis of individual cell volume of gfpBMDM infected with mcBCG in 2D and 3D culture conditions over 72 hours. A) Averaged over all time B) Averaged based on hour range. (ns- No significant difference, * - p<.05, **-p<.01,***-p<.001,****-p<.0001)

Table 93: Average Individual Cell Volume 2D vs. 3D Over Time (timeframes): Wilcoxon

Hour Range	Condition 1	Volume μm^3	Condition 2	Volume μm^3	p value
0-24	2D Control	1.07E+03	3D Control	6.02E+02	1.85E-47
24-48	2D Control	1.16E+03	3D Control	6.67E+02	6.46E-23
48-72	2D Control	1.24E+03	3D Control	6.63E+02	7.86E-16
72-96	2D Control	1.31E+03	3D Control	5.53E+02	2.37E-06
0-24	2D Infection	1.79E+03	3D Infection	1.66E+03	0.000542
24-48	2D Infection	1.84E+03	3D Infection	1.88E+03	0.768283
48-72	2D Infection	1.77E+03	3D Infection	2.06E+03	2.72E-09
72-96	2D Infection	1.84E+03	3D Infection	2.33E+03	0.003427

Table 94: Average Individual Cell Volume Control vs. Infected Over Time (timeframes): Wilcoxon

Hour Range	Condition 1	Volume μm^3	Condition 2	Volume μm^3	p value
0-24	2D Control	1.07E+03	2D Infection	1.79E+03	6.46E-59
24-48	2D Control	1.16E+03	2D Infection	1.84E+03	1.69E-41
48-72	2D Control	1.24E+03	2D Infection	1.77E+03	2.55E-16
72-96	2D Control	1.31E+03	2D Infection	1.84E+03	0.001534
0-24	3D Control	6.02E+02	3D Infection	1.66E+03	7.78E-110
24-48	3D Control	6.67E+02	3D Infection	1.88E+03	6.93E-44
48-72	3D Control	6.63E+02	3D Infection	2.06E+03	7.89E-34
72-96	3D Control	5.53E+02	3D Infection	2.33E+03	4.69E-09

5.3.7.5 Impact of cell-state on cell dynamics

We investigated the impact of cellular state on the dynamic response of macrophages to BCG infection. Investigation of infected status of the cells as well as the spatial organization in order to further determine the impact that the proinflammatory state of a cell, and the spatial organization has on the dynamic response to infection. We quantified the percent cells associated with each state over the course of the infection study and observed that there was a decrease of 2D infected cells determined over the course of infection, but an increase in 3D infected cells. This matches our empirical observations of confocal imaging which showed a higher bacterial presence in the 3D infected condition as opposed to 2D (Figure 66).

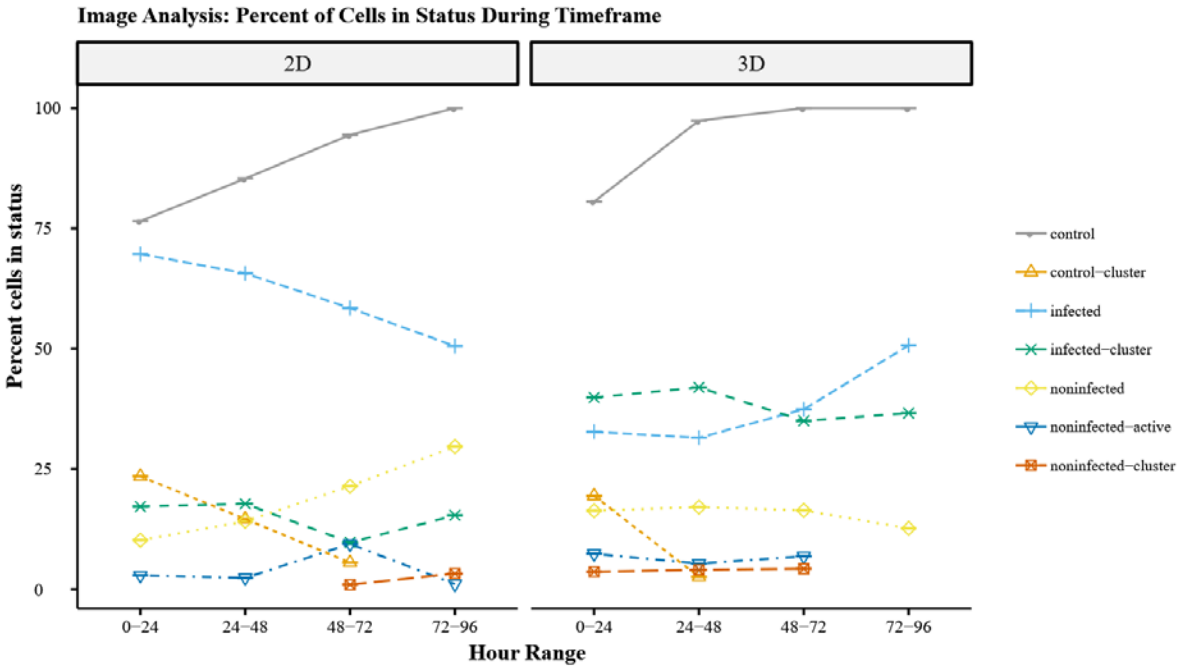

Figure 66: Percent of cells in state over course of infection. Note, percentage is relative to overall condition: 2D Infected, 2D Control, 3D infected, 3D Control.

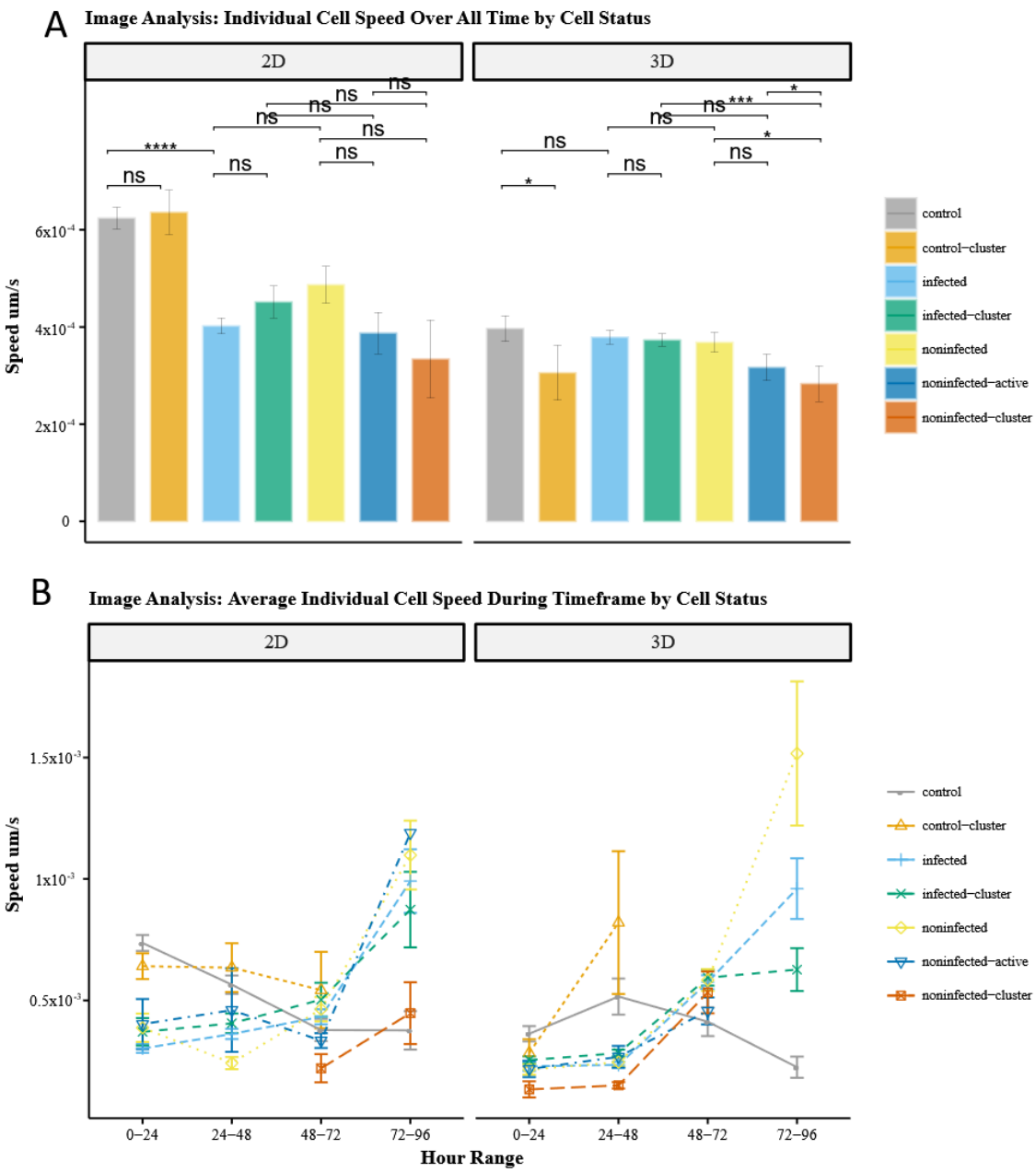

Figure 67: Individual cell speed of gfpBMDM infected with mcBCG in 2D and 3D culture conditions over 96 hours by cell status A) Averaged over all time B) Averaged based on hour range. (ns-No significant difference, * - p<.05, **-p<.01,***-p<.001,****-p<.0001)

For average cellular speed in 2D we no significant difference between control and control cluster cells, nor cells within the infected condition (Figure 67 A, Table 95,. Further investigation into the cellular speeds over time shows comparable trends in cellular speeds such as in seen in 2D. We observe the same increase in cellular speed over the course of the BCG infection between all proinflammatory cells within the infected condition (infection, infection-cluster, and noninfected-active). Control cells have an observed decrease in cellular speed over time. Noninfected cells not in a cluster, as well as noninfected-cluster cells at the hour ranges they are observed have cellular speeds matching that of the proinflammatory cells within the environment (Figure 67 B), which can potentially be attributed to the excess proinflammatory state of the system as a whole in response to the more virulent BCG infection.

Table 95: 2D Average Individual Cell Speed Over All Time: Wilcoxon

2D Cell State	*Speed µm/s*	*2D Cell State*	*Speed µm/s*	*p value*
Control	6.24E-04	Control-Cluster	6.36E-04	0.280171
Control	6.24E-04	Noninfected	4.87E-04	0.012378
Control	6.24E-04	Infected	4.02E-04	2.75E-11
Infected	4.02E-04	Infected-Cluster	4.51E-04	0.110652
Infected	4.02E-04	Noninfected	4.87E-04	0.118123
Infected-Cluster	4.51E-04	Noninfected-Active	3.87E-04	0.84244
Infected-Cluster	4.51E-04	Noninfected-Cluster	3.34E-04	0.722814
Noninfected	4.87E-04	Noninfected-Cluster	3.34E-04	0.821324
Noninfected	4.87E-04	Noninfected-Active	3.87E-04	0.910523
Noninfected-Cluster	3.34E-04	Noninfected-Active	3.87E-04	0.772579

Average cellular speed in 3D we a significant increase in cellular speed of infected-cluster cells as compared to non-infected cluster cells ($p<.05$) as well as an increase in cellular speed of noninfected-active cells compared to noninfected-cluster cells($p<.05$). Most notably, we see that there is no significant difference in cellular speed

of noninfected cells within the infected condition comparable to what is observed in 2D. (Figure 67 A, Table 96),. Further investigation into the cellular speeds over time shows comparable trends in cellular speeds to 2D between all proinflammatory cells within the 2D infected condition (infection, infection-cluster, and noninfected-active), but these cellular speeds have a marked increase over the course of the BCG infection, whereas control cells have an observed decrease in cellular speed over time. Noninfected cells not in a cluster have cellular speeds matching that of the proinflammatory cells within the environment noninfected cells not in a cluster, as well as noninfected-cluster cells at the hour ranges they are observed have cellular speeds matching that of the proinflammatory cells within the environment (Figure 67 B).

Table 96: 3D Average Individual Cell Speed Over All Time: Wilcoxon

3D Cell State	*Speed µm/s*	*3D Cell State*	*Speed µm/s*	*p value*
Control	3.97E-04	Control-Cluster	3.06E-04	0.028705625
Control	3.97E-04	Noninfected	3.68E-04	0.025338189
Control	3.97E-04	Infected	3.79E-04	0.054125105
Infected	3.79E-04	Infected-Cluster	3.73E-04	0.384919999
Infected	3.79E-04	Noninfected	3.68E-04	0.493718816
Infected-Cluster	3.73E-04	Noninfected-Active	3.17E-04	0.128696839
Infected-Cluster	3.73E-04	Noninfected-Cluster	2.83E-04	0.000397162
Noninfected	3.68E-04	Noninfected-Cluster	2.83E-04	0.013362906
Noninfected	3.68E-04	Noninfected-Active	3.17E-04	0.691648353
Noninfected-Cluster	2.83E-04	Noninfected-Active	3.17E-04	0.036321344

Cellular acceleration follows comparable trends to cell speed in both the 2D and 3D environment, while overall values of cellular acceleration between states does not have much statistical significance (Figure 68 A ,Table 97,Table 98), the trends apparent in the changes in acceleration over time show a trend in dynamics. We note that we do see comparable trends of cellular acceleration in proinflammatory cells

within the 2D and 3D environment (infected, infected-cluster, and noninfected-active), but we notice a high increase in the cellular acceleration of 2D infected cells at the later timepoints once the BCG infection is visibly lowered. In 3D, we see that our non-infected cells maintain a more comparable trend in acceleration to our proinflammatory cells as compared to control, potentially due to the sustained infection observed in the 3D BCG infection leading inducing a more proinflammatory environment leading to further proinflammatory activation outside the immediate cellular neighborhood (20 µm DBSCAN cluster) of the infected cells in the 3D condition (Figure 68 B).

Table 97:	2D Average Individual Cell Acceleration Over All Time: Wilcoxon			
2D Cell State	Acceleration *µm/s²*	*2D Cell State*	Acceleration *µm/s²*	*p value*
Control	4.74E-08	Control-Cluster	4.38E-08	0.23471374
Control	4.74E-08	Noninfected	4.15E-08	0.398537738
Control	4.74E-08	Infected	3.92E-08	0.05420048
Infected	3.92E-08	Infected-Cluster	4.33E-08	0.597487
Infected	3.92E-08	Noninfected	4.15E-08	0.740406
Infected-Cluster	4.33E-08	Noninfected-Active	4.92E-08	0.085334
Infected-Cluster	4.33E-08	Noninfected-Cluster	3.08E-08	0.631991
Noninfected	4.15E-08	Noninfected-Cluster	3.08E-08	0.671515
Noninfected	4.15E-08	Noninfected-Active	4.92E-08	0.040152
Noninfected-Cluster	3.08E-08	Noninfected-Active	4.92E-08	0.123225

Table 98:	3D Average Individual Cell Acceleration Over All Time: Wilcoxon			
3D Cell State	Acceleration *µm/s²*	*3D Cell State*	Acceleration *µm/s²*	*p value*
Control	3.39E-08	Control-Cluster	2.72E-08	0.115779
Control	3.39E-08	Noninfected	3.67E-08	0.022999
Control	3.39E-08	Infected	3.54E-08	0.137231
Infected	3.54E-08	Infected-Cluster	3.52E-08	0.680192
Infected	3.54E-08	Noninfected	3.67E-08	0.197096
Infected-Cluster	3.52E-08	Noninfected-Active	2.87E-08	0.018199
Infected-Cluster	3.52E-08	Noninfected-Cluster	3.20E-08	0.273494
Noninfected	3.67E-08	Noninfected-Cluster	3.20E-08	0.107423
Noninfected	3.67E-08	Noninfected-Active	2.87E-08	0.005393
Noninfected-Cluster	3.20E-08	Noninfected-Active	2.87E-08	0.473382

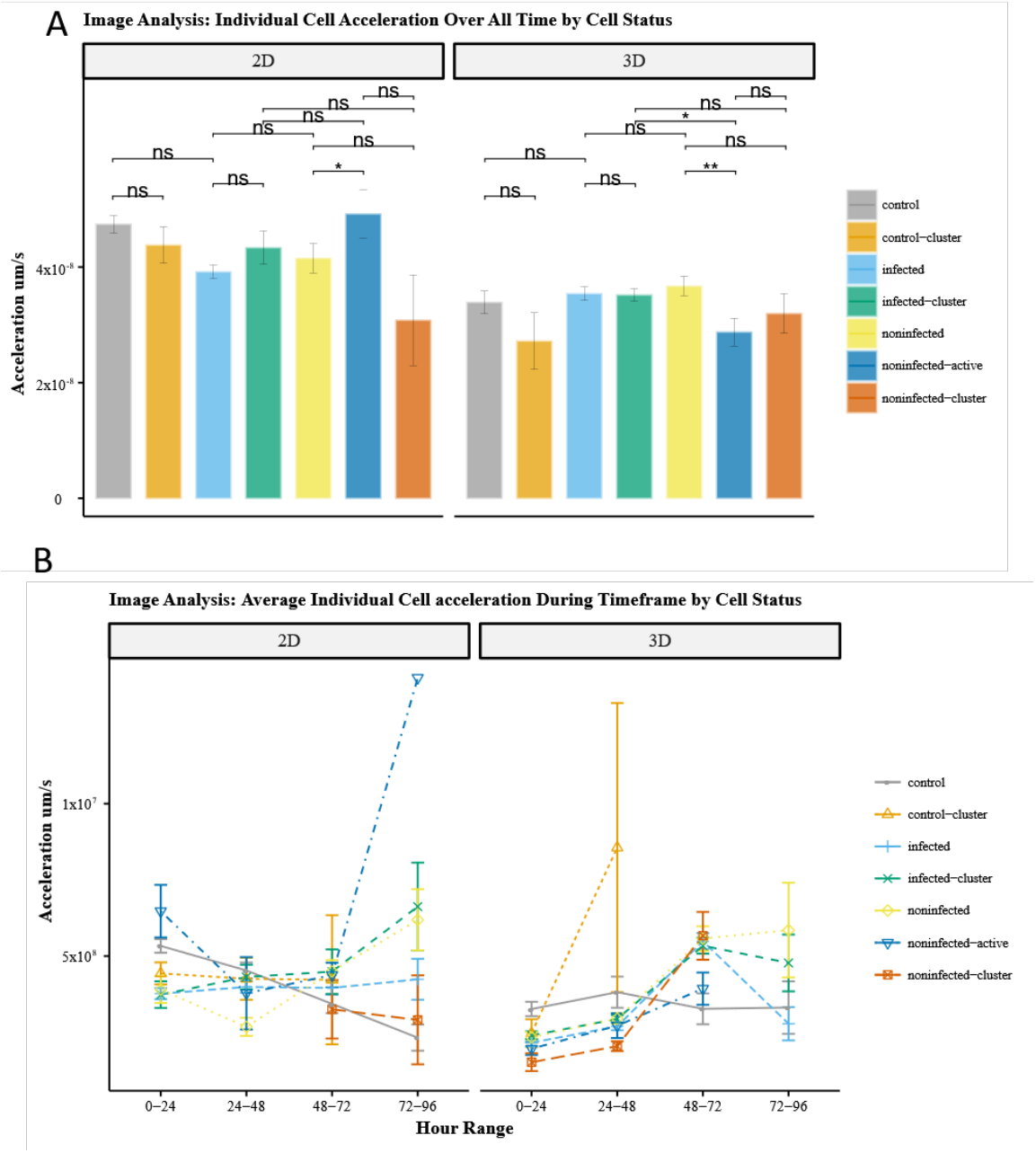

Figure 68: Individual cell acceleration of gfpBMDM infected with mcBCG in 2D and 3D culture conditions over 96 hours by cell status A) Averaged over all time B) Averaged based on hour range. (ns- No significant difference, * - p<.05, **-p<.01,***-p<.001,****-p<.0001)

Cellular directedness by cell state shows comparable results to the overall directedness in 2D and 3D infection. We see that as a whole, control cells have a markedly significantly higher directedness than infected cells regardless of 2D or 3D

environment (Figure 69 A, Table 99, Table 100). We also note that overtime, we see a that in the 3D infected condition, all proinflammatory cells as well as non-infected cells show an increase in directedness in the later timepoints. This trend, which was apparent overall in the 2D infected condition directedness, holds for noninfected cells and infected cells in 2D (Figure 69 B). Notably in 2D, we see a decrease in cell directedness in noninfected-active cells that does not follow the overall trends of the 2D infected condition, showing a divergence from previously trends of proinflammatory cells in the 2D infected condition maintaining trends to each other over the course of infection.

Table 99: 2D Average Individual Cell Directedness Over All Time: Wilcoxon

2D Cell State	*Directedness*	*2D Cell State*	*Directedness*	*p value*
Control	0.251845	Control-Cluster	0.310013	5.94E-06
Control	0.251845	Noninfected	0.158898	3.39E-15
Control	0.251845	Infected	0.157856	3.97E-24
Infected	0.157856	Infected-Cluster	0.189298	0.007195197
Infected	0.157856	Noninfected	0.158898	0.00125119
Infected-Cluster	0.189298	Noninfected-Active	0.136458	5.72E-05
Infected-Cluster	0.189298	Noninfected-Cluster	0.087525	0.006483911
Noninfected	0.158898	Noninfected-Cluster	0.087525	0.028733264
Noninfected	0.158898	Noninfected-Active	0.136458	0.009325137
Noninfected-Cluster	0.087525	Noninfected-Active	0.136458	0.535669509

Table 100: 3D Average Individual Cell Directedness Over All Time: Wilcoxon

3D Cell State	*Directedness*	*3D Cell State*	*Directedness*	*p value*
Control	0.201658	Control-Cluster	0.30529	8.83E-06
Control	0.201658	Noninfected	0.104667	6.02E-17
Control	0.201658	Infected	0.12919	2.99E-11
Infected	0.12919	Infected-Cluster	0.161608	2.87E-13
Infected	0.12919	Noninfected	0.104667	4.67E-06
Infected-Cluster	0.161608	Noninfected-Active	0.13293	0.000177116
Infected-Cluster	0.161608	Noninfected-Cluster	0.083655	2.07E-14
Noninfected	0.104667	Noninfected-Cluster	0.083655	0.172317362
Noninfected	0.104667	Noninfected-Active	0.13293	0.000885583
Noninfected-Active	0.13293	Noninfected-Cluster	0.083655	0.000128

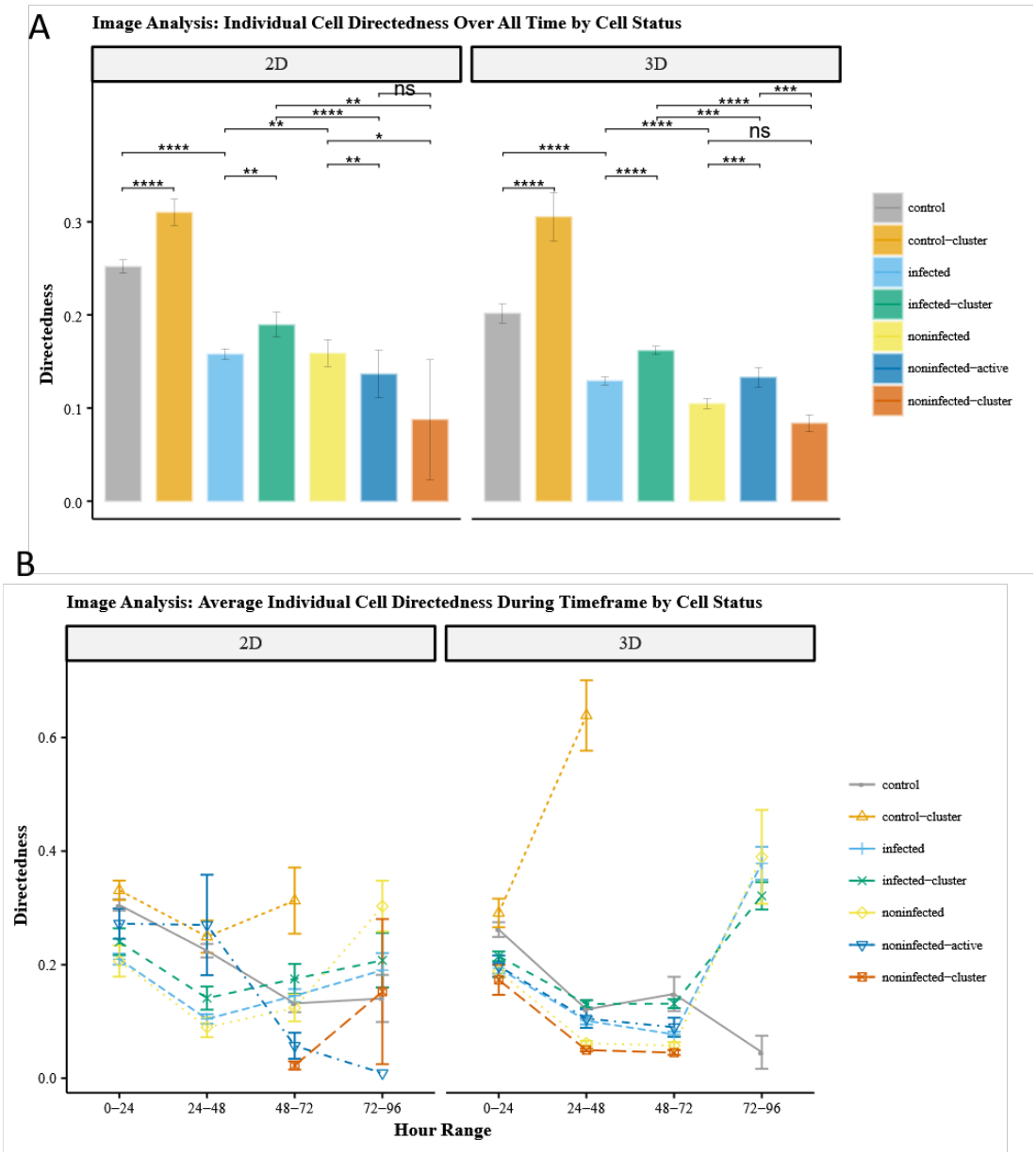

Figure 69: Individual cell directedness of gfpBMDM infected with mcBCG in 2D and 3D culture conditions over 96 hours by cell status A) Averaged over all time B) Averaged based on hour range. (ns- No significant difference, * - p<.05, **-p<.01,***-p<.001,****-p<.0001)

Cellular volume of infected macrophages has been noted to increase under conditions of phagocytosis of bacterium [43]. Cellular volume shows, as expected the increase in cellular volume of infected cells in both the 2D and 3D conditions regardless of time under infection (Figure 70, Table 101, Table 102). However, we do see that the

trends of cell volume in the 2D condition maintain comparable levels regardless of the number of infected cells in the system and the bacterial load. However, in the 3D environment, we notice an increase in cellular volume over the course of infection. This increase in volume mimics the trends shown in the increasing number of infected cells over time in the condition as well as the observable presence of bacteria within the system (Figure 70 B).

Table 101: 2D Average Individual Cell Volume Over All Time: Wilcoxon

2D Cell State	*Volume µm³*	*2D Cell State*	*Volume µm³*	*p value*
Control	1.15E+03	Control-Cluster	1.00E+03	4.57E-06
Control	1.15E+03	Noninfected	1.48E+03	8.38E-12
Control	1.15E+03	Infected	1.96E+03	1.50E-124
Infected	1.96E+03	Infected-Cluster	1.74E+03	0.00010371
Infected	1.96E+03	Noninfected	1.48E+03	3.51E-20
Infected-Cluster	1.74E+03	Noninfected-Active	1.09E+03	1.35E-12
Infected-Cluster	1.74E+03	Noninfected-Cluster	1.28E+03	0.077570948
Noninfected	1.48E+03	Noninfected-Cluster	1.28E+03	0.933688514
Noninfected	1.48E+03	Noninfected-Active	1.09E+03	0.000120605
Noninfected-Cluster	1.28E+03	Noninfected-Active	1.09E+03	0.026712769

Table 102: 3D Average Individual Cell Volume Over All Time: Wilcoxon

3D Cell State	*Volume µm³*	*3D Cell State*	*Volume µm³*	*p value*
Control	6.44E+02	Control-Cluster	4.58E+02	6.02E-07
Control	6.44E+02	Noninfected	1.56E+03	7.95E-133
Control	6.44E+02	Infected	2.16E+03	2.31E-165
Infected	2.16E+03	Infected-Cluster	1.92E+03	7.14E-10
Infected	2.16E+03	Noninfected	1.56E+03	1.37E-52
Infected-Cluster	1.92E+03	Noninfected-Active	1.28E+03	1.68E-31
Infected-Cluster	1.92E+03	Noninfected-Cluster	1.40E+03	4.86E-15
Noninfected	1.56E+03	Noninfected-Cluster	1.40E+03	0.000183462
Noninfected	1.56E+03	Noninfected-Active	1.28E+03	1.21E-15
Noninfected-Cluster	1.40E+03	Noninfected-Active	1.28E+03	0.001157834

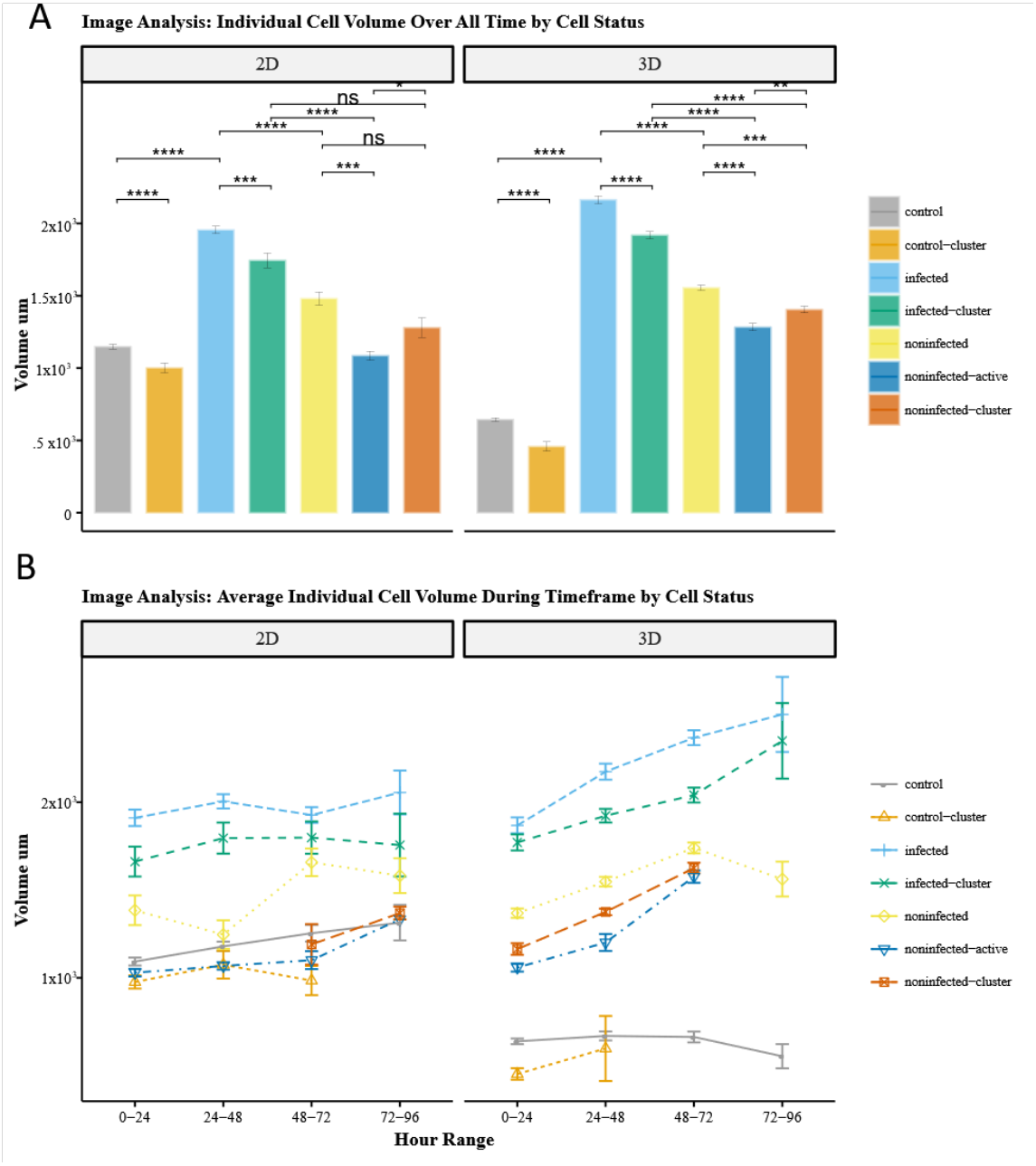

Figure 70: Individual cell volume of gfpBMDM infected with mcBCG in 2D and 3D culture conditions over 96 hours by cell status A) Averaged over all time B) Averaged based on hour range. (ns-No significant difference, * - p<.05, **-p<.01,***-p<.001,****-p<.0001)

5.4 Discussion

The hour zero images from confocal microscopy of the 2D and 3D infection shows an apparent higher concentration of extracellular bacteria in the 3D infection environment relative to 2D infection. Because the infection takes place prior to placement in either 2D or 3D culture, both environments should maintain the same ratio of macrophages to bacterium. Closer inspection of the 3D images shows an initial degree of cell death in a number of the macrophages that were infected with mcBCG due to the presence of a faint GFP signal around the bacterium equivalent to what is observed after visible cell death under confocal imaging (Figure 56). This initial cell death occurred between the time of being placed in the gel, and the minimum requirement of 4 hours necessary for gelation, media addition and confocal imaging setup. This observation is not one that we have made previously in the less virulent infection with *Mycobacterium smegmatis* (mSmeg) and can possibly be due to the more virulent nature of the mcBCG bacterium and the exposure to the 3D environment. Further investigation into the early stages of the BCG infection in the 3D environment may illuminate why this phenomenon is occurring. In the context of Mtb infection, extracellular bacterium is noted to have a lower grow rate than in the macrophage intracellular environment[120]. Extracellular growth in Mtb infection has been primarily noted in the cases of necrotic granulomas that generate an acidic environment that is beneficial for the bacterial replication and transfer of the bacterium to new hosts.

The evidence of apoptosis visualized under 2D infection is of note as it was not previously observed in mSmeg infection. Apoptosis, as opposed to necrosis does not induce a significant inflammatory response [121], and the resulting uptake of bacteria and apoptotic bodies provides the bacterium with the intracellular environment that is favorable to the bacterium[120].In the context of tuberculosis, apoptosis has been found to be promoted by Mtb infection in human alveolar macrophages[122], and the primary indicator for the benefit of this form of cell death to the pathogen is that the apoptotic bodies released signals uptake of cell debris and bacterium by other phagocytes within the system promoting dissemination [15], [123], [124],. Specifically in the role of macrophage aggregation in response to mycobacterial infection, Davis and Ramakrishnan identified the apoptotic death of infected macrophages appeared to be a driving factor in granuloma formation[15]. However, the quantification of the benefit that apoptosis or necrosis provides the pathogen is a complicated matter. Where apoptosis can induce further intracellular uptake, it also temporarily deprives the bacterium of its intracellular environment necessary for replication[125], [126]. Current consensus shows that the disparate modes of cell death both play important, but different roles in the progression of infection. The induction of apoptosis by bacteria may promote and favor dissemination of mycobacterium[15], [123], [124], whereas the necrosis may lead to an environment more suitable for bacterial replication[127], [128]. Investigations of BCG macrophage infection have identified that the

promotion of apoptosis through the induction of caspase-dependent Wnt/β-catenin signaling activation[129].

Comparison to our previous investigation of 2D and 3D infection with mSmeg shows that under confocal imaging we see a more persistent intracellular infection with mcBCG as compared to the low-level clearing infection of mSmeg. This is confirmed with our investigation of the comparative dynamics of wild type BCG infection to mcBCG where we see a consistent intracellular bacterial load over the 96 hours of infection with a decrease in the concentration of extracellular bacterium. In our investigation of 2D and 3D bacterial load, we quantify the total bacterial load over time and see differences in the dynamics were in the previous study of mSmeg infection there were none. Where we had previously seen a low level clearing infection, the mcBCG infection is more robust and persistent over the course of time. This is particularly true in the 3D environment where we see a divergence from the 2D infection study and see an increase in the overall bacterial load after 48 hours of infection, the 2D bacterial load continues to decrease, but there is an increase in the 3D bacterial load. This divergence from the previously observed dynamics of mSmeg and the new addition of the significant difference of the 3D cultured cells not clearing the bacterial infection in the same manner as their 2D counterpart raises questions for future investigations into the phagocytic and effector molecule host defense against pathogens and how this may differed for more virulent infections in a 3D environment as opposed to 2D. This observation coupled with the imaging observations of initial host cell death in 3D leading to the

presence of extracellular bacterium may provide a path for future quantification of these complex dynamics.

While overall cellular dynamics remain comparable between the two studies, we see marked differences in the trends over time. The initial study of 2D and 3D infection demonstrated a very distinct difference between cellular speed 2D mSmeg Infection and 3D mSmeg infection, with 2D speed being significantly higher over all periods of time. Cellular speed in 2D mSmeg infection and 3D mSmeg infection decreased overtime with the decreasing infection. A very different dynamic is present in the BCG infection. We see that the trends for cellular speed in BCG infection have a dramatic increase in both 2D and 3D over time. While 2D BCG infection cellular speed is significantly higher overall, the difference is much less drastic (mSmeg infection 3D/2D log2 Fold change: 1.0015, BCG infection 3D/2D log2 Fold change: -0.24508), and there is no significant difference between 2D and 3D speed under BCG infection after 48 hours.

In both the initial mSmeg investigation and the BCG study we see that cellular volume is significantly higher under infection than control. This is consistent with the literature that shows that macrophage volume can be correlated to phagocytosis of the bacterium [43]. However, we see a more dramatic fold change increase under BCG infection than mSmeg infection. The log2 foldchange increase in cellular volume under mSmeg infection in 3D is 0.357, whereas the log2 fold change cell volume increase under BCG infection is 1.6. In the 2D condition we see a similar result with the cellular volume increases under mSmeg infection by a log2

fold change of .025, whereas the BCG infection increases the cellular volume by a log2 fold change of .68567. This dramatic difference is of interested, but no current studies have observed the volumetric increase of macrophages undergoing phagocytosis of varying virulent bacterium. Further research into this area can determine if this volumetric increase is due to the increased virulence of the BCG, or due to some other underlying factor in the study.

In our analysis of cell state-based dynamics we noticed that the percent of cells identified as infected in the 2D infection model reduced over the course of time, whereas we saw an increase in the 3D model. This diverges from our previous analysis of mSmeg infection where we saw a comparable drop in the percent of identified infected cells over the course of infection. This divergence in dynamics indicates a difference in the bacterial load over time between the two conditions, further confirmed by confocal imaging. While we are utilizing a higher bacterial load than many *ex vivo* or *in vitro* studies, the disparity between the two environmental conditions is of interest. This draws into question the levels of BCG utilized in traditional 2D *in vitro* studies compared to the levels seen *in vivo*. Traditionally in research it is established that it requires few BCG bacilli in *in vivo* studies for infection, but the majority of *in vitro* studies utilize higher relative bacterial loads[130].

5.4.1 Future Work

The existence of visible extracellular bacteria during the BCG studies is a novel observation that was not noted in the original studies with a low level mSmeg

infection. The presence of 10 μg/mL gentamicin in the cell culture media is sufficient to suppress the growth of mSmeg in the extracellular environment [54] [53]. While BCG is responsive to gentamicin [131], we observe less bacterial death in the extracellular environment that can be contributed to this presence. The increased virulence of BCG, as compared to mSmeg, allows for a study of mycobacterial infection more comparable to human infection with Mtb. However, virulence factors present in human pathogenic mycobacterial strains such as the RD1 virulence locus are not present in BCG.[97]. Previous investigations into mycobacterium induced recruitment and aggregation of macrophages in the innate immune response note the significance that the RD1 virulence locus plays in this initial response[15]. Davis and Ramakrishnan identified the RD1 locus as not only the factor leading to the enhanced recruitment of macrophages to the sight of infection, but as a contributor of expansion of bacterial growth to the recruited macrophages and subsequent egression from the aggregation leading to bacterial expansion within the host [15]. Expansion to more virulent models of Mtb that contain the virulence loci RD1 will provide more comparable aggregation and bacterial expansion to early human Mtb infection.

In addition, we also assessed through confocal imaging the presence of considerable extracellular bacteria within the 3D infection environment. However, the extraction of bacteria for enumeration in 3D requires the isolation of the entire sample that is then disrupted to enumerate the total bacterial counts within the environment (intracellular and extracellular combined). In 2D, we can sample the

extracellular supernatant and enumerate the extracellular bacteria independent of intracellular in order to quantify the full bacterial infection process. This difference in sampling makes direct comparison of extracellular bacteria in the 2D environment to the 3D environment highly problematic and requires that we observe only the total bacterial load in each environment for comparison. Further research into methods that can isolate the extracellular bacteria from the intracellular within the 3D environment may elucidate the differences we observe during our infection studies. Currently, due to the confocal imaging in our study, we could in future work, extend the current application of our computational platform to analyze not only the presence of intracellular bacteria but approximate the extracellular bacterium as well. Utilizing the total summation of the RFP signal (RFP sum of all voxels) from the entire imaging space and subtracting the total summation of the RFP signal within each cell in the infected conditions we can generate an approximation in the fold change of extracellular bacteria over the time course of infection.

6 SUMMARY AND FUTURE DIRECTIONS

6.1 Summary

In this study we present a large-scale comparative 2D and 3D infection platform with 4D confocal imaging of live infection for biological and cellular dynamic analysis of bone marrow derived macrophages in response to *Mycobacterium smegmatis* and *Mycobacterium bovis BCG.* Through careful consideration of variables including, gas diffusion, transgenic strain comparison, and buffer solution impact on bacterial growth, we present a platform that allows for the isolation of dimensionality and cell-matrix interaction for the study of overall cell, and cell state-based dynamics. Through an expansion into a computational platform we enable the semi-automatic analysis of 2D and 3D mycobacterial infection. The use of outlier detection single-class classification model LOF allows for rapid detection of infected cells in an unknown heterogenous cell population with very low error (<1%).

We demonstrate significant differences that arise in cell motility and behavior in response to bacterial infection and the 2D or 3D environment and through the utilization of analysis and image processing we can quantitatively represent the magnitude and significance of the observed differences.

6.2 Future Directions

Future work will continue the investigation of the impact of environment and spatial organization on mycobacterial infection with the more virulent *M. bovis* BCG as it provides a long-term persisting infection with a bacterium more comparable to

Mycobacterium tuberculosis [132], [133]. Recent work has denoted the impact of immunomodulatory effects of alcohol and vitamin D nutrition in the progression of BCG infection [36], [50]. An extension of this platform to include this study is easily adapted. In addition, further investigation into multicellular response to mycobacterial infections, with the inclusion of the other main responder in the innate immune response, natural killer (NK) cells, can help us better understand the resulting dynamics of the more innate immune response to mycobacterial infection. The NK cells in the innate immune response to mycobacterial infection produce interferon-gamma, which subsequently activates macrophages leading to the increase in the reactive oxygen and nitrogen species produced by in response to infection [134], [135].

REFERENCES

[1] B. Al Shammari, T. Shiomi, L. Tezera, M. K. Bielecka, V. Workman, T. Sathyamoorthy, F. Mauri, S. N. Jayasinghe, B. D. Robertson, J. D'Armiento, J. S. Friedland, and P. T. Elkington, "The Extracellular Matrix Regulates Granuloma Necrosis in Tuberculosis," *J. Infect. Dis.*, vol. 212, no. 3, pp. 463–473, Aug. 2015.

[2] D. O. Adams, "The granulomatous inflammatory response. A review.," *Am. J. Pathol.*, vol. 84, no. 1, pp. 164–191, Jul. 1976.

[3] S. Bhavanam, G. R. Rayat, M. Keelan, D. Kunimoto, and S. J. Drews, "Understanding the pathophysiology of the human TB lung granuloma using *in vitro* granuloma models," *Future Microbiol.*, vol. 11, no. 8, pp. 1073–1089, Aug. 2016.

[4] R. D. Berg and L. Ramakrishnan, "Insights into tuberculosis from the zebrafish model," *Trends Mol. Med.*, vol. 18, no. 12, pp. 689–690, Dec. 2012.

[5] E. Guirado, L. S. Schlesinger, and G. Kaplan, "Macrophages in Tuberculosis: Friend or Foe," *Semin. Immunopathol.*, vol. 35, no. 5, pp. 563–583, Sep. 2013.

[6] M. J. Marakalala, R. M. Raju, K. Sharma, Y. J. Zhang, E. A. Eugenin, B. Prideaux, I. B. Daudelin, P.-Y. Chen, M. G. Booty, J. H. Kim, S. Y. Eum, L. E. Via, S. M. Behar, C. E. Barry, M. Mann, V. Dartois, and E. J. Rubin, "Inflammatory signaling in human Tuberculosis granulomas is spatially organized," *Nat. Med.*, vol. 22, no. 5, pp. 531–538, May 2016.

[7] C. Wiesner, V. Le-Cabec, K. El Azzouzi, I. Maridonneau-Parini, and S. Linder, "Podosomes in space: Macrophage migration and matrix degradation in 2D and 3D settings," *Cell Adhes. Migr.*, vol. 8, no. 3, pp. 179–191, May 2014.

[8] J. D. Ernst, “The immunological life cycle of tuberculosis,” *Nat. Rev. Immunol.*, vol. 12, no. 8, p. 581, Aug. 2012.

[9] T. D. Bold and J. D. Ernst, “Who Benefits from Granulomas, Mycobacteria or Host?,” *Cell*, vol. 136, no. 1, pp. 17–19, Jan. 2009.

[10] J. G. Egen, A. G. Rothfuchs, C. G. Feng, N. Winter, A. Sher, and R. N. Germain, “Macrophage and T Cell Dynamics during the Development and Disintegration of Mycobacterial Granulomas,” *Immunity*, vol. 28, no. 2, pp. 271–284, Feb. 2008.

[11] A. M. Dannenberg, “Roles of Cytotoxic Delayed-Type Hypersensitivity and Macrophage-Activating Cell-Mediated Immunity in the Pathogenesis of Tuberculosis,” *Immunobiology*, vol. 191, no. 4, pp. 461–473, Jan. 1994.

[12] B. M. Saunders and A. M. Cooper, “Restraining mycobacteria: role of granulomas in mycobacterial infections,” *Immunol. Cell Biol.*, vol. 78, no. 4, pp. 334–341, 2000.

[13] T. Ulrichs and S. H. Kaufmann, “New insights into the function of granulomas in human tuberculosis,” *J. Pathol.*, vol. 208, no. 2, pp. 261–269, Jan. 2006.

[14] J. M. Davis, H. Clay, J. L. Lewis, N. Ghori, P. Herbomel, and L. Ramakrishnan, “Real-Time Visualization of Mycobacterium-Macrophage Interactions Leading to Initiation of Granuloma Formation in Zebrafish Embryos,” *Immunity*, vol. 17, no. 6, pp. 693–702, Dec. 2002.

[15] J. M. Davis and L. Ramakrishnan, “The Role of the Granuloma in Expansion and Dissemination of Early Tuberculous Infection,” *Cell*, vol. 136, no. 1, pp. 37–49, Jan. 2009.

[16] I. Kramnik and G. Beamer, “Mouse models of human TB pathology: roles in the analysis of necrosis and the development of host-directed therapies,” *Semin. Immunopathol.*, vol. 38, no. 2, pp. 221–237, Mar. 2016.

[17] J. L. Flynn, S. V. Capuano, D. Croix, S. Pawar, A. Myers, A. Zinovik, and E. Klein, “Non-human primates: a model for tuberculosis research,” *Tuberculosis*, vol. 83, no. 1, pp. 116–118, Feb. 2003.

[18] J. L. Flynn, H. P. Gideon, J. T. Mattila, and P. L. Lin, “Immunology studies in non-human primate models of tuberculosis,” *Immunol. Rev.*, vol. 264, no. 1, pp. 60–73, Mar. 2015.

[19] C. A. Scanga and J. L. Flynn, “Modeling Tuberculosis in Nonhuman Primates,” *Cold Spring Harb. Perspect. Med.*, vol. 4, no. 12, p. a018564, Dec. 2014.

[20] A. K. Singh and U. D. Gupta, “Animal models of tuberculosis: Lesson learnt,” *Indian J. Med. Res.*, vol. 147, no. 5, pp. 456–463, May 2018.

[21] L. G. Griffith and M. A. Swartz, “Capturing complex 3D tissue physiology in vitro,” *Nat. Rev. Mol. Cell Biol.*, vol. 7, no. 3, 2006.

[22] M.-P. Puissegur, C. Botanch, J.-L. Duteyrat, G. Delsol, C. Caratero, and F. Altare, “An in vitro dual model of mycobacterial granulomas to investigate the molecular interactions between mycobacteria and human host cells,” *Cell. Microbiol.*, vol. 6, no. 5, pp. 423–433, May 2004.

[23] C. Braian, M. Svensson, S. Brighenti, M. Lerm, and V. R. Parasa, “A 3D Human Lung Tissue Model for Functional Studies on Mycobacterium tuberculosis Infection,” *JoVE J. Vis. Exp.*, no. 104, pp. e53084–e53084, Oct. 2015.

[24] M. K. Bielecka, L. B. Tezera, R. Zmijan, F. Drobniewski, X. Zhang, S. Jayasinghe, and P. Elkington, “A Bioengineered Three-Dimensional Cell Culture Platform Integrated with Microfluidics To Address Antimicrobial Resistance in Tuberculosis,” *mBio*, vol. 8, no. 1, pp. e02073-16, Mar. 2017.

[25] N. Kapoor, S. Pawar, T. D. Sirakova, C. Deb, W. L. Warren, and P. E. Kolattukudy, “Human Granuloma In Vitro Model, for TB Dormancy and Resuscitation,” *PLoS ONE*, vol. 8, no. 1, Jan. 2013.

[26] A. T. N. Hoang, P. Chen, J. Juarez, P. Sachamitr, B. Billing, L. Bosnjak, B. Dahlén, M. Coles, and M. Svensson, “Dendritic cell functional properties in a three-dimensional tissue model of human lung mucosa,” *Am. J. Physiol.-Lung Cell. Mol. Physiol.*, vol. 302, no. 2, pp. L226–L237, Jan. 2012.

[27] V. R. Parasa, M. J. Rahman, A. T. N. Hoang, M. Svensson, S. Brighenti, and M. Lerm, “Modeling Mycobacterium tuberculosis early granuloma formation in experimental human lung tissue,” *Dis. Model. Mech.*, vol. 7, no. 2, pp. 281–288, Feb. 2014.

[28] V. R. Parasa, J. R. Muvva, J. F. Rose, C. Braian, S. Brighenti, and M. Lerm, “Inhibition of Tissue Matrix Metalloproteinases Interferes with Mycobacterium tuberculosis-Induced Granuloma Formation and Reduces Bacterial Load in a Human Lung Tissue Model,” *Front. Microbiol.*, vol. 8, 2017.

[29] L. B. Tezera, M. K. Bielecka, A. Chancellor, M. T. Reichmann, B. Al Shammari, P. Brace, A. Batty, A. Tocheva, S. Jogai, and B. G. Marshall, “Dissection of the host-pathogen interaction in human tuberculosis using a bioengineered 3-dimensional model,” *Elife*, vol. 6, 2017.

[30] R. Avraham and D. T. Hung, “A perspective on single cell behavior during infection,” *Gut Microbes*, vol. 7, no. 6, pp. 518–525, Nov. 2016.

[31] H. M. S. Algood, P. L. Lin, D. Yankura, A. Jones, J. Chan, and J. L. Flynn, “TNF Influences Chemokine Expression of Macrophages In Vitro and That of CD11b+ Cells In Vivo during Mycobacterium tuberculosis Infection,” *J. Immunol.*, vol. 172, no. 11, pp. 6846–6857, Jun. 2004.

[32] R. Edmondson, J. J. Broglie, A. F. Adcock, and L. Yang, “Three-Dimensional Cell Culture Systems and Their Applications in Drug Discovery and Cell-Based Biosensors,” *Assay Drug Dev. Technol.*, vol. 12, no. 4, pp. 207–218, May 2014.

[33] V. R. Parasa, M. J. Rahman, A. T. Ngyuen Hoang, M. Svensson, S. Brighenti, and M. Lerm, “Modeling Mycobacterium tuberculosis early granuloma formation in experimental human lung tissue,” *Dis. Model. Mech.*, vol. 7, no. 2, pp. 281–288, Feb. 2014.

[34] G. Y. Lee, P. A. Kenny, E. H. Lee, and M. J. Bissell, “Three-dimensional culture models of normal and malignant breast epithelial cells,” *Nat. Methods*, vol. 4, no. 4, pp. 359–365, Apr. 2007.

[35] A. Colom, R. Galgoczy, I. Almendros, A. Xaubet, R. Farré, and J. Alcaraz, “Oxygen diffusion and consumption in extracellular matrix gels: Implications for designing three-dimensional cultures,” *J. Biomed. Mater. Res. A*, vol. 102, no. 8, pp. 2776–2784, Aug. 2014.

[36] M. E. Gough, E. A. Graviss, and E. E. May, “The dynamic immunomodulatory effects of vitamin D3 during Mycobacterium infection,” *Innate Immun.*, vol. 23, no. 6, pp. 506–523, Aug. 2017.

[37] Y. Kong, D. Yang, S. L. G. Cirillo, S. Li, A. Akin, K. P. Francis, T. Maloney, and J. D. Cirillo, “Application of Fluorescent Protein Expressing Strains to Evaluation of Anti-Tuberculosis Therapeutic Efficacy In Vitro and In Vivo,” *PLOS ONE*, vol. 11, no. 3, p. e0149972, Mar. 2016.

[38] C. A. Giurumescu, S. Kang, T. A. Planchon, E. Betzig, J. Bloomekatz, D. Yelon, P. Cosman, and A. D. Chisholm, “Quantitative semi-automated analysis of morphogenesis with single-cell resolution in complex embryos,” *Development*, vol. 139, no. 22, pp. 4271–4279, Nov. 2012.

[39] N. Karthikeyani Visalakshi and K. Thangavel, “Impact of Normalization in Distributed K-Means Clustering,” *Int. J. Soft Comput.*, vol. 4, no. 4, pp. 168–172, 2009.

[40] D. Arthur and S. Vassilvitskii, “k-means++: The advantages of careful seeding,” in *Proceedings of the eighteenth annual ACM-SIAM symposium on Discrete algorithms*, 2007, pp. 1027–1035.

[41] C. Ding and X. He, “K-means clustering via principal component analysis,” in *Proceedings of the twenty-first international conference on Machine learning*, 2004, p. 29.

[42] J. Liang, L. Bai, C. Dang, and F. Cao, “The K-Means-Type Algorithms Versus Imbalanced Data Distributions,” *IEEE Trans. Fuzzy Syst.*, vol. 20, no. 4, pp. 728–745, Aug. 2012.

[43] Gregor Rothe and Günter Valet, “Phagocytosis, intracellular pH, and cell volume in the multifunctional analysis of granulocytes by flow cytometry - Rothe - 1988 - Cytometry Part A - Wiley Online Library,” *Cytometry*, no. 9, pp. 316–24, Sep. 1987.

[44] J. Huang and C. X. Ling, “Using AUC and accuracy in evaluating learning algorithms,” *IEEE Trans. Knowl. Data Eng.*, vol. 17, no. 3, pp. 299–310, Mar. 2005.

[45] M. R. Feldesman, “Classification trees as an alternative to linear discriminant analysis,” *Am. J. Phys. Anthropol.*, vol. 119, no. 3, pp. 257–275, Nov. 2002.

[46] S. Pavlou, J. Lindsay, R. Ingram, H. Xu, and M. Chen, “Sustained high glucose exposure sensitizes macrophage responses to cytokine stimuli but reduces their phagocytic activity,” *BMC Immunol.*, vol. 19, no. 1, Dec. 2018.

[47] L. D. Loose, “Characterization of Macrophage Dysfunction in Rodent Malaria,” *J. Leukoc. Biol.*, vol. 36, no. 6, pp. 703–718, 1984.

[48] C. L. Sershen, S. J. Plimpton, and E. E. May, “Oxygen Modulates the Effectiveness of Granuloma Mediated Host Response to Mycobacterium tuberculosis: A Multiscale Computational Biology Approach,” *Front. Cell. Infect. Microbiol.*, vol. 6, Feb. 2016.

[49] F. M. Marim, T. N. Silveira, D. S. Lima, and D. S. Zamboni, “A Method for Generation of Bone Marrow-Derived Macrophages from Cryopreserved Mouse Bone Marrow Cells,” *PLoS ONE*, vol. 5, no. 12, Dec. 2010.

[50] M. E. Gough, E. A. Graviss, T.-A. Chen, E. M. Obasi, and E. E. May, “Compounding effect of vitamin D3 diet, supplementation, and alcohol exposure on macrophage response to mycobacterium infection,” *Tuberculosis*, p. S1472979219301490, Apr. 2019.

[51] K. Blochlinger and H. Diggelmann, “Hygromycin B phosphotransferase as a selectable marker for DNA transfer experiments with higher eucaryotic cells.,” *Mol. Cell. Biol.*, vol. 4, no. 12, pp. 2929–2931, Dec. 1984.

[52] C. Xu, M. S. Inokuma, J. Denham, K. Golds, P. Kundu, J. D. Gold, and M. K. Carpenter, “Feeder-free growth of undifferentiated human embryonic stem cells,” *Nat. Biotechnol.*, vol. 19, no. 10, p. 971, Oct. 2001.

[53] B. Lagier, V. Pelicic, D. Lecossier, G. Prod’hom, J. Rauzier, C. Guilhot, B. Gicquel, and A. J. Hance, “Identification of genetic loci implicated in the survival of Mycobacterium smegmatis in human mononuclear phagocytes,” *Mol. Microbiol.*, vol. 29, no. 2, pp. 465–475, Jul. 1998.

[54] E. Anes, P. Peyron, L. Staali, L. Jordao, M. G. Gutierrez, H. Kress, M. Hagedorn, I. Maridonneau-Parini, M. A. Skinner, A. G. Wildeman, S. A. Kalamidas, M. Kuehnel, and G. Griffiths, “Dynamic life and death interactions between Mycobacterium smegmatis and J774 macrophages,” *Cell. Microbiol.*, vol. 8, no. 6, pp. 939–960, Jun. 2006.

[55] F. Krombach, S. Münzing, A.-M. Allmeling, J. T. Gerlach, J. Behr, and M. Dörger, “Cell Size of Alveolar Macrophages: An Interspecies Comparison,” *Environ. Health Perspect.*, vol. 105, pp. 1261–1263, 1997.

[56] S. Vijay, R. R. Nair, D. Sharan, K. Jakkala, N. Mukkayyan, S. Swaminath, A. Pradhan, N. V. Joshi, and P. Ajitkumar, “Mycobacterial Cultures Contain Cell Size and Density Specific Sub-populations of Cells with Significant Differential Susceptibility to Antibiotics, Oxidative and Nitrite Stress,” *Front. Microbiol.*, vol. 8, Mar. 2017.

[57] A. Ettinger and T. Wittmann, “Fluorescence Live Cell Imaging,” *Methods Cell Biol.*, vol. 123, pp. 77–94, 2014.

[58] J. Icha, C. Kunath, M. Rocha-Martins, and C. Norden, “Independent modes of ganglion cell translocation ensure correct lamination of the zebrafish retina,” *J. Cell Biol.*, vol. 215, no. 2, pp. 259–275, Oct. 2016.

[59] V. Magidson and A. Khodjakov, “Circumventing photodamage in live-cell microscopy,” *Methods Cell Biol.*, vol. 114, 2013.

[60] T. Yamane, “Elementary sampling theory,” 1967.

[61] D. L. Stolley and E. E. May, “Spatiotemporal Analysis of Mycobacterium-Dependent Macrophage Response,” in *2018 40th Annual International Conference of the IEEE Engineering in Medicine and Biology Society (EMBC)*, 2018, pp. 2390–2393.

[62] J. Zhang, M. Calafiore, Q. Zeng, X. Zhang, Y. Huang, R. A. Li, W. Deng, and M. Zhao, “Electrically Guiding Migration of Human Induced Pluripotent Stem Cells,” *Stem Cell Rev. Rep.*, vol. 7, no. 4, pp. 987–996, Nov. 2011.

[63] R Core Team, *R: A Language and Environment for Statistical Computing*. Vienna, Austria: R Foundation for Statistical Computing, 2018.

[64] Ha. Kassambara, *ggpubr: “ggplot2” Based Publication Ready Plots*. 2018.

[65] H. Wickham, *ggplot2: Elegant Graphics for Data Analysis*. Springer-Verlag New York, 2016.

[66] H. Wickham, R. Francois, L. Henry, and K. Muller, *dplyr: A Grammar of Data Manipulation*. 2019.

[67] R. J. Petrie and K. M. Yamada, "At the leading edge of three-dimensional cell migration," *J. Cell Sci.*, vol. 125, no. 24, pp. 5917–5926, Dec. 2012.

[68] S. E. Webb, J. W. Pollard, and G. E. Jones, "Direct observation and quantification of macrophage chemoattraction to the growth factor CSF-1," *J. Cell Sci.*, vol. 109, no. 4, pp. 793–803, Apr. 1996.

[69] K. C. Onwueme, C. J. Vos, J. Zurita, J. A. Ferreras, and L. E. N. Quadri, "The dimycocerosate ester polyketide virulence factors of mycobacteria," *Prog. Lipid Res.*, vol. 44, no. 5, pp. 259–302, Sep. 2005.

[70] C. J. Cambier, K. K. Takaki, R. P. Larson, R. E. Hernandez, D. M. Tobin, K. B. Urdahl, C. L. Cosma, and L. Ramakrishnan, "Mycobacteria manipulate macrophage recruitment through coordinated use of membrane lipids," *Nature*, vol. 505, no. 7482, pp. 218–222, Jan. 2014.

[71] K. Cui, C. L. Ardell, N. P. Podolnikova, and V. P. Yakubenko, "Distinct Migratory Properties of M1, M2, and Resident Macrophages Are Regulated by αDβ2 and αMβ2 Integrin-Mediated Adhesion," *Front. Immunol.*, vol. 9, Nov. 2018.

[72] J. L. Segovia-Juarez, S. Ganguli, and D. Kirschner, "Identifying control mechanisms of granuloma formation during M. tuberculosis infection using an agent-based model," *J. Theor. Biol.*, vol. 231, no. 3, pp. 357–376, Dec. 2004.

[73] J. C. J. Ray, J. L. Flynn, and D. E. Kirschner, “Synergy between individual tumor necrosis factor-dependent functions determines granuloma performance for controlling Mycobacterium tuberculosis infection,” *J. Immunol. Baltim. Md 1950*, vol. 182, no. 6, pp. 3706–3717, Mar. 2009.

[74] M. Fallahi-Sichani, M. A. Schaller, D. E. Kirschner, S. L. Kunkel, and J. J. Linderman, “Identification of Key Processes that Control Tumor Necrosis Factor Availability in a Tuberculosis Granuloma,” *PLOS Comput. Biol.*, vol. 6, no. 5, p. e1000778, May 2010.

[75] C. Warrender, S. Forrest, and F. Koster, “Modeling Intercellular Interactions in Early Mycobacterium Infection,” *Bull. Math. Biol.*, vol. 68, no. 8, pp. 2233–2261, Nov. 2006.

[76] M. I. Sadek, E. Sada, Z. Toossi, S. K. Schwander, and E. A. Rich, “Chemokines induced by infection of mononuclear phagocytes with mycobacteria and present in lung alveoli during active pulmonary tuberculosis,” *Am. J. Respir. Cell Mol. Biol.*, vol. 19, no. 3, pp. 513–521, Sep. 1998.

[77] W. Iijima, H. Ohtani, T. Nakayama, Y. Sugawara, E. Sato, H. Nagura, O. Yoshie, and T. Sasano, “Infiltrating CD8+ T cells in oral lichen planus predominantly express CCR5 and CXCR3 and carry respective chemokine ligands RANTES/CCL5 and IP-10/CXCL10 in their cytolytic granules: a potential self-recruiting mechanism,” *Am. J. Pathol.*, vol. 163, no. 1, pp. 261–268, Jul. 2003.

[78] S. V. Capuano, D. A. Croix, S. Pawar, A. Zinovik, A. Myers, P. L. Lin, S. Bissel, C. Fuhrman, E. Klein, and J. L. Flynn, “Experimental Mycobacterium tuberculosis

Infection of Cynomolgus Macaques Closely Resembles the Various Manifestations of Human M. tuberculosis Infection," *Infect. Immun.*, vol. 71, no. 10, pp. 5831–5844, Oct. 2003.

[79] G. T. Brice, N. L. Graber, S. L. Hoffman, and D. L. Doolan, "Expression of the chemokine MIG is a sensitive and predictive marker for antigen-specific, genetically restricted IFN-gamma production and IFN-gamma-secreting cells.," *J. Immunol. Methods*, vol. 257, no. 1–2, pp. 55–69, Nov. 2001.

[80] M. J. Staruch, R. Camacho, and F. J. Dumont, "Distinctive calcineurin-dependent (FK506-sensitive) mechanisms regulate the production of the CC chemokines macrophage inflammatory protein (MIP)-1alpha, MIP-1beta, and RANTES vs IL-2 and TNF-alpha by activated human T cells," *Cell. Immunol.*, vol. 190, no. 2, pp. 121–131, Dec. 1998.

[81] A. D. O'Brien, T. J. Standiford, P. J. Christensen, S. E. Wilcoxen, and R. Paine, "Chemotaxis of alveolar macrophages in response to signals derived from alveolar epithelial cells," *J. Lab. Clin. Med.*, vol. 131, no. 5, pp. 417–424, May 1998.

[82] R. Van Furth, M. C. Diesselhoff-den Dulk, and H. Mattie, "Quantitative study on the production and kinetics of mononuclear phagocytes during an acute inflammatory reaction," *J. Exp. Med.*, vol. 138, no. 6, pp. 1314–1330, Dec. 1973.

[83] L. G. Wayne and L. G. Hayes, "An in vitro model for sequential study of shiftdown of Mycobacterium tuberculosis through two stages of nonreplicating persistence.," *Infect. Immun.*, vol. 64, no. 6, pp. 2062–2069, Jun. 1996.

[84] S. Paul, P. Laochumroonvorapong, and G. Kaplan, “Comparable Growth of Virulent and Avirulent Mycobacterium tuberculosis in Human Macrophages In Vitro,” *J. Infect. Dis.*, vol. 174, no. 1, pp. 105–112, Jul. 1996.

[85] M. Zhang, J. Gong, Y. Lin, and P. F. Barnes, “Growth of Virulent and Avirulent Mycobacterium tuberculosis Strains in Human Macrophages,” *Infect. Immun.*, vol. 66, no. 2, pp. 794–799, Feb. 1998.

[86] S. Marino, I. B. Hogue, C. J. Ray, and D. E. Kirschner, “A Methodology For Performing Global Uncertainty And Sensitivity Analysis In Systems Biology,” *J. Theor. Biol.*, vol. 254, no. 1, pp. 178–196, Sep. 2008.

[87] R. J. Petrie and K. M. Yamada, “Multiple mechanisms of 3D migration: the origins of plasticity,” *Curr. Opin. Cell Biol.*, vol. 42, pp. 7–12, Oct. 2016.

[88] F. Y. McWhorter, T. Wang, P. Nguyen, T. Chung, and W. F. Liu, “Modulation of macrophage phenotype by cell shape,” *Proc. Natl. Acad. Sci. U. S. A.*, vol. 110, no. 43, pp. 17253–17258, Oct. 2013.

[89] D. Birant and A. Kut, “ST-DBSCAN: An algorithm for clustering spatial–temporal data,” *Data Knowl. Eng.*, vol. 60, no. 1, pp. 208–221, Jan. 2007.

[90] H. Wadell, “Sphericity and Roundness of Rock Particles,” *J. Geol.*, vol. 41, no. 3, pp. 310–331, Apr. 1933.

[91] F. T. Liu, K. M. Ting, and Z.-H. Zhou, “Isolation Forest,” in *2008 Eighth IEEE International Conference on Data Mining*, Pisa, Italy, 2008, pp. 413–422.

[92] T. Salim, C. L. Sershen, and E. E. May, “Investigating the Role of TNF-α and IFN-γ Activation on the Dynamics of iNOS Gene Expression in LPS Stimulated Macrophages,” *PLoS ONE*, vol. 11, no. 6, Jun. 2016.

[93] N. Parameswaran and S. Patial, “Tumor Necrosis Factor-α Signaling in Macrophages,” *Crit. Rev. Eukaryot. Gene Expr.*, vol. 20, no. 2, pp. 87–103, 2010.

[94] D. A. Zaitsev, “k-neighborhood for Cellular Automata,” *ArXiv160508870 Cs*, May 2016.

[95] H. Akaike, “A new look at the statistical model identification,” *IEEE Trans. Autom. Control*, vol. 19, no. 6, pp. 716–723, Dec. 1974.

[96] K. P. Burnham and D. R. Anderson, “Multimodel Inference: Understanding AIC and BIC in Model Selection,” *Sociol. Methods Res.*, vol. 33, no. 2, pp. 261–304, Nov. 2004.

[97] G. G. Mahairas, P. J. Sabo, M. J. Hickey, D. C. Singh, and C. K. Stover, “Molecular analysis of genetic differences between Mycobacterium bovis BCG and virulent M. bovis.,” *J. Bacteriol.*, vol. 178, no. 5, pp. 1274–1282, Mar. 1996.

[98] J. R. Goldsmith and C. Jobin, “Think Small: Zebrafish as a Model System of Human Pathology,” *J. Biomed. Biotechnol.*, vol. 2012, pp. 1–12, 2012.

[99] M. P. Sepulcre, F. Alcaraz-Pérez, A. López-Muñoz, F. J. Roca, J. Meseguer, M. L. Cayuela, and V. Mulero, “Evolution of lipopolysaccharide (LPS) recognition and signaling: fish TLR4 does not recognize LPS and negatively regulates NF-kappaB activation,” *J. Immunol. Baltim. Md 1950*, vol. 182, no. 4, pp. 1836–1845, Feb. 2009.

[100] H. Kothari, L. V. M. Rao, R. Vankayalapati, and U. R. Pendurthi, “Mycobacterium tuberculosis Infection and Tissue Factor Expression in Macrophages,” *PLOS ONE*, vol. 7, no. 9, p. e45700, Sep. 2012.

[101] N. Reiling, C. Hölscher, A. Fehrenbach, S. Kröger, C. J. Kirschning, S. Goyert, and S. Ehlers, “Cutting Edge: Toll-Like Receptor (TLR)2- and TLR4-Mediated Pathogen Recognition in Resistance to Airborne Infection with Mycobacterium tuberculosis,” *J. Immunol.*, vol. 169, no. 7, pp. 3480–3484, Oct. 2002.

[102] J. Basu, D.-M. Shin, and E.-K. Jo, “Mycobacterial signaling through toll-like receptors,” *Front. Cell. Infect. Microbiol.*, vol. 2, Nov. 2012.

[103] C. Morgan, J. W. Pollard, and E. R. Stanley, “Isolation and characterization of a cloned growth factor dependent macrophage cell line, BAC1.2F5,” *J. Cell. Physiol.*, vol. 130, no. 3, pp. 420–427, 1987.

[104] D. M. Mosser, “The many faces of macrophage activation,” *J. Leukoc. Biol.*, vol. 73, no. 2, pp. 209–212, 2003.

[105] S. Gordon and P. R. Taylor, “Monocyte and macrophage heterogeneity,” *Nat. Rev. Immunol.*, vol. 5, no. 12, pp. 953–964, Dec. 2005.

[106] M. Benoit, B. Desnues, and J.-L. Mege, “Macrophage Polarization in Bacterial Infections,” *J. Immunol.*, vol. 181, no. 6, pp. 3733–3739, Sep. 2008.

[107] Z. Huang, Q. Luo, Y. Guo, J. Chen, G. Xiong, Y. Peng, J. Ye, and J. Li, “Mycobacterium tuberculosis-Induced Polarization of Human Macrophage Orchestrates the Formation and Development of Tuberculous Granulomas In Vitro,” *PLOS ONE*, vol. 10, no. 6, p. e0129744, Jun. 2015.

[108] S. Marino, N. A. Cilfone, J. T. Mattila, J. J. Linderman, J. L. Flynn, and D. E. Kirschner, “Macrophage Polarization Drives Granuloma Outcome during Mycobacterium tuberculosis Infection,” *Infect. Immun.*, vol. 83, no. 1, pp. 324–338, Jan. 2015.

[109] L. Vincent and P. Soille, “Watersheds in digital spaces: an efficient algorithm based on immersion simulations,” *IEEE Trans. Pattern Anal. Mach. Intell.*, vol. 13, no. 6, pp. 583–598, Jun. 1991.

[110] Bo Zhang, C. Zimmer, and J.- Olivo-Marin, “Tracking fluorescent cells with coupled geometric active contours,” in *2004 2nd IEEE International Symposium on Biomedical Imaging: Nano to Macro (IEEE Cat No. 04EX821)*, 2004, pp. 476-479 Vol. 1.

[111] F. Cloppet and A. Boucher, “Segmentation of complex nucleus configurations in biological images,” *Pattern Recognit. Lett.*, vol. 31, no. 8, pp. 755–761, Jun. 2010.

[112] G. Hamarneh and X. Li, “Watershed segmentation using prior shape and appearance knowledge,” *Image Vis. Comput.*, vol. 27, no. 1, pp. 59–68, Jan. 2009.

[113] C. Zimmer and J.- Olivo-Marin, “Coupled parametric active contours,” *IEEE Trans. Pattern Anal. Mach. Intell.*, vol. 27, no. 11, pp. 1838–1842, Nov. 2005.

[114] T. Wollmann, M. Gunkel, I. Chung, H. Erfle, K. Rippe, and K. Rohr, “GRUU-Net: Integrated convolutional and gated recurrent neural network for cell segmentation,” *Med. Image Anal.*, vol. 56, pp. 68–79, Aug. 2019.

[115] J. Stegmaier, T. V. Spina, A. X. Falcão, A. Bartschat, R. Mikut, E. Meyerowitz, and A. Cunha, “Cell segmentation in 3D confocal images using supervoxel merge-

forests with CNN-based hypothesis selection," in *2018 IEEE 15th International Symposium on Biomedical Imaging (ISBI 2018)*, 2018, pp. 382–386.

[116] D. Eschweiler, T. V. Spina, R. C. Choudhury, E. Meyerowitz, A. Cunha, and J. Stegmaier, "CNN-Based Preprocessing to Optimize Watershed-Based Cell Segmentation in 3D Confocal Microscopy Images," in *2019 IEEE 16th International Symposium on Biomedical Imaging (ISBI 2019)*, 2019, pp. 223–227.

[117] P. R. Jungblut, U. E. Schaible, H.-J. Mollenkopf, U. Zimny-Arndt, B. Raupach, J. Mattow, P. Halada, S. Lamer, K. Hagens, and S. H. E. Kaufmann, "Comparative proteome analysis of Mycobacterium tuberculosis and Mycobacterium bovis BCG strains: towards functional genomics of microbial pathogens," *Mol. Microbiol.*, vol. 33, no. 6, pp. 1103–1117, 1999.

[118] C. Deb, C.-M. Lee, V. S. Dubey, J. Daniel, B. Abomoelak, T. D. Sirakova, S. Pawar, L. Rogers, and P. E. Kolattukudy, "A Novel In Vitro Multiple-Stress Dormancy Model for Mycobacterium tuberculosis Generates a Lipid-Loaded, Drug-Tolerant, Dormant Pathogen," *PLOS ONE*, vol. 4, no. 6, p. e6077, Jun. 2009.

[119] M. L. Coleman, E. A. Sahai, M. Yeo, M. Bosch, A. Dewar, and M. F. Olson, "Membrane blebbing during apoptosis results from caspase-mediated activation of ROCK I," *Nat. Cell Biol.*, vol. 3, no. 4, p. 339, Apr. 2001.

[120] D. Mahamed, M. Boulle, Y. Ganga, C. Mc Arthur, S. Skroch, L. Oom, O. Catinas, K. Pillay, M. Naicker, S. Rampersad, C. Mathonsi, J. Hunter, E. B. Wong, M. Suleman, G. Sreejit, A. S. Pym, G. Lustig, and A. Sigal, "Intracellular growth of Mycobacterium

tuberculosis after macrophage cell death leads to serial killing of host cells," *eLife*, vol. 6.

[121] Y. Weinrauch and A. Zychlinsky, "The Induction of Apoptosis by Bacterial Pathogens," *Annu. Rev. Microbiol.*, vol. 53, no. 1, pp. 155–187, 1999.

[122] J. Keane, M. K. Balcewicz-Sablinska, H. G. Remold, G. L. Chupp, B. B. Meek, M. J. Fenton, and H. Kornfeld, "Infection by Mycobacterium tuberculosis promotes human alveolar macrophage apoptosis.," *Infect. Immun.*, vol. 65, no. 1, pp. 298–304, Jan. 1997.

[123] J. I. Aguilo, H. Alonso, S. Uranga, D. Marinova, A. Arbués, A. de Martino, A. Anel, M. Monzon, J. Badiola, J. Pardo, R. Brosch, and C. Martin, "ESX-1-induced apoptosis is involved in cell-to-cell spread of Mycobacterium tuberculosis," *Cell. Microbiol.*, vol. 15, no. 12, pp. 1994–2005, Dec. 2013.

[124] J. Augenstreich, A. Arbues, R. Simeone, E. Haanappel, A. Wegener, F. Sayes, F. Le Chevalier, C. Chalut, W. Malaga, C. Guilhot, R. Brosch, and C. Astarie-Dequeker, "ESX-1 and phthiocerol dimycocerosates of Mycobacterium tuberculosis act in concert to cause phagosomal rupture and host cell apoptosis," *Cell. Microbiol.*, vol. 19, no. 7, 2017.

[125] D. M. Kelly, A. M. C. ten Bokum, S. M. O'Leary, M. P. O'Sullivan, and J. Keane, "Bystander Macrophage Apoptosis after Mycobacterium tuberculosis H37Ra Infection," *Infect. Immun.*, vol. 76, no. 1, pp. 351–360, Jan. 2008.

[126] J. Lee, M. Hartman, and H. Kornfeld, "Macrophage Apoptosis in Tuberculosis," *Yonsei Med. J.*, vol. 50, no. 1, pp. 1–11, Feb. 2009.

[127] T. Dallenga, U. Repnik, B. Corleis, J. Eich, R. Reimer, G. W. Griffiths, and U. E. Schaible, “M. tuberculosis-Induced Necrosis of Infected Neutrophils Promotes Bacterial Growth Following Phagocytosis by Macrophages,” *Cell Host Microbe*, vol. 22, no. 4, pp. 519-530.e3, Oct. 2017.

[128] T. R. Lerner, S. Borel, D. J. Greenwood, U. Repnik, M. R. G. Russell, S. Herbst, M. L. Jones, L. M. Collinson, G. Griffiths, and M. G. Gutierrez, “Mycobacterium tuberculosis replicates within necrotic human macrophages,” *J. Cell Biol.*, vol. 216, no. 3, pp. 583–594, Mar. 2017.

[129] X. Wu, G. Deng, X. Hao, Y. Li, J. Zeng, C. Ma, Y. He, X. Liu, and Y. Wang, “A Caspase-Dependent Pathway Is Involved in Wnt/β-Catenin Signaling Promoted Apoptosis in Bacillus Calmette-Guerin Infected RAW264.7 Macrophages,” *Int. J. Mol. Sci.*, vol. 15, no. 3, pp. 5045–5062, Mar. 2014.

[130] L. Chávez-Galán, D. Vesin, D. Martinvalet, and I. Garcia, “Low Dose BCG Infection as a Model for Macrophage Activation Maintaining Cell Viability,” *J. Immunol. Res.*, vol. 2016, 2016.

[131] C. Durek, S. Rüsch-Gerdes, D. Jocham, and A. Böhle, “Sensitivity of BCG to modern antibiotics,” *Eur. Urol.*, vol. 37 Suppl 1, pp. 21–25, 2000.

[132] S. Niemann, E. Richter, and S. Rüsch-Gerdes, “Differentiation among Members of the Mycobacterium tuberculosis Complex by Molecular and Biochemical Features: Evidence for Two Pyrazinamide-Susceptible Subtypes of M. bovis,” *J. Clin. Microbiol.*, vol. 38, no. 1, pp. 152–157, Jan. 2000.

[133] R. Frothingham, H. G. Hills, and K. H. Wilson, “Extensive DNA sequence conservation throughout the Mycobacterium tuberculosis complex.,” *J. Clin. Microbiol.*, vol. 32, no. 7, pp. 1639–1643, Jul. 1994.

[134] P. Schierloh, N. Yokobori, M. Alemán, V. Landoni, L. Geffner, R. M. Musella, J. Castagnino, M. Baldini, E. Abbate, S. S. de la Barrera, and M. C. Sasiain, “Mycobacterium tuberculosis-Induced Gamma Interferon Production by Natural Killer Cells Requires Cross Talk with Antigen-Presenting Cells Involving Toll-Like Receptors 2 and 4 and the Mannose Receptor in Tuberculous Pleurisy,” *Infect. Immun.*, vol. 75, no. 11, pp. 5325–5337, Nov. 2007.

[135] M. Allen, C. Bailey, I. Cahatol, L. Dodge, J. Yim, C. Kassissa, J. Luong, S. Kasko, S. Pandya, and V. Venketaraman, “Mechanisms of Control of Mycobacterium tuberculosis by NK Cells: Role of Glutathione,” *Front. Immunol.*, vol. 6, Oct. 2015.